

5. SITE 766¹

Shipboard Scientific Party²

HOLE 766A

Date occupied: 19 October 1988
Date departed: 26 October 1988
Time on hole: 5 days
Position: 19°55.925'S, 110°27.243'E
Bottom felt (rig floor; m, drill pipe measurement): 4008.0
Distance between rig floor and sea level (m): 10.50
Water depth (drill pipe measurement from sea level, m): 3997.5
Total depth (rig floor, m): 4535.20
Penetration (m): 527.20
Number of cores (including cores with no recovery): 55
Total length of cored section (m): 527.16
Total core recovered (m): 347.49
Core recovery (%): 66
Oldest sediment cored:
Depth (mbsf): 466.70
Nature: Greenish gray to black sandstone and bioturbated siltstone
Earliest age: late Valanginian
Latest age: Hauterivian
Measured velocity (km/s): 1.90
Hard rock:
Depth (mbsf): 458
Nature: Sparsely clinopyroxene and phytic basalt flow (sill)
Measured velocity (km/s): 4.216

Principal results: Site 766 is located at 19°55.925'S, 110°27.243'E, at the foot of the western escarpment of the Exmouth Plateau, facing the Gascoyne Abyssal Plain, in a water depth of 3997.5 m. The site is on the geophysical continent/ocean boundary of the southernmost seafloor-spreading compartment of the Gascoyne Abyssal Plain. The Cape Range Fracture Zone, which separates the Gascoyne Abyssal Plain from the Cuvier Abyssal Plain to the south, extends in a southeast-northwest direction, slightly south of the site location. Site surveys were conducted by the Australian Bureau of Mineral Resources (BMR), which delineated the drill site on the crossover of BMR *Rig Seismic* Lines 55/002 and 55/003E.

The initial drilling program proposed for this site called for Advanced Piston Corer/Extended-Core Barrel (APC/XCB) coring to refusal, Rotary Core Barrel (RCB) coring to what was interpreted as basement intermediate between continental and oceanic rocks, and physical and geochemical well logging. However, because of time restrictions, a reduced program that eliminated the APC/XCB coring was conducted. The major objective at Site 766 was to reach and sample the basal, synrift, or early drift sediments and underlying basement. This revised drilling program gave the scientists the flexibility to extend sediment or basement penetration if necessary.

The principal objective of drilling at Site 766 was to understand the tectonic, sedimentary, and magmatic evolution of the outermost edge of a passive margin. As a result of the extensive sediment cover

at most passive margins, it is rarely possible to core the transition zone from continental to oceanic basement; the sediment-starved nature of the northwestern Australian margin made this objective attainable at Site 766.

The specific questions posed at Site 766 were as follows:

1. What is the nature of "basement" transitional to continental and oceanic crust in a rifted passive margin?
2. What are the ages of the onset of rifting between Australia and India, and of earliest seafloor spreading in the Gascoyne and Cuvier abyssal plains?
3. What is the lithologic and seismo-stratigraphic sequence stratigraphy along the continental margin to deep-ocean transect from Sites 762 and 763, drilled during Leg 122 on the adjacent Exmouth Plateau, to Site 766?

Total penetration at Site 766 was 527 mbsf, and average core recovery was 66%, with the best recovery in the critical, lower section. The base of the sedimentary section was placed at 466.7 meters below seafloor (mbsf), after which coring retrieved only igneous rock. However, the first igneous rocks were encountered at 458 mbsf. These rocks are interpreted as intrusive sheets (small sills) of igneous material, which are interlayered with green-gray siltstones; below 466.7 mbsf two or more large igneous intrusions were encountered and were cored for a total of 60 m.

The geological location of Site 766 places it within 10 km of marine magnetic anomaly M10, the 130-Ma isochron mapped along the Exmouth margin. The published oceanic spreading rate of 3.2 cm/yr predicts onset of seafloor spreading at 134 Ma, in the M11 isochron of late Valanginian age. As a result, basal sediments and volcanics in Site 766 should also be of late Valanginian age. This age is exactly as determined by radiolarian/dinoflagellate/nannofossil stratigraphy for the oldest sediments at Site 766. The basement at Site 766 must have therefore been rifted, buried by sediments, and intruded by tholeiitic magmas immediately before the formation of true oceanic crust at the continent/ocean boundary. Whether Triassic crust is preserved at Site 766 or the hypabyssal intrusives grade downward into larger intrusive bodies remains unsolved.

The sedimentary succession consists of eight units and subunits. These are, from bottom to top:

1. 466.7-304.2 mbsf; greenish-gray to black sandstone and bioturbated siltstone, with glauconite, quartz, bioclasts, and altered volcanics; uppermost Valanginian through Hauterivian.
2. 304.2-239.4 mbsf; dark greenish-gray to black claystone; upper Hauterivian through Barremian.
3. 239.4-191.0 mbsf; tan to light green nannofossil chalk, zeolitic and clayey in upper portion, siliceous in the lower half; Aptian through lower Albian.
4. 191.0-136.5 mbsf; brown to tan, bioturbated chalk with zeolite and clay; Albian through Cenomanian.
5. 136.5-114.8 mbsf; zeolitic calcareous ooze and clay, banded in brownish colors; Turonian through lower Campanian.
6. 114.8-82.8 mbsf; pink to pale brown nannofossil ooze, with graded beds; Campanian through lower Paleocene.
7. 82.8-8.0 mbsf; pale brown to white nannofossil ooze; Paleocene through lower Eocene and middle Pliocene.
8. 8.0 mbsf—seafloor; pink nannofossil ooze; lower Pleistocene.

We interpret the Hauterivian to Barremian sand, silt, and clay sequence as a distal part of a submarine fan, that in seismic images can be seen to thicken toward the continental margin. Hydrocarbon levels are extremely low. The Aptian to Barremian boundary repre-

¹ Ludden, J. N., Gradstein, F. M., et al., 1990. *Proc. ODP, Init. Repts.*, 123: College Station, TX (Ocean Drilling Program).

² Shipboard Scientific Party is as given in list of participants preceding the contents.

sents a marked change in sedimentation, from hemipelagic, gravity, and traction deposition of largely terrigenous and shallow-marine sediment with abundant plant spores, to pelagic, hemipelagic, and lesser gravity deposition of calcareous material (largely nannofossils). The peak occurrence of zeolites coincides with the Cenomanian/Turonian boundary. Restored sedimentation rates of approximately 1.5 cm/k.y. for the Hauterivian through Aptian sequence, change to rates below 0.65 cm/k.y. for the remainder of the section. This rapid change in sedimentation rate in the Aptian agrees with that in Site 765, on the Argo Abyssal Plain, and may be a global trend. Subsidence and sedimentation analysis indicates that the site originated in a water depth of about 800 m, with rapid early subsidence that declined from 20 to 4 cm/k.y. in the Early Cretaceous, and much lower rates beyond, to its present water depth at 4 km. The site was always above the calcium carbonate compensation level.

The first igneous rock, interpreted as an intrusive sheet, was encountered at 458 mbsf. This was followed by an 8-m interlayered sequence of 1- to 1.5-m-thick intrusions and dark green to dark gray siltstone. While coring from 467.7 to 527 mbsf, we recovered a thick diabase intrusion; recovery in the intrusion was 100%.

Only one definitive intrusive contact was preserved in the sequence. This contact inclines at 30° and is chilled against sediments that have been baked to within 5 to 10 cm from the contact. No hyaloclastite breccia was drilled, and all the igneous bodies display a symmetric gradational increase in grain size from base to center and top to center. All of these observations indicate that these igneous bodies are intrusions.

The base of the large diabase was not encountered and by the end of drilling, a total of 60 m had been recovered. The diabase contains gabbroic segregations that incline at 60° to 80°, relative to the drill core. In addition, cooling fractures are oriented in the same plane as the gabbroic segregation in all but the last two cores; both of these types of evidence indicate that this intrusion may be flat in the lowermost cores recovered (i.e., a sill) and grade upward into a dike, with a dip of up to 60°.

Geochemical data demonstrate that the intrusions are iron-rich tholeiites of mid-ocean ridge basalt (MORB) affinity. Some differences can be seen among the different intrusions, which can be explained by fractional crystallization, indicating that the intrusions may be cogenetic.

These intrusions are slightly to moderately altered by low-temperature processes. Veins and vesicles are filled with calcite, smectite, and zeolite; pyrite occurs with smectite and zeolite.

Physical properties, including bulk density and porosity, display similar average values as the igneous rocks at Site 765; the only difference is that at Site 766, values fluctuate much less, which supports the interpretation of a single massive intrusive below 467 mbsf.

Three petrophysical logging runs were completed at Site 766. The drill pipe was set at 260 mbsf (below the upper sequence of pelagic clays and oozes). Seismo-stratigraphic and porosity logs were run below this depth; both logging tools could not be lowered below a ledge immediately above the volcanics (approximately 445 mbsf). The Lower Cretaceous sands and siltstones were logged successfully between 445 and 245 mbsf.

The geochemical log, run through the drill pipe, was completed with drill pipe within 10 m of the base of the hole (approximately 515 mbsf). This log clearly delineates the sediment-intrusion contacts between 450 and 470 mbsf. Noteworthy on the logs are (1) an increase of thorium at 14 mbsf that may be associated with the hiatus between Eocene and Pliocene; (2) a similar enrichment in a 3-m zone above the K/T boundary, which suggests a hiatus, as also observed on the plot of the Site 766 burial history; (3) anoxic bottom conditions in the Hauterivian, as deduced from the thorium/uranium ratio, which agrees with the observation of many pyrite concretions in the sediment; and (4) petrophysical trends in the Hauterivian to Aptian section may indicate fluctuations in sea level.

BACKGROUND AND SCIENTIFIC OBJECTIVES

Site 766 is located at the foot of the western escarpment of the Exmouth Plateau, in a water depth of 4 km. The site was originally designated Site EP2A and was proposed in ODP proposal 121B (von Rad et al., 1986a, 1986b). Site surveys for the proposed location of Site EP2A were conducted by the Aus-

tralian Bureau of Mineral Resources (BMR) research vessel *Rig Seismic* during Legs 55 and 56 (Exon and Williamson, 1986).

The geographic location of Site 766, relative to the other Exmouth Plateau sites, is shown in Figure 1; its geographic coordinates are 19°55.925'S, 110°27.243'E. Site 766 is located on the crossing of BMR *Rig Seismic* Lines 55/002 and 55/003E, near Line 55/003B (Fig. 2). Details of the seismic and regional geology interpretations may be found in the "Underway Geophysics" chapter (this volume). The presence of a series of fault blocks resulting in a lack of stratigraphic continuity, both toward Exmouth Plateau and toward the Gascoyne Abyssal Plain from Site 766, considerably limits stratigraphic and tectonic scenarios for this part of the Australian continental margin (see below in "Scientific Objectives" section).

The initial drilling program proposed for Site 766 called for Advanced Piston Corer/Extended Core Barrel (APC/XCB) coring to refusal, Rotary Core Barrel (RCB) coring to what was interpreted as "intermediate" basement, and Schlumberger logging. However, because of time restrictions, a reduced program, which eliminated the APC/XCB coring, was conducted. Given the major objective, which was to reach and sample acoustically intermediate rocks that were interpreted as basement, this drilling program allowed us the flexibility to extend sediment or basement penetration if necessary.

Scientific Objectives

The principal objective for drilling at Site 766 was to understand the tectonic, sedimentary, and magmatic evolution of the extreme edge of a passive margin. The site is located on crust having an acoustic character intermediate to that of oceanic and continental crust. Because of extensive sediment cover at most passive margins, it is rarely possible to core the transition zone from continental to oceanic basement; the sediment-starved nature of the northwestern Australian margin made this possible at Site 766.

The transition of continental crust to oceanic basement is associated with asthenospheric upwelling, with consequent magmatic underplating and thinning of the continental lithosphere. The mechanisms involved in the initiation of constructive ridge volcanism in an oceanic ridge environment, and the ultimate thinning and elimination of continental crust by subsidence, stretching, and erosion, can be studied at Site 766.

Specific scientific questions raised at Site 766 are as follows:

1. What is the nature of "basement" transitional to continental and oceanic crust in a rifted passive margin?
2. What is the age of the onset of rifting in the Gascoyne and Cuvier abyssal plains?
3. What are the subsidence rates at Site 766 in comparison to Sites 762 and 763 on the Exmouth Plateau?
4. What is the lithologic and seismostratigraphic sequence stratigraphy along the continental margin to deep-ocean transect from Sites 762 and 763 to Site 766?
5. What is the regional tectonic evolution of the western Exmouth margin in relation to the post-Triassic rifting history of the northwestern Australian margin?
6. How does the timing of tectonic and paleoceanographic events at Site 766 compare with those observed in Site 765 on the Argo Abyssal Plain?

GEOLOGIC SETTING

Site 766 is located on transitional crust, i.e., continental crust alternating with volcanic flows and sills extruded or intruded during breakup, when magmatic underplating and upwelling of the asthenosphere occurred owing to the extreme thinning to 20 km of the continental crust (Mutter et al., 1988). At Site 766 we can learn more about the petrography and geo-

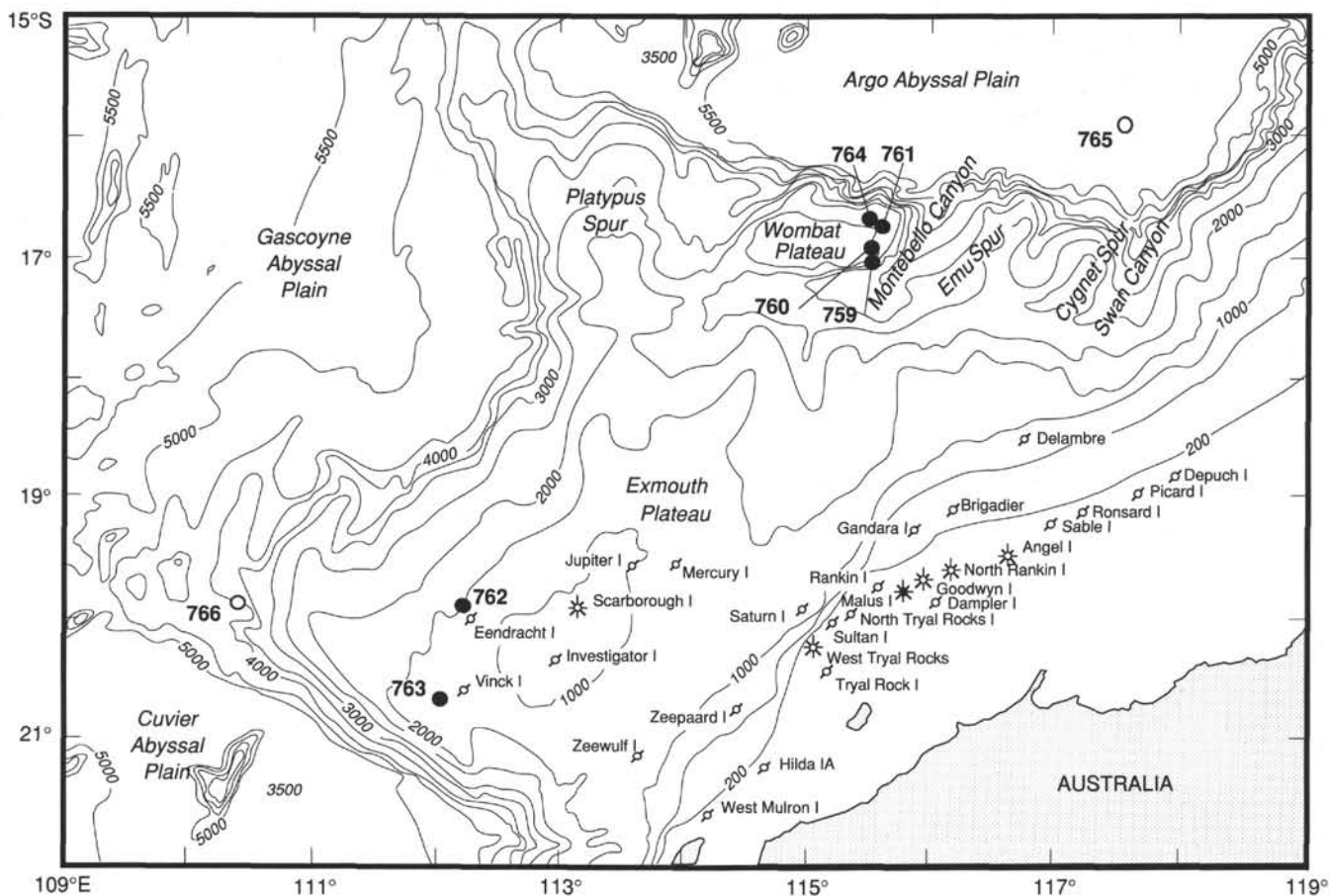


Figure 1. Bathymetric map (contours in meters) of Exmouth Plateau and vicinity, with location of Leg 123 Site 766 at the foot of the southwestern escarpment of the Exmouth Plateau. Also shown are Leg 123 Site 765 (Argo Abyssal Plain) and Leg 122 Sites 761, 764, 762, and 763 (Exmouth Plateau). Leg 122 sites shown by solid circles, Leg 123 sites by open circles. Commercial wells are indicated by other symbols.

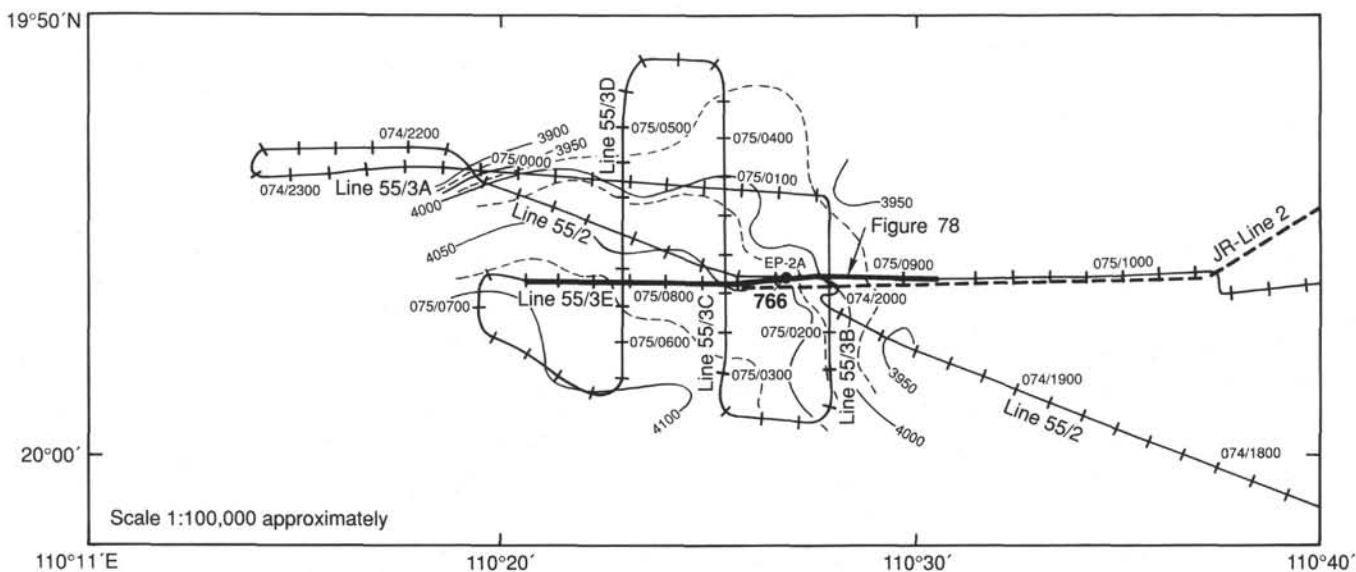


Figure 2. Detailed map of the seismic survey conducted to delineate Site 766 (planned as Site EP2A), located on the crossing of BMR Rig Seismic Lines 55/002 and 55/003E, near Line 55/003B. Detail track of the BMR multifold site survey in proposed Site EP2 area. Also shown are location of Site 766, Figure 78, and route of JOIDES Resolution during approach to Site 766 (dashed) (Line 2). Bathymetry in uncorrected meters.

chemistry of “transitional” type basement, and test stretching and subsidence models for rifting and the subsequent stratigraphic evolution leading to marginal plateau formation. We can also study the nature of the pre-breakup facies (sediments and/or volcanics), the paleobathymetric evolution, and the transition of the rift stage into a juvenile ocean.

Figure 3 shows the location of Site 766 on an 8-km segment of east-to-west seismic profile Line 55/003E. The section spans about 0.5 s to the red reflector that is interpreted as the top of oceanic or transitional basement. Three geological models have been envisaged for the nature of the sequence below the red reflector:

1. As described in the initial BMR prospectus (Exon and Williamson, 1986), the post-rift sediments are underlain by sequences of Triassic or Jurassic pre-rift sediment; the section thus represents a fault block with a comparable stratigraphy to the Exmouth Plateau. However, as shown in the “Underway Geophysics” section (this volume), the acoustic signature of this section is substantially different from the Triassic section on the Exmouth Plateau.

2. The syn-rift sediments (<0.5 s) overlie Lower Cretaceous oceanic basement.

3. Syn-rift sedimentary and pre-rift sequences intruded or intercalated with volcanic or intrusive suites associated with continental breakup magmatism.

The blue reflector defines the top of a sedimentary wedge that thickens toward the Exmouth Plateau and may be related to the Lower Cretaceous Barrow delta system. The sequence above this reflector, which includes the green reflector, is interpreted as Upper Cretaceous to Holocene pelagic sediments.

Figure 4 is based on the interpretation of the geology by Exon and Williamson (1986) and outlines a schematic geological section from the Exmouth escarpment toward the Gascoyne Abyssal Plain. The blocks westward of Site 766 rise up to 1 km above the Gascoyne Abyssal Plain and possibly reflect both uplift associated with syn-rift to post-rift volcanism and down-thrown fault blocks associated with syn-rift to post-rift faulting. The southwestern limit of the Exmouth Plateau is separated from the Cuvier Abyssal Plain by the Cape Range Transform Fault (CRTF in Fig. 1, “Background and Scientific Objectives” section, this chapter). The chain of highs in the abyssal plain, such as the Joey and Roo rises (see Fig. 1, “Background and Scientific Objectives” section, this chapter) may reflect extended volcanic episodes associated with this transform margin.

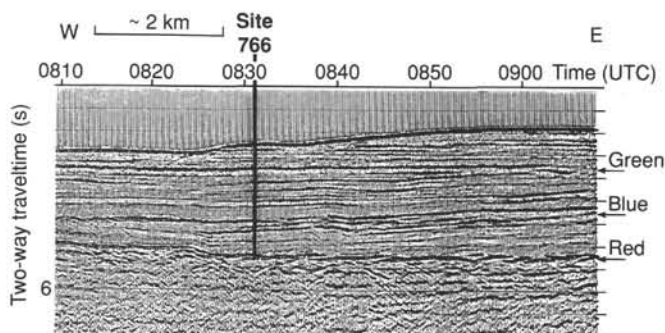


Figure 3. The 8-km east-west segment of multifold seismic Line 55/003E (see Fig. 2, “Background and Scientific Objectives” section, this chapter) over Site 766. BMR multifold seismic Line 55/3E is shown, with proposed Site EP2A and major reflectors/unconformities identified in the site area (von Rad et al., 1986a, 1986b, 1988).

As explained in the “Background and Introduction” chapter (this volume), the oldest marine magnetic anomalies on the Gascoyne and Cuvier abyssal plains are interpreted as M10, upper Valanginian to lower Hauterivian (Fullerton et al., 1989). Presumably, the CRTF has been active since this time and will have affected the subsidence history of the transitional basement and overlying sediments at Site 766. Two simplified subsidence and burial models, based on the contrasting hypotheses for the origin and tectonic history of the sedimentary sequence at Site 766, are shown in Figure 5: model 1 assumes an oceanic site, based on the scenario of oceanic basement overlain by continentally derived and pelagic sediments; model 2 assumes that Site 766 represents part of the Exmouth Plateau.

OPERATIONS

Transit and Approach to Site

At 0005 hr local time (L) on 18 October 1988, *JOIDES Resolution* departed from Site 765 (15°97.586'S, 117°52.512'E) in the southern Argo Abyssal Plain and set course for Site 766 (19°55.8'S, 110°37.45'E) at the foot of the western escarpment of the Exmouth Plateau. The sonobuoy experiment executed during departure from Site 765 is described in the “Operations” section of that site chapter (this volume).

Operations at Site 766 are summarized in Figure 6 and Table 1. Table 2 presents the coring summary for Site 766. A total of 41 hr of transit time was required to reach a point on the BMR *Rig Seismic* multifold seismic survey Line 55/3E, 10 nmi due east of Site 766. On 19 October at 1900L, at location 19°55.8'S, 110°37.4'E, speed was reduced to 6 kt, and the seismic gear deployed.

The western escarpment of the plateau and the seafloor of the small ponded basin at the foot of the escarpment were clearly visible on the echo-sounders. The 3.5-kHz record showed erosion at the seafloor, but indicated a reasonably soft seabed down to 60 mbsf. At 2015L we were 3 nmi due east of the selected site; match of the *Rig Seismic* profile with the profile obtained on board *JOIDES Resolution* was excellent. A beacon was deployed at location 19°55.98'S, 110°27.09'E. The final geographic location of Site 766 using Global Positioning System (GPS) navigation is 19°55.925'S, 110°27.243'E. Water depth was recorded at 4016 m.

Because of time restrictions, the RCB bit was employed, rather than the APC/XCB configuration. This saved us a pipe trip prior to deeper penetration in harder formations. Acoustic basement was defined as “intermediate” to oceanic and continental crust and was estimated at 500 to 550 mbsf.

The weather deteriorated during our first two days at the site, with winds reaching 25 to 30 kt for sustained periods. However, this did not adversely affect operations. The first core was retrieved at 0530L on 20 October; the mud line was established at 4008 m below the rig floor. Coring operations continued smoothly, with a recovery of one core every hour. Recovery of the soft Tertiary section, down to about 90 mbsf, was poor, in part because of use of the RCB. Recovery improved in the Upper Cretaceous, but decreased in Albian grayish-green chalk with minor chert. Outstanding recovery was obtained in the mid-Cretaceous dark clays, and Core 123-766A-31R also yielded a 6-cm-diameter lump of massive pyrite. From Core 123-766A-32R to Core 123-766A-48R, massive glauconitic sands and dark clays of Hauterivian age were penetrated, with outstanding recovery. At Core 123-766A-41R, the paleomagnetists noted that stratification was approximately 7° off vertical in the lower part. On 22 October, according to the seismic interpretations, we had entered the basal sedimentary sequence at Site 766, and it became apparent from the velocity in the sediments measured

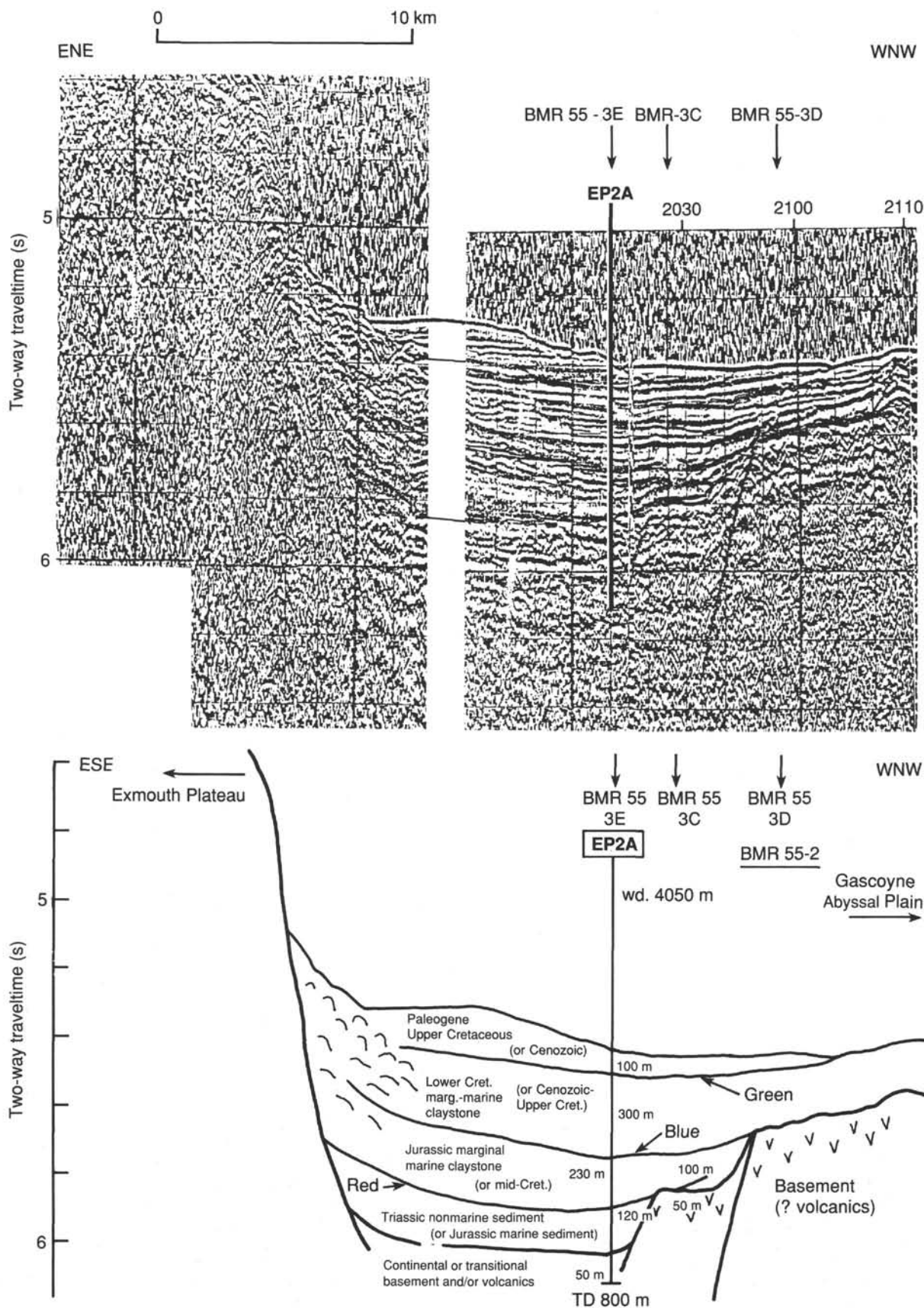


Figure 4. Schematic east-to-west geology over Site 766, from the Exmouth escarpment seaward to ?volcanic basement "blocks" that rise about 1 km above the Gascoyne Abyssal Plain itself. Portion of BMR singlefold seismic Line 55/2 and line drawing showing preliminary interpretations of proposed Site EP2A (modified from von Rad et al., 1986a, 1986b, 1988).

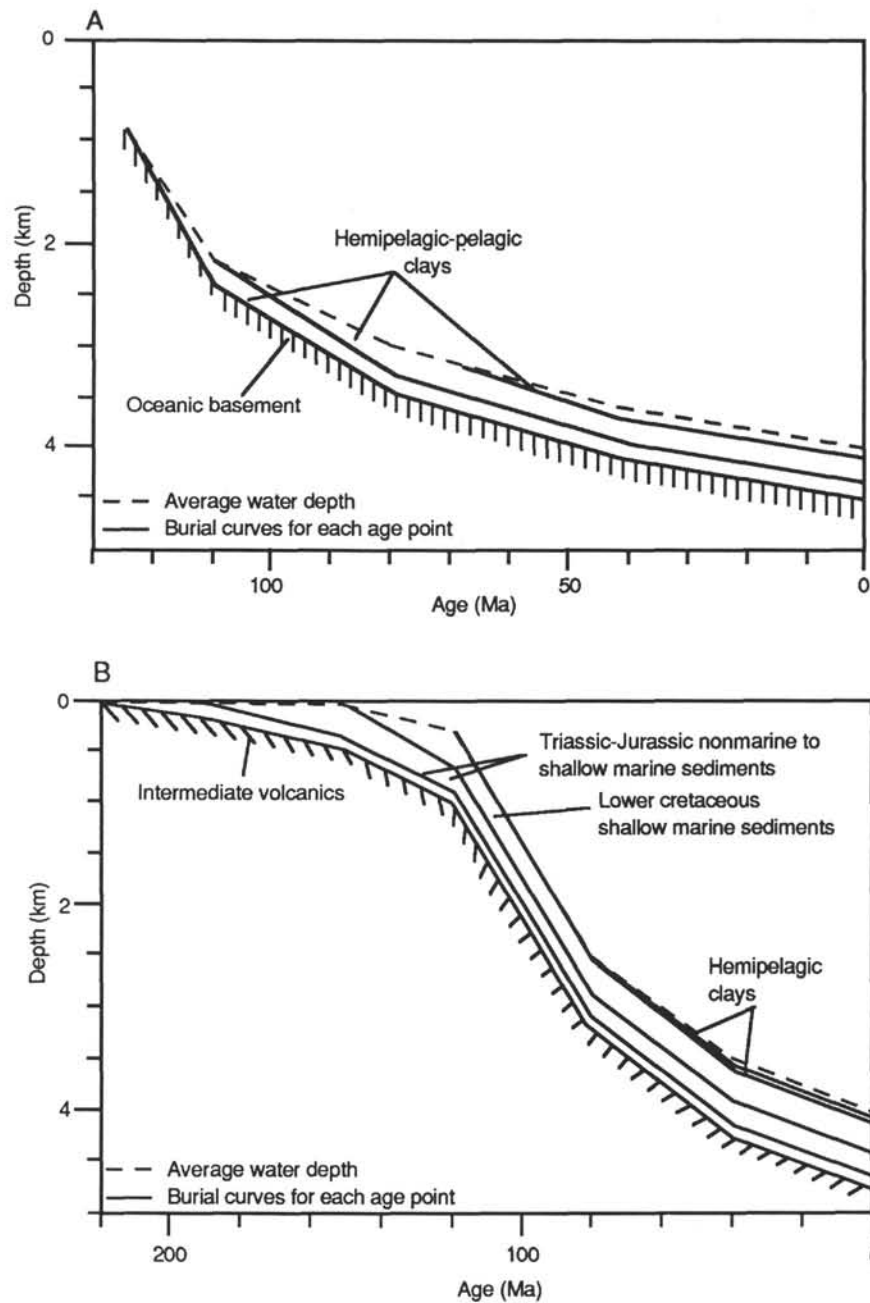


Figure 5. Schematic subsidence and burial history diagrams of the contrasting hypotheses for the origin and tectonic history of the foot of the Exmouth Plateau. A. Hypothesis 1 assumes that Site 766 reflects a relatively shallow oceanic basement setting. B. Hypothesis 2 interprets the site as continental, with rapid subsidence of continental or intermediate volcanic crust resulting from extensive thinning of the continental margin.

aboard ship that basement might be nearer 450 mbsf, rather than the 500+ mbsf predicted initially. This was confirmed at 0130L on 23 October, when from Core 123-766A-48R (451.8–461.5 mbsf) we retrieved about 8 m of dark shaly sediment overlying 1.6 m of fractured basalt.

Cutting time of the first underlying basalt core was two to three times faster than we experienced at Site 765, in part because of weathering of the basalt and in part because of intercalated sediments between the basalt flows. Cores in the basal sill in Site 766 were cut at the same rate as those in Hole 765B. Coring continued to 527.2 mbsf (Core 123-766A-55R), and the last core was retrieved at 1530L on 24 October, 1988.

Recovery in basalt was outstanding; 87% of the 58.4 m of basalt cored was recovered. Rotating time was approximately 40 hr, with only 10 to 15 hr for the sediments above. Average sediment recovery was 63%, with poor recovery in Cores 123-766A-22R to -25R in the Aptian-Albian cherty chalk and in Cores 123-766A-35R and -36R, the Hauterivian greensands. Sediment and volcanic basement recovery is indicated in Figure 7; rotating time per core is shown in Figure 8. Cumulative recovery was 66%, or 347.49 m of rock recovered from 527.16 m cored (Fig. 9).

By 2100L on 24 October, Hole 766A had been conditioned, filled with heavy mud, and the bit released. The newly designed sleeve that blocked the mechanical bit-release holes was also in

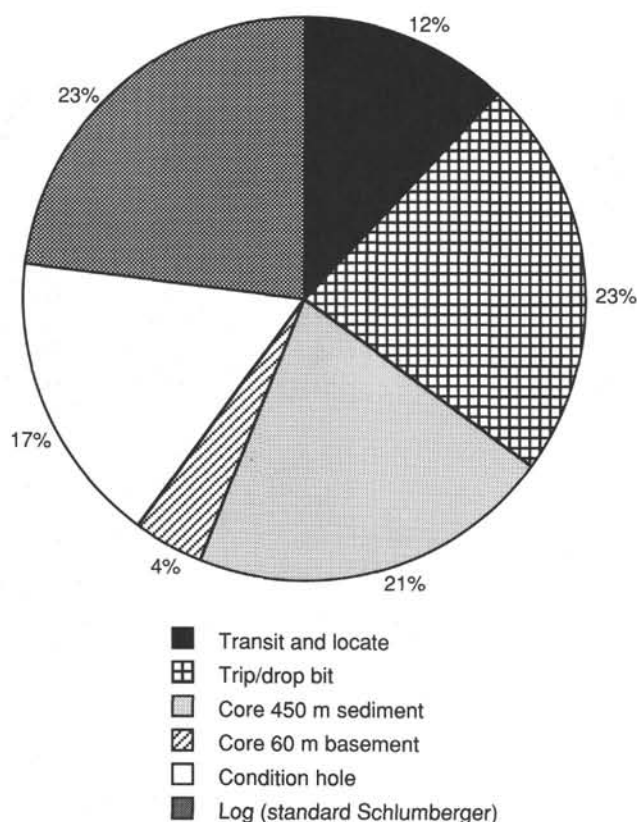


Figure 6. Pie diagram summarizing operations at Site 766 (total time = 8.0 days).

Table 1. Details of operations at Site 766.

Operation	Date (1988)	Days cumulate
Transit from Site 765 to Site 766	18 Oct	0.0
Location of Site 766	19 Oct	1.9
Pipe trip down with RCB	20 Oct	2.3
First Core 123-766-1R	20 Oct	2.4
458-m RCB coring to basement	23 Oct	5.4
66-m RCB coring into basement	24 Oct	6.4
Schlumberger logging (3 tools)	25 Oct	7.7
Pipe trip up	26 Oct	8.3
Sonobuoy and seismic grid near site	26 Oct	8.7
Transit to Singapore	1 Nov	

place. No fill was encountered during conditioning. Pipe was raised to 260 mbsf at the level of the hard cherty chalk. Logging started immediately with the seismo-stratigraphy tool. A ledge at 445 mbsf stopped the tool from logging basement, but the tool was successfully run up the hole to 260 mbsf. Pipe then was lowered to the bottom of the hole and forced through the bridge at about 445 mbsf and into basement. The geochemistry tool was used to log the hole from bottom through pipe to the mud line. The third log, the litho-density tool, was run with the pipe stationary at 260 mbsf. Again, the tool could not be lowered into basement because of bridging at about 442 mbsf; the tool was run through the pipe to the mud line. The mud line identified from logging is at a 4008-m water depth. At 2100L on 25 October 1988, logging of Hole 766A was completed, and pipe was returned to the deck.

Our logging plan had allowed for 3 to 4 hr of operational contingency time. However, no problems were encountered. Accordingly, a brief survey, using the single-channel seismic gear

Table 2. Coring summary of Site 766.

Core	Date (Oct. 1988)	Time (L)	Depth (mbsf)	Length cored (m)	Length recovered (m)	Recovery (%)
1R	20	0800	0-7.7	7.7	7.68	99.7
2R	20	0900	7.7-17.3	9.6	9.69	101.0
3R	20	1035	17.3-27.0	9.7	9.26	95.4
4R	20	1130	27.0-36.7	9.7	3.05	31.4
5R	20	1335	36.7-46.3	9.6	8.29	86.3
6R	20	1445	46.3-56.0	9.7	9.32	96.1
7R	20	1550	56.0-65.7	9.7	9.55	98.4
8R	20	1650	65.7-75.3	9.6	2.44	25.4
9R	20	1745	75.3-85.0	9.7	7.73	79.7
10R	20	1855	85.0-94.7	9.7	4.59	47.3
11R	20	1955	94.7-104.3	9.6	9.44	98.3
12R	20	2140	104.3-113.9	9.6	2.20	22.9
13R	20	2330	113.9-123.6	9.7	4.54	46.8
14R	21	0050	123.6-133.2	9.6	7.39	77.0
15R	21	0155	133.2-142.9	9.7	8.16	84.1
16R	21	0300	142.9-152.5	9.6	9.34	97.3
17R	21	0400	152.5-162.1	9.6	9.80	102.0
18R	21	0500	162.1-171.7	9.6	8.21	85.5
19R	21	0605	171.7-181.4	9.7	6.96	71.7
20R	21	0705	181.4-191.0	9.6	5.18	53.9
21R	21	0835	191.0-200.6	9.6	2.62	27.3
22R	21	1025	200.6-210.3	9.7	0.37	3.8
23R	21	1210	210.3-219.9	9.6	0.54	5.6
24R	21	1345	219.9-229.6	9.7	1.80	18.5
25R	21	1600	229.6-239.3	9.7	1.13	11.6
26R	21	1740	239.3-248.9	9.6	4.57	47.6
27R	21	1915	248.9-258.6	9.7	3.42	35.2
28R	21	2050	258.6-268.3	9.7	9.38	96.7
29R	21	2225	268.3-277.9	9.6	6.59	68.6
30R	22	0010	277.9-287.5	9.6	6.11	63.6
31R	22	0145	287.5-297.2	9.7	3.91	40.3
32R	22	0310	297.2-306.8	9.6	7.20	75.0
33R	22	0430	306.8-316.5	9.7	4.00	41.2
34R	22	0550	316.5-326.1	9.6	2.64	27.5
35R	22	0721	326.1-335.8	9.7	0.54	5.6
36R	22	0817	335.8-345.5	9.7	1.82	18.7
37R	22	0920	345.5-355.1	9.6	3.62	37.7
38R	22	1020	355.1-364.8	9.7	4.33	44.6
39R	22	1120	364.8-374.5	9.7	4.08	42.0
40R	22	1230	374.5-384.2	9.7	9.70	100.0
41R	22	1350	384.2-393.8	9.6	7.94	82.7
42R	22	1500	393.8-403.5	9.7	6.81	70.2
43R	22	1625	403.5-413.2	9.7	7.43	76.6
44R	22	1750	413.2-422.8	9.6	8.86	92.3
45R	22	1950	422.8-432.5	9.7	9.59	98.8
46R	22	2130	432.5-442.2	9.7	9.14	94.6
47R	22	2315	442.2-451.8	9.6	9.81	102.0
48R	23	0115	451.8-461.5	9.7	9.82	101.0
49R	23	0445	461.5-471.2	9.7	6.71	69.2
50R	23	0835	471.2-480.4	9.2	4.10	44.5
51R	23	1430	480.4-489.9	9.5	9.50	100.0
52R	23	1915	489.9-499.1	9.2	8.02	87.2
53R	24	0050	499.1-508.3	9.2	9.10	98.9
54R	24	0800	508.3-517.7	9.4	9.51	101.0
55R	24	1515	517.7-527.2	9.5	9.96	105.0
Coring totals				527.2	347.49	65.9

and 12- and 3.5-kHz sonar, was conducted to chart a nearby canyon that may have been responsible for funnelling sediment to Site 766 in Cenozoic (and possibly even Cretaceous) time. The short, 40-nmi survey grid ended with a sonobuoy experiment over Site 766 at 1500L on 26 October, while steaming 7 to 8 kt on course 341° (see "Underway Geophysics" chapter, this volume).

Leaving Site 766, *JOIDES Resolution* set a 341° heading for Singapore. Crossing of the northeast Indian Ocean was uneventful, except for scenic views of Christmas Island and Krakatoa en route. The weather stayed perfect, as it had been during the whole cruise, with light winds, minor swells, and pleasant temperatures of about 25°C. We docked in Singapore harbor on 1 November at 0500 hr. Thus ended Leg 123 of the Ocean Drilling Program.

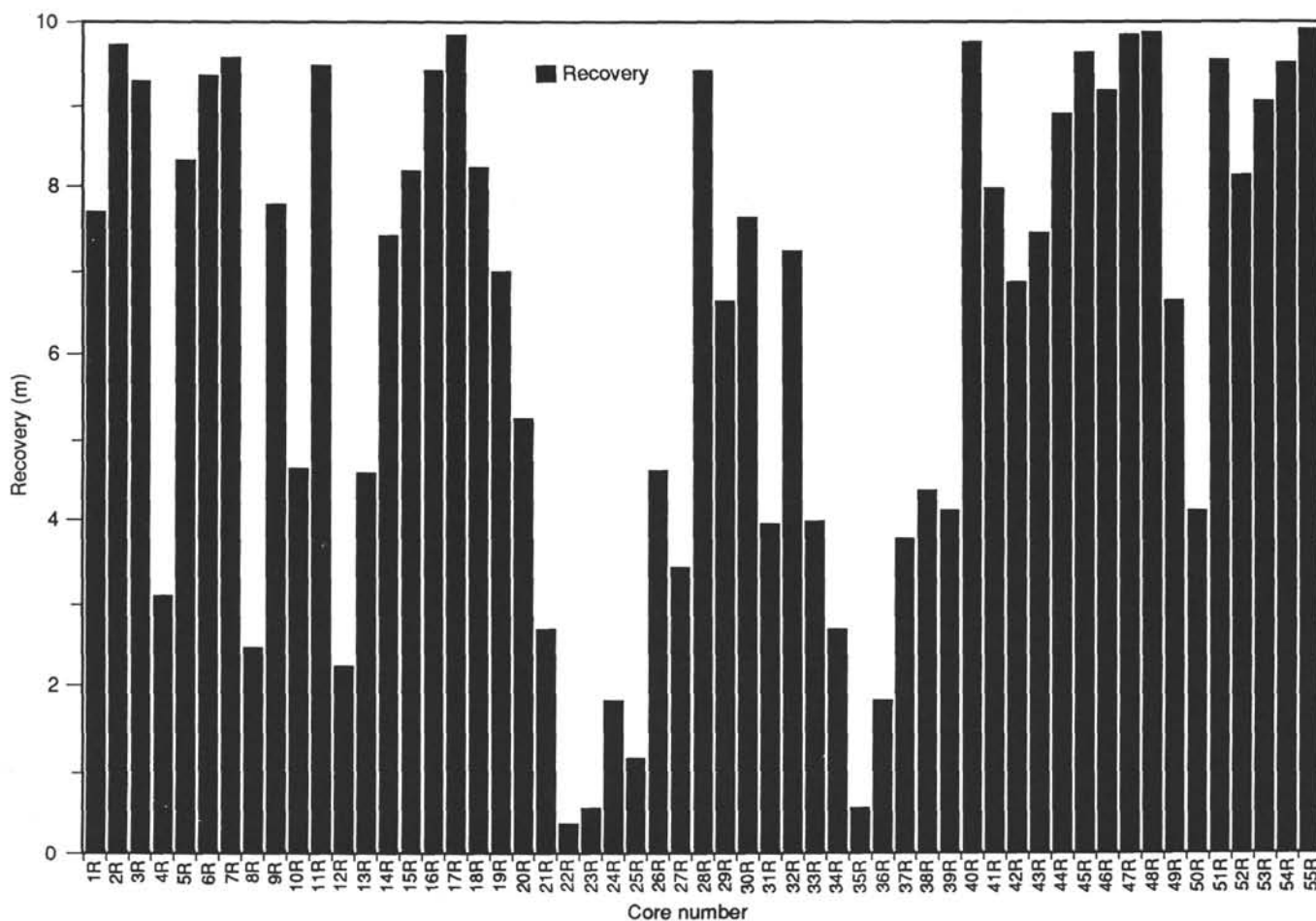


Figure 7. Recovery in meters for sediment (Cores 123-766-1R to 123-766A-48R), and basalt (Cores 123-766-48R to 123-766A-55R).

SEDIMENT LITHOSTRATIGRAPHY

A total of 466.7 m of Pleistocene to upper Valanginian sediments were rotary cored at Site 766 (Fig. 10). Average recovery was 63.1%. Recovery was less than 50% in the following cores: Cores 123-766A-3R, -8R, -10R, -12R, -21R to -27R, -31R, and 123-766A-33R to -39R. Fourteen of the 20 cores having poor recovery occur in two intervals of seven cores each. Both of these intervals are lithologically distinct, and poor recovery is attributed to the occurrence of specific lithologies that are not easily recovered: the interval from Cores 123-766A-21R to 123-766A-27R contains hard cherty layers interlaminated with softer sediments; the interval from Cores 123-766A-33R to 123-766A-39R contains fine- to medium-grained, poorly consolidated sandstones. Extremely soft nannofossil oozes in Cores 123-766A-1R through -10R were highly disturbed by drilling, but there is no evidence that any visible structure originally existed in these sediments. Firmer sediments below Core 123-766A-9R were highly disturbed only locally. The sedimentary sequence is divided into three units and eight subunits. The unit and subunit boundaries largely coincide with boundaries between seismic units, magnetic susceptibility units, and biostratigraphic units (Fig. 10). The basal sediments in Core 123-766A-49R are interbedded with igneous intervals interpreted as sills.

Unit I consists almost entirely of pink to pale brown nannofossil ooze. This unit is massive and homogeneous, is of Pleistocene to early Paleocene age, and is characterized by low magnetic susceptibility. Subunits IA and IB are distinguished on the basis of pink colors and siliceous fossil debris (especially radio-

larans) in Subunit IA, vs. pale brown colors and essentially no siliceous fossil debris in Subunit IB.

Unit II is extremely variable. Subunit IIA consists of pink, white, and pale brown nannofossil oozes, graded carbonate sequences, polymictic conglomerates, and brown clayey nannofossil oozes. This subunit is of early Paleocene to early Campanian or late Santonian age and is characterized by intermediate magnetic susceptibilities, except for a thin interval near the top having magnetic susceptibilities as high as 200×10^{-6} cgs. Subunit IIB consists of color-banded calcareous oozes and clays, both commonly zeolitic. Thin, graded carbonate sequences are abundant. This subunit is of early Campanian or late Santonian to Turonian age; the base is approximately at the Turonian/Cenomanian boundary. This subunit has high magnetic susceptibilities. Subunit IIC, the highest unit to contain lithified carbonate sediments, also has high magnetic susceptibilities (locally exceeding 500×10^{-6} cgs) and consists of bioturbated, commonly zeolitic and clayey, nannofossil ooze and chalk. Subunit IID is of Cenomanian to Albian age. Subunit IID consists of impure nannofossil and calcareous chalks. These are locally zeolitic, clayey, silicified, or graded. Magnetic susceptibilities do not exceed 20×10^{-6} cgs, except at the top of the unit. The age of Subunit IID is Albian to early Aptian; the base may correspond to the Aptian/Barremian boundary.

Unit III is distinctly different from Unit II. It is divided into two subunits on the basis of grain size and mineralogy. Subunit IIIA consists of claystones with disseminated glauconite(?) and radiolarians. The latter are commonly empty molds, or molds filled with glauconite(?) or clay. This subunit is of Barremian

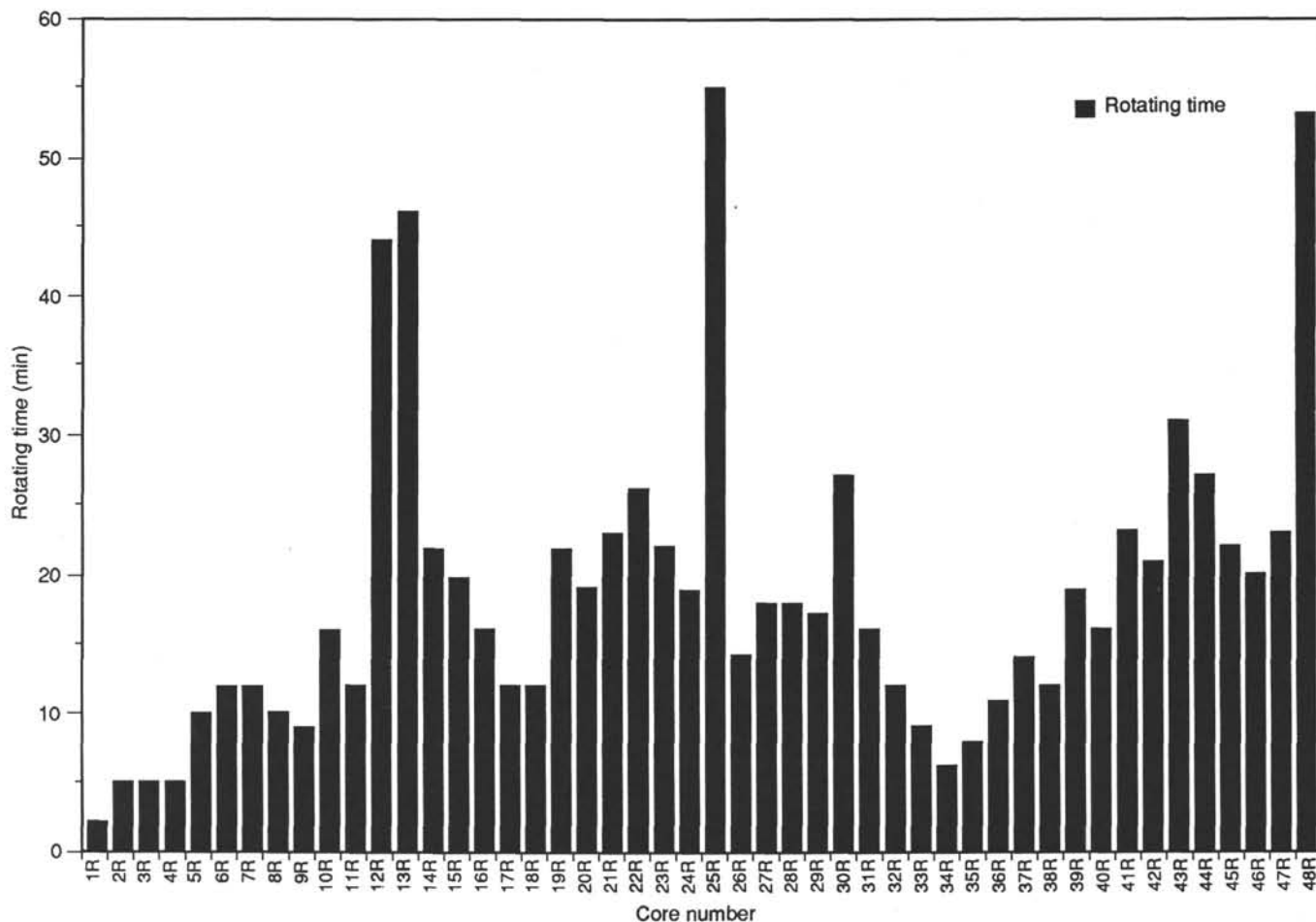


Figure 8. Rotating time in minutes for Cores 123-766-1R to 123-766A-48R. Cores 123-766A-22R to 123-766A-25R contain chert, and Core 123-766A-48R contains basalt; this explains the higher rotating times.

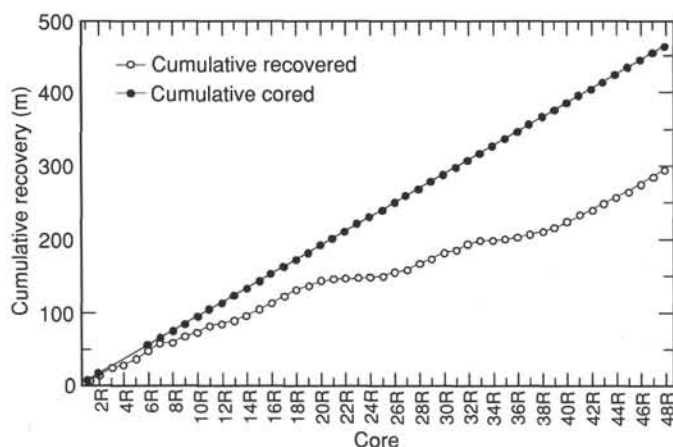


Figure 9. Cumulative cored and cumulative recovered sedimentary section in Hole 766A.

age, and the base is approximately the Barremian/Hauterivian boundary. The sediments of this subunit are characterized by extremely low magnetic susceptibility. Subunit IIIB is of Hauterivian age (the base may be late Valanginian) and consists of sandstones and siltstones dominated by any of the following: altered volcanoclastic(?) grains, glauconite(?), quartz, or neritic

carbonate bioclasts (dominantly echinoderms). Magnetic susceptibility of these sediments is high (100 to more than 500×10^{-6} cgs) and increases downward to about 410 mbsf. Magnetic susceptibility is dramatically lower in the lower part (dominantly less than 100×10^{-6} cgs). This magnetic-susceptibility boundary corresponds to the boundary between dominantly sandy sediments above and siltstones below.

Unit I

Sections 123-766A-1R-1, top, through 123-766A-9R-CC, top; Depth, 0-82.8 mbsf.
Age = early Pleistocene to early Paleocene.

Unit I consists almost entirely of pink to pale brown nannofossil ooze, locally color mottled but typically massive, homogeneous, and silt-sized. It lacks the graded sequences and brown clays (commonly zeolitic) that characterize Unit II and the siliciclastic sediments that dominate Unit III. Few sedimentary structures were observed; this may be because of homogenization by rotary coring, but may also reflect the original character of the sediment. Unit I oozes may have formed as pelagic deposits; there is no evidence that these oozes were redeposited as sediment gravity flows.

Two subunits are distinguished on the basis of color, grain size, and the presence of siliceous components in Subunit IA.

The lower boundary of Unit I is at the top of the highest dark brown nannofossil ooze with clay.

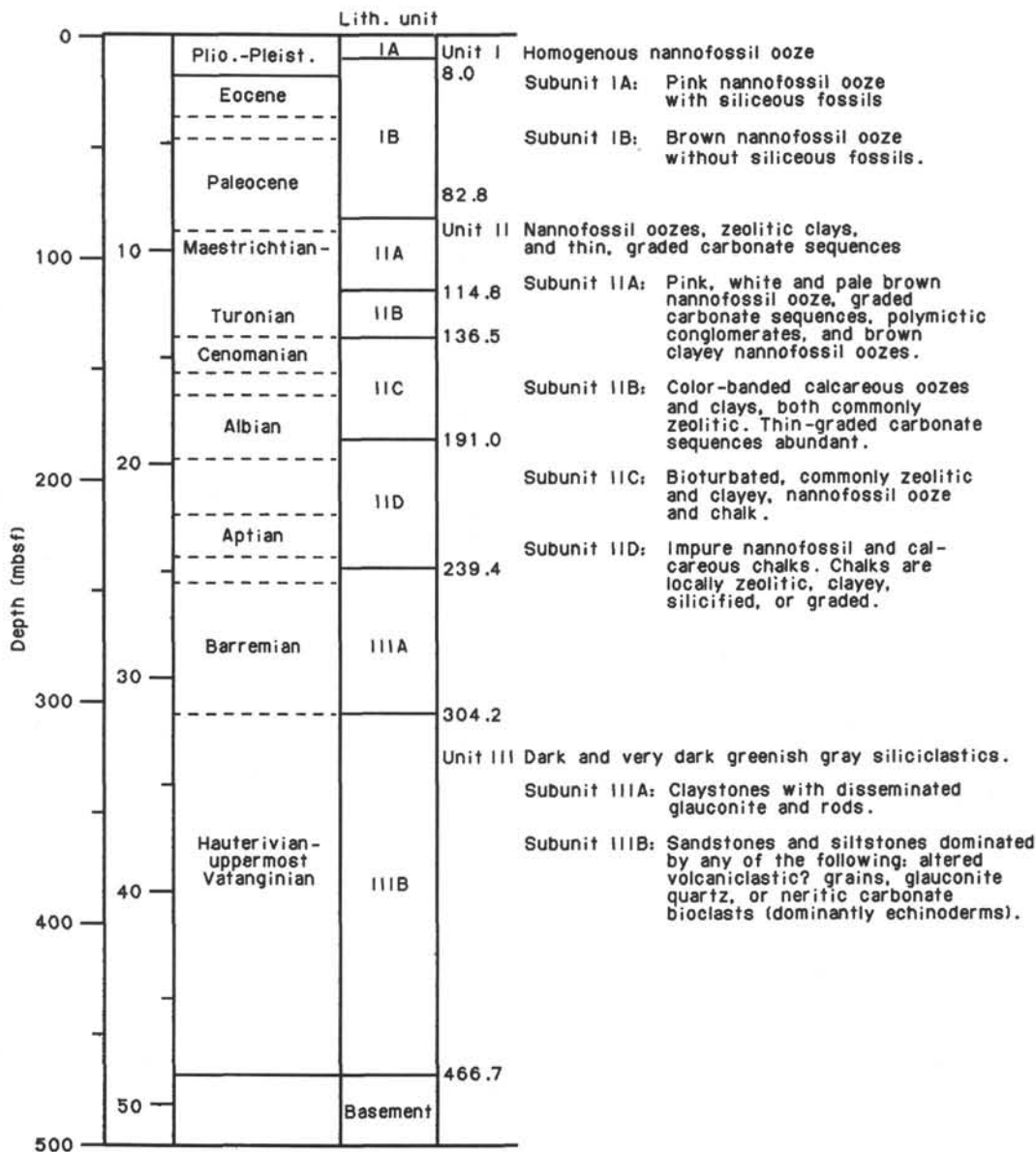


Figure 10. Lithostratigraphic section of sedimentary succession at Site 766.

Subunit IA (Depth, 0.0-8.0 mbsf, Sections 123-766A-1R-1, top through 123-766A-2R-1 at 35 cm).
Age = early Pleistocene.

Subunit IA consists of pink nannofossil ooze with local mottles of reddish yellow, gray, dark gray, or light brownish-gray. Oozes are dominantly clay-sized but contain 30%-40% floating silt- and sand-sized grains; these grains are mostly foraminifers, radiolarians, siliceous fragments, calcareous fragments, and siliceous spicules. No sedimentary structures were observed. The lower boundary of Subunit IA is placed at the color change from pink to pale brown; this color change apparently coincides with the boundary between Pleistocene and Pliocene fossil assemblages.

Subunit IB (Depth, 8.0-82.8 mbsf, Sections 123-766A-2R-1 at 35 cm through 123-766A-9R, CC, top).
Age = late early Pliocene to early late early Pliocene to early Paleocene.

Subunit IB consists of very pale brown to white, dominantly silt-sized nannofossil ooze. The ooze is generally featureless and homogeneous, but with local oblong to streaky mottles of white, yellowish-brown, brownish-yellow, very pale brown, or gray. Oozes in this subunit lack the floating coarser-grained material and siliceous components characteristic of Subunit IA; foraminifers, calcareous fragments, and muscovite occur as minor components. A total of 2% authigenic euhedral dolomite was noted in a smear slide from Section 123-766A-5R-5 at 68 cm and may be more widely distributed throughout the subunit. Zeolitic nannofossil ooze and nannofossil ooze with zeolite occur locally; these lithologies are typically brownish-yellow or yellowish-brown, may contain clay, and form mottles or layers as much as 80 cm thick.

Pebble- to sand-sized clasts of sedimentary and volcanic rocks are scattered in Subunit IB, principally in Cores 123-766A-3R, -4R, -5R, and -9R (Fig. 11). These clasts are mainly bioclastic grainstones, dominated by echinoderm and molluscan debris,

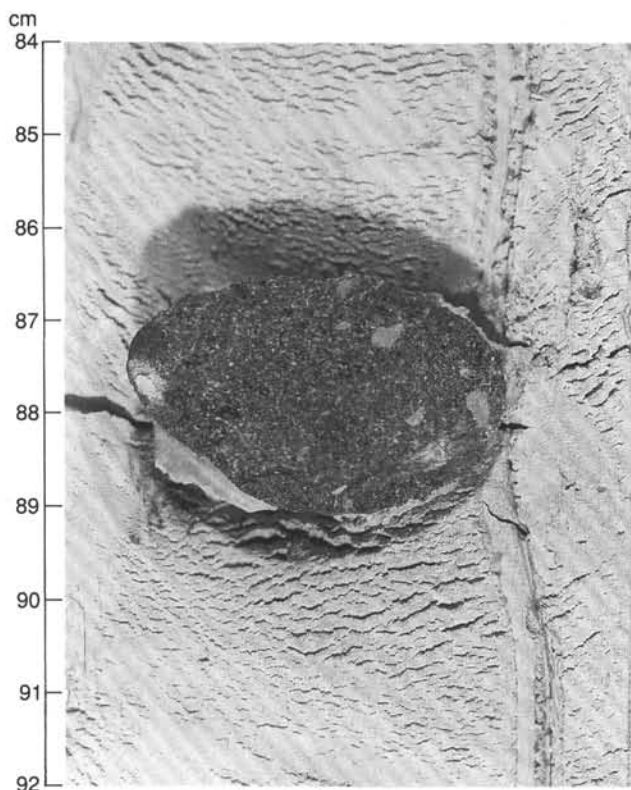


Figure 11. Sedimentary pebble in nannofossil ooze. Pebble contains abundant volcaniclastic grains and neritic calcite bioclasts. Lithologic Subunit IB; Section 123-766A-4R-2 at 84-92 cm.

but have 30% to 40% mafic volcanic detritus. These lithified clasts float in a matrix of nannofossil ooze like that elsewhere in the subunit.

Unit II

Sections 123-766A-9R-CC, top, through 123-766A-26R-1 at 12 cm;
Depth, 82.8-239.4 mbsf).
Age = early Paleocene to Aptian.

Unit II is a heterogeneous succession of nannofossil oozes (locally silicified), zeolitic clays, and thin, coarser, carbonate graded sequences. This unit differs from Unit I, which consists of light-colored nannofossil oozes, by its darker color, zeolitic clays, prominent color banding and heavy bioturbation in the middle part of the unit, and presence of graded carbonate sequences throughout the unit. Unit III consists of distinctive very dark greenish-gray clays, sandstones, and siltstones, which are unlike the lighter-colored calcareous oozes and chalks of the lower part of Unit II.

Unit II is divided into four subunits, based on differences in color, mineralogy, distribution of graded sequences, and degree of bioturbation.

Subunit IIA (Depth, 82.8-114.8 mbsf, Section 123-766A-9R, CC,
top through 123-766A-13R-1 at 97 cm).
Age = early Paleocene to early Campanian.

Subunit IIA is dominated by pink, white, and very pale brown nannofossil oozes, like those of Unit I. These are interbedded with three lithologies not found in Unit I: (1) graded carbonate sequences; (2) polymictic conglomerates with calcareous matrices; and (3) brown clayey nannofossil oozes (and nannofossil oozes with clay) that are distinctly darker in color than

the sediments of Unit I. The brown clayey nannofossil oozes are restricted to the upper part of Subunit IIA (above Section 123-766A-11R-1, 97 cm [95.7 mbsf]), but the graded sequences occur throughout the subunit (Fig. 12).

The upper boundary of Subunit IIA is drawn at the top of the highest dark brown nannofossil ooze with clay, and the



Figure 12. Graded carbonate sequence consisting of a lower portion composed of foraminiferal nannofossil ooze grading up from medium-sand- to silt-sized, and an upper massive portion composed of clay- to silt-sized nannofossil ooze with clay. Lithologic Subunit IIA; Section 123-766A-10R-1 at 65-95 cm.

lower boundary is drawn above a dark-colored band at the top of a thick interval of light-to-dark color-banded nannofossil oozes and clays that makes up Subunit IIB. Subunit IIA lacks the clays that impart the distinctive color banding to Subunit IIB, and graded sequences, rare in Subunit IIA, are ubiquitous in Subunit IIB.

Subunit IIA includes the Cretaceous/Tertiary boundary, which occurs in mottled pale brown nannofossil ooze in Section 123-766A-10R-2. A thin polymictic conglomerate with a matrix of foraminiferal-nannofossil ooze (clasts mostly ?igneous; clay clast near base) occurs less than 1 m below the paleontological Cretaceous/Tertiary boundary in Section 123-766A-10R-3, from 72.5 to 90 cm (Fig. 13).

Subunit IIB (Depth, 114.8–136.5 mbsf, Section 123-766A-13R-1 at 97 cm through 123-766A-15R-3 at 26 cm).
Age = early Campanian to Turonian.

This is a distinctively color-banded interval (Fig. 14) dominated by browns, grays, and pinks. Calcareous ooze and clay (both commonly zeolitic in the lower part of the subunit) are interlaminated; calcareous oozes tend to be lighter in color and clays to be darker. Calcareous oozes consist largely of thin (less than 15 cm) graded sequences interbedded with massive or bioturbated clay- to silt-sized nannofossil oozes (Fig. 15). Bioclastic grainstones with volcanic lithic fragments, dominated by echinoderm fragments, occur locally. The subunit differs from Subunit IIC in having abundant graded carbonate sequences, more distinct color banding, a greater abundance of clay, and only slight bioturbation.

The boundary between Subunits IIB and IIC is the base of a thin conglomerate consisting of clasts of glauconitic sandstone and acidic volcanic rocks in a matrix of zeolitic clay (Fig. 16).

The base of this subunit is the Turonian/Cenomanian boundary.

Subunit IIC (Depth, 136.5–191.0 mbsf, Section 123-766A-15R-3 at 26 cm through 123-766A-20R-1, top).
Age = Turonian/Cenomanian boundary to Albian.

This heterogeneous subunit is dominated by moderately to heavily bioturbated darker zeolitic clayey nannofossil ooze and chalk (brown, gray, and green), intercalated with lighter brown or gray nannofossil ooze and chalk (Fig. 17). Clays occur in the upper part of Core 123-766A-16R, in an interval transitional from Subunit IIB. Graded carbonate sequences are rare in this transitional upper part of the subunit, but are common below Section 123-766A-19R-4. In contrast, in Subunit IID zeolites are rare (only found in the upper part), slight to moderate bioturbation occurs locally, cherty intervals occur in the upper part (Cores 123-766A-20R to -23R), and only the uppermost core in the subunit contains abundant graded carbonate sequences. The Subunit IIC/IID boundary is to some extent arbitrary, as the last three of these parameters exhibit gradual, rather than abrupt, transitions between the two subunits, but it was placed at the top of a pink nannofossil chalk that is visibly graded and laminated in its lower part. This is overlain by a brown to light reddish-brown zeolitic nannofossil ooze with foraminifers that is the basal interval of Subunit IIC. Chalks in this subunit contain as much as 20% radiolarians.

Subunit IID (Depth, 191.0–239.4 mbsf, Section 123-766A-20R-1, top, through 123-766A-26R-1 at 12 cm).
Age = Albian to Aptian.

This subunit consists of impure nannofossil and calcareous chalks and mixed sediments. Coarser sediments commonly contain as much as 25% foraminifers and locally have abundant

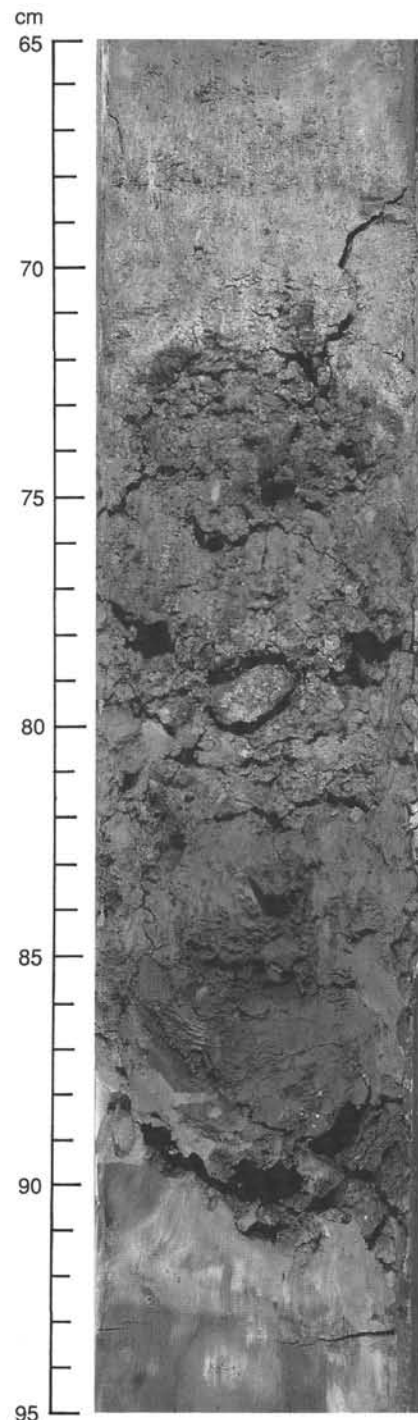


Figure 13. Thin polymictic conglomerate 66–90 cm below the Cretaceous/Tertiary boundary. Matrix consists of foraminiferal-nannofossil ooze; clasts mostly igneous(?), but a large clay clast occurs near the base of the conglomerate. Lithologic Subunit IIA; Section 123-766A-10R-3 at 65–95 cm.

poorly preserved radiolarians. Zeolites are locally common in the upper part of the subunit, whereas clay is common below; the chalks are often silicified in Cores 123-766A-20R through -23R. Graded sequences having slight bioturbation are abundant in Core 123-766A-20R (Fig. 18); lower cores are characterized by laminated, vaguely laminated, or massive and slightly bioturbated chalks. Recovery of Cores 123-766A-21R through

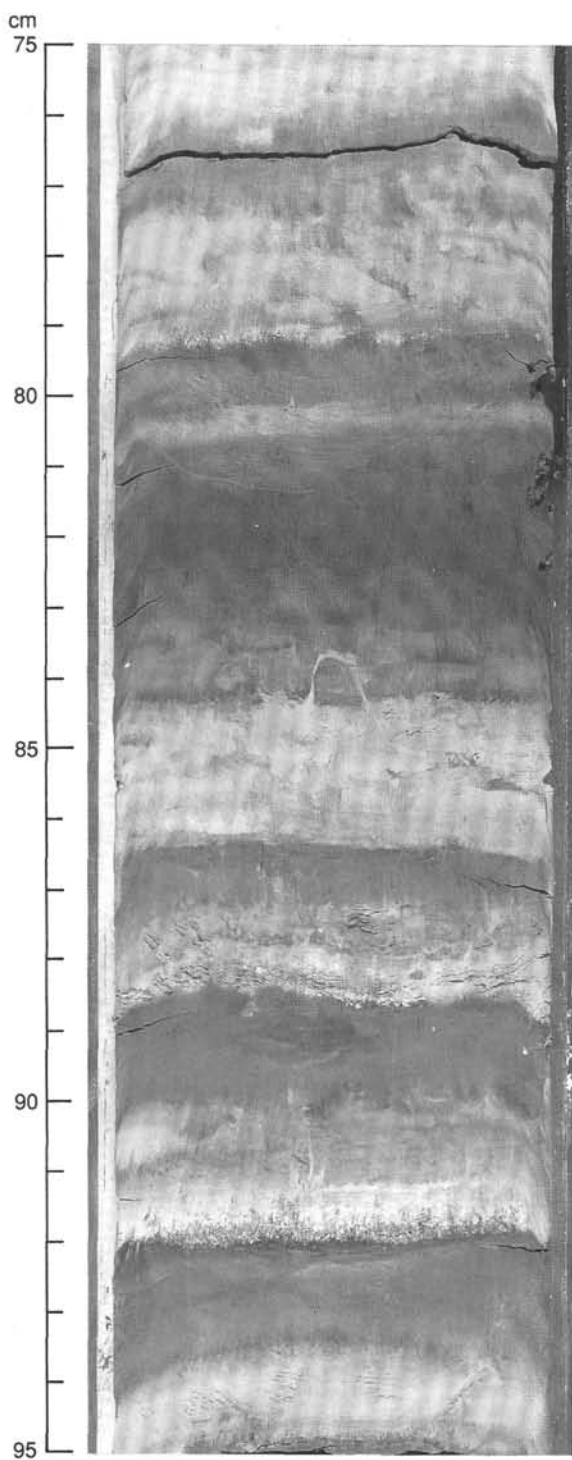


Figure 14. Color-banded interval of interlaminated, very pale brown nannofossil ooze with calcareous fragments (and minor zeolites), dark brown clay and/or clay-zeolite-nannofossil mixed sediment, and grayish brown clayey nannofossil ooze. Lithologic Subunit IIB; Section 123-766A-14R-3 at 75-95 cm.

-25R was poor, but the sediments recovered are homogeneous and thus are assumed to be characteristic of these cores. The base of Subunit IID is drawn at the boundary between the lowest light gray nannofossil chalk and the highest very dark greenish-gray claystone with quartz and glauconite.

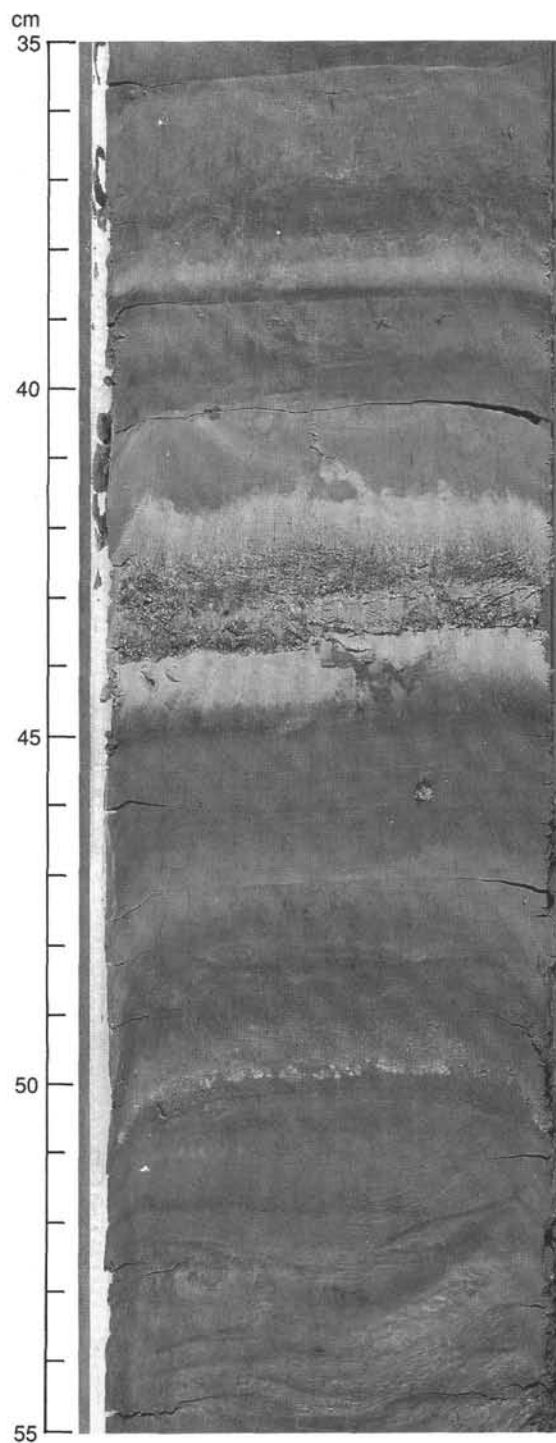


Figure 15. Color-banded interval as in Figure 14, with thin, graded carbonate sequence from 43.4 to 41.6 cm. Lithologic Subunit IIB; Section 123-766A-15R-2 at 35-55 cm.

The base of Subunit IID may be the Aptian/Barremian boundary.

Unit III

Sections 123-766A-26R-1 at 12 cm to 123-766A-49R-4 at 66 cm;
Depth, 239.4 to 466.7 mbsf.
Age = Barremian through latest Valanginian.

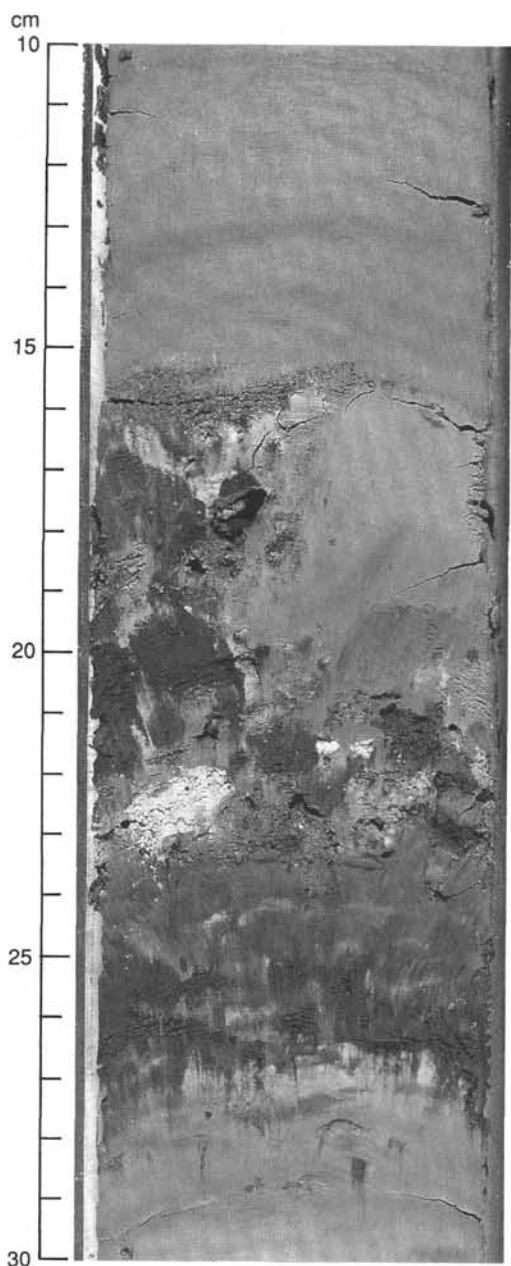


Figure 16. Boundary between Subunits IIB and IIC (Section 123-766A-15R-3 at 26 cm). Multicolored conglomerate with matrix of zeolitic clay and clasts of glauconitic(?) sandstone and acidic volcanic rocks, overlying light gray nannofossil ooze or chalk. Section 123-766A-15R-3 at 10-30 cm.

Unit III is dominated by dark and very dark greenish-gray siliciclastic claystones, siltstones, and sandstones; in contrast to Units I and II, it includes no nannofossil oozes or chalks. The top of Unit III is placed at the base of the lowest nannofossil chalk interval found at Site 766. The lower part of Unit III contains intercalated siliciclastic sediments and mafic igneous intrusions, and the base of the unit is drawn at the base of the lowest sedimentary interval.

Two subunits are distinguished. Subunit IIIA is mostly claystone with disseminated glauconite(?), quartz, and radiolarians. Subunit IIIB comprises sandstones and siltstones containing various proportions of altered volcanic lithic grains, glauconite(?), and neritic carbonate bioclasts (largely echinoderms).

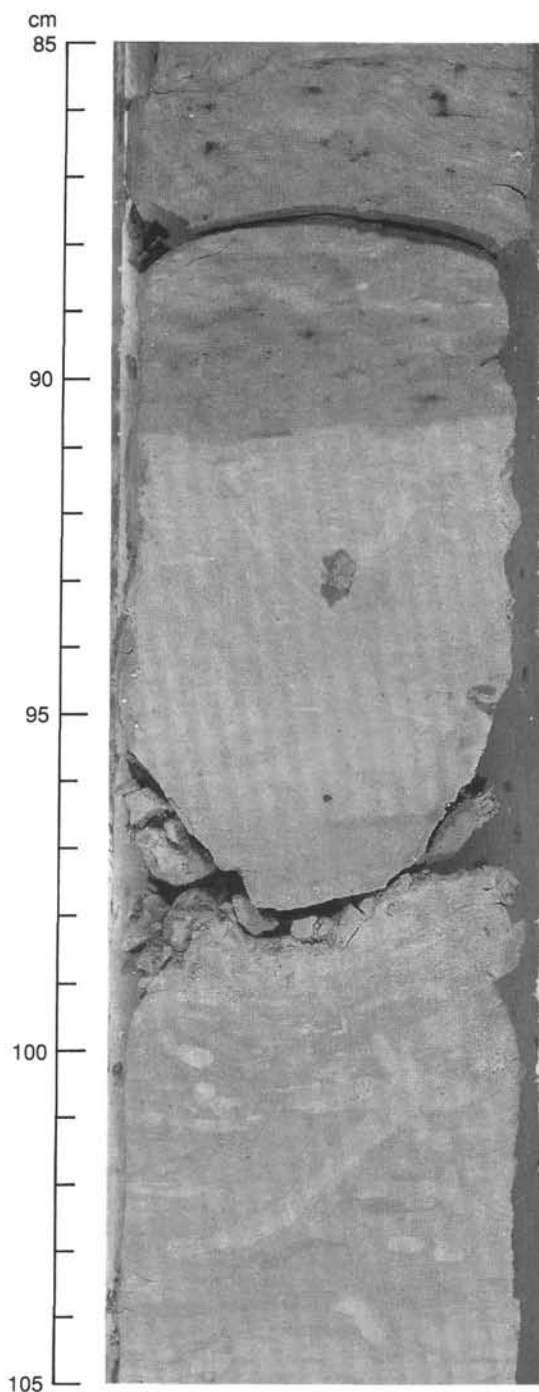


Figure 17. Bioturbated zeolitic nannofossil ooze. Lithologic Subunit IIC; Section 123-766A-18R-3 at 85-105 cm.

Subunit IIIA (Depth, 239.4 to 304.2 mbsf, Section 123-766A-26R-1 at 12 cm through 123-766A-32R, CC, top).
Age = Barremian to late Hauterivian.

Claystones dominate Subunit IIIA. In the upper part of the subunit (Cores 123-766A-26R through -28R) these are greenish-gray to dark greenish-gray, less commonly grayish-green, gray, dark gray, olive gray, or dark brown. In the lower part of the subunit, very dark grayish-green is the predominant color. Bioturbation is pervasive and the only sedimentary structure observed in most cores; burrows are largely parallel to bedding,

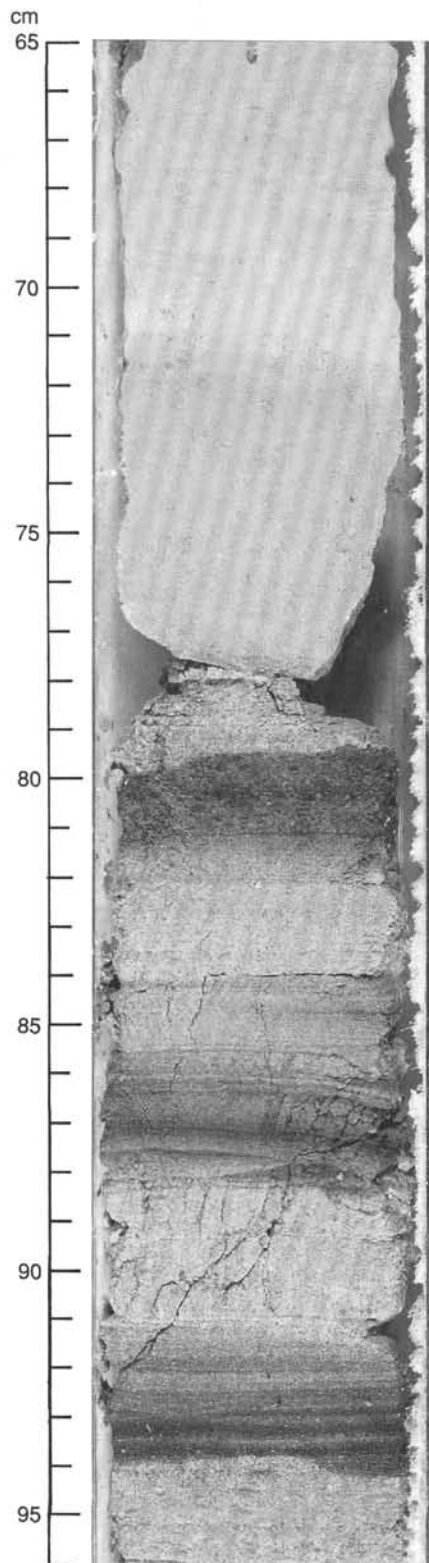


Figure 18. Graded sequence consisting of multiple graded sets of very fine-sand- to very coarse-sand-sized laminated and wavy laminated foraminiferal calcareous chalk, overlain by massive to mottled nannofossil ooze with calcareous fragments and zeolites that grades upward from very fine-sand-sized to silt- and clay-sized. Lithologic Subunit IID; Section 123-766A-20R-2, at 65–96 cm.

but vertical and high-angle oblique burrows and traces also occur and, in some cases, clearly cross-cut horizontal burrows.

Subunit IIIA claystones may contain appreciable amounts of disseminated silt- and fine-sand-sized material (Fig. 19); locally, clayey sandstones and sandy/silty claystones occur. These coarser grains are largely radiolarians (Fig. 20), quartz, glauconite(?), and volcanic lithic grains; zeolite is abundant in the upper part of the subunit. Radiolarians make up 40% to 55% of some intervals in Cores 123-766A-26R and -27R; most have poor preservation and are infilled with clay matrix. Glauconite(?) grains are bright green or reddish-brown, and some show shrinkage cracks in thin section. Volcaniclastic grains are mostly mafic, with randomly oriented plagioclase laths, or are strongly altered (to smectite and/or clays?). Nannofossils are scattered but well preserved throughout the subunit, and minor amounts of calcareous fragments and bioclasts occur in the lower cores. A possible altered volcanic ash layer (bentonite) occurs in Section 123-766A-29R-1, at 5–8 cm; it is greenish-gray and consists of nearly pure clay with elongate lath-shaped crystals as much as 1 mm long. Sandstone becomes relatively common in Core 123-766A-

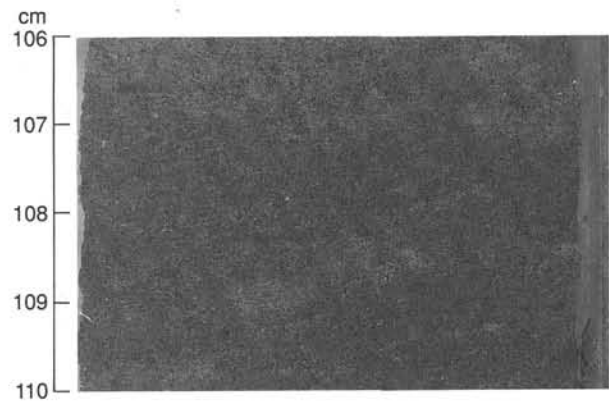


Figure 19. Grayish green claystone with disseminated silt- to fine-sand-sized particles (dominantly glauconite?). Lithologic Subunit IIIA; Section 123-766A-26R-1 at 106–110 cm.

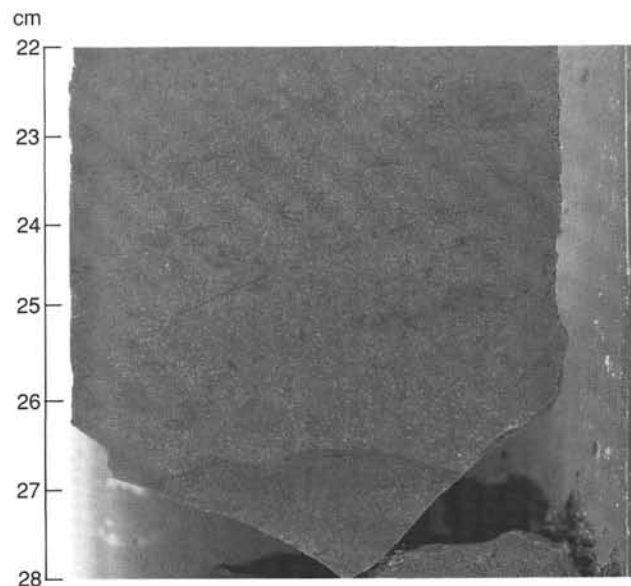


Figure 20. Claystone with disseminated radiolarians (white) and empty radiolarian molds (dark). Lithologic Subunit IIIA; Section 123-766A-27R-2 at 22–28 cm.

32R; it contains abundant glauconite(?), bioclasts, lesser quartz, and pyrite, is coarse- to very fine-grained, and may be graded, inversely graded, complexly graded, or massive (Fig. 21). Pyrite nodules occur sporadically in this subunit (Fig. 22). The base of Subunit IIIA is taken at the base of the lowest *in-situ* claystone interval, probably slightly below the Barremian/Hauterivian boundary.

Subunit IIIB (Depth, 304.2–466.7 mbsf, Section 123-766A-32R, CC, top to 123-766A-49R-4 at 66 cm).

Age = Hauterivian to ?latest Valanginian.

Dark to very dark greenish-gray sandstones constitute most of the upper part of Subunit IIIB; sandy to clayey siltstones predominate in Cores 123-766A-43R and below. These sandstones display a wide range of compositions, but two main lithologies can be defined. One is very dark greenish-gray, typically fine-grained and moderately well-sorted, only slightly calcareous. This lithology is similar in composition to the sandstones de-

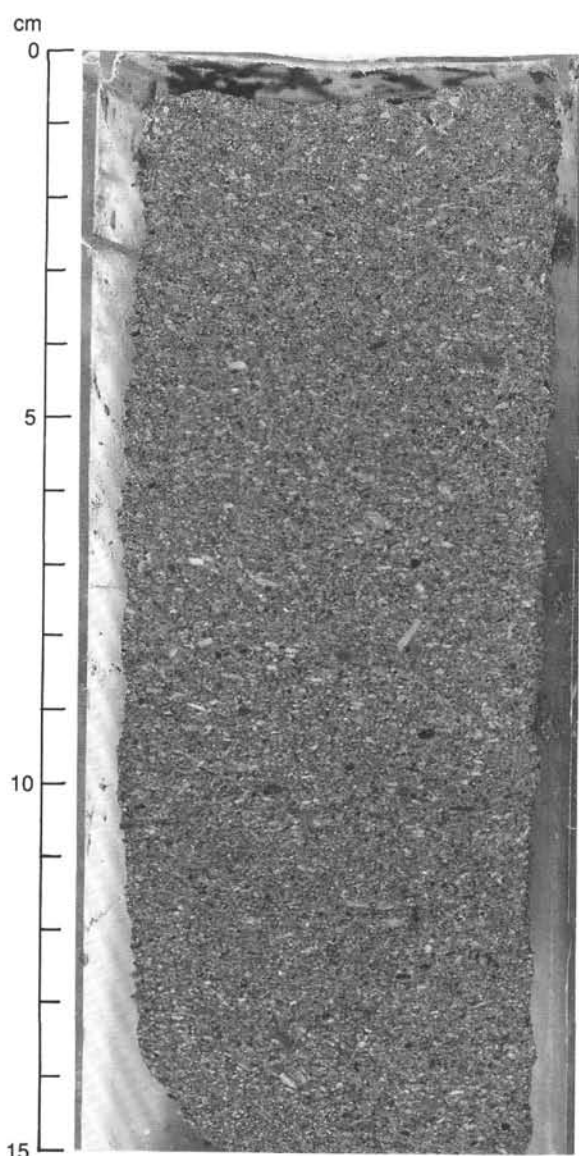


Figure 21. Glauconitic? bioclastic sandstone with quartz and altered volcanoclastic? grains. Lithologic Subunit IIIA; Section 123-766A-32R-4 at 0–15 cm.



Figure 22. Large pyrite nodule coated with cubes and less common pyritohedrons of pyrite. Lithologic Subunit IIIA; Section 123-766A-31R-1 at 15–21 cm.

scribed above in Subunit IIIA—that is, rich in quartz, glauconite(?), and/or altered volcanic grains. The second lithology is lighter in color (dark greenish-gray), typically medium- to coarse-grained and poorly sorted, and contains abundant white bioclasts in addition to the components found in the first lithology (Fig. 23). Echinoderm fragments are the most common bioclasts, but pelecypods (including “inoceramid” fragments), brachiopods, red algae, corals, foraminifers, and bryozoan clasts also occur. The bioclasts are typically larger than other grains (commonly as much as several mm in diameter), tabular in shape, and oriented parallel to bedding. In some cores (e.g., Core 123-766A-44R), fine-grained calcareous material is concentrated in millimeter-scale, white wispy layers that impart an overall mottled fabric to the rock. Other components noted in the sandstones include coal fragments (Section 123-766A-34R-1 at 40 cm), radiolarians, pyrite, and feldspar.

Both lithologies may be massive, bioturbated, graded, inversely graded, or complexly graded; in some intervals, bioclasts are inversely graded even though other grains are not. Fining-upward sequences predominate overall in Subunit IIIB. Some intervals that appear to be massive may have been so thoroughly bioturbated that all traces of original fabric have been obliterated.

Sandy to clayey siltstones make up most of the lower half of Subunit IIIB; most are very dark greenish-gray or dark gray, massive, and featureless, but some are faintly laminated, bioturbated, or display subtle fining-upward sequences. Massive intervals may have originally had primary sedimentary structures that were destroyed by pervasive bioturbation. Pyrite is particularly abundant in this lithology, both as disseminated grains and as nodules and concretions; pyrite concretions occur throughout Subunit IIIB. Sandy siltstones are intercalated with mafic igneous rocks in Cores 123-766A-48R and -49R (Fig. 24). Sedimentary/igneous contacts were typically destroyed by drilling, but at the base of Unit III (Section 123-766A-49R-4 at 66 cm) a

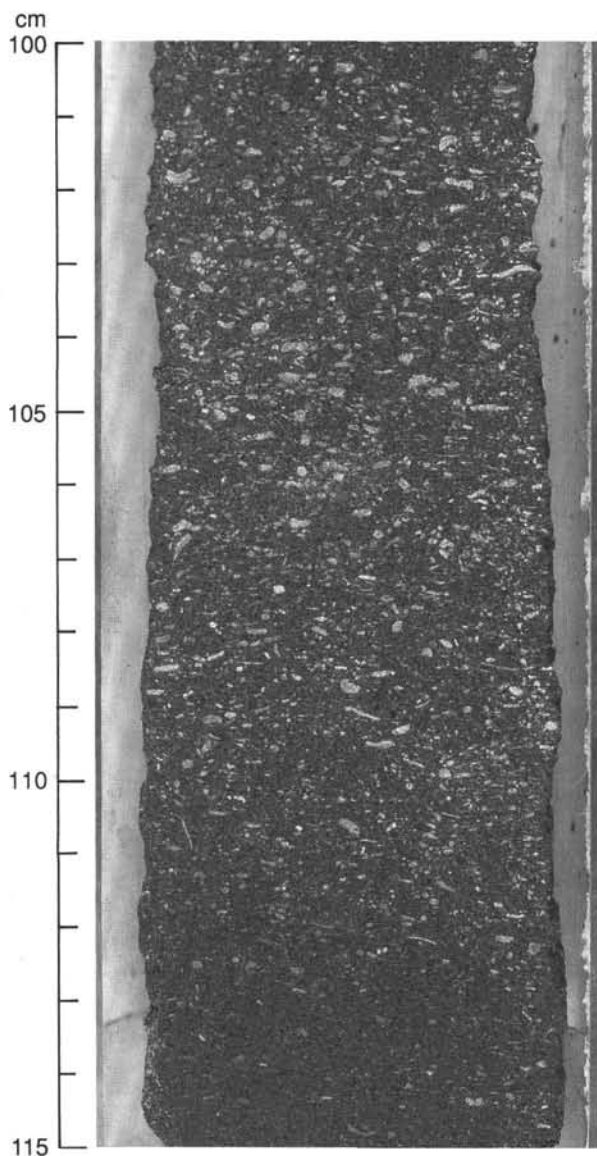


Figure 23. Silty sandstone with abundant neritic bioclasts (dominated by echinoderm fragments), glauconite?, quartz, and altered volcanoclastic? grains. Lithologic Subunit IIIB; Section 123-766A-40R-3 at 100–115 cm.

baked sediment/chilled igneous contact several millimeters thick is preserved (Fig. 25).

Minor lithologies in Subunit IIIB include claystones, bioclastic grainstones, and possible ash layers. Sandy claystone with 10% zeolite occurs in Section 123-766A-33R-2, and 1 cm of black, organic-rich? claystone was noted in Section 123-766A-36R-1. Discrete intervals of bioclastic grainstone occur in Cores 123-766A-41R, -42R, and -45R; thin layers of possible altered ash occur in Cores 123-766A-45R, -47R, -48R, and -49R. These layers have a waxy appearance and soapy texture, are light greenish-gray or very dark gray, and are composed of clay and/or altered volcanoclastic grains, some of which have a shardlike appearance.

SEDIMENTOLOGY

Site 766 is located at the base of the steep western margin of the Exmouth Plateau. The oldest sediment penetrated at Site 766, in Section 123-766A-49R-4 at 66 cm (466.7 mbsf), is uppermost Valanginian sandstone and siltstone, alternating with in-

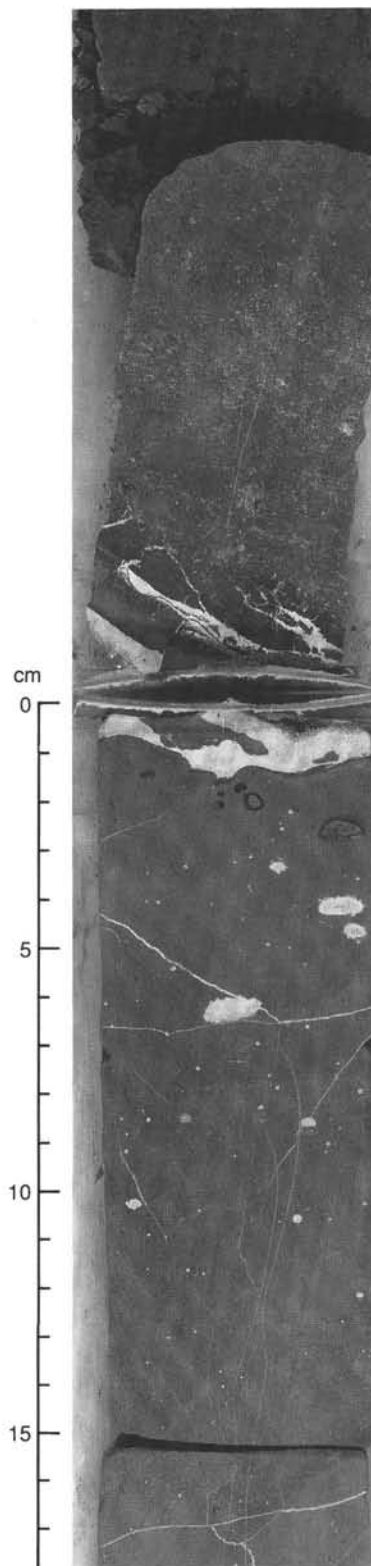


Figure 24. Uppermost contact between sedimentary and igneous rock; note white calcite veins just below boundary (at 129 cm in Section 123-766A-48R-6). Lithologic Subunit IIIB; Section 123-766A-48R-6 (base) and 123-766A-48R-7 (top). Intrusive contact between igneous lithologic Unit 1 (sparsely clinopyroxene-olivine-plagioclase phyric basalt sills) and the overlying sediments at the boundary between Sections 123-766A-48R-6 and 123-766A-48R-7. The basalt is chilled against the sediments and is fractured along the contact. Calcite fills the fractures and vesicles. The contact dips at 20°. Vesicles and veins filled by calcite at unit contact (Sections 123-766A-48R-6 and 123-766A-48R-7).

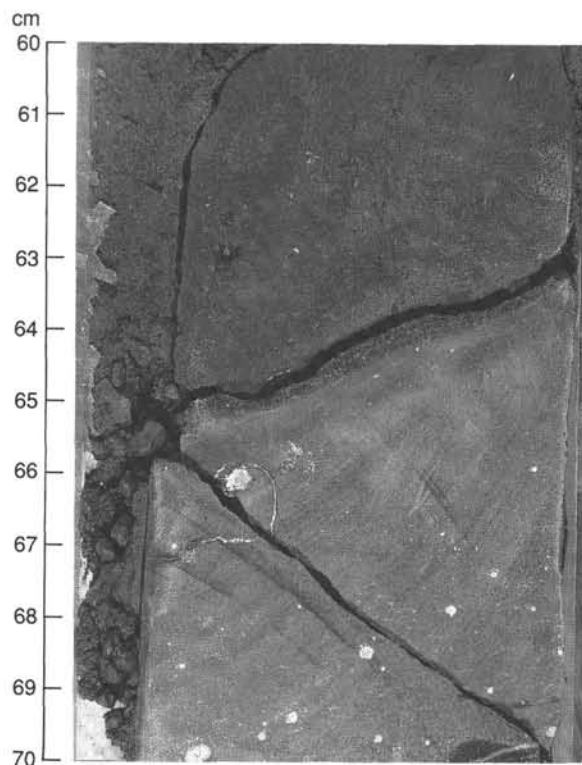


Figure 25. Contact between baked very dark greenish gray silty sandstone to silty sandstone (dominated by glauconite? or altered volcanoclastic? grains and quartz) and chilled igneous rock at 63 to 65 cm. Lithologic Subunit IIIB; Section 123-766A-49R-4 at 60–70 cm. Intrusive contact between igneous lithologic Unit 3 (aphyric basalt sill) and the overlying sediments in Section 123-766A-49R-4, 60–70 cm. The basalt is chilled against the sediments, which are baked and hardened. The basalt just below the chilled margin is vesicular. The contact dips at 30°.

clined basaltic intrusions (see “Igneous Rock Lithostratigraphy” section, this chapter). The uppermost sediment/basalt interface occurs in Section 123-766A-48R-6 at 129 cm (460.6 mbsf). At least 300 m (approximately 65%) of the sediments penetrated accumulated during the Lower Cretaceous, compared with less than 150 m thereafter. At Site 765, on the Argo Abyssal Plain, the Lower Cretaceous also is slightly more than 300 m thick. However, approximately 65% of the total sediment column at this site accumulated after the Lower Cretaceous, primarily during the Neogene. The sedimentation history, based on the age and present depth of basement(?) and time-depth relationship for oceanic crust, suggests that Site 766 began at a depth of about 800 m. However, the presence of shallow marine components in the oldest lithologic unit, if not redeposited, suggests that initial depths were shallower. Site 766 appears to have remained above or near the carbonate compensation depth (CCD) throughout its history, whereas Site 765 may have started near the CCD, but remained below it throughout most of its history.

Figure 26 displays the stratigraphy of Site 766, with lithostratigraphy from multivariate analysis of all smear-slide lithologic data (more than 150 samples). The graphic representation of lithologies is based on the distribution of the cluster elements shown in Figure 27 (methods of cluster analysis and graphic representation of their results are described in the Site 765 chapter, “Sedimentology” section, this volume). Most lithologic unit boundaries correspond well to boundaries between stratigraphic intervals, which are distinctly different in Figure 26. Discrepancies result, in part, to the averaging of one to three cores in Figure 26, as well as to the distribution of original smear-slide data.

Uppermost Valanginian to Barremian

The inclined basaltic intrusions present in Cores 123-766A-48R and -49R, are interpreted as sills (see “Igneous Rock Lithostratigraphy” section, this chapter); therefore, the oldest sediments at this site may not have been recovered. The dominant lithologies in Subunit IIIB are dark greenish-gray silty sandstones and sandy siltstones, with varying amounts of glauconite?, quartz, echinoderm and bryozoan bioclasts, calcite prisms, and altered volcanoclastic grains. In general, the lithologies coarsen upward, with a relative increase in bioclasts, glauconite, and quartz(?). Clay-sized material is rare throughout the subunit. Normal grading is the most common sedimentary structure within the coarser-grained lithologies; reverse grading and complex grading also occur. Mottling and burrowing are common within finer-grained intervals. Other sedimentary structures are rare.

Subunit IIIB apparently consists of redeposited material, displaying a wedge-shaped morphology, thickening eastward toward the Exmouth Plateau and southward toward the Cuvier Abyssal Plain (see “Seismic Stratigraphy” section, this chapter). The scarcity of sedimentary structures typically associated with turbidites (Bouma, 1962) and the conspicuous absence of clay-sized material required for sustaining turbidity current transport suggest grain flow transport may have been the dominant process of redeposition. However, the role of bioturbation in destroying sedimentary structures and that of bottom currents in removing fine-grained components should be weighed before eliminating turbidity currents from consideration. Scenarios of strong currents winnowing turbidites or a steep slope capable of sustaining grain flows are both reasonable for Site 766, which is situated at the steep western margin of the Exmouth Plateau. Slopes in excess of 17° (Middleton, 1970) are required to sustain grain flow transport, and such a slope, if present at the time of accumulation, suggests rapid subsidence of the depositional center before and/or at the time of deposition, arguing for a deep environment of deposition. Glauconite(?) grains, generally accepted as good indicators of shallow marine conditions, are well-rounded in Subunit IIIB, suggesting they may have undergone significant transport. The coarsening-upward trend in this subunit is interpreted as representing progradation of the system. The Exmouth Plateau is the likely source for the marginal to shallow marine constituents (e.g., glauconite[?], quartz, and echinoderm and bryozoan bioclasts), and it is logical that their relative abundance increases during the proposed progradation of the abundance.

The lower part of Subunit IIIB (uppermost Valanginian to lower Hauterivian) is characterized locally by thin laminae consisting almost entirely of altered volcanoclastic grains associated with noncalcareous intervals of waxy appearance. These thin laminae are interpreted as altered ash layers. The age of the uppermost ash layers at Site 766 is roughly the same as that of these layers at Site 765, although their lithological characteristics are somewhat different.

Subunit IIIA consists predominantly of greenish-gray claystone containing abundant silt- to sand-sized glauconite(?) and as much as 50% radiolarians. Common coarser-grained intercalations consist predominantly of glauconite(?), quartz, calcite, and bioclasts. This facies apparently signals redirection of the coarse sediment away from Site 766, or abandoning of the progradational wedge system, possibly related to the late Hauterivian to Barremian highstand of sea level proposed by Haq et al. (1987).

Unit III is roughly equivalent to an unconformity on the Exmouth Plateau. Berriasian to lower Valanginian prodeltaic sediments of the Barrow Group, at Sites 762 and 763 on the Exmouth Plateau (von Rad, Haq, et al., 1990) are overlain by Aptian carbonates. The lower Valanginian sediments at Site 762

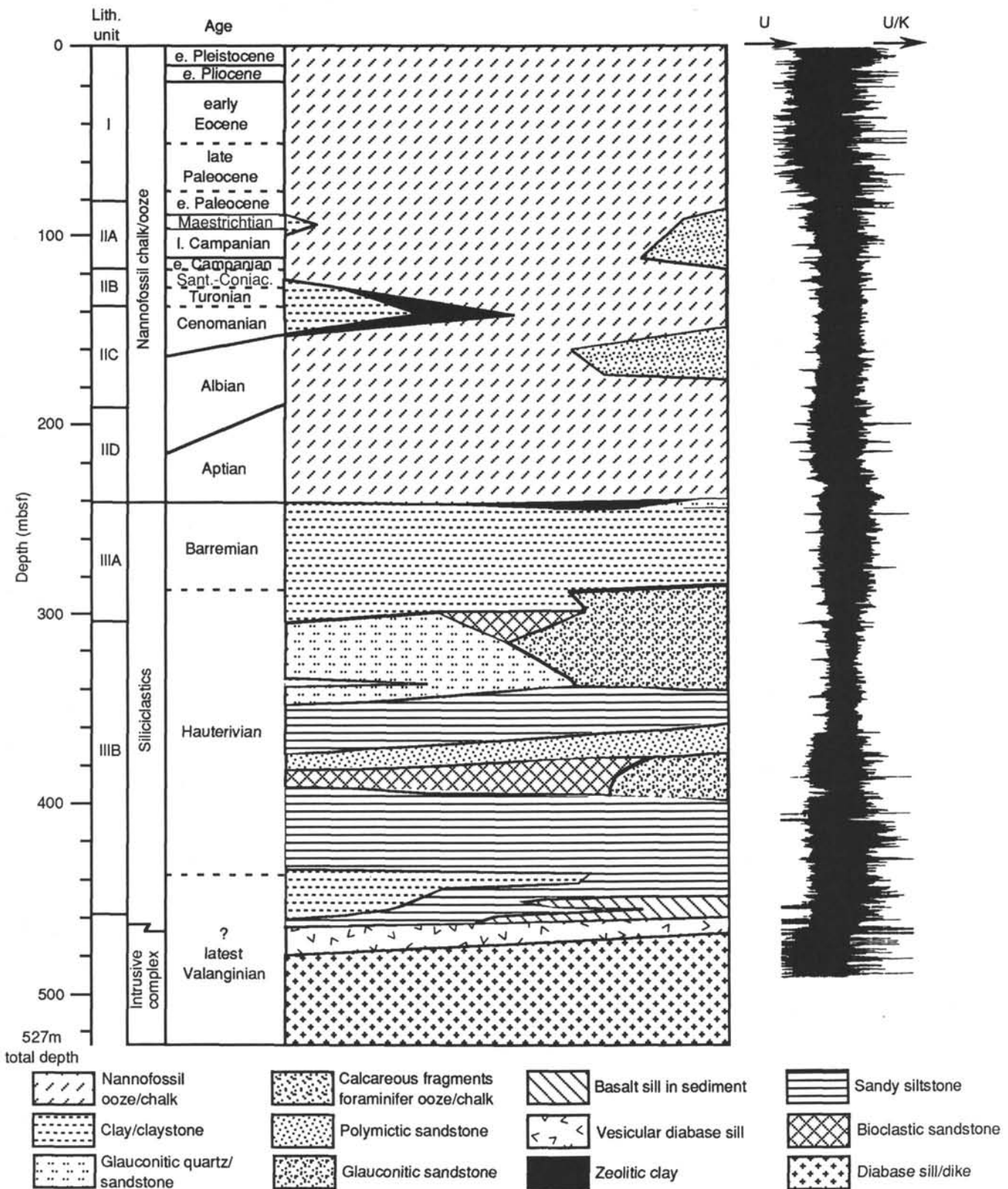


Figure 26. Stratigraphy of Site 766, with principal lithologies derived from multivariate analysis of all smear-slide lithologic data (more than 150 samples). The downhole K and U/K anomalies that assist the lithostratigraphy were obtained from spectrometer logs. Graphic representation of the distribution of the main lithologies of Site 766 is based on Figure 27. The average relative frequency of the groups (in relation to their lithologies) for one to three cores is represented by a single point on this graph. The graphic representation of lithologies is sorted by grain size (fining to the left). Thus, at a given horizon, the relative amounts of lithologies shown represent an average for one to three cores.

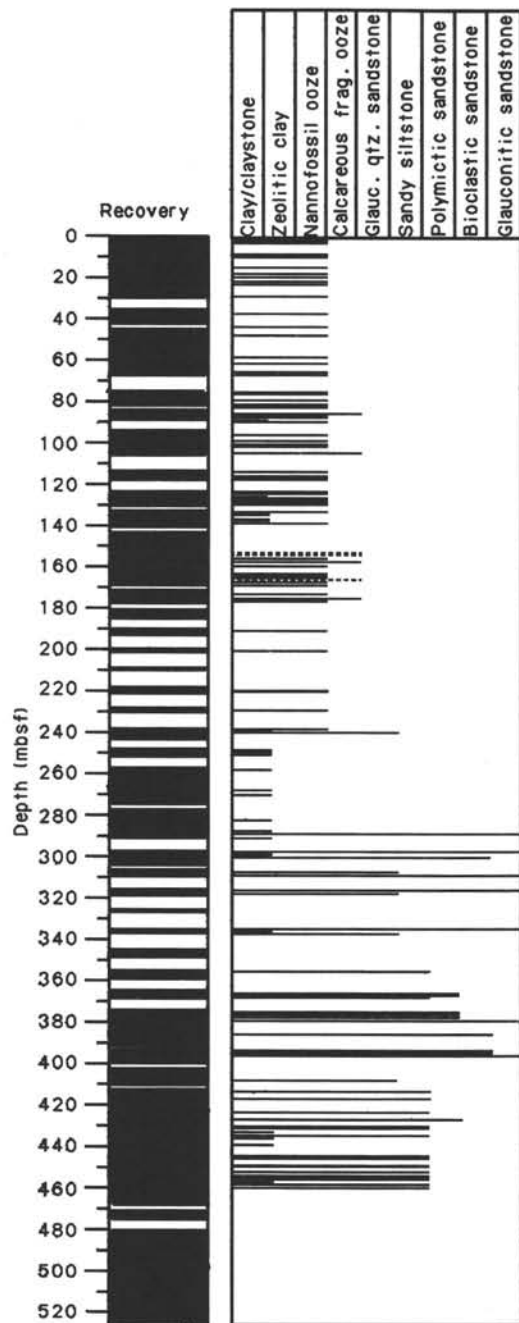


Figure 27. Cluster analysis for Site 766. Similar lithologies, which are grouped on the basis of preliminary cluster analyses, to facilitate further analysis and graphic representation. Recovered intervals indicated in black.

(outer plateau) include minor shallow marine components and have a greater degree of similarity to Unit IIIB at Site 766, than do the lower Valanginian sediments at Site 763 (middle plateau). A likely source of sediment for Subunit IIIB is shallow marine and volcanoclastic material from the outer margin of the Exmouth Plateau, presumably transported off the plateau during the lower Valanginian to Aptian hiatus. Possible mechanisms for an unconformity on the plateau at this time include a prominent lowstand of sea level in the lower Valanginian, proposed by Haq et al. (1987), or uplift associated with Hauterivian breakup along the western margin of the Exmouth Plateau.

Aptian to Lower Paleocene

The distinct sedimentological break between Units II and III, which coincides with a brief lower Aptian hiatus at Site 766, separates Barremian claystones from Aptian nannofossil chalks. Subunit IID (Aptian to Albian) consists of laminated to massive nannofossil chalks, becoming locally zeolitic and silicified upward, and grading upward into Subunit IIC. Subunit IIC (Albian to Cenomanian) is dominated by bioturbated zeolitic clayey nannofossil oozes and chalks, and lighter-colored, relatively homogeneous nannofossil oozes and chalks. Subunit IIB (Turonian to lower Campanian) is a distinctly color-banded interval of calcareous ooze (commonly graded) and clay, both increasingly zeolitic downward. Subunit IIA (Campanian to lower Paleocene) is predominantly nannofossil ooze with interbedded calcareous graded sequences, conglomerates, and clayey intervals.

The Barremian/Aptian boundary (hiatus?) represents a marked change in sedimentation at Site 766, from hemipelagic, gravity, and traction deposition of largely terrigenous and shallow marine materials, to pelagic, hemipelagic, and lesser gravity deposition of calcareous material (largely nannofossils). The overlying nannofossil oozes and chalks were deposited at bathyal depths, above the CCD. Graded carbonate sequences and conglomerates, interpreted as turbidites and debris flows, respectively, tend to be thin and relatively fine-grained. The observed change from terrigenous clastic to pelagic sediment types and reduced sedimentation rates appears to mark the transition from juvenile to mature oceanic conditions. Elimination of terrigenous material suggests a reduction of margin relief relative to the depth of the basin, such as a relative rise in sea level. Similar reduction of sedimentation rates observed in Site 765 and in abyssal Atlantic sites at the same time implies a global sea-level event.

Siliceous biogenic components occur in fairly large to trace amounts through most of the sedimentary section at Site 766, but siliceous sediments are uncommon. Cherty limestone occurs locally in Subunit IID (Aptian to lower Albian) and may be associated with the bases of carbonate graded sequences. Coarse calcareous components (dominantly foraminifers) are commonly silicified, probably due to recrystallization of coarse siliceous components deposited along with the coarse calcareous components. Radiolarians associated with silicified foraminifers commonly exist as molds or ghosts, and thus may be an important source for the silica that replaced many of the foraminifers. The increase of siliceous biomass may relate to widening of seaways between the northern and southern Indian Ocean at this time.

The peak abundance of zeolites in sediments coincides with the Turonian to Cenomanian highstand of sea level. The alternation of fine-grained carbonates and clayey sediments, both lacking visible primary sedimentary structures, possibly results from the influence of a fluctuating CCD near the water/sediment interface, but similar sediments at Site 763 suggest that variation in the hemipelagic influx from the nearby Exmouth Plateau, possibly as a result of short-term fluctuations of relative sea level, may be a more plausible explanation. The predominant light brown colors of the sediments, with lesser whites, grays, and greens, suggest neither strongly reduced nor strongly oxidized pore waters within the sediment column. This contrasts with the indications of strongly reducing conditions in the underlying dark greenish-gray pyritic sediments assigned to Unit III.

Paleocene to Pleistocene

Unit I consists almost entirely of homogeneous to mottled nannofossil ooze, in contrast to the heterogeneous succession of Unit II. Unit IB (early Paleocene to early Pliocene) consists of

generally featureless nannofossil ooze, representing bathyal to abyssal pelagic sedimentation above the CCD. Sparse pebble- to sand-sized clasts of sedimentary (mainly bioclastic grainstones having components similar to those occurring in Unit III) and volcanic rocks occur throughout, floating within the nannofossil ooze. Volcanic eruptive forces may have transported the displaced volcanic pebbles, although discrete ashes or dispersed fine-grained volcanic materials were not observed. The mode of displacement of the bioclastic pebbles into homogeneous, bathyal oozes is not yet understood. These pebbles may have been washed off nearby steep cliffs, which reached up into shallow water. A pronounced hiatus stretching from early Eocene to early Pliocene occurs in Core 123-766A-3R, but is not apparent lithologically, although a large zeolite component observed in this core may be related to this stratigraphic break. This hiatus may result from erosive contour currents (suggested by seismic data) or from large-scale slumping, which is common in steep marginal settings (e.g., McIlreath, 1977; Yurewicz, 1977; Davies, 1977). Subunit IA (early Pleistocene) consists of nannofossil ooze with abundant foraminifers, radiolarians, siliceous fragments, calcareous fragments, and siliceous spicules, and represents bathyal to abyssal pelagic sedimentation.

Trends in Sedimentation

Methods of analysis of burial history are discussed in the "Sedimentology" section of the Site 765 chapter (this volume). Decompacted sedimentation rates (Fig. 28) are comparable to those for Site 765. Backtracking and sedimentation rate data are presented in Tables 3 and 4.

BIOSTRATIGRAPHY

Introduction

One hole was drilled at Site 766 that penetrated a sedimentary section ranging from Pleistocene to late Valanginian-early Hauterivian in age. A condensed Cenozoic sequence spans Cores 123-766A-1R through 123-766A-10R and contains several significant hiatuses. The presence of foraminiferal, nannofossil, and radiolarian cool-water indicators suggests the influence of cool water at this site during much of the Cenozoic. The Mesozoic section is more complete than the Cenozoic section and spans Cores 123-766A-10R through 123-766A-49R. A particularly thick Hauterivian section is present.

Biostratigraphy of Cenozoic through Upper Cretaceous sediments was accomplished mainly by calcareous nannofossil, planktonic foraminifer, and benthic foraminifer markers. Radiolarians are useful markers for relative age assignments in the Pleistocene and Albian through Barremian. Palynomorphs provide the most detailed biostratigraphic dating from the Barremian to the base of the hole. Dinoflagellate markers yield an age of late Valanginian for sediment directly above and between diabase sills at the base of the drill hole. A summary of the biostratigraphic results of the hole is presented in Figure 29.

Calcareous Nannofossils

Abundance and Preservation

Calcareous nannofossils from Cenozoic and Mesozoic sediments of Hole 766A are generally abundant as a sedimentary component, and overall preservation is moderate to good. Little evidence of reworking is seen in samples from this hole. The apparent normal pelagic deposition has minimized the effects of extensive reworking and preservational variations caused by turbidite deposition found in Holes 765A, 765B, and 765C. The low-latitude zonation of Okada and Bukry (1980) was applicable, but the middle-latitude position of this site during the early Pliocene is evident in the successful application of the temperate

or middle-latitude nannofossil Subzone *Amaurolithus delicatus* (CN10d) of Bukry (1981). Other evidence for the temperate nature of this site during much of the Cenozoic is seen in the compositional changes in nannofossil assemblages apparent between this site and Site 765, such as the presence of various *Dictyococcites* spp. persisting through the Neogene and the lack of *Tribra-chiatus* spp. in the lower Eocene.

Assemblages are abundant and moderately to well-preserved in the Upper Cretaceous sediments. Lower Cretaceous assemblages are less abundant and diverse, but are found consistently and in a good state of preservation despite unfavorable lithologies toward the base of the hole (i.e., siliciclastic sandstones and siltstones).

Cenozoic

The highest samples examined in Hole 766A, Samples 123-766A-1R-1, 30-31 cm, and 123-766A-1R, CC, contain common *Calcidiscus macintyreii*, *Gephyrocapsa oceanica*, *Helicopontosphaera selli*, and *Pseudoemiliania lacunosa*. These samples are placed in the lower Pleistocene *C. macintyreii* Zone of Gartner (1977), based on the presence of these species and the lack of *Emiliania huxleyi*. Other common species include *Ceratolithus lesliei*, *Dictyococcites productus*, *Helicopontosphaera kamptneri*, *Reticulofenestra minutula*, and *Umbilicosphaera sibogae*. The common presence here of *D. productus* and its absence at Site 765 is suggestive of cool-water influences at Site 766 during the early Pleistocene (Perch-Nielsen, 1985).

Sample 123-766A-2R, CC has been assigned an age of early Pliocene. It is placed in the *Amaurolithus delicatus* Subzone (CN10d) of Bukry (1981), based on the common co-occurrence of *Discoaster asymmetricus* and *Amaurolithus delicatus*. Bukry (1981) proposed this local subzone in a study of coccolith stratigraphy from DSDP Leg 63 off the south coast of California. One presumes it is a mid-latitude subzone since low-latitude assemblages display no overlap in range between *D. asymmetricus* and *Amaurolithus* spp. (Bukry, 1981). This lack of overlap also was observed at Site 765, which is further evidence for the influence of cooler water at Site 766, as compared to Site 765 during the Neogene. Other common species in this subzone include *C. macintyreii*, *D. brouweri*, *D. challengerii*, *D. tridenus*, *D. productus*, *R. pseudoumbilica*, *R. minutula*, *Sphenolithus moriformis*, and *U. sibogae*. The early Pliocene age of this sample implies a condensed Pliocene section in Core 123-766A-2R or a hiatus between Samples 123-766A-1R, CC, and 123-766A-2R, CC, of about 2.02 m.y.

Lower Eocene sediment occurs in Sample 123-766A-3R, CC, and contains common *Campylosphaera eodela*, *Discoaster lodoensis*, and *Toweius crassus*, indicative of Zone CP10 (*D. lodoensis* Zone). A highly condensed section or hiatus is present in Core 123-766A-3R since there is a difference of approximately 50 m.y. between Samples 123-766A-2R, CC, and 123-766A-3R, CC. Samples 123-766A-4R, CC, and 123-766A-5R, CC, are placed in Zone CP9 (*Discoaster diastypus* Zone), based on the common occurrence of *C. eodela*, *D. multiradiatus*, and *D. diastypus*, and the lack of *D. lodoensis*. The lack of *Tribra-chiatus contortus* or *T. orthostylus* does not allow one to subdivide this zone. Perch-Nielsen (1985) reported that in many areas *Tribra-chiatus* is absent and suggested that this may be a result of ecological factors. Cooler climatic conditions at Site 766 during the early Eocene, along with the possibility of restricted oceanic circulation, may explain the lack of this genus.

The upper Paleocene includes Samples 123-766A-6R, CC, through 123-766A-8R, CC. Sample 123-766A-6R, CC, is placed in Subzone CP8b (*C. eodela* Subzone), based on the common presence of *C. eodela* and *D. multiradiatus* and the lack of *D. diastypus*. The next core-catcher section downhole, Sample 123-766A-7R, CC, contains a nannofossil assemblage consisting of

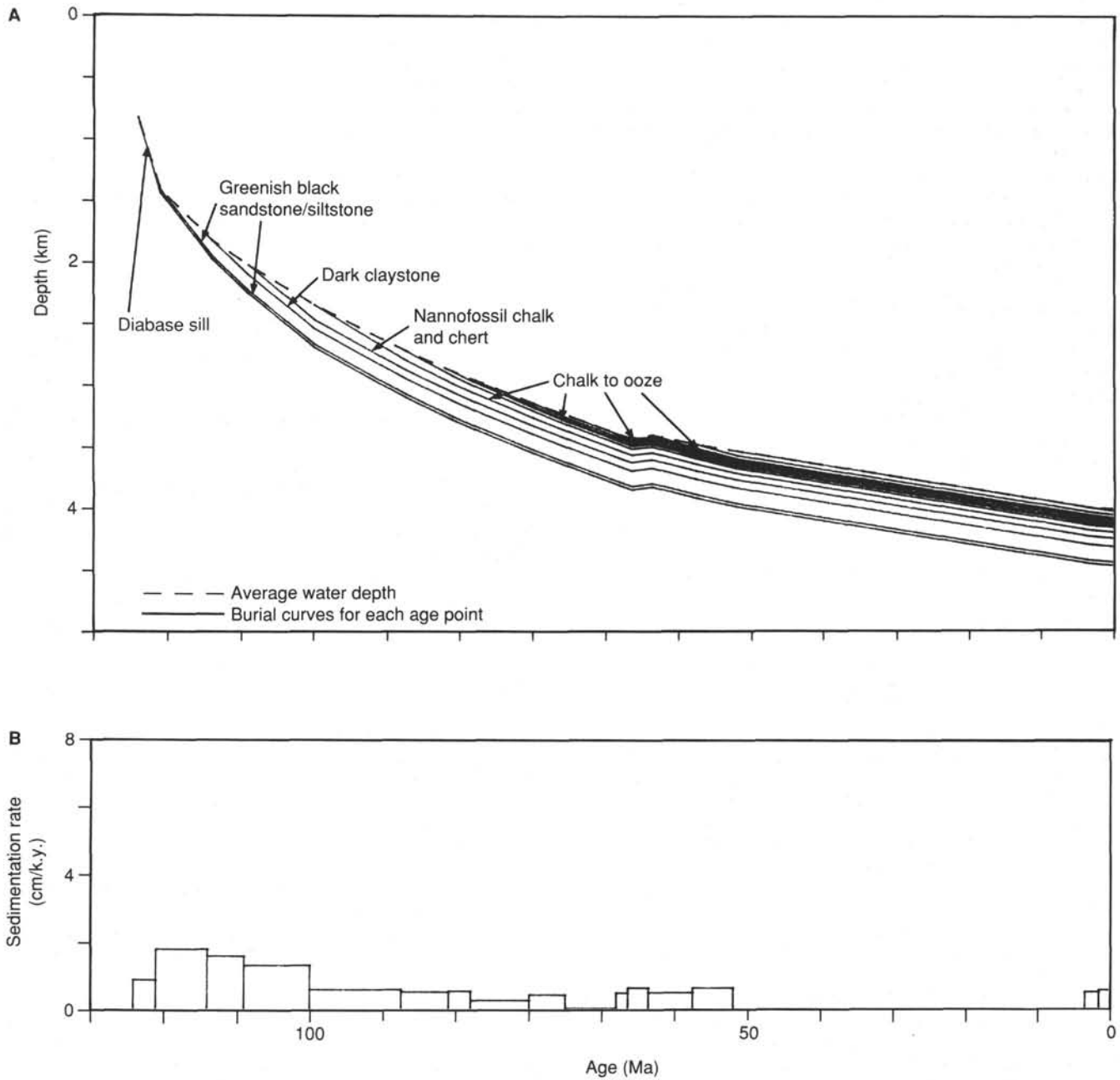


Figure 28. A. Decompressed sedimentation rates and burial history of Site 766. B. For an explanation of the methods used see "Sedimentology" section (Site 765 chapter).

common specimens of *D. multiradiatus*, *Fasciculithus tympaniformis*, *F. involutus*, and *F. lillianae* and lacks *Camplyosphaera eodela*. This section is therefore placed in Subzone CP8a (*Chiasmolithus bidens* Subzone). In Hole 766A, a rich variety of species of *Fasciculithus* disappear before the Paleocene/Eocene boundary (Zones CP8/CP9 to NP9/NP10). This agrees with Shackleton et al. (1984), who placed the extinction of *Fasciculithus* spp. 1.3 m.y. before the Zone NP9/NP10 (CP8/CP9) boundary (based on the first appearance of *C. eodela*). Sample 123-766A-8R, CC, is placed in Zone CP6 (*D. mohleri* Zone) be-

cause of the common presence of *D. mohleri* and *F. tympaniformis* and the lack of *D. nobilis* and *Heliolithus riedelii*.

Nannofossil assemblages in the upper Paleocene through lower Eocene are extremely diverse. In modern waters, the highest diversity of coccolithophorid assemblages occurs in mid-latitude zones of upwelling (between 15° and 30°) (Okada and Honjo, 1973). The high diversity of assemblages and the lack of certain ecologically controlled markers, such as *Tribrachiatius*, are consistent with the interpretation of a mid-latitude position at this site during the late Paleocene-early Eocene.

Table 3. Input and output data for backtracking Site 766.

Input data		Output data	
Time	Sediment thickness (m)	Paleodepth	
		Unsedimented	Sedimented
0	459	4333	4008
1.6	449.5	4323	4005
3.5	411	4311	3999
52	441	3844	3532
57.5	409	3765	3476
63.6	384	3668	3396
66.4	371	3689	3427
68	367	3655	3395
75	365	3500	3242
80	348	3383	3137
88	332	3185	2950
91	324	3107	2878
97.1	307	2926	2709
110	268	2526	2337
119	219	2167	2012
124	153	1918	1810
131	27	1418	1399
134	0	812	812

Note: Present water depth = 4008 m; Basemt. depth (bsf) = 459 m; Ave. sed. density = 1.7 g/cm³; Age of basement = 134 Ma; Present unsedimented water depth = 4333 m; Theoretical, present unsedimented water depth = 6021 m; Offset = -1688 m.

Table 4. Input data for sedimentation and burial history for Site 766.

Age (Ma)	Depth (mbsf)	Paleowater depth (m)	Eustatic sea level (m)	Lithology
0	0	4008	0	Nannofossil ooze
1.6	9.5	4004	5	Nannofossil ooze
3.5	18	3998	9	Nannofossil ooze
52	18	3531	70	Nannofossil ooze
57.5	50	3475	75	Nannofossil ooze
63.6	75	3397	80	Nannofossil ooze
66.4	88	3426	85	Nannofossil ooze
68	93	3395	86	Nannofossil ooze
75	95	3241	90	Nannofossil ooze
80	111	3136	92	Nannofossil ooze
88	127	2950	95	Clays 1
91	135	2877	100	Clays 1
97.5	152	2708	95	Clays 1
110	191	2336	70	Chalk-chert
119	240	2012	40	Clays 2
124	306	1810	30	Sand-silt
131	432	1399	25	Sand-silt
134	459	812	25	Sand-silt

Depth-porosity (decompaction) functions			
		Alpha	Beta
Nannofossil ooze	"Power law"	0.6171	0.1407
Clay 1	Linear	0.8271	1.692
Chalk-chert	Linear	0.8902	2.224
Clay 2	Linear	0.6621	0.3152
Sand-silt	Linear	0.5068	0.0000

Sample 123-766A-9R, CC, is placed in Subzone CP1b (*Cruciplacolithus tenuis* Subzone), based on the presence of common primitive *Coccolithus pelagicus* and *Cruciplacolithus tenuis* s.s. (Hay and Mohler, 1967) and the lack of *Chiasmolithus danicus*. This implies a condensed lower Paleocene section in Core 123-766A-9R. The lowest Paleocene nannofossil zone, Subzone CP1a (*Cruciplacolithus primus* Subzone to basal Danian), is found in Samples 123-766-10R-1, 68–69 cm, and 123-766A-10R-1, 100–101 cm. This zone can be recognized by the presence of *Cruciplacolithus primus*, *Cr. edwardsii*, and *Biantholithus*

sparsus and the lack of both *Cruciplacolithus tenuis* s.s. (Hay and Mohler, 1967) and unworked Cretaceous coccoliths. Reworking of Cretaceous nannofossils increases down Section 123-766A-10R-1.

Upper Cretaceous

The interval from Sample 123-766A-10R-2, 100–101 cm, to Sample 123-766A-17R, CC, belongs to the Upper Cretaceous.

Sample 123-766A-10R-2, 130–131 cm, contains *Nephrolithus frequens*, together with *B. sparsus*, *P. sigmoides*, *Thoracosphaera* sp., and *M. inversus*, and is late Maestrichtian in age (CC26, *N. frequens* Zone). Sample 123-766A-10R-3, 0–1 cm, is placed in the *Arkhangelskiella cymbiformis* Zone (CC25C, uppermost Maestrichtian), as indicated by the presence of *Micula murus*. The interval from Sample 123-766A-10R, CC, to Sample 123-766A-12R, CC, is late Campanian in age (CC22b–CC23a, *Quadrum trifidum* Zone to *Tranolithus phacelosus* Zone), as indicated by the presence of *Aspidolithus parvus constrictus* and *Reinhardtites levis*. The first occurrence of *A. parvus constrictus* was observed in Sample 123-766A-13R-1, 75–76 cm, along with an assemblage containing *Aspidolithus parvus parvus*, indicating a Campanian age (CC18–CC23a). Sample 123-766A-13R-2, 114–115 cm, contains an early Campanian assemblage (*A. parvus* Zone, CC18) characterized by the presence of *Marthasterites furcatus* and *A. parvus parvus*.

Samples 123-766A-13R-3, 70–71 cm, and 123-766A-13R, CC, are Santonian in age, indicated by the occurrence of *Lithastrinus septenarius*, *Lithastrinus grillii*, *Reinhardtites anthophorus*, and *Marthasterites furcatus* (*R. anthophorus* Zone, CC15). The *Lucianorhabdus cayeuxii* Zone (CC16, upper Santonian) and *Calculites obscurus* Zone (CC17, lower Campanian) were not observed in the samples examined, but this may be because of ecological reasons or diagenetic removal of the marker species.

Sample 123-766A-14R-1, 14–15 cm, contains *M. furcatus*, *Eprolithus floralis* (last occurrence), *Micula decussata* (first occurrence), *L. septenarius*, and *Quadrum gartneri* and lacks *R. anthophorus*, indicating a late Coniacian/early Santonian age (*M. decussata* Zone, CC14). The lack of *M. decussata* in Sample 123-766A-14R-1, 48–49 cm, suggests a Coniacian age (*M. furcatus* Zone, CC13). Sections 123-766A-14R-2 and 123-766A-14R-3 contain *M. furcatus*, *Q. gartneri*, and *E. floralis*, which suggests an age of Coniacian (Zone CC13).

Sections 123-766A-14R-4, 123-766A-14R-5, and 123-766A-15R-1 contain *Q. gartneri* but lack *M. furcatus*, *Eiffelithus eximius*, and *Lucianorhabdus maleformis*, indicating a Turonian age (*Q. gartneri* Zone, CC11). The *L. maleformis* Zone (CC12, upper Turonian) may not be recognized because of the absence of holococcoliths at this site (see above) and the rarity of *E. eximius* in this section.

The Cenomanian/Turonian boundary lies in the interval between Sample 123-766A-15R-1, 100–101 cm, which contains the first occurrence of *Q. gartneri* (CC11), and Sample 123-766A-15R-3, 100–101 cm, which includes the last occurrence of *Corolithion kennedyi* (marking the *Microrhabdulus decoratus* Zone, CC10 of Cenomanian age). Samples 123-766A-15R, CC, and 123-766A-16R, CC, contain *C. kennedyi* and *Prediscosphaera columnata*, indicating a Cenomanian age (CC10).

Lower Cretaceous

The interval from Sample 123-766A-17R, CC, to Core 123-766A-49R is Early Cretaceous (Albian to early Hauterivian/latest Valanginian) in age. The Cenomanian/Albian boundary is situated between Samples 123-766A-15R, CC, and 123-766A-16R, CC. The first occurrence of *Eiffelithus turriseiffelii* in Sample 123-766A-16R, CC, characterizes the boundary between the *Prediscosphaera columnata* Zone (CC8) and the overlying *E. turriseiffelii* Zone (CC 9), which is of late Albian age.

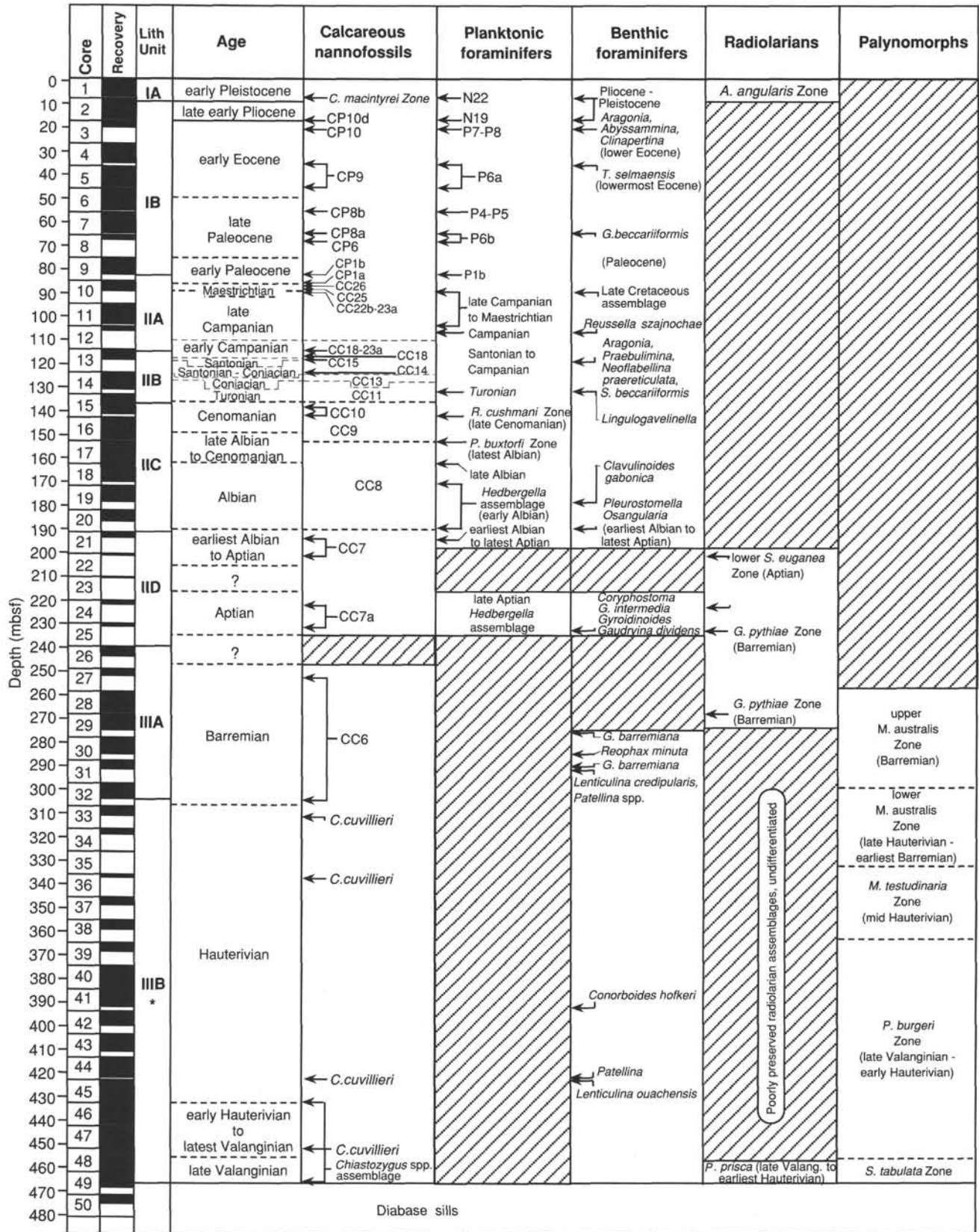


Figure 29. Biostratigraphic summary of Hole 766A.

The interval between Samples 123-766A-17R, CC, and 123-766A-20R, CC, contains an Albian assemblage (*P. columnata* Zone, CC8), as suggested by the presence of *Chiastozygus litterarius*, *Eprolithus apertior*, *Eprolithus floralis*, *P. columnata* s.l., *Flabellites biforaminis*, *Stoverius achylosus*, and *Hayesites albiensis*. The first occurrence of *P. columnata* in Sample 123-766A-20R, CC, marks the base of this zone. The underlying *Chiastozygus litterarius* Zone (CC7B), which is of early Albian to late Aptian age, is situated in the interval from Samples 123-766A-21R, CC, to 123-766A-22R, CC, based on the first occurrence of *H. albiensis* in Sample 123-766A-22R, CC. The Aptian/Albian boundary falls within Zone CC7B and thus is situated in the interval between Samples 123-766A-21R, CC, to 123-766A-22R, CC. The first occurrence of *E. floralis* in Sample 123-766A-21R, CC, approximates the boundary. Samples 123-766A-23R, CC, to 123-766A-25R, CC, yielded an assemblage of early Aptian age (CC 7A), including *Rhagodiscus angustus*, *Flabellites biforaminis*, and *E. apertior*. Sample 123-766A-26R, CC, contains a flora of low diversity, dominated by *Watznaueria barnesae*. Strata of Barremian age are characterized by floras lacking index species. These are found in Samples 123-766A-27R, CC, to 123-766A-32R, CC. The age assignment is based on the absence of both typical Aptian and Hauterivian markers. The well-preserved low-diversity flora of this interval, however, yielded rare fragments of *Micrantholithus obtusus*.

The interval covered by Samples 123-766A-33R, CC, to 123-766A-44R, CC, yielded well-preserved nannofossil assemblages of low abundance and low diversity, including *Crucellipsis cuvillieri*, *Seribiscutum salebrosum*, and *Micrantholithus hoschulzii*, indicative of a Hauterivian age. The interval from Samples 123-766A-45R, CC, to 123-766A-48R, CC, is characterized by a relatively rich *Tegumentum* spp. assemblage. Since a similar *Tegumentum* assemblage, rich in *S. salebrosum*, has been described recently from the latest Valanginian to early Hauterivian of northwest Germany, this interval can be dated accordingly. Thus, the oldest sediments recovered in Hole 766A are of latest Valanginian to early Hauterivian age.

Planktonic Foraminifers

Neogene

The uppermost two cores of Hole 766A belong to the Neogene. Sample 123-766A-1R, CC contains a Zone N22 assemblage that includes *Globorotalia truncatulinoides*, *Globorotalia tosaensis*, *Globorotalia crassaformis*, *Globorotalia inflata*, *Pulleniatina obliquiloculata*, *Neogloboquadrina dutertrei*, *Sphaeroidinella dehiscens*, *Globigerinoides sacculifer*, *Globigerinoides conglobatus*, *Globigerinoides ruber*, *Globigerinoides quadrilobatus*, *Orbulina universa*, sinistral *Globorotalia tumida*, sinistral *Globorotalia limbata*, and sinistral *Globorotalia menardii*. The microfauna indicates that Core 123-766A-1R penetrated to the lower Pleistocene. Moderate dissolution of thin-shelled foraminifers has occurred in the core-catcher sample. The assemblage contains a mixture of tropical species (*G. sacculifer*, *G. menardii*, *N. dutertrei*, *P. obliquiloculata*; see Bé, 1977) and taxa more common in the subtropical to transition zones of the modern ocean (e.g., *G. inflata*, *G. truncatulinoides*, *G. conglobatus*). The common occurrence of *G. inflata* contrasts with its sporadic distribution in the lower Pleistocene at Site 765.

Although severe selective dissolution of thin-shelled specimens is apparent in Sample 123-766A-2R, CC, a diverse planktonic assemblage was identified from this level and attributed to lower Pliocene Zone N19. The assemblage contains *Globorotalia puncticulata* (including morphotypes transitional to *G. inflata*), *Globorotalia margaritae*, *Globigerina nepenthes*, *Sphaeroidinellopsis seminulina*, *Sphaeroidinellopsis kochi*, *Pullenia-*

tina praecursoria, *Dentoglobigerina altispira altispira*, *Globoquadrina venezuelana*, sinistral *G. limbata*, sinistral *G. menardii*, sinistral *G. cf. tumida*, *G. sacculifer*, *Globigerinoides extremus*, *G. quadrilobatus*, and *O. universa*. The occurrence of advanced *G. puncticulata* specimens suggests that the sample lies within the upper part of Zone N19, high in the lower Pliocene. *Sphaeroidinella* is absent from the zone, although ancestral *Sphaeroidinellopsis* is abundant. The assemblage has a subtropical aspect, as indicated by the common occurrence of *G. puncticulata* and the absence of typical *Globorotalia tumida*.

Paleogene

Lower Eocene and Paleocene assemblages occur in Cores 123-766A-3R to 123-766A-9R. Within this interval, selective dissolution of planktonic tests increases downhole and the basal foraminiferal assemblages are dominated by thick-shelled calcareous benthic species.

Sample 123-766A-3R, CC contains an early Eocene assemblage dominated by *Acarinina* and including *Morozovella aragonensis*, *Morozovella lensiformis*, *Pseudohastigerina wilcoxensis*, *Acarinina soldadoensis*, *Acarinina nitida*, and *Acarinina primitiva*. The co-occurrence of *M. aragonensis* and *M. lensiformis* and the absence of *Morozovella subbotinae* and related species suggest that this level lies high within Zone P7 or in Zone P8.

Acarininid species dominate Samples 123-766A-4R, CC, 123-766A-5R, CC, and 123-766A-6R, CC. The associated keeled morozovellids belong to the *Morozovella subbotinae* complex of species characteristic of Zone P6, which spans the Paleocene/Eocene boundary. Sample 123-766A-4R, CC, contains *M. subbotinae*, *Morozovella marginodentata*, and *Morozovella formosa gracilis*, together with *Morozovella aequa*, *Planorotalites chapmani*, and *Acarinina primitiva*. Small forms that resemble *Planorotalites pseudomenardii* (typical of upper Paleocene Zone P4) also occur in this assemblage. Abundant *M. subbotinae* is associated with abundant *Acarinina soldadoensis*, *A. primitiva*, and rare *M. aequa* in Sample 123-766A-5R, CC. A similar assemblage occurs in Sample 123-766A-6R, CC, but here it is associated with common *Morozovella acuta*, which ranges only to Zone P6a. This suggests that Sample 123-766A-6R, CC, lies within the uppermost Paleocene Zone P6a; whereas, Samples 123-766A-5R, CC, and 123-766A-4R, CC, belong to the lower Eocene Zone P6b above the extinction level of the *Morozovella velascoensis* group of species.

Planktonic foraminifers from the lower part of the Paleogene interval have been affected by severe dissolution and form a rare component of the foraminiferal assemblages. Sample 123-766A-7R, CC contains *M. velascoensis* and *Acarinina mckannai*, indicative of Zones P4 to P5 of the upper Paleocene. Rare *A. mckannai* occurs in Sample 123-766A-8R, CC, which suggests that this level also lies within the upper Paleocene (Zones P4 to P5). The planktonic foraminiferal assemblage from Sample 123-766A-9R, CC, is dominated by Maestrichtian taxa (including *Gublerina*, *Globotruncanella*, and *Globotruncana*) that are thought to be reworked. These completely overshadow the Paleocene species that occur at this level: *Subbotina pseudobulloides* and *Subbotina cf. triloculinoides*, indicative of lower Paleocene Zone P1b.

Upper Cretaceous

Upper Cretaceous planktonic foraminiferal assemblages occur in the core-catcher samples of Cores 123-766A-10R to 123-766A-15R. Foraminifers in the upper cores of this interval were affected by severe selective dissolution: thick-shelled calcareous benthic species dominate the assemblages and the planktonic types are generally rare, small-sized, and have poor preservation.

The occurrence of rare *Globotruncanella havanensis* and *Rugoglobigerina milamensis* in Sample 123-766A-10R, CC, suggests that this level is no lower than uppermost Campanian. A more diverse assemblage belonging to the uppermost Campanian or lower Maestrichtian occurs in Sample 123-766A-11R, CC, and contains *G. havanensis*, *Gublerina* cf. *cuivillieri*, *Heterohelix pseudotessera*, *Schackoina multispinata*, *Globotruncana linneiana*, *Globotruncana arca*, *Rosita fornicata*, and *G. cf. prairiehillensis*. The Campanian is also represented in Sample 123-766A-12R, CC, where the assemblage includes *Globotruncana orientalis*, *Globotruncana ventricosa*, *G. linneiana*, *G. arca*, *R. fornicata*, *S. multispinata*, and *G. cf. prairiehillensis*. The poorly preserved assemblage recovered from Sample 123-766A-13R, CC, may contain *Globotruncana* spp. and probably belongs to the Santonian or Campanian.

An abundant but poorly preserved Turonian assemblage dominated by the *Dicarinella imbricata/hagni* group occurs in Sample 123-766A-14R, CC. Other elements of the fauna include *Praeglobotruncana stephani*, *Praeglobotruncana gibba*, and *Schackoina cenomana*. The upper Cenomanian is represented in Sample 123-766A-15R, CC, by a *Rotalipora cushmani* Zone assemblage containing *Rotalipora greenhornensis*, *Praeglobotruncana delrioensis*, *P. stephani*, *Whiteinella brittonensis*, *S. cenomana*, *Hedbergella punctata*, and *Hedbergella simplex*. *Planomalina buxtorfi* also commonly occurs here, but is apparently reworked from the upper Albian.

Lower Cretaceous

Planktonic foraminiferal assemblages belonging to the Lower Cretaceous occur in Cores 123-766A-16R to 123-766A-25R. The highest assemblage (Sample 123-766A-16R, CC) belongs to the upper Albian *Planomalina buxtorfi* Zone and contains poorly preserved *P. buxtorfi*, primitive *Praeglobotruncana* spp., and *H. punctata*. The lowest record of *H. punctata* occurs in Sample 123-766A-17R, CC, where it is associated with rare *Hedbergella simplex* (= *Hedbergella amabilis*) and abundant *Hedbergella* sp. cf. *Ticinella primula*. A similar assemblage has been recorded from the upper Albian of the Australian Great Artesian Basin and in New Guinea (Playford et al., 1975; Haig, 1979, 1981). The assemblage of abundant *Hedbergella planispira*, together with less common *Hedbergella delrioensis*, from Samples 123-766A-18R, CC, 123-766A-19R, CC, and 123-766A-20R, CC, resembles the lower Albian planktonic fauna of the Great Artesian Basin. The occurrence of common *Hedbergella trocoidea* in Sample 123-766A-21R, CC, together with *Favusella* sp. and *H. delrioensis*, suggests that this level lies near the Aptian/Albian boundary.

Species of *Hedbergella* and *Globigerinelloides* occur in Samples 123-766A-24R, CC, and 123-766A-25R, CC. The *Hedbergella* fauna includes abundant small representatives of *H. planispira* and *H. delrioensis*, together with morphotypes that resemble *H. sigali* and *H. gorbachikae*. Rare *H. trocoidea* occurs in Sample 123-766A-24R, CC. This assemblage suggests a late Aptian age. A thick-chambered species of *Globigerinelloides* resembling *G. bentonensis* (usually taken as indicative of the Albian) occurs in both samples and is associated with more compressed forms of the genus. A comparable microfauna was recorded by Krashennikov (1974) from DSDP Site 260 in the Gascoyne Abyssal Plain, and was considered to be upper Albian-lower Cenomanian. In a review of eastern Indian Ocean planktonic assemblages, Herb and Scheibnerova (1977) noted that the chronostratigraphic significance of the fauna was ambiguous.

Benthic Foraminifers

Benthic foraminifers were examined from core-catcher samples from Hole 766A. Since the abundance of foraminifers is

generally low in the lower portion of the hole, additional samples from within the cores were also washed. All of the 44 core-catcher samples contained benthic foraminifers. Preservation is good in the Cenozoic interval, but ranges from good to poor in the Cretaceous.

Cenozoic

All samples from the Cenozoic sediments in Hole 766A contain abundant, well-preserved assemblages of deep-water calcareous benthic foraminifers. Neogene assemblages were recovered from two core-catcher samples from Hole 766A. The assemblages in both Samples 123-766A-1R, CC, and 123-766A-2R, CC, contain common specimens of *Nuttallides umbonifera*, together with *Cibicidoides bradyi*, *Cibicidoides mundulus*, *Epistominella exigua*, *Globocassidulina subglobosa*, *Gyroidinoides*, *Melonis barleeianum*, *M. pompilioides*, *Oridorsalis*, *Planulina wuellerstorfi*, *Pullenia bulloides*, *P. quinqueloba*, *Pyrgo murrhina*, and *Stilostomella*. The absence of typical Miocene species implies a Pliocene to Pleistocene age for this assemblage. The common occurrence of *N. umbonifera*, together with the lack of typical upper bathyal to neritic forms, indicates lower bathyal to abyssal depths and little or no redeposition from shallower depths.

Samples 123-766A-3R, CC, to 123-766A-6R, CC, contain well-preserved lower Eocene benthic assemblages. These assemblages contain common *Nuttallides truempyi* and *Bulimina* spp., with accessory *Abyssammina*, *Anomalina*, *Aragonia*, *Cibicidoides*, *Clinapertina*, *Globocassidulina*, *Oridorsalis*, *Osangularia*, *Pullenia*, and *Quadriformina*. The proportions of *N. truempyi* and *Bulimina* are roughly equal, which suggests a paleodepth near the boundary between the lower bathyal and abyssal assemblages of Tjalsma and Lohmann (1983). Several biostratigraphically important occurrences were observed in this interval. The age of the uppermost sample (123-766A-3R, CC) is constrained by the occurrence of *Aragonia semireticulata*, which has its last occurrence in Zone P8 (Tjalsma and Lohmann, 1983). Sample 123-766A-4R, CC, contains several specimens of *Tappanina selmensis*, which in the Atlantic ranges to the top of Zone P6b (Van Morkhoven et al., 1986). We also observed a single specimen of *Neoflabellina jarvisi*, which according to Van Morkhoven et al. (1986) has its last occurrence in Zone P5. This occurrence is anomalously high, since nannofossil and planktonic foraminiferal evidence yield an early Eocene age for Sample 123-766A-4R, CC. The first occurrence of *Clinapertina inflata* was observed in Sample 123-766A-5R, CC. This species is reported to range upward from the base of Zone P6a (Tjalsma and Lohmann, 1983). In Sample 123-766A-6R, CC, we observed the first occurrence of *Quadriformina*, which has been reported to occur in the upper part of Zone P5 (Tjalsma and Lohmann, 1983).

The uppermost Paleocene assemblage was encountered in Sample 123-766A-7R, CC. This sample contains common specimens of *Gavelinella beccariiiformis*, along with *Gavelinella danica*, *Pullenia coryelli*, *Neoflabellina reticulata*, and *Aragonia velascoensis*. The last occurrence of these species is near the top of Zone P5, according to Van Morkhoven et al. (1986). Sample 123-766A-7R, CC, also contains the last occurrence of *Gyroidinoides globosus*, which ranges into Zone P6a (Van Morkhoven et al. 1986).

Mesozoic

The highest Upper Cretaceous assemblage was encountered in Sample 123-766A-10R, CC. This sample contains a diverse assemblage with *Globorotalites*, *Nuttallinella*, *Quadriformina*, and *Praebulimina*. Samples 123-766A-11R, CC, and 123-766A-12R, CC, also contain *Reussella szajnochae*, a species which is common in the upper Campanian and lower Maestrichtian in

the South Atlantic (Dailey, 1983) and in the Santonian-Campanian of western Australia (Belford, 1960). The first occurrence of this typical Upper Cretaceous assemblage was observed in Sample 123-766A-13R, CC. This sample also contains the first occurrence of *Aragonia*, *Bolivinooides*, *Neoflabellina praereticulata*, *Nuttallinella*, *Praebulimina*, *Pullenia*, and *G. beccariiiformis*.

A markedly different assemblage was observed in Sample 123-766A-14R, CC. This lower Senonian assemblage is less diverse than the overlying assemblage and is dominated by species of *Gaudryina*, *Gavelinella*, and *Marssonella*. The highest occurrence of *Lingulogavelinella* was observed in this sample.

Samples 123-766A-15R, CC, to 123-766A-21R, CC, contain upper Aptian to Cenomanian assemblages that are dominated by species of *Clavulinoides*, *Gyroidinoides*, *Gavelinella*, and *Osangularia*. These assemblages are accompanied by species of *Arenobulimina*, *Dorothia*, *Lenticulina*, *Lingulogavelinella*, *Marginulina*, *Nodosaria*, *Pleurostomella*, *Spiroplectammina*, and rare primitive agglutinated species. Within this interval, several first occurrences were observed: that of *Marssonella* in Sample 123-766A-15R, CC, and of *Spiroplectammina subhaeringensis* in Sample 123-766A-16R, CC; the first occurrence of *Clavulinoides gabonica* in Sample 123-766A-19R, CC, and that of *Osangularia* and *Pleurostomella* in Sample 123-766A-21R, CC. Samples 123-766A-22R, CC, and 123-766A-23R, CC, are barren of foraminifers.

An Aptian assemblage dominated by *Gavelinella* ex gr. *intermedia* and *Gyroidinoides* was found in Samples 123-766A-24R, CC, and 123-766A-25R, CC. The first occurrence of these two species, as well as *Gaudryina dividens* and *Coryphostoma*, was observed in Sample 123-766A-25R, CC. The core-catcher samples from Cores 123-766A-26R to 123-766A-28R are barren of foraminifers.

Well-preserved Barremian to Hauterivian assemblages were encountered in Sample 123-766A-29R, CC, to the base of the hole. These assemblages are dominated by nodosariids (*Denticulina*, *Fronicularia*, *Globulina*, *Lagena*, *Lenticulina*, *Lingulina*, *Marginulina*, *Marginulopsis*, *Nodosaria*, *Saracenaria*, and *Tristix*), but several distinctive non-nodosariid forms also were found, including *Conorboides*, *Gavelinella*, and *Patellina*. Several of these species may be useful markers for biostratigraphy at Site 766. *Gavelinella barremiana* was observed in Samples 123-766A-29R, CC, to 123-766A-31R, CC. The last occurrence of this species is in the mid-Aptian, according to Kent and Gradstein (1985). Sample 123-766A-30R, CC, contains an assemblage with common agglutinated species, including *Reophax minutus*. This species was reported by Geroch and Nowak (1984) to range upward from the Barremian. *Conorboides hofkeri* occurs consistently between Samples 123-766A-30R, CC, and 123-766A-41R, CC. Sample 123-766A-31R, CC, contains the last occurrence of *Patellina* and *Lenticulina crepidularis*.

Below Core 123-766A-31R, benthic assemblages appear to be Hauterivian. The last occurrence of *Marginulopsis collignoni* was observed in Sample 123-766A-32R, CC, and that of *Tristix acutiangulata* in Sample 123-766A-33R, CC. The last occurrence of both species has been reported to occur near the Barremian/Hauterivian boundary at Site 416 in the Atlantic (Sliter, 1980). The assemblages in the glauconitic sandy sediments in the lower portion of the hole (lithologic Subunit IIIB) are generally more poorly preserved, and the abundance and diversity of benthic foraminifers is low. Most samples are dominated by *Lenticulina* spp., although Sample 123-766A-46R, CC, contains abundant *Globulina* sp. The first occurrence of *Conorboides hofkeri* was observed in Sample 123-766A-41R, CC, and the last occurrence of *Lenticulina ouachensis* in Sample 123-766A-44R, CC. Several samples near the base of the hole (Samples 123-766A-44R, CC, to 123-766A-48R, CC) contain common agglutinated species, such as *Ammodiscus*, *Glomospira*, *Haplophrag-*

moides, *Rhabdammina*, *Rhizammina*, and *Reophax*. Many of these agglutinated species are built of coarse agglutinated grains, reflecting the sandy substrate. The sample nearest the diabase sill in Core 123-766A-49R (Sample 123-766A-49R-3, 70–72 cm) contains only agglutinated species. The benthic foraminiferal assemblages near the base of the hole do not yield good age assignments because many of the age-diagnostic Lower Cretaceous species were not found.

Radiolarians

This report is based on the examination of all core-catcher samples plus some additional samples selected during normal sampling of the cores (a total of 65 samples was studied). Abundance and preservation of radiolarians recovered at Site 766 are graphically represented in Figure 30 and tabulated in Table 5.

Quaternary

Common and well-preserved Quaternary radiolarians were recovered from Samples 123-766A-1R-1, 1–5 cm, to 123-766A-2R-1, 4–7 cm. The assemblages can be assigned to the *A. angulare* Zone (Sanfilippo et al., 1985), based on the presence of *Anthocorythidium angulare*, *Spongaster tetras*, *Amphirhopalum ypsilon*, *Theocorythium trachelium trachelium*, and *Didymocorytis tetrathalamus*. This indicates that the top of the sedimentary column is early Pleistocene (older than 1 Ma) and that any younger sediment must have been eroded or was not deposited. Traces of reworked Paleocene to lower Eocene radiolarians were found (*Buryella tetratica*, *Carpocanistrum astyx*).

The common presence of the subspecies *Spongaster tetras tetras*, known from latitudes higher than 30°, indicates a colder water influence, which can be attributed to a northward-flowing eastern boundary current carrying higher latitude radiolarians. Alternatively, this form may indicate upwelling conditions caused by strong offshore winds during glacial periods (Fig. 37B of Veevers, 1984).

Cores 123-766A-3R to 123-766A-17R are either barren or showed poor preservation and low abundance of radiolarians.

Cretaceous

Lower Cretaceous radiolarians recovered from Cores 123-766A-18R through 123-766A-49R are poorly to moderately preserved, except for the interval of Cores 123-766A-22R through 123-766A-25R, characterized by a sporadically high abundance of radiolarians concentrated in siliceous mudstone and occasional chert.

The interval between Samples 123-766A-22R, CC, and 123-766A-24R, CC, is assigned to the lower *Sethocapsa euganea* Zone (Schaaf, 1985). Recorded species include *Sethocapsa euganea*, *?Parvicingula malleola*, *Pseudodictyomitra carpathica* (large form), and *Eucyrtis micropora*. The first occurrence of *?P. malleola* was observed in Sample 123-766A-23R, CC, and the last occurrence of *Alievum helenae*, co-occurring with rare *S. euganea*, was recorded in Sample 123-766A-24R, CC. These associations indicate an age near the Barremian/Aptian boundary, probably in the lowermost Aptian for Sample 123-766A-24R, CC.

Sample 123-766A-25R, CC, lacks *S. euganea* and *?P. malleola* and contains *Pseudodictyomitra lilyae* and *Parvicingula cosmoconica*, indicating a Barremian age (the equivalent of the *C. pythiae* Zone).

Sample 123-766A-28R, CC, is characterized by the dominance of a spindle-shaped form resembling *Eucyrtis hanni*. A similar acme of this form was observed at Site 765, in Cores 123-765C-50R to 123-765C-52R. In addition, the sample shows the last occurrence of *E. columbaria*, indicating a Barremian age. Cores 123-766A-29R through 123-766A-30R yielded similar, but less well-preserved, assemblages dominated by spindle-shaped forms of *Eucyrtis* spp.

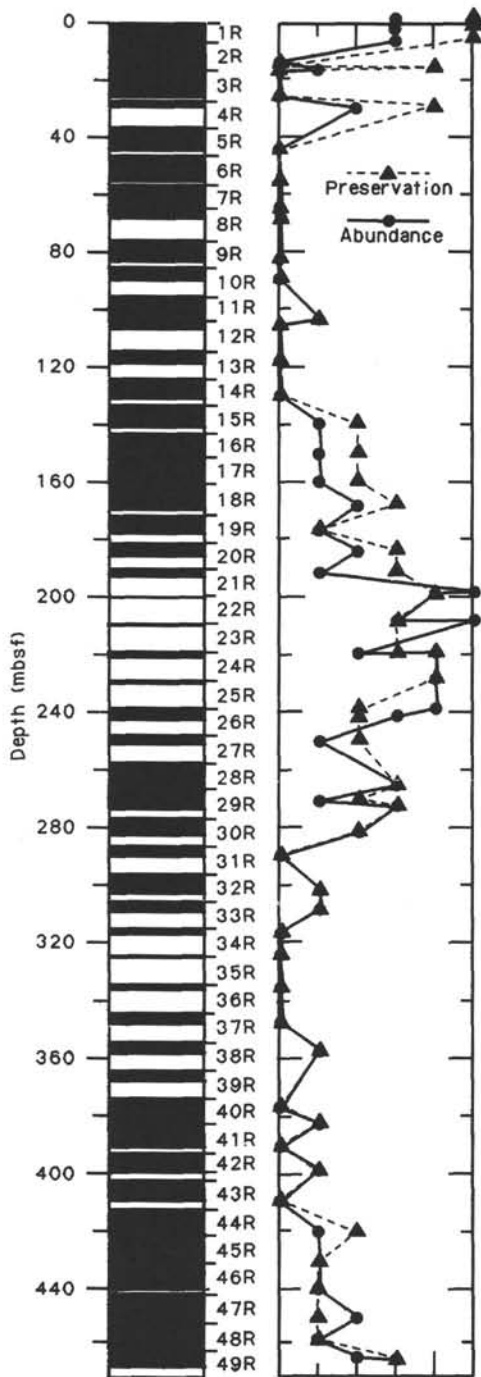


Figure 30. Abundance and preservation of radiolarians in Hole 766A, based on core-catcher samples and samples selected during sampling. Key: 0 = barren/preservation indeterminate; 1 = very rare/very poor; 2 = rare/poor; 3 = few/moderate; 4 = common/good; 5 = abundant/very good. Only samples that score at least 3/3 (few/moderate) are biostratigraphically useful. For definitions of abundance and preservation of radiolarians see "Explanatory Notes" chapter (this volume).

Cores 123-766A-31R through 123-766A-48R yielded poorly preserved indeterminate inner casts of radiolarians.

Two samples in Sections 123-766A-49R-3 and 123-766A-49R-4, from sediment layers between basalt sills, yielded a moderately preserved assemblage, including *E. micropora*, *Praeconocaryomma prisca*, and other *Praeconocaryomma* spp., as well as *Parvicingula* spp. known from Site 765, Cores 123-765C-57R to

Table 5. Abundance, preservation, and determination of radiolarians in Hole 766A.

Core, section interval (cm)	Depth (mbsf)	NA	NP	Abun.	Pres.
123-766A-					
1R-1, 1-5	0.01	3	5	C	VG
1R-1, 104-105	1.04	3	5	C	VG
1R-3, 25-29	3.25	3	5	C	VG
1R-5, 100-103	7.00	3	5	C	VG
1R-CC, 18-20	7.66	3	5	C	VG
2R-1, 4-7	7.74	3	5	VR	G
2R-5, 83-84	14.43	0	0	barren	
2R-6, 16-21	15.36	0	0	barren	
2R-CC, 17-19	17.30	1	4	VR	G
3R-1, 3-6	17.33	0	0	barren	
3R-6, 121-125	25.71	0	0	barren	
3R-CC, 22-24	26.54	0	0	barren	
4R-CC, 7-10	30.92	2	4	R	G
5R-CC, 8-11	44.92	0	0	barren	
6R-CC, 7-10	55.59	0	0	barren	
7R-CC, 10-14	65.51	0	0	barren	
8R-CC, 12-16	68.10	0	0	barren	
9R-CC, 23-28	82.98	0	0	barren	
10R-CC, 10-16	89.53	0	0	barren	
11R-CC, 5-10	104.09	1	1	VR	VP
12R-CC, 12-18	105.99	0	0	barren	
13R-CC, 7-13	118.38	0	0	barren	
14R-CC, 7-14	130.92	0	0	barren	
15R-CC, 0-7	141.29	1	2	VR	P
16R-CC, 0-6	152.09	1	2	VR	P
17R-7, 30-33	161.80	1	2	VR	P
17R-CC, 6-14	162.02	1	2	VR	P
18R-CC, 0-0	170.26	2	3	R	M
19R-CC, 0-0	178.62	1	1	VR	VP
20R-CC, 0-0	186.53	2	3	R	M
21R-CC, 0-0	193.57	1	3	VR	M
22R-CC, 0-0	200.94	5	4	A	G
22R-CC, 0-0	200.96	4	4	C	G
23R-1, 0-1	210.30	3	3	F	M
23R-CC, 0-0	210.82	5	3	A	M
24R-CC, 0-5	221.57	2	3	C	G
24R-CC, 10-13	221.67	4	4	R	M
25R-CC, 12-16	230.61	4	4	C	G
26R-2, 150-151	241.30	4	2	C	P
26R-CC, 0-4	243.71	3	2	F	P
27R-CC, 16-23	252.25	1	2	VR	P
28R-CC, 10-16	267.92	3	3	F	M
29R-4, 0-1	272.80	1	2	VR	P
29R-CC, 10-16	274.83	3	3	C	M
30R-CC, 0-6	283.95	2	2	R	P
31R-CC, 3-10	291.32	0	0	barren	
32R-CC, 0-10	304.24	1	1	VR	VP
33R-CC, 2-9	310.70	1	1	VR	VP
34R-CC, 0-7	319.02	0	0	barren	
35R-CC, 0-0	326.63	0	0	barren	
36R-CC, 0-0	337.57	0	0	barren	
37R-CC, 0-0	349.07	0	0	barren	
38R-CC, 0-0	359.38	1	1	VR	VP
39R-CC, 0-0	378.53	0	0	barren	
40R-CC, 0-0	393.85	1	1	VR	VP
41R-CC, 0-0	384.05	0	0	barren	
42R-CC, 0-0	400.56	1	1	VR	VP
43R-CC, 0-4	410.88	0	0	barren	
44R-CC, 10-15	421.96	1	2	VR	P
45R-CC, 0-7	432.32	1	1	VR	VP
46R-CC, 0-7	441.61	1	1	VR	VP
47R-CC, 0-0	451.74	2	1	R	VP
48R-6, 0-2	459.00	1	1	VR	VP
49R-3, 92-94	465.42	2	3	R	M
49R-4, 23-26	466.23	3	3	R	M

Note: Based on core-catcher samples and samples selected during sampling. Key: 0 = barren/preservation indeterminate; 1 = very rare/very poor; 2 = rare/poor; 3 = few/moderate; 4 = common/good; 5 = abundant/very good. Only samples that score at least 3/3 (few/moderate) are biostratigraphically useful. NA = nannofossil abundance; NP = nannofossil preservation.

123-765C-59R. The presence of *P. prisca* indicates a late Valanginian (to possibly early Hauterivian) age for the lowermost sediment at Site 766.

Palynology

All core-catcher samples in Hole 766A were examined for their palynomorph content. Where these were composed predominantly of sandstone, an additional claystone sample from the core was also processed. All samples down to Core 123-766A-21R were barren. Sample 123-766A-22R, CC, contains a meager assemblage; Samples 123-766A-23R, CC, to 123-766A-27R, CC, were barren, but virtually all lower samples contained abundant, well-preserved and diverse microfloras. Spore-pollen assemblages were present in each palynomorph assemblage, but as these are entirely confined to a single zone, the *Biretisporites eneabbaensis* Zone (Helby et al., 1987), they will not be discussed further. All dinoflagellate assemblages are correlated according to the Mesozoic zonation of Helby et al. (1987).

Sample 123-766A-22R, CC, contains an assemblage of low abundance and moderate preservation and diversity. Index species are mostly absent, although the presence of *Spinidinium styloniferum* indicates a late Aptian to Albian age. Cores 123-766A-23R to 123-766A-27R are barren. Samples 123-766A-28R, CC, to 123-766A-32R, CC (i.e., Samples 123-766A-28R, CC; 123-766A-29R, CC; 123-766A-30R, CC; 123-766A-31R, CC; 123-766A-32R-4, 45–47 cm; and 123-766A-32R, CC) contain assemblages of the upper *Muderongia australis* Zone. This zone is defined as the interval between the last occurrences of *Muderongia testudinaria* and *Phoberocysta burgeri* and the first occurrence of *Odontochitina operculata*. It can be informally subdivided into an upper and lower interval by the first occurrence of *Herendeenia postprojecta* and last occurrence of *Phoberocysta neocomica*. Assemblages from the lower *M. australis* Zone were found in Samples 123-766A-33R, CC, 123-766A-34R, CC, and 123-766A-35R, CC. Prominent taxa include *Cribroperidinium* spp., *Circulodinium deflandrei*, and *Leptodinium* spp.; *Herendeenia postprojecta* is common in the upper section of the zone. The *M. australis* Zone is mostly of Barremian age, although it does extend into the late Hauterivian, and it is possible that the lower *M. australis* Zone is confined to this latter interval.

Samples 123-766A-36R-1, 79–80 cm, 123-766A-36R, CC, and 123-766A-37R-2, 5–7 cm, contain assemblages of the *Muderongia testudinaria* Zone. This zone is defined as the interval between the first occurrence of *Dingodinium cerviculum* and the last occurrence of *Muderongia testudinaria* and is thought to be middle Hauterivian in age. Abundant taxa include *Cribroperidinium* spp. and *Leptodinium* spp.

Samples 123-766A-40R, CC, to 123-766A-47R, CC (a core-catcher sample from each core) contain assemblages equivalent to the *Phoberocysta burgeri* Zone. This zone is defined as the interval between the first occurrences of *P. burgeri* and *D. cerviculum* and is considered to be of late Valanginian to early Hauterivian age. Abundant taxa include *Phoberocysta* spp., *Cribroperidinium* spp., and *Oligosphaeridium* spp.

The lowest two assemblages, i.e., from Samples 123-766A-48R-5, 0–3 cm, and 123-766A-49R-2, 138–140 cm, are equivalent to the *Senoniasphaera tabulata* Zone. This zone is defined as the interval between the first occurrences of *S. tabulata* and *P. burgeri* and is late Valanginian in age. Abundant taxa include *Canningia reticulata*, *Cribroperidinium* spp., *Kaiwaradinium scrutillinum*, *S. tabulata*, *Systematophora areolata*, and *Epitricysta* sp.

Spores and pollen constitute no more than 40% to 50% of the palynomorph assemblages in the upper *M. australis* Zone, but this increases to more than 80% in the lowest samples. As the Early Cretaceous spore-pollen assemblage is similar to Late

Jurassic assemblage, however, it is not possible to differentiate contemporaneous pollen from reworked Jurassic grains.

In summary, a complete late Valanginian (*S. tabulata* Zone) to Barremian (upper *M. australis* Zone) sequence was recorded from Cores 123-766A-28R to 123-766A-49R at Site 766. Most samples were derived from siltstones and claystones, but sandstones also proved productive. The lowermost sample was taken from between basaltic sills.

Macrofossils

Belemnites

Fragments of belemnite guards were recovered from three intervals of the Lower Cretaceous of Site 766A: Section 123-766A-42R-2, at 40 cm; Section 123-766A-48R-1 at 81–83 cm; and Section 123-766A-48R-1 at 130 cm. The complete guard from 123-766A-42R-2, 40 cm, can be assigned to the genus *Duvalia*, which is common in the Mediterranean area. The occurrence of this duvaliid species is of paleobiogeographic interest, since it reflects the first record of the genus *Duvalia* in the Australian region.

The remaining two guards are represented only by small fragments of the apical region, too poorly preserved to give any reliable determination. However, the circular cross section of the apical region suggests an assignment to the genus *Hibolithes*.

SEDIMENT PALEOMAGNETISM

Overview

The lithologic succession at Site 766 consists of two main lithologic and age units: chalks of Late Cretaceous through Tertiary age and clastics of Early Cretaceous age. Within each of these major facies, the variation in magnetic properties, especially susceptibility, enabled us to subdivide them into "susceptibility units." Magnetostratigraphy of most of the Cretaceous succession was obtained using the 2G long-core cryogenic magnetometer. The preliminary polarity pattern indicates the presence of polarity Chrons M3 through M10N, and possibly M11.

Susceptibility Units

Susceptibility was measured at 10-cm intervals on every core before splitting. Determining low-field susceptibility is useful for estimating the total magnetic content of a specimen and as an important monitor of any chemical changes affecting magnetic minerals (Tarling, 1983). Susceptibility is expressed as the dimensionless ratio, *K*, of the magnetization acquired per unit field applied, normalized to a unit volume. Values of susceptibility in gauss per oersted, where 1 gauss/oersted = 1 cgs unit = 4π units in SI units.

There is considerable stratigraphic variation in susceptibility characteristics, enabling one to subdivide the lithologic column into several "susceptibility units" (Fig. 31). These susceptibility units are defined on the basis of the average susceptibility of the sediments and of the abundance and magnitude of peaks.

Susceptibility Unit S-1 corresponds to the Tertiary nannofossil ooze (Cores 123-766A-1R through -9R; 0–83 mbsf). This unit is characterized by a constant low susceptibility with average values of *K* of 10 to 20×10^{-6} cgs.

Susceptibility Unit S-2 corresponds to alternations of tan clayey nannofossil chalk and brown zeolitic clay of Albian through Maestrichtian age. Unit S-2 is characterized by a much higher susceptibility, with an average value of *K* of approximately 70×10^{-6} cgs and by closely spaced peaks having values of *K* in excess of 120×10^{-6} cgs. The high average susceptibility is probably the combined result of an oxidizing depositional environment and of the presence of significant iron oxides or iron hydroxides as-

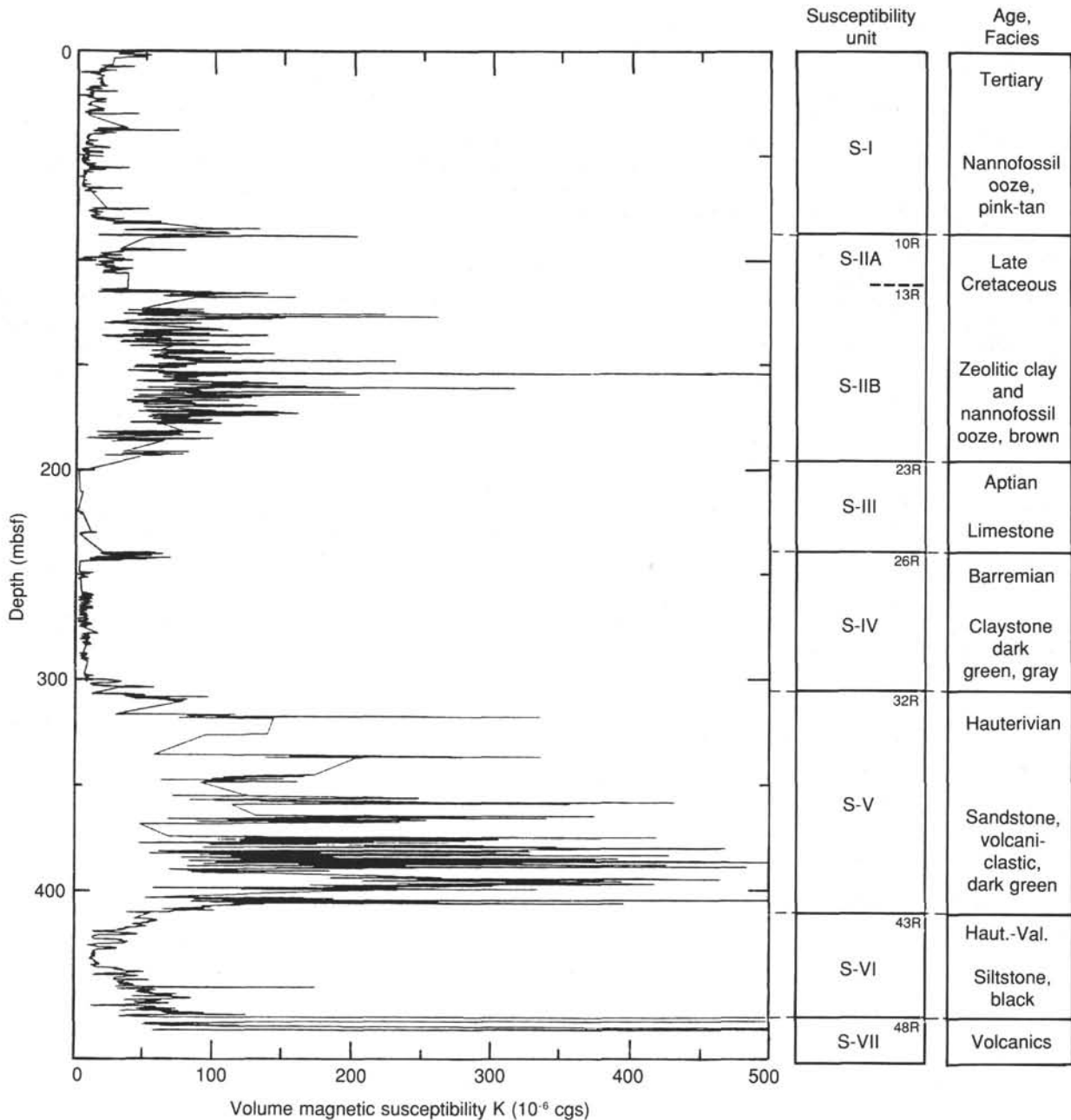


Figure 31. Stratigraphic plot of susceptibility values at Site 766. Measurements were taken at 10-cm intervals in all cores. Susceptibility facies units are distinguished on the basis of average susceptibility and abundance and magnitude of major peaks (1 cgs measurement unit = 1 gauss/oersted = 4π in SI units).

sociated with the brown clay. These very high peaks correspond to bands of darker brown clay. The uppermost cores of Unit S-2 (Core 123-766A-10R to the middle of Core 123-766A-13R; 83-115 mbsf) have a significantly lower clay content that results in a lower susceptibility, with values of K averaging approximately 30×10^{-6} cgs. This susceptibility Subunit S-2a corresponds to lithologic Subunit IIA of Maestrichtian to Campanian age. Lower Subunit S-2b extends from the Albian to the Turonian (middle of Core 123-766A-13R through Core 123-766A-22R; 115-210 mbsf).

Susceptibility Unit S-3 is in sharp contrast to Unit S-2, with an extremely low constant susceptibility (values of K of 5 to 10×10^{-6} cgs). This unit corresponds to the distinctive Aptian white limestone facies of Core 123-766A-23R to the top of Core

123-766A-26R (210-240 mbsf). The lack of clay is responsible for this very low susceptibility. The sudden upward increase by an order of magnitude in susceptibility from Cores 123-766A-26R to -25R suggests that a significant hiatus occurs at this change in facies. An earliest Aptian hiatus is also supported by the magnetostratigraphy.

Susceptibility Unit S-4, of Barremian age, also has a low susceptibility, but is separated from Unit S-3 by a brief interval of high peaks. These peaks correspond to the glauconitic sandy siltstones marking the hiatus between the Barremian and Aptian in Core 123-766A-26R. The remainder of susceptibility Unit S-4 (Cores 123-766A-26R to the middle of Core 123-766A-32R; 240-300 mbsf) consists of greenish-gray bioturbated claystones. The very low intensity is probably the result of a post-burial re-

ducing environment that converted most of the iron oxides to pyrite.

Susceptibility Unit S-5 corresponds to the rapidly deposited, dark greenish-gray glauconitic-volcaniclastic sandstones of Hauterivian age (middle of Core 123-766A-32R to the lower part of Core 123-766A-43R; 300–410 mbsf). Unit S-5 is characterized by high susceptibility (average value of K of approximately 150×10^{-6} cgs) with frequent very high peaks (values of K exceeding 300×10^{-6} cgs). These values are the highest of any sediments encountered during Leg 123 and indicate a high content of magnetite. This magnetite abundance also explains the exceptionally high magnetic intensity of these clastic sediments (discussed below). Such a high concentration of magnetite within a greenish coarse-grained sediment is probably the result of the presence of grains of volcanic lithic fragments.

In contrast, susceptibility Unit S-6 has a moderate susceptibility without significant peaks. This unit corresponds to the homogeneous black siltstones of latest Valanginian to early Hauterivian age (lower part of Core 123-766A-43R to the lowest sediment in Core 123-766A-49R; 410–466.7 mbsf). The low susceptibility (and magnetic intensity) within these fine-grained clastics is probably the result of conversion of iron oxides to pyrite after burial in an initially organic-rich sediment. The siltstones contain abundant small pyrite nodules, and their black coloration appears to be mainly the result of dispersed pyrite and minor organics. The rapid upward transition from low susceptibility of Unit S-6 to the very high susceptibility of Unit S-5 occurs within Core 123-766A-43R, as coarse-grained sandstone turbidites become abundant.

Siltstone layers between the diabase sills within Core 123-766A-49R have similar low-value susceptibility characteristics to the overlying black siltstones. This indicates that there was no iron enrichment and no oxidation of pyrite to hematite associated with the intrusion of these bodies.

Magnetic Properties

Susceptibility values proved to be a reliable indicator of the relative intensities of magnetization among and within lithologies (Fig. 31). Natural remanent magnetization (NRM) intensity varied by a factor of 1000 through the section. Low average NRM intensities, 0.1 to 1 milliamperes per meter (mA/m; $1 \text{ mA/m} = 10^{-6} \text{ emu/cm}^3$), are typical of the Aptian white limestone of susceptibility Unit S-3 and of the Barremian dark greenish-gray claystone of susceptibility Unit S-4. High average NRM intensities, 30 to 100 mA/m, are typical of the Upper Cretaceous brown zeolitic clays of susceptibility Subunit S-2b and of the Hauterivian greenish sandstones of susceptibility Unit S-5.

This correspondence of susceptibility values with the intensity of magnetization implies that most of the magnetization in the various lithologies is carried by magnetite. Magnetite has a low coercivity, hence a high response to susceptibility measurement. If high-coercivity hematite or goethite was an important carrier of magnetization, then there would not be this quasi-linear relationship of NRM intensity to susceptibility.

Nearly all lithologies displayed a 40% to 70% reduction in magnetic intensity upon alternating field (AF) demagnetization at 10 milliteslas (mT; $1 \text{ mT} = 10 \text{ oersteds}$). The only important exception was the Barremian claystone of lithologic Subunit IIIA (susceptibility Unit 4), which often displayed a 100% increase in magnetic intensity upon 10 mT demagnetization. This increase in intensity is the result of the removal of a normal-polarity overprint from an opposite reversed-polarity primary direction.

Magnetostratigraphy of the Lower Cretaceous

Rotary coring of the Tertiary through Uppermost Cretaceous oozes resulted in the disruption of the sedimentary fabric and

resetting of magnetization. It may yet be possible to derive some indication of the original magnetization from discrete samples taken from the undisturbed central portion of some of the cores of Uppermost Cretaceous. The homogenized outer region of these cores dominated the half-core measurements, rendering the shipboard results ambiguous.

The undisturbed Upper Cretaceous and Albian zeolitic clay-rich chalks and Aptian limestones yielded normal polarity, consistent with deposition during the Cretaceous Normal "Quiet Zone" (Fig. 32).

A detailed shipboard analysis was made of all cores from the Lower Cretaceous (Cores 123-766A-22R through -55R). Measurements were performed with the long-core cryogenic magnetometer at 5-cm intervals with demagnetization steps of NRM, 10 mT, and usually 15 mT. Polarity interpretations were generally obvious. Removal of normal-polarity present-day or shipboard overprints was generally complete with demagnetization at 10 mT. The only exceptions were some of the friable silty sandstone intervals within the Hauterivian, in which the recovery consisted of "biscuits" imbedded in a compacted slurry of sand; in such zones, the remagnetized slurry obscured the magnetic directions of the intact pieces during long-core measurements. Discrete samples from such cores should enable scientists to determine unambiguous polarity during shore-based studies.

Preliminary shore-based measurements of 20 discrete samples from Cores 123-766A-40R through -46R had been performed by the time of preparation of this initial report. All of the samples showed stable magnetic remanences, with polarities consistent with those measured on board the ship. A typical behavior upon AF and thermal demagnetizations of the Hauterivian dark greenish-gray sandstone is shown in Figure 33.

A pattern of polarity zones was obtained from the clastic-rich Lower Cretaceous. The assignment of polarity chrons to the observed polarity zones is constrained by three biostratigraphic age control points:

1. The dark green claystones of lithologic Subunit IIIA are Barremian in age. The lack of significant coarse-grained clastics within this heavily bioturbated unit suggests a low sedimentation rate. Therefore, the long reversed-polarity zone that extends through this unit is probably reversed-polarity Chron M3r. Adjacent polarity Chron M1r may be the reversed-polarity zone in poorly recovered Core 123-766A-27R. There is no indication of reversed-polarity Zone M0r at the top of the claystone unit or within the Aptian white limestone; therefore, it is probable that this sudden facies change corresponds to a major hiatus incorporating the uppermost Barremian and lowermost Aptian.

2. The uppermost occurrence of nannofossil *Crucellipsis cuviellieri* is in Core 123-766A-33R. This event occurs during reversed-polarity Chron M7r in the Central Atlantic (Ogg, 1987; Ogg and Steiner, 1988) or perhaps during reversed-polarity Chron M8r in Italian sections (Bralower, 1987). This datum constrains the uppermost polarity chron of the sandstone unit (upper part of lithologic Subunit IIIB) at M8 or older. Therefore, the cluster of reversed-polarity zones in the lower portion of the slowly deposited Barremian claystone has been tentatively assigned to the close-spaced set of reversed-polarity Chrons M5-M6-M7. The Hauterivian/Barremian boundary thus should be placed within this interval.

3. The basal black siltstones (susceptibility Unit 6, or lower part of lithologic Subunit IIIB) were deposited during the earliest Hauterivian and latest Valanginian, based upon a nannofossil *Chastozygus acme* assemblage noted in the North Sea from the Valanginian-Hauterivian interval (boreal ammonite definition) and upon a dinoflagellate assemblage, *S. tabulata* Zone, assigned to uppermost Valanginian in Australia (correlated to eastern Tethyan ammonite zones?; see "Biostratigraphy" sec-

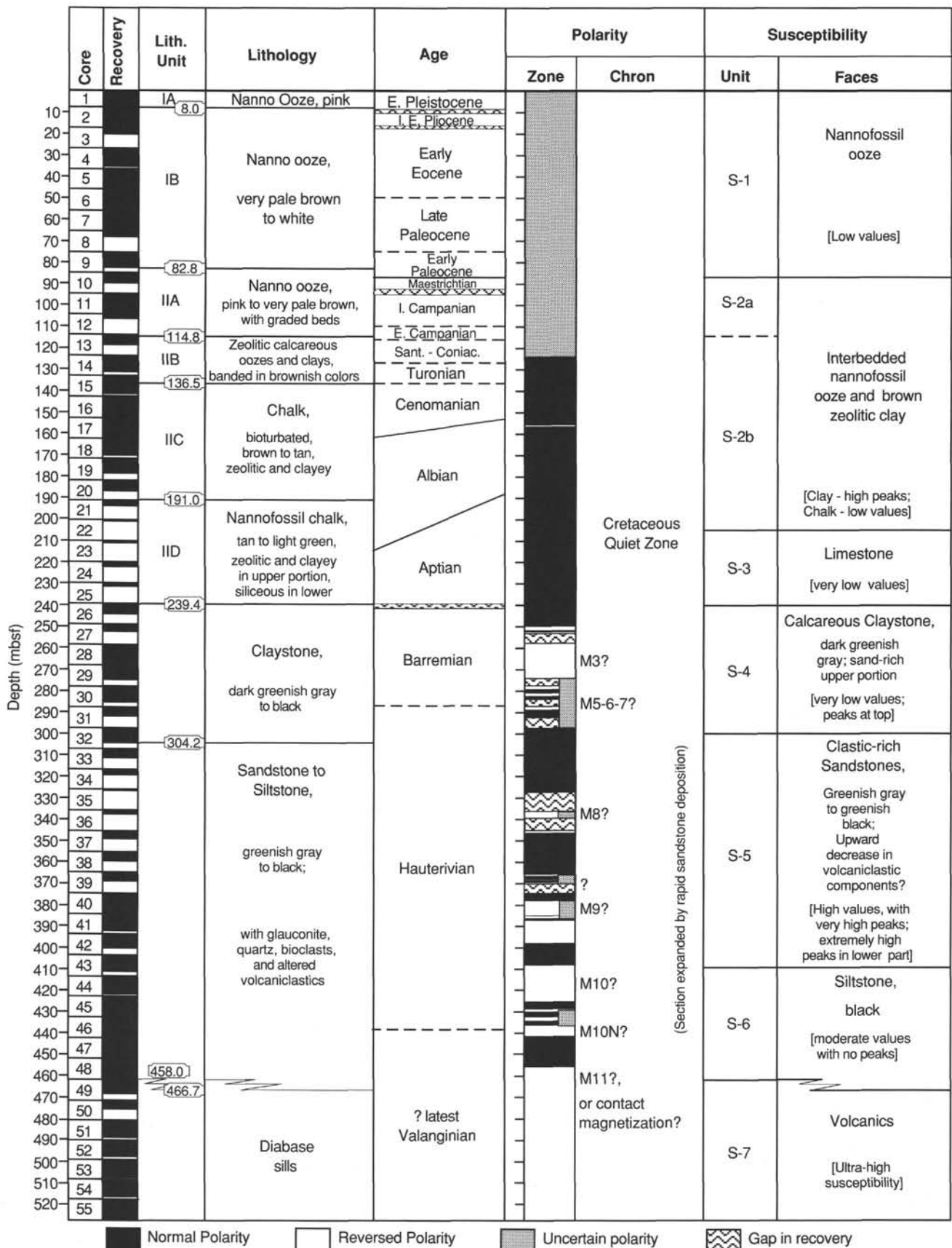


Figure 32. Magnetostratigraphy of Site 766 with correlations to lithostratigraphy, biostratigraphy, and susceptibility units and facies. Assignment of polarity chrons to polarity zones is based upon biostratigraphic constraints and adjustments for changes in sedimentation rates.

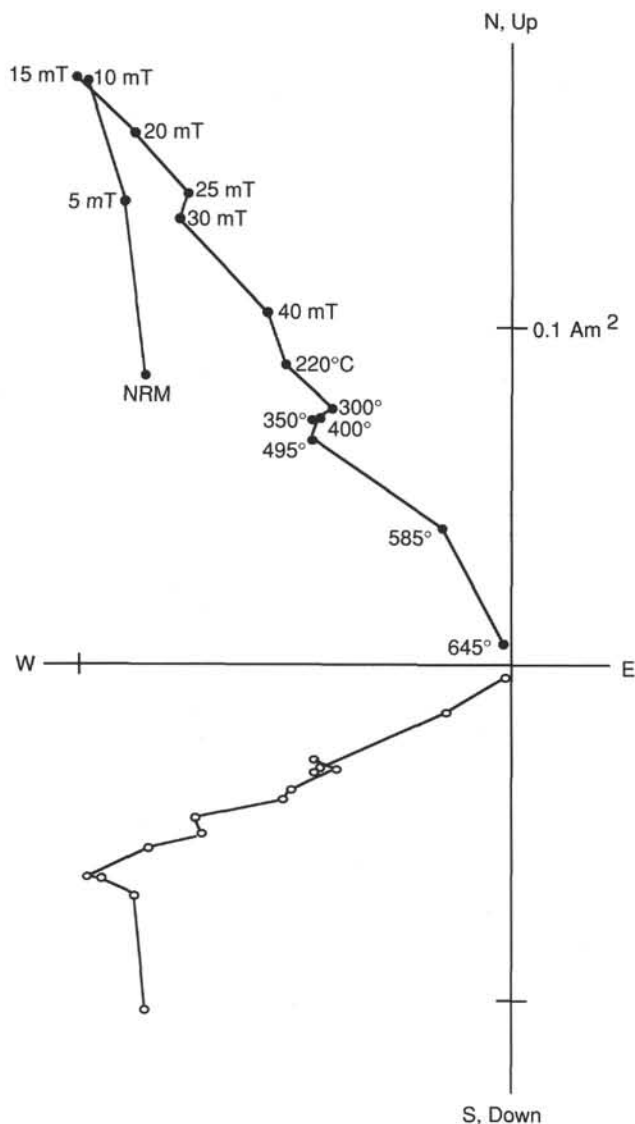


Figure 33. Orthogonal plot of magnetic vector of an Early Cretaceous dark greenish-gray sandstone (Sample 123-766A-40R-5, 140–142 cm) during alternating field (5 to 40 mT) and thermal (220° to 645°) demagnetizations. Solid circles are projections onto vertical plane; open circles are projection onto horizontal plane. A secondary overprint of normal polarity was removed upon applying alternating-field demagnetization at 10 mT.

tion, this chapter). The upper half of this siltstone unit displayed a polarity pattern nearly identical to polarity Chrons M10r to M10Nr, including the two brief reversed-polarity intervals during normal-polarity Chron M10Nn. Reversed-polarity Chron M10Nr is located at the Valanginian/Hauterivian boundary, as defined by the highest occurrence of dinoflagellate *Scriniodinium dictyotum* in the Central Atlantic (Habib and Drugg, 1983; Ogg, 1987) or, less precisely, by nannofossil datums (Bralower, 1987; Ogg and Steiner, 1988).

These bio-magnetostratigraphic age controls of Chron M7r above and Chron M10r below the rapidly deposited sandstones of susceptibility Unit S-5 imply that the two reversed-polarity zones within the sandstone unit probably correspond to reversed-polarity Chrons M8r and M9r of late Hauterivian age.

Overlying and within the volcanic sills at the base of the section are black siltstones displaying reversed polarity (lower Core

123-766A-48R and Core 123-766A-49R), similar to the polarity of the interbedded volcanics. There are two possible interpretations for this reversed-polarity zone:

1. The volcanic intrusions were quasi-contemporaneous with sedimentation during reversed-polarity Chron M11r of late Valanginian age. Perhaps the uppermost fine-grained "sill" was a flow. In this case, thermal resetting of magnetization of the overlying sediments during volcanism was not significant, and the magnetic reversal at the Chron M11r/M11n boundary was faithfully recorded.

2. Volcanic intrusions occurred significantly later than deposition of the sediments. In this case, the reversed polarity of the basal siltstones is purely an artifact of thermal resetting, although it is possible that the original pre-heating magnetization was also of reversed polarity and had been set during polarity Chron M11r, as would be predicted from the sedimentation rates.

Regardless of how the reversed polarity of the basal sediments was acquired, if the pattern of Chrons M10-M10N within the upper portion of these siltstones is continued into the lower portion of the unit using a constant sedimentation rate (the lithology remains uniform), then an age of polarity Chron M11r can be predicted for the base of the drilled sediment section.

SEDIMENT-ACCUMULATION RATES

Cenozoic

Sedimentation rates were estimated from an age-vs.-depth plot for Hole 766A (Fig. 34). The graph is defined by 15 nannofossil and foraminiferal events listed in Table 6. Absolute ages follow the Cenozoic time scale outlined in the "Explanatory Notes" (this volume).

The average sedimentation rate for the Pliocene-Pleistocene section is approximately 5 m/m.y., but this is based on only three samples. A major hiatus exists within Core 123-766A-3R and includes the interval from the upper lower Eocene to the lowermost Pliocene. The average sedimentation rate for the Paleocene-lower Eocene is also approximately 5 m/m.y.

Cretaceous

For establishing the sediment-accumulation rate (age vs. depth) curve for the Cretaceous of Hole 766A, 38 chronostratigraphic events (first and last occurrences of benthic foraminifers, calcareous nannofossils, dinoflagellates, radiolarians, and planktonic foraminifers) were used (Table 7). The resulting curve (Fig. 35) suggests continuous deposition from the late Valanginian to the Maestrichtian. Calcareous nannofossils were most helpful for compiling the Cretaceous age-depth curve, while dinoflagellates were used to a lesser extent in the Hauterivian and Valanginian. The numeric ages of the microfossil zones were taken from the Cretaceous time scale and zonal schemes given in the "Explanatory Notes" (this volume).

The calculated sediment-accumulation rates vary. A steady decrease from the uppermost Valanginian to the Maestrichtian was observed, with the highest rates in the Valanginian and Hauterivian (60 m/m.y.) and the lowest rates in the Campanian and Maestrichtian (1.7 m/m.y.). The age-depth curve can be subdivided into four segments from the Berriasian to the Maestrichtian. Cores 123-766A-49R to 123-766A-33R, which are composed of beds of lower Valanginian and Hauterivian age, have a sedimentation rate of 60 m/m.y. and are constrained by calcareous nannofossils, dinoflagellate zones, and, to a lesser extent, radiolarians. All three groups of markers provide comparable ages.

The second segment of the sedimentation-accumulation curve, which is composed of Barremian sediments (Cores 123-766A-

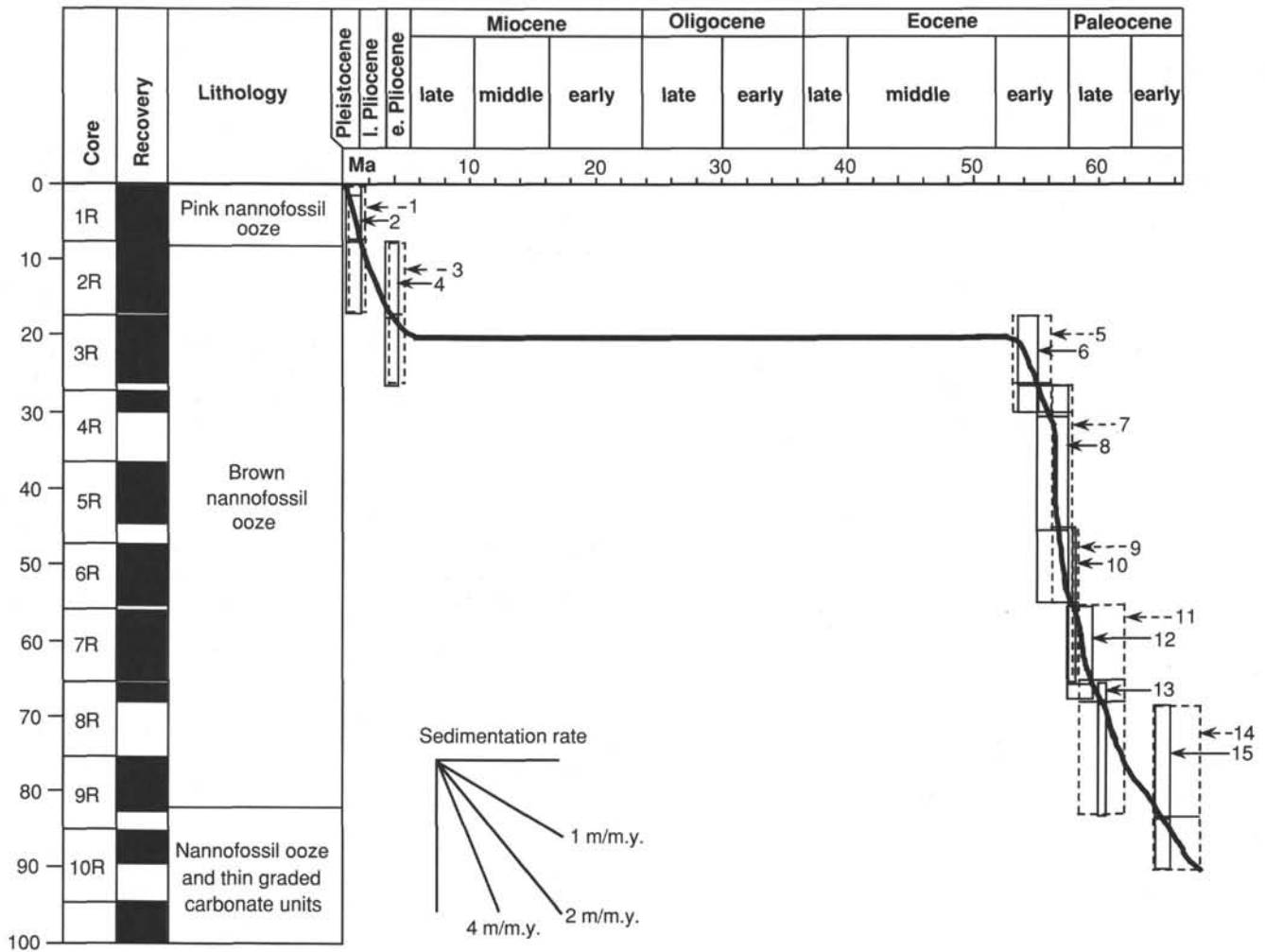


Figure 34. Age-depth curve for the Cenozoic of Hole 766A. Boxes define interval of potential stratigraphic occurrence of microfossil zones or concurrent ranges.

Table 6. Nannofossil and foraminiferal events used to define the Cenozoic age-depth curve for Hole 766A.

Number	Datum levels/zones	Downhole occurrence	Age (Ma)
1	Co-occurrence of <i>G. truncatulinoides</i> and <i>G. tosaensis</i>	123-766A-1R-CC	0.6-1.9
2	FO of <i>G. oceanica</i> to FO <i>E. huxleyi</i>	766A-1R-CC	0.28-1.68
3	Co-occurrence of <i>G. puncticulata</i> and <i>G. nepenthes</i>	766A-2R-CC	3.9-4.4
4	Co-occurrence of <i>A. delicatus</i> and <i>D. asymmetricus</i>	766A-2R-CC	3.7-4.1
5	Range of foraminiferal Zones P7 through P8	766A-3R-CC	53.2-56.1
6	Range of nannofossil Zone CP10	766A-3R-CC	53.7-55.3
7	Range of foraminiferal Zone P6b	766A-4R-CC and 766A-5R-CC	56.1-57.8
8	Range of nannofossil Zone CP9	766A-4R-CC and 766A-5R-CC	55.3-57.8
9	Range of foraminiferal Zone P6a	766A-6R-CC	57.8-58.2
10	Range of nannofossil Zone CP8b	766A-6R-CC	57.8-58.2
11	Range of foraminiferal Zones P4 through P5	766A-7R-CC and 766A-8R-CC	58.2-61.0
12	Range of nannofossil Zone CP8a	766A-7R-CC	58.2-59.2
13	Range of nannofossil Zone CP6	766A-8R-CC	60.0-64.0
14	Range of foraminiferal Zone P1b	766A-9R-CC	64.4-66.1
15	Range of nannofossil Zone CP1b	766A-9R-CC	65.0-66.0

32R to 123-766A-25R), is characterized by a decrease in sedimentation rate (10 m/m.y.). Biostratigraphic control is based on data from calcareous nannofossils, benthic foraminifers, and radiolarians. The third part of the section shows a further decrease of sedimentation rate from the Aptian to lower Campanian (Cores 123-766A-24R to 123-766A-13R), with a steady sedimentation rate of 3.2 m/m.y. This is mainly constrained by data from calcareous nannofossils. In the upper Campanian to Maestrichtian, the sedimentation rates decrease further, and this change occurs near the boundary between lithologic Subunits IIC and IIB. The average rate for this interval (Cores 123-766A-13R to 123-766A-10R) is approximately 1.7 m/m.y.

SEDIMENT INORGANIC GEOCHEMISTRY

Interstitial-Water Chemistry

Introduction

A total of 21 interstitial-water (IW) samples were taken at Site 766. No *in-situ* samples were taken. The sampling strategy of Site 765 was continued at Site 766. Two whole-round core samples, 3 cm long, were taken from the first core (1.5 and 3.0 mbsf), and an IW sample was taken every core in the uppermost 100 mbsf to define the concentration gradients near the sedi-

Table 7. Microfossil events used to define the Cretaceous age-depth.

Species	Group	Occ.	Age (Ma)	Core, section, interval (cm)
1-Nuttallinella florealis	BF	LO	66.5	10R-CC
2-Micula prinsii	CN	FO	68.5	10R-2, 100
3-Micula murus	CN	FO	70	10R-3, 50
4-Reinhardtites levis	CN	LO	71	10R-CC
4-Broinsonia parca constricta	CN	LO	71	10R-CC
5-Reinhardtites levis	CN	FO	76.5	12R-CC
6-Reussella szajnochae	BF	FO	81	12R-CC
7-Marthasterites furcatus	CN	LO	82	13R-2, 114
8-Broinsonia parca constricta	CN	FO	83	13R-1, 75
9-Lithastrinus septenarius	CN	LO	85.5	13R-3, 70
10-Micula decussata	CN	FO	87.5	14R-1, 14
11-Lithastrinus septenarius	CN	FO	89	14R-1, 40
12-Marthasterites furcatus	CN	FO	89	14R-3, 35
13-Quadrum gartneri	CN	FO	91	15R-1, 100
14-Corollithion kennedyi	CN	LO	91	15R-3, 100
15-Corollithion kennedyi	CN	FO	96	15R-CC
16-Gavelinella intermedia	CN	LO	97.5	21R-24-CC
17-Eiffelithus turreseiffelii	CN	FO	100	16R-CC
18-Rucinolithus irregularis	CN	LO	102	18R-CC
19-Prediscosphaera columinata s.l.	CN	FO	111	20R-CC
20-Pleurostomella spp.	BF	FO	114	21R-CC
21-Hayesites albiensis	CN	FO	114.5	22R-CC
22-Gavelinella barremiana	BF	LO	117	29R-CC
23-Lenticulina ouachensis	BF	LO	117	44R-CC
24-Flabellites biforaminis	CN	FO	118	24R-CC
25-Rhagodiscus angustus	CN	FO	119	25R-CC
25-Eprolithus apertior	CN	FO	119	25R-CC
26-Lenticulina crepidularis	BF	LO	119	31R-CC
27-Crucellipsis cuvillieri	CN	LO	129	33R-CC
28-Muderongia testudinaria	DF	LO	128	36R-1,
29-Dingodinium cerviculum	DF	FO	130	38R-CC
30-Tegumetium tripes	CN	LO	130	45R-CC
31-Phoberacysta burgeri	DF	FO	133	48R-5,
32-Sethocapsa euganea	RA	FO	119	24R-CC
32-Alievium helena	RA	LO	119	24R-CC
33-Pseudodictyomitra lilyae	RA	LO	120	25R-CC
34-Praeconocaryomma perisca	RA	OC	130-134	49R-3,
35-Globotruncanella havanensis	PF	FO	74	11R-CC
36-Globotruncana ventricosa	PF	FO	81	12R-CC
37-Dicarinella imbricata/hagni	PF	LO	86.5	14R-CC
38-Rotalipora cushmani	PF	Zone	91-93	14R-CC

Note: BF = benthic foraminifers, CN = calcareous nannofossils, DF = dinoflagellates, RA = radiolarians, PF = planktonic foraminifers. FO = first occurrence, LO = last occurrence.

ment/seawater interface in more detail. Below 100 mbsf, an IW sample was taken every third core when sufficient core was recovered. All of Site 766 was cored with the Rotary Core Barrel (RCB). No drilling fluid was pumped during coring of the first five cores. Surface seawater was pumped to Core 123-766A-22R and drilling mud was pumped from Core 123-766A-23R on down. Whole-round core samples, 5 cm long, yielded IW volumes greater than 20 cm³ to 105.8 mbsf. Below 105.8 mbsf, whole-round cores, 10 cm long, were taken and yielded IW volumes between 7 and 46 cm³. Established ODP sample squeezing and analytical methods were used (see "Explanatory Notes," this volume). The interstitial-water analytical results are summarized in Table 8. Included in Table 8 are the analyses of surface seawater and filtered (0.45 μm) drilling mud.

Salinity and Chloride

Most IW samples at Site 766 have salinity and chloride values within 1% of IAPSO seawater (Fig. 36). Three samples are 2% to 3% lower, and one sample is 2% higher than IAPSO salinity and chloride values. Salinity and chloride are more variable below 166.6 mbsf. Variations in salinity correspond to variations in chloride, which suggests that the IW had the addition or removal of H₂O. Although the chloride variations are much greater at Site 765, the same arguments apply when explaining the lower chloride concentrations observed at Site 766. Unlike

Site 765, sulfate and magnesium at Site 766 are far less depleted and, therefore, have only a minor effect on salinity values.

pH and Alkalinity

The pH is nearly constant in the upper 240.8 mbsf at a value of approximately 7.5, except for a single sample at 3 mbsf that may have been contaminated, since it has a low chloride concentration and appeared disturbed (soupy). Below 240.8 mbsf, the pH is more variable, but generally decreases to a value of 7.0 at 438.5 mbsf (Fig. 36). The alkalinity correlates roughly with pH; nearly constant at a value of 3 mM to 240.8 mbsf, and then decreases to 0.7 mM at 438.5 mbsf (Fig. 36). The organic-matter content of the sediment at Site 766 is low in the uppermost 260 mbsf (<0.1 wt%) and low to moderate below 260 mbsf (0.2 to 1.6 wt% organic carbon). In addition, the organic matter of the lower sediment is largely terrestrial, rather than marine in origin (see "Organic Geochemistry" section, this chapter). The high sulfate and low alkalinity, phosphate, and ammonium concentrations can be explained by the low organic-matter content of the sediment at Site 766.

Sulfate, Phosphate, and Ammonium

Sulfate decreases gradually and linearly with increasing sediment depth, from near seawater values at 1.5 mbsf to 18.7 mM at 438.5 mbsf (Fig. 36). Phosphate concentrations are low, ranging from 1.8 μM at 1.5 mbsf to <0.5 μM below 21.8 mbsf (Fig. 36). Below 105.8 mbsf, the phosphate starts to increase slightly, but phosphate was not determined below 166.6 mbsf because of smaller IW volumes. In a similar manner to phosphate, ammonium decreases rapidly in the uppermost sediment, from 315 μM at 1.5 mbsf to a more or less constant value of 40 μM from 21.8 to 88 mbsf. Below 88 mbsf, ammonium steadily increases to 325 μM at 438.5 mbsf (Fig. 36).

The decrease in sulfate is related to degradation of organic matter by sulfate-reducing bacteria. The low organic-matter content of these sediments limits the rate of sulfate reduction, and thus sulfate is only partially depleted. The low phosphate and ammonium values are consistent with low contents of organic matter, since they were introduced during organic matter degradation. The increase in ammonium below 88 mbsf may correlate with the higher organic-carbon content lower in the section.

Calcium, Magnesium, Manganese, and Strontium

Calcium increases from a value near that of seawater near the sediment/seawater interface to a maximum of 41 mM at the base of the section. Magnesium decreases from a value near that of seawater to a minimum of 33.5 mM at 379 mbsf (Fig. 36). The calcium and magnesium profiles are typical of marine sediments overlying basalt, and are interpreted as alteration reactions involving volcanic material in the sediment and/or alteration of the basement basalt (Gieskes, 1983). The magnesium/calcium ratio decreases linearly from 5.1 near the sediment/seawater interface to an approximately constant value of 1.0 below 240.8 mbsf (Fig. 37). In the uppermost 240.8 mbsf, magnesium and calcium concentrations change on a 1:1 molar ratio, but below 240.8 mbsf, calcium increases more rapidly than magnesium decreases (Fig. 36). Some magnesium may be introduced by clay mineral exchange with ammonium in the lower part of the section, where the ammonium concentration is high. Manganese decreases rapidly from a high of 13.5 μM at 1.5 mbsf to nearly zero at 88 mbsf. Below 88 mbsf, manganese increases to a second maximum of 9.3 μM at 279.4 mbsf, and then decreases to 3.4 μM at 379 mbsf (Fig. 36). The uppermost maximum is probably related to reduction of manganese oxides. The manganese maximum at 279.4 mbsf corresponds to the marked increase in the organic-carbon content of the sediment (see "Organic Geochemistry" section, this chapter). Strontium increases

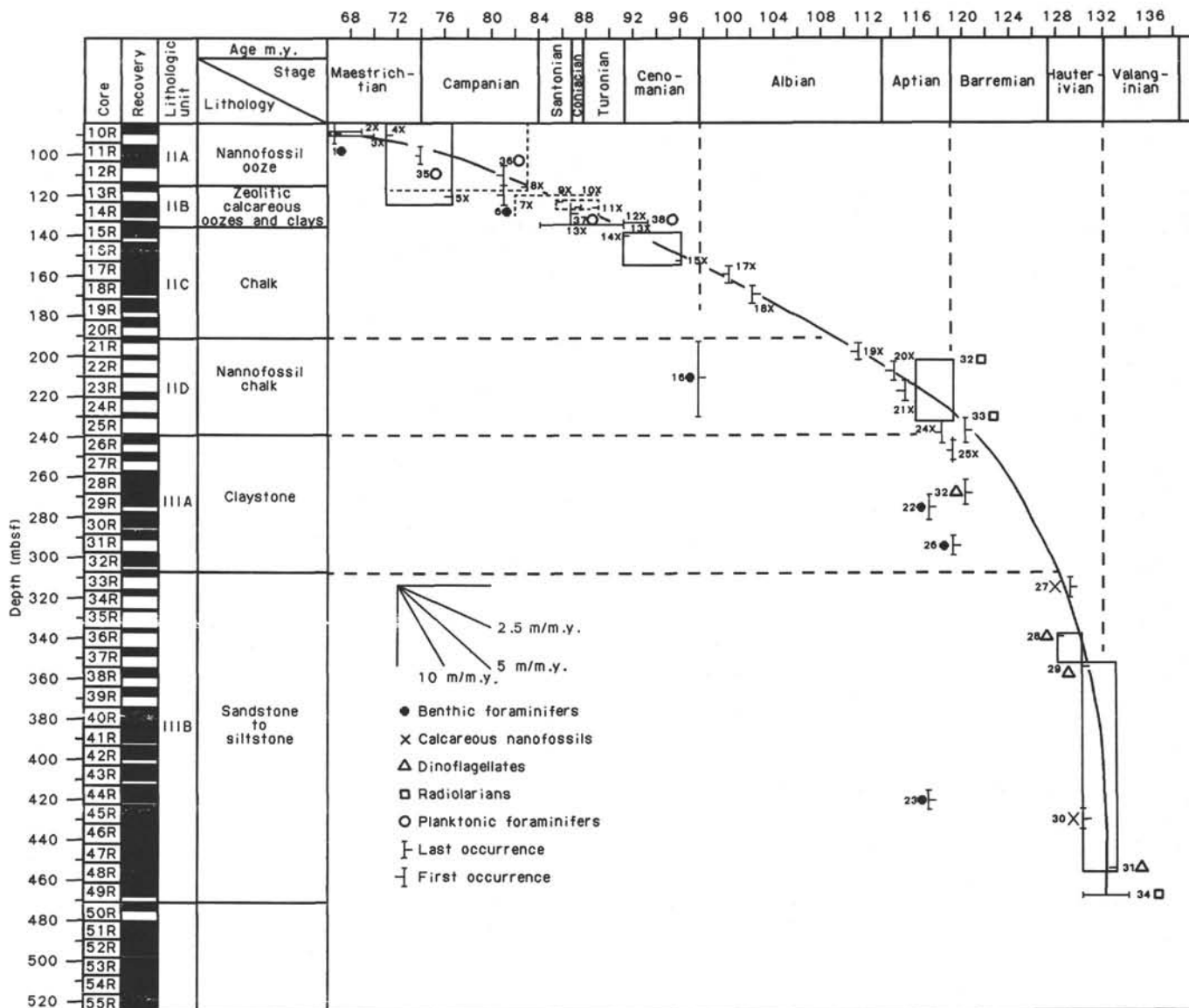


Figure 35. Age-depth curve for the Cretaceous of Hole 766A. Boxes define potential range of nannofossil, planktonic or benthic foraminifers, dinoflagellate, or radiolarian datum levels.

gradually from near-seawater values to 0.35 μM at 438.5 mbsf (Fig. 36). The increase is probably from alteration of volcanic sediment and basement basalt.

Silica and Potassium

Silica decreases rapidly from 747 μM at 1.5 mbsf to about 200 μM at 67.2 to 105.8 mbsf. From 105.8 to 279.4 mbsf, silica concentrations are high, with a second maximum of 800 μM at 166.6 mbsf. In this high silica zone, from 166.6 to 240.8 mbsf, the lithology is much more siliceous, and core recovery was poor. Below 279.4 mbsf, silica decreases to concentrations ranging from 114 to 184 μM (Fig. 36). Silica correlates well with radiolarian abundance and preservation (see "Biostratigraphy" section, this chapter). Potassium decreases from values at 1.5 mbsf to 2.7 μM at 438.5 mbsf (Fig. 36). Depletion of potassium is from alteration reactions in the sediment (e.g., conversion of smectite) and in the basement basalt. The rate of potassium depletion is typical of other ODP and DSDP sites (to 2 μM) (Gieskes, 1983).

Conclusions

Changes in the interstitial-water chemistry at Site 766 are less pronounced than at Site 765, mostly because the lower organic-carbon content at Site 766 results in a slower rate of sulfate reduction, and associated lower production of bicarbonate (alkalinity), phosphate, and ammonium. There is a gradual increase in calcium and decrease in magnesium, with sediment depth in an approximate 1:1 molar ratio, which results from the alteration of volcanic material in the sediment and basement basalt (Gieskes, 1983). High silica concentrations correlate with sediment zones having abundant and well-preserved radiolarians. Manganese exhibits an interesting second maximum at depth in the sediment that correlates with a large increase in the organic-carbon content of the sediment.

ORGANIC GEOCHEMISTRY

A total of 137 samples were analyzed for inorganic carbon, and 19 samples were analyzed for total carbon at Site 766.

Table 8. Interstitial-water data, Site 766.

Core, section, interval (cm)	Depth (mbsf)	IW		Alkalinity (mM)	Salinity (‰)	Mg (mM)	Ca (mM)	Mg/Ca	Cl (mM)	SO ₄ (mM)	PO ₄ (μM)	NH ₄ (μM)	Silica (μM)	Mn (μM)	Sr (mM)	K (mM)
		volume (cm ³)	pH													
123-766A-1R-1, 147-150	1.5	25	7.46	3.358	35.2	53.3	10.5	5.08	557	27.6	1.8	315	747	13.5	0.10	10.8
123-766A-1R-2, 147-150	3.0	27	6.33	1.997	35.2	52.0	10.6	4.91	549	26.8	1.1	146	744	9.6	0.10	13.1
123-766A-2R-3, 145-150	12.2	60	7.49	2.951	35.4	52.2	11.1	4.70	557	27.8	0.8	64	628	7.6	0.10	10.8
123-766A-3R-3, 145-150	21.8	30	7.58	3.315	35.2	53.4	11.7	4.56	557	27.3	0.5	26	495	1.8	0.11	10.9
123-766A-4R-1, 145-150	28.5	40	7.53	3.019	35.5	51.1	12.0	4.26	560	27.6	0.3	33	366	0.8	0.11	10.5
123-766A-5R-3, 145-150	41.2	29	7.54	2.982	35.2	51.5	12.5	4.12	558	27.2	0.4	59	355	2.0	0.12	11.3
123-766A-6R-3, 145-150	50.8	40	7.56	2.871	35.3	51.2	12.6	4.06	562	27.1	0.4	51	282	0.8	0.12	10.6
123-766A-7R-3, 145-150	60.5	38	7.48	2.850	35.2	49.5	13.1	3.78	559	26.3	0.3	53	264	0.8	0.12	10.3
123-766A-8R-1, 145-150	67.2	33	7.46	2.912	35.5	50.8	13.9	3.65	560	28.0	0.5	38	212	0.4	0.13	10.0
123-766A-9R-3, 145-150	79.8	36	7.45	2.947	35.3	50.1	14.2	3.53	559	26.0	0.3	44	194	1.9	0.13	9.8
123-766A-10R-2, 145-150	88.0	29	7.44	2.877	35.2	49.1	14.7	3.34	558	25.4	0.3	36	219	0.1	0.13	9.7
123-766A-12R-1, 145-150	105.8	28	7.43	2.948	35.2	48.3	15.4	3.14	559	25.3	0.3	56	198	0.6	0.16	10.2
123-766A-15R-3, 140-150	137.7	46	7.41	2.840	35.2	47.1	18.3	2.57	561	25.6	0.5	74	726	2.8	0.17	9.8
123-766A-18R-3, 140-150	166.6	36	7.47	2.538	35.2	45.7	20.3	2.25	561	25.0	0.7	74	800	2.0	0.19	9.3
123-766A-26R-1, 140-150	240.8	14	7.63	2.614	34.8	37.9	30.2	1.25	548	21.8		116	709		0.27	6.1
123-766A-30R-1, 140-150	279.4	15	7.12	1.586	35.2	38.9	32.5	1.20	555	21.5		137	607	9.3	0.29	4.3
123-766A-33R-1, 140-150	308.3	45	7.80	0.896	35.2	35.2	34.4	1.02	562	20.8		154	184	5.0	0.31	5.3
123-766A-37R-1, 140-150	347.0	22	7.25	0.753	35.0	35.1	36.7	0.96	558	20.7		192	128	5.5	0.33	4.0
123-766A-40R-3, 140-150	379.0	27	7.31	0.954	36.0	33.5	37.9	0.88	571	19.8		210	114	3.4	0.33	3.7
123-766A-43R-3, 140-150	408.0	13	6.91	0.722	35.3	35.6	41.0	0.87	561	20.0		310	128		0.35	3.1
123-766A-46R-4, 140-150	438.5	7	7.04	0.734	34.0	37.5	40.8	0.92	541	18.7		325	147		0.35	2.7
Surface seawater			8.21	2.257	35.2	52.8	10.1	5.23	548	27.6		0	0		0.09	10.5
Drilling mud			8.42	1.992	15.0	13.9	4.0	3.48	237	13.4		24	219		0.06	7.2

Eighty-four samples were analyzed by Rock-Eval pyrolysis to determine the organic-carbon contents and to help characterize the nature and source of organic matter. Light hydrocarbons (C₁-C₃) were monitored on the Carle GC for safety considerations, and C₁-C₆ hydrocarbons were measured in 45 sediment samples, using the Natural Gas Analyzer (NGA), to examine processes controlling the production and migration of hydrocarbons in sediments. Methods used for these analyses are described in the "Explanatory Notes" (this volume).

Coulometric Analyses of Total and Inorganic Carbon

Data obtained from Coulometric analyses of sediments are summarized in Table 9. Inorganic carbon (IC) was measured, and calcium carbonate calculated (wt% CaCO₃ = wt% IC × 8.33) for all sediments collected for natural gas analyses, interstitial-water measurements, Rock-Eval pyrolysis, and selected "bomb" samples for sedimentology. Total carbon was measured only on some samples from the top 200 m of sediments, where Rock-Eval pyrolysis indicated that the content of organic carbon was extremely low and generally undetectable. The downhole distribution of calcium carbonate is plotted in Figure 38. Contents of calcium carbonate in the top 80 m of Tertiary nanofossil ooze sediments are high, varying between 60 and 100 wt%. Calcium carbonate is more variable (0 to >90 wt%) in Upper Cretaceous sediments, and this may reflect a higher frequency of turbidite deposition than in the overlying strata. These sediments are mixtures of nanofossil chalk with zeolitic clays (see "Sedimentology" section, this chapter). Carbonate content is higher in Aptian cherty-limestone sediments, although fewer samples were obtained from this interval, which had a poor recovery. Below about 230 mbsf, carbonate contents of sediments are consistently less than 20 wt%, and except for two sample intervals in the Barremian-Hauterivian, sediments are less than 10 wt% throughout the Lower Cretaceous. Carbonate content is less than 5 wt% in uppermost Valanginian-Hauterivian sediments above sills at the bottom of this hole. The low calcium carbonate content in these sandstone-siltstone sediments reflects the predominance of terrigenous sedimentation. The transition stratigraphically upward from these low-carbonate Lower Cretaceous sediments to the high-carbonate Aptian limestones having abundant radiolarians reflects the rapid increase in importance of pelagic sedimentation. This transition is related to the tectonic evolution of the outer Exmouth Plateau, as this site

subsided and moved away from the source(s) of the terrigenous sediments.

Rock-Eval Pyrolysis

Total organic carbon (TOC) contents and some indications as to the nature of the organic matter in these sediments were determined by Rock-Eval pyrolysis (Espitalié et al., 1977). These data are summarized in Table 10, and the downhole distribution of TOC is shown in Figure 39. Organic carbon contents are mostly undetectable in carbonate-rich sediments to about 230 mbsf, and these are of Late Cretaceous through Tertiary ages. Organic carbon contents approached 1 wt% TOC in the dark green calcareous claystones of Barremian age at depths between about 280 and 320 mbsf. TOC contents were lower in the Barremian-Hauterivian sandstones, but increased with increasing depth in the hole, reaching a maximum concentration near 1.5 wt% at depths of about 430 mbsf near the Hauterivian-Valanginian boundary. Rock-Eval data below about 280 mbsf are plotted on a van Krevelen-type diagram (Fig. 40). Most of these data have hydrogen indexes of less than 100 and oxygen indexes of less than 350, and plot near the type III organic matter line, indicating that these samples are composed primarily of terrestrial organic carbon. Rock-Eval pyrolysis does not indicate any distinction between the organic matter in the dark green Barremian calcareous claystones and the younger, more organic-rich Valanginian-Hauterivian sediments below about 430 mbsf. Furthermore, inspection of the T_{max} data (Table 10) indicates that most samples are immature and exhibit no evidence of any thermal effects. Only one interval (Sample 123-766A-49R-2, 0-2 cm) has a T_{max} value that indicates heating of organic matter to overmaturity. This sample was collected about 60 cm from an apparent intrusion of basalt, which is the probable heat source that generated gas in these sediments (see below). However, other samples collected from Core 123-766A-49R and analyzed by pyrolysis did not indicate any heating of the organic matter.

Gases in Sediments

The concentrations of gases measured in sediments (expressed as parts per million [ppm] by volume of headspace) are summarized in Table 11. Hydrocarbon concentrations measured by the Carle gas chromatograph (GC) were typical of "background" in sediments to depths of about 250 mbsf. Below about 250 mbsf,

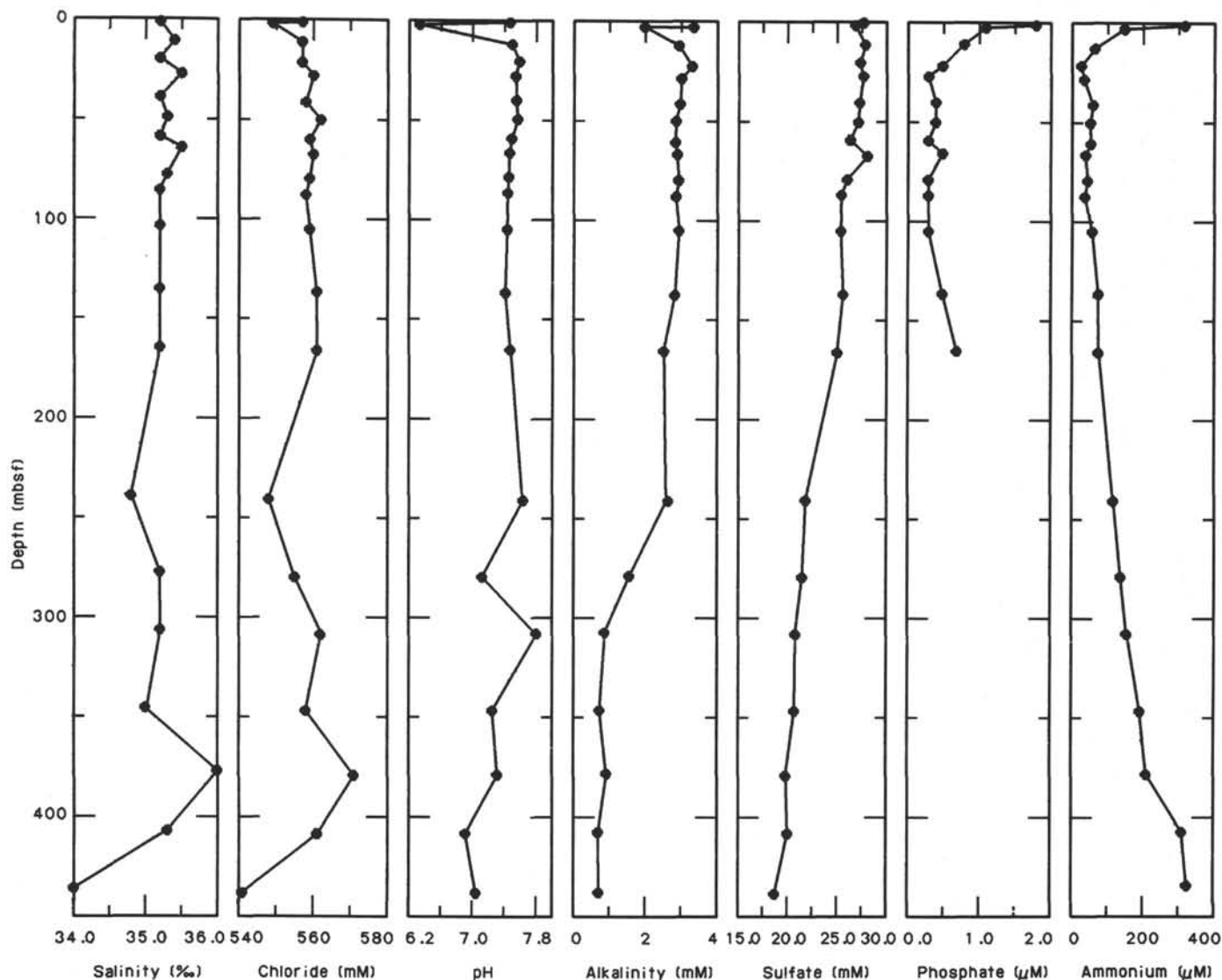


Figure 36. Interstitial-water composition as a function of sub-bottom depth at Site 766 (salinity, chloride ion, pH, alkalinity, sulfate, phosphate, ammonium, calcium (open circles) and magnesium (open circles), Mg/Ca ratio, manganese, strontium, silica, and potassium).

where organic carbon contents increase in the dark green Barre-mian calcareous claystones, the total hydrocarbon abundance increases and higher C_{2+} molecular weight compounds are present, including unsaturated (ethylene, propylene, and butane) and ring (methylcyclopentane and cyclohexane) compounds. Furthermore, hydrogen sulfide, produced during anaerobic oxidation of organic matter, was found in five samples below 250 mbsf. The frequent appearance of unsaturated compounds and hydrogen sulfide suggests that the gases in these sediments were produced by biogenic processes (Claypool and Kvenvolden, 1983; Whelan and Hunt, 1983). The Rock-Eval pyrolysis data support this interpretation and indicate the predominance of immature organic matter. The persistence of these low molecular-weight compounds, of an apparent biogenic origin, in these Lower Cretaceous sediments is unexpected. This result may be related to the sediments below about 300 mbsf being deposited in a closed basin, bounded both shoreward and seaward by vol-

canics. The sediments within this basin are capped by impermeable Aptian cherty limestone that acts to limit diffusion to the overlying sediments and, hence, trap hydrocarbons generated in the sediments. This interpretation is consistent with the persistence of dissolved manganese that is produced in anoxic sediments by reductive dissolution of sedimentary manganese oxyhydroxides (see "Sediment Inorganic Geochemistry" section, this chapter). Only one sediment sample (123-766A-49R-2, 0-2 cm) had high C_1 and C_2 concentrations (approximately 600 and 800 ppm headspace, respectively), and C_1/C_2 and $C_2/C_{2.1}$ ratios that suggest a thermogenic origin for saturated hydrocarbons. This same sample had a T_{max} that indicates the presence of over-mature organic matter and proximity to a local heat source. One explanation for this apparent thermal generation of gas in an isolated sample may be the proximity of a basalt intrusion into these sediments approximately 60 cm above where the gas sample was taken.

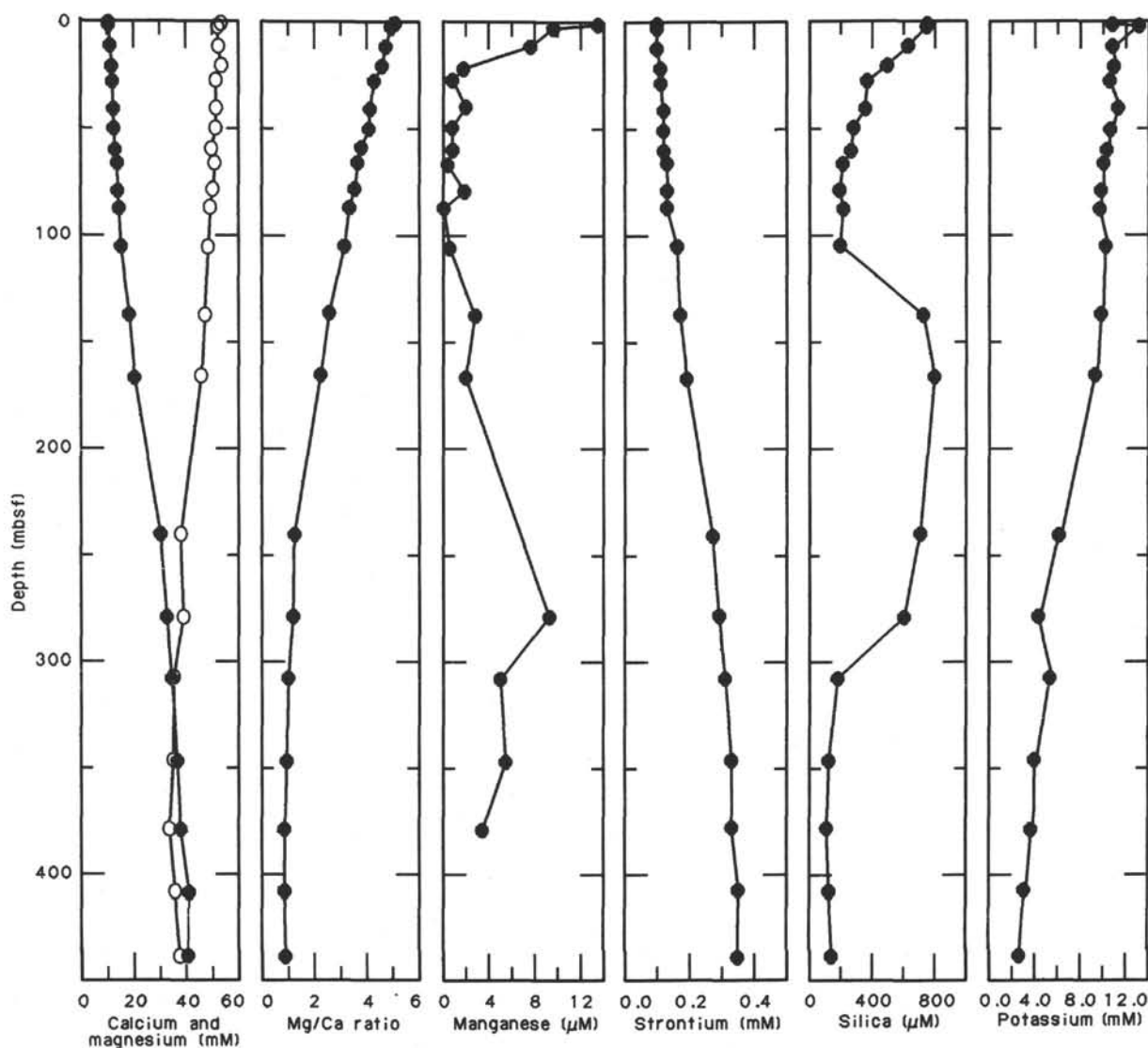


Figure 36 (continued).

SEDIMENT PHYSICAL PROPERTIES

Introduction

The physical properties determined from sediments of Site 766 include compressional-wave velocity (as measured using a Hamilton Frame), index properties (i.e., bulk density, grain density, porosity, and water content, as determined by a pycnometer and balance), GRAPE bulk density, thermal conductivity, and vane shear strength. Velocities and index properties were measured on most of the cores. GRAPE bulk-density measurements were performed to a depth of 160 mbsf. Thermal conductivity measurements were conducted on competent material. Vane-shear measurements were not obtained below 150 mbsf because of the brittle nature of the material. In Tables 12 to 14, values of the various physical-property measurements are listed, and variations of these properties with depth are illustrated in Figures 41 through 45.

Results

Index Properties

Bulk density, grain (or matrix) density, porosity, and water content (dry basis) of the samples from Hole 766A are listed in

Table 12 and plotted relative to depth in Figures 41 and 42. Five basic units can be identified in terms of physical properties, namely, Unit A (0–100 mbsf), Unit B (100–185 mbsf), Unit C (185–240 mbsf), Unit D (240–300 mbsf), and Unit E (300–459 mbsf).

Unit A (0–100 mbsf) consists of calcareous ooze with significant changes in the index properties in the upper 22 mbsf, followed by more gradual changes, which are consistent with normal compaction trends. The grain density remains relatively constant, with an average value of $2.66 \pm 0.10 \text{ g/cm}^3$. A distinct decrease in water content and porosity was observed. The former has values ranging from 92% at the mud line to near 37% at 100 mbsf. The latter ranges from 75% to 51% for the same interval. An increasing trend was observed for the bulk densities, with values going from approximately 1.6 to near 2.0 g/cm^3 over the 100-m interval.

Unit B (100–185 mbsf) consists of mixed sediments of claystone and chalk. Physical-property data show greater variability, but remain relatively constant with depth. Average grain density increases to $2.78 \pm 0.14 \text{ g/cm}^3$ for the unit. Average water content and porosity are $45.6\% \pm 6.6\%$ and $57.8\% \pm 3.6\%$, respectively. Bulk densities increase slightly from about 1.9 to 2.0 g/cm^3 . A noticeable change in bulk density occurs at 141

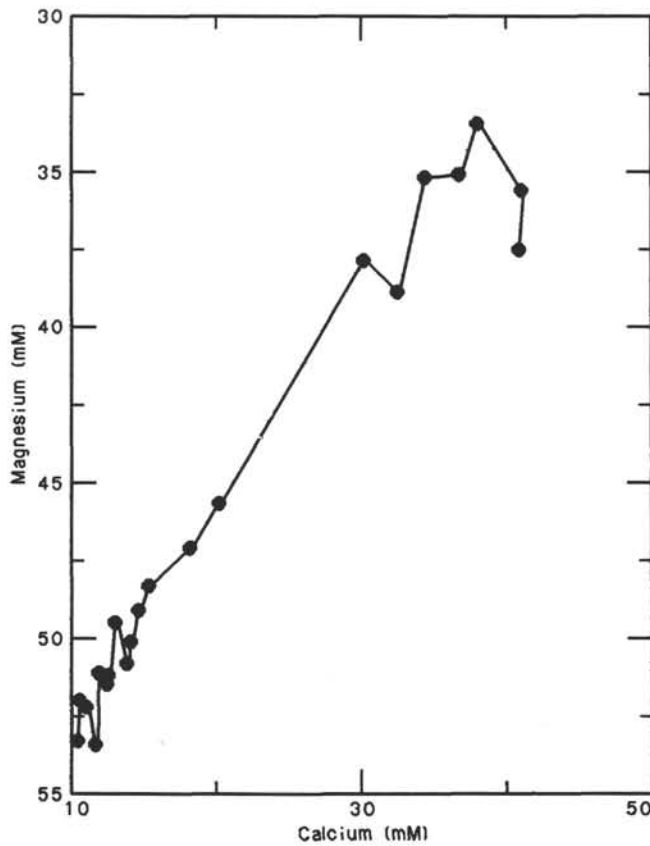


Figure 37. Mg/Ca ratio, Site 766.

mbsf, where the value decreases to 1.74 g/cm³. In addition, both porosity and water content increase slightly at this depth.

Unit C (185–240 mbsf) consists predominantly of chalk with hard chert layers. Index properties appear to remain constant throughout the unit, but show a high degree of variability because of the chalk and chert layers. Grain densities for the unit decrease and have an average value of 2.47 ± 0.19 g/cm³. Bulk densities average 2.12 ± 0.09 g/cm³ for the unit. In addition, porosities and moisture contents show considerable variation across the unit, depending upon the type of material encountered. Porosities range from about 30% in the chert to 50% in the chalk. Likewise, moisture contents range from approximately 20% to 32% for the chert and chalk, respectively.

Unit D (240–300 mbsf) consist predominantly of a dark brown to reddish brown claystone. This claystone tends to slake or delaminate when exposed to water or when air dried. In general, grain densities increase with depth, going from about 2.5 g/cm³ in the carbonate-rich Unit C to near 2.7 g/cm³ at the lower boundary. Bulk densities for the unit decrease to about 1.8 g/cm³, compared with 2.1 g/cm³ for the upper unit. In addition, both water content and porosity appear to be slightly higher than the surrounding units.

Unit E (300–459 mbsf) is composed primarily of green to gray glauconitic siltstones and sandstones, with periodic layers of highly lithified bioclastic sandstone. Index properties basically remain constant with depth; however, these properties are highly variable as a result of the layered nature of the material. Average grain density is 2.71 ± 0.08 g/cm³. Bulk densities range from an overall value of about 1.95 g/cm³ for the unit to values as high as 2.76 g/cm³ for the lithified sandstone. Average water content and porosity for the unit are 36% ± 11% and 51% ± 10%, respectively. Again, these two quantities show a high degree of variability due to the occurrence of very low values observed in the lithified material. The lowermost 20 m of

Table 9. Organic carbon and carbonate carbon data for Site 766.

Core, section, interval (cm)	Depth (mbsf)	Total carbon (%)	Inorganic carbon (%)	Organic carbon (%)	CaCO ₃ (%)
123-766A-					
1R-1, 147-50	1.47	9.50	9.65	0.00	80.4
1R-2, 30-33	1.80	9.71	9.68	0.03	80.6
1R-2, 147-150	2.97	8.73	8.58	0.15	71.5
1R-3, 0-7	3.00		8.12		67.6
1R-3, 39-42	3.39	8.94	8.88	0.06	74.0
2R-1, 12-13	7.82		8.88		74.0
2R-2, 59-62	9.85	8.53	8.51	0.02	70.9
2R-3, 140-145	12.16		7.51		62.6
2R-3, 145-150	12.21		7.79		64.9
2R-6, 76-78	16.02		7.80		65.0
2R-7, 23-25	16.99	7.89	7.91	0.00	65.9
3R-1, 10-12	17.40	10.78	10.86	0.00	90.5
3R-3, 145-150	21.75	11.06	11.28	0.00	94.0
3R-4, 35-38	22.15	10.97	11.07	0.00	92.2
3R-4, 143-150	23.23		8.40		70.0
4R-1, 129-133	28.29	11.13	11.26	0.00	93.8
4R-1, 145-150	28.45		11.50		95.8
4R-2, 0-7	28.50		11.21		93.4
5R-2, 87-89	39.07		9.25		77.1
5R-3, 145-150	41.15		11.24		93.6
5R-4, 143-150	42.63		10.78		89.8
5R-5, 70-73	43.40	10.86	10.96	0.00	91.3
6R-3, 145-150	50.75	11.10	11.14	0.00	92.8
6R-4, 143-150	52.23		10.55		87.9
7R-3, 145-150	60.45		11.44		95.3
7R-4, 143-150	61.93		11.11		92.6
8R-1, 138-145	67.08		11.13		92.7
8R-1, 145-150	67.15		11.39		94.9
9R-3, 145-150	79.75	11.12	11.30	0.00	94.1
9R-4, 143-150	81.23		10.37		86.4
10R-1, 143-150	86.43		6.17		51.4
10R-2, 145-150	87.95		10.47		87.2
11R-1, 78-80	95.48		6.36		53.0
11R-4, 143-150	100.63		10.53		87.7
11R-6, 91-93	103.11		10.05		83.7
12R-1, 66-68	104.96		10.27		85.6
12R-1, 138-145	105.68		10.10		84.1
12R-1, 145-150	105.75	11.76	10.90	0.86	90.8
13R-1, 84-85	114.74		8.29		69.1
13R-2, 38-39	115.78		10.04		83.6
13R-2, 51-52	115.91		3.22		26.8
13R-3, 0-7	116.90		7.04		58.6
14R-2, 0-7	125.10		8.84		73.6
14R-3, 83-84	127.43		0.11		0.9
14R-3, 85-86	127.45		8.08		67.3
14R-3, 92-93	127.52		0.83		6.9
14R-3, 93-94	127.53		7.99		66.6
14R-4, 7-8	128.17		0.70		5.8
14R-4, 79-80	128.89		0.91		7.6
15R-3, 0-7	136.20		0.03		0.3
15R-3, 140-150	137.60	7.42	7.28	0.14	60.6
16R-1, 74-75	143.64		0.28		2.3
16R-2, 62-63	145.02		5.40		45.0
16R-5, 0-7	148.90		2.78		23.2
17R-3, 143-150	156.93		5.83		48.6
17R-6, 105-106	161.05		5.11		42.6
18R-1, 127-128	163.37		3.75		31.2
18R-3, 102-103	166.12		5.61		46.7
18R-3, 140-50	166.50	6.37	6.39	0.00	53.2
18R-5, 0-7	168.10		5.75		47.9
19R-1, 145-146	173.15		2.79		23.2
19R-2, 52-54	173.72		1.18		9.8
19R-3, 11-13	174.81		5.45		45.4
19R-3, 55-56	175.25		5.76		48.0
19R-4, 0-7	176.20		5.77		48.1
20R-3, 0-7	184.40		8.23		68.6
21R-2, 0-7	192.50		7.04		58.6
24R-1, 53-55	220.43	8.30	8.39	0.00	69.9
24R-1, 143-150	221.33		5.17		43.1
26R-1, 59-61	239.89		0.05		0.4
26R-1, 140-150	240.70	0.12	0.14	0.00	1.2
26R-2, 143-150	242.23		0.06		0.5
27R-1, 143-150	250.33		0.96		8.0
27R-2, 30-32	250.70		1.28		10.7

Table 9 (continued).

Core, section, interval (cm)	Depth (mbsf)	Total carbon (%)	Inorganic carbon (%)	Organic carbon (%)	CaCO ₃ (%)
123-766A- (Cont.)					
27R-CC, 3-5	252.13		0.77		6.4
28R-2, 25-28	260.35		1.09		9.1
28R-3, 85-88	262.45		1.19		9.9
28R-3, 132-135	262.92		1.00		8.3
28R-5, 0-7	264.60		1.48		12.3
28R-6, 109-112	267.19		1.25		10.4
29R-2, 44-46	270.24		1.01		8.4
29R-4, 0-2	272.80		1.45		12.1
29R-4, 100-102	273.80		0.42		3.5
30R-1, 140-150	279.30	1.12	0.49	0.63	4.1
30R-3, 143-150	282.33		0.56		4.7
30R-4, 41-44	282.81		0.66		5.5
31R-1, 67-70	288.17		0.50		4.2
31R-2, 143-150	290.43		0.81		6.8
32R-4, 138-141	303.08		0.40		3.3
32R-4, 143-150	303.13		0.34		2.8
33R-1, 140-150	308.20		0.12		1.0
33R-2, 147-149	309.77		0.53		4.4
33R-3, 54-58	310.33		0.39		3.3
34R-1, 75-76	317.25		0.93		7.8
34R-1, 148-150	317.98		0.40		3.3
35R-1, 47-49	326.57		5.62		46.8
36R-1, 138-139	337.18		0.45		3.8
36R-1, 148-150	337.28		0.58		4.8
37R-1, 69-70	346.19		0.55		4.6
37R-1, 132-142	346.82		0.32		2.7
37R-2, 0-2	346.92		0.26		2.2
38R-2, 0-2	356.60		4.49		37.4
39R-1, 148-150	366.28		0.97		8.1
39R-2, 0-2	366.30		0.80		6.7
39R-2, 122-124	367.52		0.62		5.2
39R-3, 32-34	368.12		0.75		6.3
40R-3, 55-57	378.05		0.45		3.8
40R-3, 140-150	378.90		1.81		15.1
40R-4, 146-148	380.46		0.99		8.3
40R-4, 148-150	380.48		0.96		8.0
41R-3, 148-150	388.68		0.77		6.4
41R-4, 92-93	389.62		0.33		2.8
42R-1, 94-97	394.74		0.30		2.5
42R-3, 148-150	398.28		0.70		5.8
43R-3, 140-150	407.90		0.38		3.2
43R-4, 114-119	409.14		0.46		3.8
43R-4, 148-150	409.48		0.66		5.5
44R-4, 0-2	417.70		0.61		5.1
44R-6, 15-17	420.85		0.52		4.3
45R-4, 0-2	427.30		0.80		6.7
45R-4, 106-108	428.36		0.61		5.1
46R-2, 0-2	434.04		0.61		5.1
46R-3, 32-34	435.86		0.55		4.6
46R-4, 140-150	438.44		0.52		4.3
46R-5, 141-143	439.95		0.78		6.5
46R-6, 58-59	440.62		0.55		4.6
47R-3, 103-105	446.23		0.65		5.4
47R-3, 148-150	446.68		0.59		4.9
47R-4, 102-104	447.72		0.45		3.8
48R-1, 131-133	453.11		0.43		3.6
48R-4, 16-18	456.46		0.39		3.3
48R-5, 0-2	457.80		0.41		3.4
49R-1, 97-98	462.47		0.12		1.0
49R-2, 0-2	463.00		0.27		2.3
49R-2, 142-143	464.42		0.29		2.4
49R-3, 108-109	465.58		0.17		1.4
49R-4, 34-35	466.34		0.21		1.8

this section consists of a gray to black clayey sandstone. Index properties for this layer did not vary significantly from those described above for the unit as a whole.

Velocity

Compressional-wave velocity data, as determined with the Hamilton Frame apparatus, are shown in Figure 43. From this figure, one observes an underlying trend of progressively increasing velocities from a value of approximately 1525 m/s in

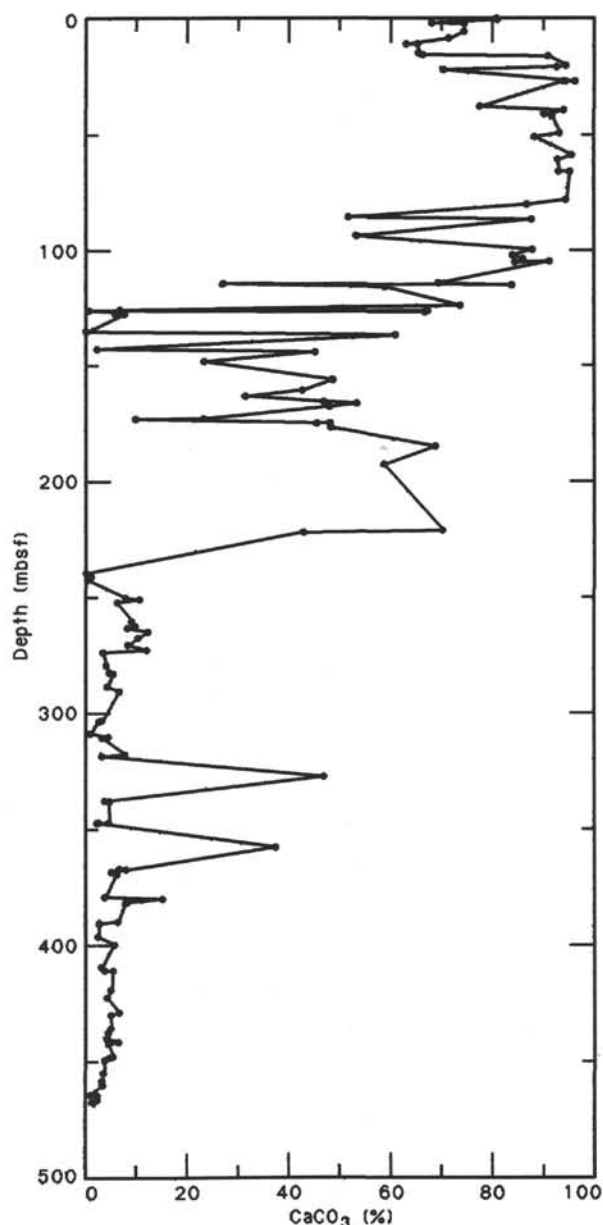


Figure 38. Calcium carbonate vs. depth, Site 766.

the calcareous ooze, near the sea-bottom sediment boundary, increasing to about 1900 m/s near the sediment basement boundary. Superimposed on this trend is a series of high velocity excursions. These values are associated with layers of chert and lithified bioclastic sandstone. Some variability in the data is caused, in part, by the sampling procedure used. Samples were taken as representative as possible of the sediment section as a whole; however, sample selection depended upon the relative frequency, thickness, and homogeneity of a particular sequence. Thin, unrepresentative lithologies were avoided.

A low-velocity peak was observed at a depth of 141 mbsf; as discussed in the above section, a significant variation in the index properties also occurs at this depth. The stratigraphic unit consists of a mixed sediment of claystone and chalk. The sample tested came from a less-lithified chalk section. From about 160 to 260 mbsf, a slight increase in velocity was observed. This interval corresponds to Unit C, as described in the above section, and is composed of a chalk with layers of chert. The two velocity spikes at 201 and 222 mbsf correspond to chert. At 300 mbsf and in the interval from 350 to 440 mbsf, another series of

Table 10. Rock-Eval analyses of sediment, Site 766.

Core, section, interval (cm)	Depth (mbsf)	S ₁ (mg/g)	S ₂ (mg/g)	S ₃ (mg/g)	TOC (%)	C (%)	HI	OI	T _{max} (°C)	PI	S ₂ /S ₃
123-766A-											
1R-1, 147-150	1.47	0.07	0.00	2.25	0.00	0.00	0	0	300	1.00	0.00
1R-2, 147-150	2.97	0.05	0.00	2.39	0.00	0.00	0	0	227	1.00	0.00
1R-3, 0-7	3.00	0.07	0.00	3.77	0.00	0.00	0	0	354	1.00	0.00
2R-3, 140-145	12.16	0.06	0.00	2.92	0.00	0.00	0	0	267	1.00	0.00
2R-3, 145-150	12.21	0.02	0.00	1.76	0.00	0.00	0	0	265	1.00	0.00
3R-3, 145-150	21.75	0.03	0.00	0.62	0.00	0.00	0	0	224	1.00	0.00
4R-1, 145-150	28.45	0.01	0.00	0.55	0.00	0.00	0	0	254	0.00	0.00
4R-2, 0-7	28.50	0.02	0.00	1.27	0.00	0.00	0	0	222	1.00	0.00
5R-3 145-150	41.15	1.14	0.40	2.48	0.12	0.12	333	2066	342	0.74	0.16
5R-4, 143-150	42.63	0.01	0.00	1.22	0.00	0.00	0	0	304		0.00
6R-3, 145-150	50.75	0.03	0.00	0.80	0.00	0.00	0	0	353	1.00	0.00
6R-4, 143-150	52.23	0.05	0.04	1.75	0.00	0.00	0	0	222	0.62	0.02
7R-3, 145-150	60.45	0.01	0.00	0.43	0.00	0.00	0	0	245	0.00	0.00
7R-4, 143-150	61.93	0.00	0.00	0.84	0.00	0.00	0	0	306		0.00
10R-1, 143-150	86.43	0.01	0.01	2.46	0.00	0.00	0	0	269	0.50	0.00
13R-2, 38-39	115.78	0.01	0.00	1.48	0.00	0.00	0	0	305	0.00	0.00
13R-3, 0-7	116.90	0.01	0.00	2.42	0.00	0.00	0	0	222		0.00
14R-4, 7-8	128.17	0.03	0.15	1.67	0.01	0.01	1500	16700	409	0.17	0.08
14R-4, 79-80	128.89	0.01	0.00	0.93	0.00	0.00	0	0	217	0.00	0.00
16R-5, 0-7	148.90	0.01	0.00	1.99	0.00	0.00	0	0	306		
17R-6, 105-106	161.05	0.02	0.00	1.90	0.00	0.00	0	0	204	1.00	0.00
19R-1, 145-146	173.15	0.02	0.00	2.39	0.00	0.00	0	0	223	1.00	0.00
19R-3, 55-56	175.25	0.01	0.00	2.34	0.00	0.00	0	0	206	0.00	0.00
19R-4, 0-7	176.20	0.15	0.12	1.92	0.02	0.02	600	9600	295	0.58	0.06
21R-2, 0-7	192.50	0.01	0.00	1.48	0.00	0.00	0	0	222		0.00
24R-1, 143-150	221.33	0.12	0.02	2.24	0.01	0.01	200	22400	306	0.86	0.00
27R-1, 143-150	250.33	0.45	0.16	1.61	0.04	0.05	400	4025	305	0.75	0.09
28R-2, 25-28	260.35	0.07	0.14	1.78	0.14	0.01	100	1271	270	0.35	0.07
28R-3, 132-135	262.92	0.05	0.18	1.68	0.20	0.01	90	840	268	0.23	0.10
28R-6, 109-112	267.19	0.05	0.17	1.62	0.21	0.01	80	771	331	0.23	0.10
29R-2, 44-46	270.24	0.06	0.24	1.65	0.39	0.02	61	423	306	0.20	0.14
29R-4, 100-102	273.80	0.00	0.09	1.19	0.10	0.00	90	1190	388	0.00	0.07
30R-1, 140-150	279.30	0.06	0.56	1.49	0.56	0.05	100	266	436	0.10	0.37
30R-4, 41-44	282.81	0.00	0.16	1.60	0.58	0.01	27	275	386	0.00	0.10
31R-1, 67-70	288.17	0.00	0.36	1.27	0.55	0.03	65	230	418	0.00	0.28
31R-2, 143-150	290.43	0.43	0.90	2.08	0.79	0.11	113	263	399	0.33	0.43
32R-4, 138-141	303.08	0.01	0.28	1.00	0.71	0.02	39	140	414	0.04	0.28
32R-4, 143-150	303.13	0.09	0.67	0.70	0.75	0.06	89	93	411	0.12	0.95
33R-1, 140-150	306.20	0.00	0.07	0.50	0.19	0.00	36	263	329	0.00	0.14
33R-2, 147-149	309.77	0.09	0.32	0.93	0.28	0.03	114	350	359	0.22	0.32
33R-3, 54-58	310.33	0.02	0.03	1.33	0.12	0.00	25	1100	306	0.05	0.02
34R-1, 75-76	317.25	0.02	0.08	1.89	0.13	0.00	61	1453	328	0.20	0.04
34R-1, 148-150	317.98	0.04	0.37	0.66	0.21	0.03	176	314	306	0.10	0.56
36R-1, 138-139	337.18	0.04	0.26	1.34	0.23	0.02	113	582	331	0.13	0.19
36R-1, 148-150	337.28	0.05	0.35	1.05	0.38	0.03	92	276	364	0.12	0.33
37R-1, 69-70	346.19	0.13	0.37	1.79	0.57	0.04	64	314	400	0.26	0.20
37R-1, 132-142	346.82	0.04	0.37	0.69	0.48	0.03	77	143	342	0.10	0.53
37R-2, 0-2	346.92	0.12	0.60	0.89	0.39	0.06	153	228	460	0.17	0.67
38R-2, 0-2	356.60	0.04	0.16	0.57	0.01	0.01	1600	5700	283	0.20	0.28
39R-1, 148-150	366.28	0.15	0.38	1.29	0.31	0.04	122	416	306	0.29	0.29
39R-2, 0-2	366.30	0.03	0.29	1.30	0.26	0.02	111	500	306	0.09	0.22
39R-2, 122-124	367.52	0.05	0.29	1.53	0.46	0.02	63	332	306	0.15	0.18
39R-3, 32-34	368.12	0.03	0.10	1.11	0.07	0.01	142	1585	417	0.25	0.09
40R-3, 55-57	378.05	0.04	0.32	1.01	0.32	0.03	100	315	306	0.11	0.31
40R-3, 140-150	378.90	0.00	0.01	0.58	0.00	0.00	0	0	264	0.00	0.01
40R-4, 146-148	380.46	0.04	0.23	0.57	0.02	0.02	1150	2850	329	0.15	0.40
40R-4, 148-150	380.48	0.02	0.13	0.59	0.01	0.01	1300	5900	265	0.14	0.22
41R-3, 148-150	388.68	0.03	0.14	0.74	0.27	0.01	51	274	276	0.19	0.18
41R-4, 92-93	389.62	0.04	0.58	0.96	0.38	0.05	152	252	327	0.06	0.60
42R-1, 94-97	394.74	0.04	0.42	0.71	0.03	0.03	1400	2366	404	0.09	0.59
42R-3, 148-150	398.28	0.00	0.07	1.14	0.30	0.00	23	380	283	0.00	0.06
43R-3, 140-150	407.90	0.01	0.12	0.88	0.35	0.01	34	251	305	0.08	0.13
43R-4, 114-119	409.14	0.03	0.24	1.39	0.41	0.02	58	339	350	0.12	0.17
43R-4, 148-150	409.48	0.04	0.26	0.84	0.39	0.02	66	215	360	0.13	0.30
44R-4, 0-2	417.70	0.17	0.62	0.85	0.79	0.06	78	107	412	0.22	0.72
44R-6, 15-17	420.85	0.01	0.41	1.23	0.62	0.03	66	198	416	0.02	0.33
45R-4, 0-2	427.30	0.00	0.28	0.80	0.57	0.02	49	140	419	0.00	0.35
45R-4, 106-108	428.36	0.08	1.59	1.57	1.60	0.13	99	98	423	0.05	1.01
46R-2, 0-2	434.04	0.00	0.50	0.90	0.81	0.04	61	111	419	0.00	0.55
46R-3, 32-34	435.86	0.04	0.48	1.42	0.79	0.04	60	179	422	0.08	0.33
46R-4, 140-150	438.44	0.04	0.41	0.86	0.65	0.03	63	132	402	0.09	0.47
46R-5, 141-143	429.95	0.06	1.20	1.84	1.53	0.10	78	120	422	0.05	0.65
46R-6, 58-59	440.62	0.04	0.39	1.55	0.69	0.03	56	224	415	0.10	0.25
47R-3, 103-105	446.23	0.04	0.41	1.75	0.66	0.03	62	265	416	0.09	0.23
47R-3, 148-150	446.68	0.01	0.29	1.17	0.51	0.02	56	229	409	0.03	0.24

Table 10 (continued).

Core, section, interval (cm)	Depth (mbsf)	S ₁ (mg/g)	S ₂ (mg/g)	S ₃ (mg/g)	TOC (%)	C (%)	HI	OI	T _{max} (°C)	PI	S ₂ /S ₃
123-766A- (continued)											
47R-4, 102-104	447.72	0.04	0.36	1.42	0.64	0.03	56	221	412	0.10	0.25
48R-1, 131-133	453.11	0.08	0.44	1.01	0.63	0.04	69	160	401	0.15	0.43
48R-4, 16-18	456.46	0.05	0.33	0.99	0.50	0.03	66	198	330	0.13	0.33
48R-5, 0-2	457.80	0.02	0.33	0.68	0.57	0.02	57	119	418	0.06	0.48
49R-1, 97-98	462.47	0.01	0.51	1.01	0.67	0.04	76	150	426	0.02	0.50
49R-2, 0-2	463.00	0.04	0.71	0.72	0.75	0.06	94	96	596	0.05	0.98
49R-2, 142-143	464.42	0.11	0.51	1.01	0.82	0.05	62	123	414	0.18	0.50
49R-3, 108-109	465.58	0.03	0.34	1.03	0.40	0.03	85	257	382	0.08	0.33
49R-4, 34-35	466.34	0.01	0.28	1.29	0.57	0.02	49	226	413	0.04	0.21

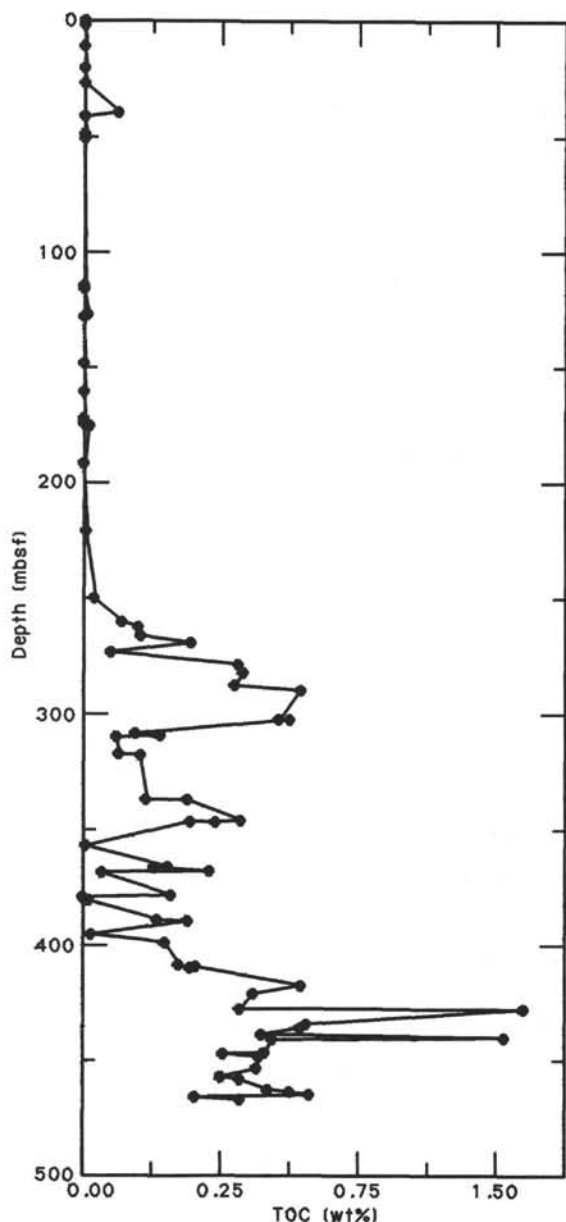


Figure 39. Total organic carbon vs. depth, Site 766.

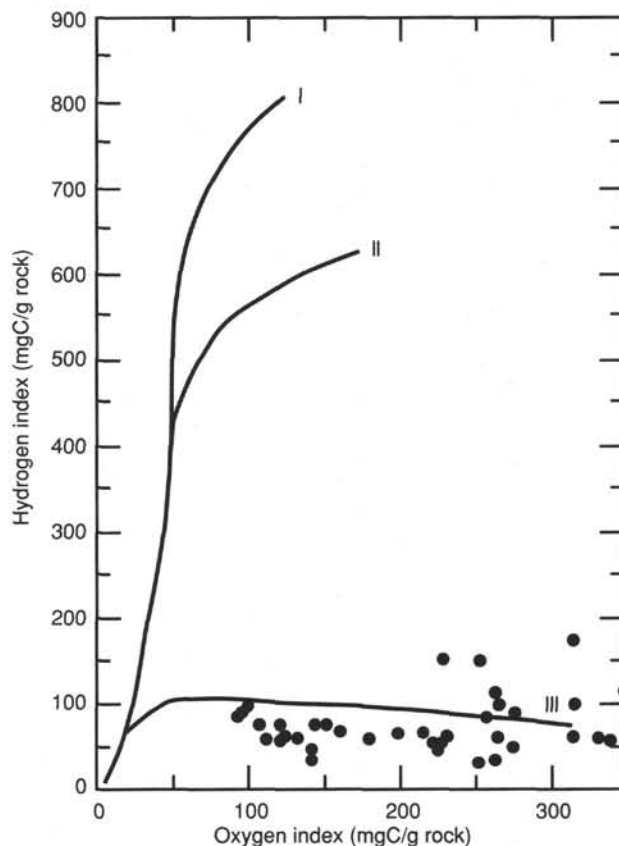


Figure 40. Van Krevelen plot, Site 766.

velocity peaks was observed. These peaks correspond to the highly lithified bioclastic sandstone layers.

As means of comparing physical properties with seismic data, an acoustic impedance plot (Fig. 43) was created by multiplying the sediment bulk density by the corresponding velocity and plotting the result as a function of depth. From this figure, one can readily observe the occurrence of a weak seismic reflector associated with the chalk strata at 141 mbsf and the numerous high amplitude reflectors related to the chert and lithified sandstone layers.

GRAPE

GRAPE bulk densities, along with the corresponding values determined from index properties, are shown in Figure 44. Grape bulk densities were obtained from RCB cores, and data are available to a depth of 160 mbsf. Below this depth, the sample

Table 11. Gases in sediments, Site 766.

Core, section interval (cm)	Depth (mbsf)	C ₁ (ppm)	C ₂ (ppm)	C ₃ (ppm)	CD	Other gases (ppm)
123-766A-						
1R-3, 0-7	3.00	ND	ND	ND	NG	<i>i</i> -butane = 4.7
1R-3, 0-5	3.00	3.0	ND	ND	HS	
2R-3, 0-7	10.76	ND	ND	ND	NG	
3R-4, 143-150	23.23	11.0	ND	ND	NG	
4R-2, 0-7	28.50	8.5	ND	ND	NG	<i>i</i> -butane = 2.7
4R-2, 0-5	28.50	2.4	ND	ND	HS	
5R-4, 143-150	42.63	ND	ND	ND	NG	
6R-4, 143-150	52.23	1950.0	3.3	ND	NG	
7R-4, 143-150	61.93	5.5	ND	ND	NG	<i>i</i> -butane = 3.7, <i>n</i> -pentane = 2.0
7R-4, 145-150	61.95	3.7	ND	ND	HS	
8R-1, 138-145	67.08	2.2	ND	2.5	NG	
8R-1, 140-145	67.10	2.7	ND	ND	HS	
9R-4, 143-150	81.23	ND	ND	2.1	NG	
9R-4, 145-150	81.25	3.2	ND	ND	HS	
10R-1, 143-150	86.43	7.1	ND	ND	NG	propylene = 4.9
10R-1, 145-150	86.45	2.4	ND	ND	HS	
11R-4, 145-150	100.65	3.3	ND	ND	HS	
12R-1, 140-145	105.70	2.1	ND	ND	HS	
12R-1, 140-145	105.70	3.3	ND	ND	NG	propylene = 2.8
13R-3, 0-7	116.90	4.4	ND	ND	NG	<i>n</i> -butane = 3.4, hydrogen sulfide = 20.2
14R-2, 0-7	125.10	5.5	2.0	3.4	NG	<i>i</i> -butane = 1.8
14R-2, 0-5	125.10	3.6	ND	ND	HS	
15R-3, 0-7	136.20	6.6	ND	ND	NG	ethylene = 12.2
15R-3, 0-5	136.20	2.9	ND	ND	HS	
16R-5, 0-7	148.90	8.8	ND	0.9	NG	
16R-5, 0-5	148.90	4.6	ND	ND	HS	
17R-3, 143-150	156.93	3.3	ND	2.1	NG	<i>i</i> -butane = 1.3, propylene = 1.8
17R-3, 145-150	156.95	2.7	ND	ND	HS	
18R-5, 0-7	168.10	9.8	2.9	2.5	NG	
18R-5, 0-5	168.10	3.7	ND	ND	HS	
19R-4, 0-7	176.20	8.3	2.3	ND	NG	
19R-4, 0-5	176.20	3.4	ND	ND	HS	
20R-3, 0-7	184.40	4.4	2.8	ND	NG	
20R-3, 0-5	184.40	4.1	ND	ND	HS	
21R-2, 0-7	192.50	11.1	ND	1.9	NG	<i>n</i> -butane = 0.8, <i>i</i> -butane = 2.9
21R-2, 0-5	192.50	4.1	ND	ND	HS	
24R-1, 143-150	221.33	ND	ND	ND	NG	propylene = 4.5
24R-1, 145-150	221.35	3.3	ND	ND	HS	
26R-2, 143-150	242.23	ND	ND	ND	NG	
26R-2, 145-150	242.25	7.0	ND	ND	HS	
27R-1, 143-150	250.33	6.6	ND	8.1	NG	
27R-1, 145-150	250.35	6.4	ND	ND	HS	
28R-5, 0-7	264.60	ND	ND	15.3	NG	<i>i</i> -butane = 3.7
28R-5, 0-7	264.60	8.8	ND	ND	HS	
29R-4, 0-2	272.80	6.5	ND	1.8	NG	ethylene = 5.2, <i>i</i> -butene = 1.6
29R-4, 0-2	272.80	8.1	ND	ND	HS	
30R-3, 143-150	282.33	13.4	ND	ND	NG	
30R-3, 145-150	282.35	12.9	ND	ND	HS	
31R-2, 145-150	290.45	28.8	ND	ND	NG	<i>n</i> -butane = 2.3, propylene = 5.1
31R-2, 145-150	290.45	5.9	ND	ND	HS	
32R-4, 143-150	303.13	15.7	2.6	ND	NG	<i>i</i> -butane = 2.0, <i>i</i> -butene = 1.2
32R-4, 145-150	303.15	9.4	ND	ND	HS	
33R-2, 148-150	309.78	10.7	ND	ND	NG	<i>n</i> -pentane = 2.6, <i>n</i> -hexane = 18.1, <i>i</i> -hexene = 27.6
33R-2, 147-149	309.77	6.5	ND	ND	HS	
34R-1, 148-150	317.98	17.0	ND	3.1	NG	<i>i</i> -butane = 1.7, <i>i</i> -butene = 3.0, methylcyclopentane = 1.7
34R-1, 148-150	317.98	13.1	ND	ND	HS	
35R-1, 47-49	326.57	13.9	ND	3.1	NG	<i>i</i> -butene = 4.8, ethylene = 1.1, cyclohexane = 7.4
35R-1, 47-49	326.57	7.8	ND	ND	HS	
36R-1, 148-150	337.28	18.0	2.6	4.5	NG	<i>n</i> -butane = 4.4, <i>i</i> -butane = 3.8, <i>i</i> -butene = 6.4, ethylene = 4.1, propylene = 3.7, hydrogen sulfide = 10.1
36R-1, 148-150	337.28	10.4	ND	ND	HS	
37R-2, 0-2	346.92	12.4	2.1	ND	NG	<i>i</i> -butene = 3.4, <i>i</i> -hexene = 45.4, cyclohexane = 8.8
37R-2, 0-2	346.92	8.8	ND	ND	HS	
38R-2, 0-2	356.60	4.4	1.2	ND	NG	propylene = 3.2, <i>i</i> -butene = 3.4, <i>n</i> -butane = 1.9, <i>i</i> -butane = 1.8, hydrogen sulfide = 10.0, <i>i</i> -hexene = 7.6, cyclohexane = 3.7
38R-2, 0-2	356.60	5.0	ND	ND	HS	
39R-3, 0-2	367.80	9.9	ND	3.7	NG	ethylene = 8.6, propylene = 1.8, <i>i</i> -butane = 2.0, cyclohexane = 2.8
39R-3, 0-2	367.80	12.0	ND	ND	HS	
40R-4, 148-150	380.48	19.3	4.9	3.1	NG	<i>i</i> -butane = 3.6, ethylene = 13.8, propylene = 2.1, <i>i</i> -butene = 5.1, methylcyclopentane = 1.2, hydrogen sulfide = 250.2
40R-4, 148-150	380.48	10.1	ND	ND	HS	
41R-3, 148-150	388.68	101.6	1.5	ND	NG	ethylene = 15.8, hydrogen sulfide = 18.2
41R-3, 148-150	388.68	7.5	ND	0.6	HS	
42R-3, 148-150	398.28	ND	1.6	ND	NG	<i>i</i> -butane = 2.7, <i>i</i> -butene = 3.9, hydrogen sulfide = 14.1
42R-3, 148-150	398.28	10.4	ND	ND	HS	

Table 11 (continued).

Core, section interval (cm)	Depth (mbsf)	C ₁ (ppm)	C ₂ (ppm)	C ₃ (ppm)	CD	Other gases (ppm)
123-766A- (Cont.)						
43R-4, 148-150	409.48	56.3	2.5	ND	NG	<i>i</i> -butane = 1.7, <i>l</i> -butene = 3.7, ethylene = 19.6
43R-4, 148-150	409.48	15.6	ND	ND	HS	
44R-4, 0-2	417.70	29.8	ND	5.1	NG	<i>n</i> -butane = 1.4, <i>l</i> -butene = 2.9, ethylene = 15.8, hydrogen sulfide = 72.6
44R-4, 0-2	417.70	ND	ND	HS		
45R-4, 0-2	427.30	63.8	4.4	4.6	NG	<i>i</i> -butane = 5.3, <i>l</i> -butene = 5.8, propylene = 2.9, ethylene = 19.6
45R-4, 0-2	427.30	13.2	ND	ND	HS	
46R-2, 0-2	434.00	8.8	ND	ND	NG	<i>i</i> -butene = 3.4, ethylene = 5.5, propylene = 21.0
46R-2, 0-2	434.00	14.4	ND	ND	HS	
47R-3, 148-150	446.68	40.5	1.8	ND	NG	<i>n</i> -butane = 8.4, ethylene = 7.6
47R-3, 148-150	446.68	14.9	ND	ND	HS	
48R-5, 0-2	457.80	ND	6.7	5.5	NG	ethylene = 11.5, propylene = 41.2
48R-5, 0-2	457.80	17.3	ND	ND	HS	
49R-2, 0-2	463.00	620.0	860.0	2.2	NG	ethylene = 490.0
49R-2, 0-2	463.00	22.4	19.4	ND	HS	

CD = carbon determination; NG = natural-gas analysis; HS = headspace-gas analysis; ND = no data.

tended to be significantly smaller than the inside diameter of the liner tube, which resulted in erroneous results. One can observe from Figure 44 that both the index properties and GRAPE bulk densities exhibit a great deal of variability with depth. However, the two methods are in close agreement to a depth of about 100 mbsf. Below this depth, the index bulk density is higher than the GRAPE bulk density. The primary reason for the discrepancy is the error associated with the differing diameters, as discussed above.

Vane Shear Strength

Values of undrained shear strength were obtained using a four-bladed vane shear apparatus on samples taken from RCB cores. This method of coring can result in a considerable amount of sample disturbance; thus, the measured shear strengths may vary significantly from those *in situ*. The resulting shear strengths are given in Table 13 and plotted as a function of depth in Figure 44.

Undrained shear strength remains fairly constant at a very low value of approximately 10 kPa for the first 66 mbsf. From 66 to 76 mbsf, this strength increases to a value of 45 kPa, after which it remains constant at an average value of 35 kPa to 100 mbsf. A significant increase in shear strength occurs between 100 and 129 mbsf, where a maximum value of 219 kPa was attained. This interval consists of a series of very stiff clay layers. Below these layers, carbonates were again encountered, and shear strengths decrease significantly. At depths greater than 150 mbsf, samples tended to crack during vane insertion and testing was terminated.

Thermal Conductivity

Thermal conductivities given in Table 14 are shown in Figure 45. The data exhibit a significant amount of variability, however, three distinct zones can be identified. The first zone extends from 0 to 240 mbsf and includes the physical properties Units A, B, and C. Thermal conductivity for this region averages 1.40 ± 0.17 W/mK. The second section includes Unit D, which is from 240 to 300 mbsf. The average thermal conductivity for this interval is 1.15 ± 0.13 W/mK. In the lowermost section, Unit E from 300 to 459 mbsf, thermal conductivities return to the same value as was observed in the uppermost portion of the sediment column, namely, 1.40 ± 0.11 W/mK.

Conclusions

Sediment index properties, compressional-wave velocities, vane shear strengths, and thermal conductivities allow one to characterize the sediments at Site 766 into five physical properties

units. Unit A extends from the seafloor to 100 mbsf and consists predominantly of calcareous ooze. Physical properties change significantly within the upper 22 mbsf, followed by a more gradual change that is consistent with normal compaction trends. Vane shear strengths remain low because of the nature of the sediment encountered and method of drilling. Unit B includes the interval from 100 to 185 mbsf and is composed of mixed sediments of claystone and chalk. Index properties remain relatively constant with depth, with the exception of vane shear data. Significantly higher vane shear strengths can be found in the clay layers, as opposed to the weaker chalk sequences. Unit C extends from 185 to 240 mbsf and consists predominantly of a chalk with hard chert layers. Physical-properties data show a significant variation because of these chert layers, but for the most part are invariant with depth. A significant decrease in grain density was observed. Velocity spikes associated with chert layers were observed at 201 and 222 mbsf. Unit D includes the interval from 240 to 300 mbsf and consists mainly of a dark brown to reddish brown claystone. For the unit as a whole, there is a slight decrease in bulk density, with a corresponding increase in both water content and porosity. Unit E extends from 300 to 459 mbsf and is composed primarily of green to gray glauconitic siltstone and sandstone, with periodic layers of highly lithified bioclastic sandstone. Physical properties exhibit a great deal of variation with depth as a result of the layered nature of the material. Velocity spikes associated with the occurrence of highly lithified bioclastic sandstone layers were observed at 300 mbsf and throughout the interval from 350 to 440 mbsf. The lowermost 20 m of the unit consists of a gray to black clayey sandstone. Thermal conductivities remain relatively constant throughout the sediment column, with the exception of a noticeable decrease that occurs between 240 to 300 mbsf, i.e., in Unit D.

IGNEOUS ROCK LITHOSTRATIGRAPHY

In Hole 766A we encountered basaltic rocks at 458 mbsf (Core 123-766A-48R), where we penetrated 69 m of basaltic rocks having minor intercalations of black siltstone of the latest Valanginian (Early Cretaceous) age (see "Sediment Lithostratigraphy" section, this chapter). The bottom of the hole is at 527 mbsf (Core 123-766A-55R) in the middle of a thick diabase dike. Although igneous rocks constitute the acoustic "basement" of Site 765, most are apparently intrusive into the sediments and are not the basement on which sediments were deposited. Therefore, the term "basement" was not applied in this chapter, instead the term "igneous rocks" has been used. Some pebbles of igneous rocks were found in the upper part of the Pa-

Table 12. Index properties and compressional-wave velocities of samples from Hole 776A.

Core, section, interval (cm)	Depth (mbsf)	Bulk density (g/cm ³)	Grain density (g/cm ³)	Porosity (%)	Water content (%)	Velocity (m/s)
123-766A-						
1R-2, 30	1.80	1.60	2.64	74.9	92.3	1521
1R-3, 39	3.39	1.56	2.53	70.1	85.5	1529
2R-2, 60	9.86	1.63	2.68	73.2	84.9	1503
2R-7, 21	16.97	1.58	2.46	71.7	87.0	1471
3R-1, 10	17.40	1.74	2.64	64.7	61.5	1534
3R-4, 35	22.15	1.89	2.78	58.2	46.1	1568
4R-1, 129	28.29	1.77	2.71	61.9	55.7	1515
4R-2, 105	29.55	1.89	2.74	60.3	48.4	1455
5R-2, 97	39.17	1.84	2.76	62.3	53.2	1525
5R-5, 70	43.40	1.74	2.63	58.2	52.1	1544
7R-4, 56	61.06	1.79	2.83	60.9	53.5	1526
7R-6, 118	64.68	1.79	2.65	59.8	52.1	1528
8R-1, 50	66.20	1.75	2.57	58.6	52.1	1510
9R-1, 47	75.77	1.81	2.73	61.7	53.7	1587
9R-4, 94	80.74	1.80	2.68	62.4	55.1	1492
11R-1, 133	96.03	1.93	2.55	53.4	39.5	1637
11R-4, 51	99.71	1.93	2.59	51.1	37.2	1634
12R-1, 35	104.65	1.94	2.59	53.9	39.7	1611
13R-2, 13	115.53	1.77	2.82	63.6	58.2	1595
13R-3, 116	118.06	1.88	2.64	59.9	48.3	1631
14R-2, 50	125.60	1.91	2.97	58.8	45.9	1647
14R-4, 120	129.30	1.94	2.77	58.3	44.6	1649
15R-6, 20	140.90	1.74	2.77	62.0	57.8	1230
16R-1, 52	143.42	1.83	3.10	61.4	52.2	1592
16R-3, 67	146.57	1.96	2.90	56.5	41.7	1589
16R-5, 43	149.33	1.95	2.97	54.3	40.0	1601
17R-2, 106	155.06	1.87	2.72	56.5	44.8	1633
17R-5, 111	159.61	1.91	2.83	59.1	46.4	1647
18R-2, 146	165.06	1.88	2.76	60.0	48.5	1727
18R-4, 14	166.74	1.84	2.54	55.9	45.1	1723
18R-6, 33	169.93	2.04	2.67	50.6	34.0	1811
19R-1, 38	172.08	1.87	2.71	60.5	49.7	1930
19R-3, 131	176.01	1.98	2.70	59.7	44.8	1719
19R-5, 21	177.91	1.93	2.76	58.6	45.1	1704
20R-1, 17	181.57	2.07	2.74	51.0	33.7	1817
20R-3, 11	184.51	2.31	2.62	31.8	16.4	1834
21R-1, 16	191.16	2.04	2.56	46.9	30.8	1846
21R-2, 90	193.40	2.04	2.64	50.8	34.3	1806
22R-1, 25	200.85	2.13	2.25	33.5	19.2	2664
23R-1, 29	210.59	2.08	2.56	48.7	31.7	1957
24R-1, 53	220.43	2.08	2.63	48.2	31.2	1893
24R-CC, 10	221.50	2.20	2.16	29.4	15.8	2679
25R-1, 72	230.32	2.11	2.36	39.1	23.5	2332
26R-1, 109	240.39	2.04	2.64	61.0	44.2	1915
26R-3, 35	242.65	1.90	2.35	56.4	43.8	2017
27R-1, 134	250.24	1.83	2.37	52.9	42.0	2028
27R-2, 74	251.14	1.76	2.42	56.8	49.5	1838
28R-2, 78	260.88	1.85	2.45	53.0	41.6	1901
28R-4, 83	263.93	1.80	2.58	60.8	52.7	1711
28R-6, 68	266.78	1.72	2.41	60.1	55.8	1793
29R-1, 71	269.01	1.73	2.63	62.3	58.6	1702
29R-3, 126	272.56	1.72	2.54	63.2	60.3	1734
30R-1, 12	278.02	1.82	2.68	63.4	55.3	1737
30R-4, 18	282.58	1.80	2.73	63.2	55.9	1656
31R-1, 99	288.49	2.07	2.59	42.0	26.3	1708
32R-1, 27	297.47	1.83	2.44	56.6	46.4	1751
32R-3, 3	300.23	2.01	2.51	50.5	34.6	2186
32R-5, 32	303.52	1.96	2.58	55.3	40.7	1840
33R-1, 66	307.46	2.00	2.84	50.6	35.0	1964
33R-3, 9	309.88	2.14	2.74	40.9	24.4	1844
34R-1, 18	316.68	1.91	2.69	51.6	38.2	1867
34R-1, 136	317.86	1.89	2.78	57.1	45.0	1807
36R-2, 17	337.47	1.85	2.71	62.1	52.4	1760
37R-2, 129	348.21	1.85	2.66	54.2	42.8	1870
37R-3, 18	348.60	2.23	2.70	38.0	21.2	2493
38R-1, 81	355.91	2.29	2.77	35.7	19.0	3017
38R-3, 29	358.39	2.13	2.74	49.0	30.7	2369
39R-2, 44	366.74	2.16	2.79	45.7	27.7	2727
39R-3, 40	368.20	2.03	2.73	61.0	44.5	1940
40R-2, 42	376.42	1.75	2.66	61.6	56.3	1906
40R-4, 14	379.14	2.05	2.61	52.0	35.3	2317
41R-1, 95	385.15	2.03	2.71	51.3	34.9	2135
41R-3, 39	387.59	1.86	2.62	57.5	46.4	1817
41R-5, 89	391.09	1.95	2.67	55.5	41.2	1816
42R-1, 102	394.82	1.91	2.75	58.5	45.7	1991
42R-3, 109	397.89	2.47	2.66	21.8	9.9	3523
43R-1, 50	404.00	2.27	2.72	39.7	21.8	2613
43R-1, 65	404.15	1.92	2.75	56.7	43.4	1797
43R-3, 48	406.98	2.01	2.72	53.0	36.9	2150

Table 12 (continued).

Core, section, interval (cm)	Depth (mbsf)	Bulk density (g/cm ³)	Grain density (g/cm ³)	Porosity (%)	Water content (%)	Velocity (m/s)
123-766A- (Cont.)						
43R-5, 53	410.03	2.02	2.67	54.0	37.8	1866
44R-1, 90	414.10	1.88	2.65	56.9	45.0	1728
44R-3, 98	417.18	2.01	2.70	53.7	37.7	1707
44R-6, 53	421.23	2.01	2.74	53.0	37.0	1773
45R-1, 112	423.92	1.96	2.72	54.0	39.4	1868
45R-3, 36	426.16	2.76	2.86	23.8	9.7	3337
45R-5, 29	429.09	2.13	2.83	52.0	33.3	2000
46R-2, 48	434.52	2.00	2.70	57.4	41.7	1766
46R-4, 23	437.27	2.59	2.74	31.6	14.3	3050
46R-6, 110	441.14	1.93	2.66	57.3	43.8	1801
47R-1, 121	443.41	2.07	2.86	54.6	37.0	1840
47R-4, 53	447.23	1.99	2.78	56.2	40.6	1809
48R-1, 98	452.78	2.08	2.82	51.9	34.3	1921
48R-3, 36	455.16	1.96	2.61	53.8	39.2	1901
48R-5, 78	458.58	1.94	2.62	56.3	42.3	1890
48R-7, 8	460.70	2.45	2.66	13.0	5.7	4161
48R-7, 61	461.23	2.67	2.80	7.1	2.8	4603
49R-1, 25	461.75	2.76	2.84	4.0	1.5	5179
49R-1, 78	462.28	2.54	2.71	9.7	4.1	4270
49R-2, 50	463.50	2.04	2.67	47.9	31.7	1874
49R-3, 65	465.15	2.18	2.88	53.9	33.9	1822
49R-4, 116	467.16	2.84	2.89	2.9	1.0	5451
49R-5, 38	467.83	2.85	2.90	2.2	0.8	5431

Note: owing to instrument error, the values of "Bulk density" and "Porosity" printed in this table are incorrect. Corrected values will be published in the *Scientific Results* volume.

Table 13. Vane shear strength of samples from Hole 766A.

Core, section, interval (cm)	Depth (mbsf)	Shear strength (kPa)
123-766A-		
1R-2, 38	1.88	2.03
1R-3, 37	3.37	4.06
2R-2, 37	9.63	7.51
2R-7, 17	16.93	9.33
3R-1, 75	18.05	1.62
3R-4, 75	22.55	4.46
4R-1, 125	28.25	4.26
4R-2, 73	29.23	8.72
5R-2, 87	39.07	21.10
5R-5, 81	43.51	6.49
7R-4, 111	61.61	5.48
7R-6, 94	64.44	9.54
8R-1, 76	66.46	4.87
9R-1, 52	75.82	45.14
9R-1, 57	75.87	39.97
9R-4, 90	80.70	29.12
11R-1, 130	96.00	24.75
11R-4, 48	99.68	26.21
12R-1, 40	104.70	43.68
13R-2, 8	115.48	134.68
13R-3, 120	118.10	215.49
14R-2, 47	125.57	219.47
14R-4, 118	129.28	101.21
16R-1, 98	143.88	130.78
16R-3, 79	146.69	183.09
16R-5, 94	149.84	130.78

leogene to Late Cretaceous sedimentary section; these are described in "Igneous Rock Petrography" section, this chapter.

Lithostratigraphy, depth, and recovery data for the igneous rocks at Site 765 are summarized in Figure 46. These igneous rocks make up 10.8% in the lowermost part of Core 123-766A-48R, 43.5% in various sections of Core 123-766A-49R, and all of Cores 123-766A-50R to 123-766A-55R. Total recovery was

Table 14. Thermal conductivity of samples from Hole 766A.

Core, section, interval (cm)	Depth (mbsf)	Thermal conductivity (W/mK)
123-766A-		
1R-1, 110	1.10	1.4070
1R-2, 40	1.90	1.0950
1R-3, 40	3.40	1.0960
2R-1, 50	8.20	1.2280
2R-2, 50	9.76	1.2680
2R-3, 55	11.31	1.1370
2R-5, 55	14.31	1.2000
3R-2, 45	19.25	1.2700
3R-3, 45	20.75	1.5150
3R-4, 45	22.25	1.5930
3R-CC, 10	26.40	1.5290
4R-1, 60	27.60	1.5150
4R-2, 60	29.10	1.3740
5R-3, 60	40.30	1.4800
5R-6, 30	44.50	1.4120
6R-4, 60	51.40	1.3500
7R-1, 40	56.40	1.0890
7R-2, 40	57.90	1.4250
7R-4, 33	60.83	1.4130
7R-7, 30	65.30	1.4130
8R-1, 50	66.20	1.4120
8R-2, 44	67.64	1.4390
9R-1, 60	75.90	1.4170
9R-4, 60	80.40	1.4600
10R-1, 70	85.70	1.3400
10R-3, 50	88.50	1.4790
11R-3, 40	98.10	1.6300
11R-4, 40	99.60	1.7350
12R-1, 40	104.70	1.6590
12R-2, 40	106.20	1.5050
13R-1, 40	114.30	1.7420
13R-3, 40	117.30	1.7590
14R-1, 40	124.00	1.5120
14R-2, 40	125.50	1.4330
15R-2, 101	135.71	0.9770
15R-4, 90	138.60	1.5810
16R-2, 120	145.60	1.3670
16R-5, 54	149.44	1.3410
17R-2, 70	154.70	1.4360
17R-5, 38	158.88	1.3910
17R-7, 20	161.70	1.2940
18R-1, 47	162.57	1.3410
18R-3, 34	165.44	1.2760
18R-6, 38	169.98	1.3840
19R-1, 78	172.48	1.3960
19R-3, 43	175.13	1.2490
19R-5, 32	178.02	1.2160
20R-1, 98	182.38	1.4260
20R-2, 40	183.30	1.4390
20R-4, 30	186.20	1.0950
21R-1, 43	191.43	1.4720
21R-2, 82	193.32	1.4450
24R-1, 110	221.00	1.6690
25R-1, 23	229.83	1.4810
26R-2, 70	241.50	1.2260
26R-3, 56	242.86	1.1690
27R-1, 114	250.04	0.8640
27R-2, 51	250.91	1.1030
28R-2, 53	260.63	1.2420
28R-4, 60	263.70	1.3320
29R-1, 80	269.10	1.1420
29R-3, 60	271.90	1.2020
30R-2, 80	280.20	1.0480
30R-4, 40	282.80	1.1520
36R-1, 52	336.32	1.3460
36R-1, 115	336.95	1.3740
36R-2, 16	337.46	1.3990
37R-1, 62	346.12	1.4770
38R-1, 75	355.85	1.5740
38R-3, 68	358.78	1.5430
39R-1, 78	365.58	1.3510
39R-3, 71	368.51	1.3800
41R-1, 116	385.36	1.3450

Table 14 (continued).

Core, section, interval (cm)	Depth (mbsf)	Thermal conductivity (W/mK)
123-766A- (Cont.)		
42R-2, 35	395.65	1.2920
42R-4, 35	398.65	1.3250
42R-4, 38	398.68	1.4440
43R-2, 35	405.35	1.3000
43R-4, 35	408.35	1.5920
44R-2, 50	415.20	1.4650
44R-6, 50	421.20	1.4470
45R-3, 50	426.30	1.5220
45R-7, 30	432.10	1.4040
46R-3, 50	436.04	1.4220
46R-6, 50	440.54	1.3030
47R-2, 50	444.20	1.3390
47R-6, 50	450.20	1.1250
49R-4, 77	466.77	1.4900

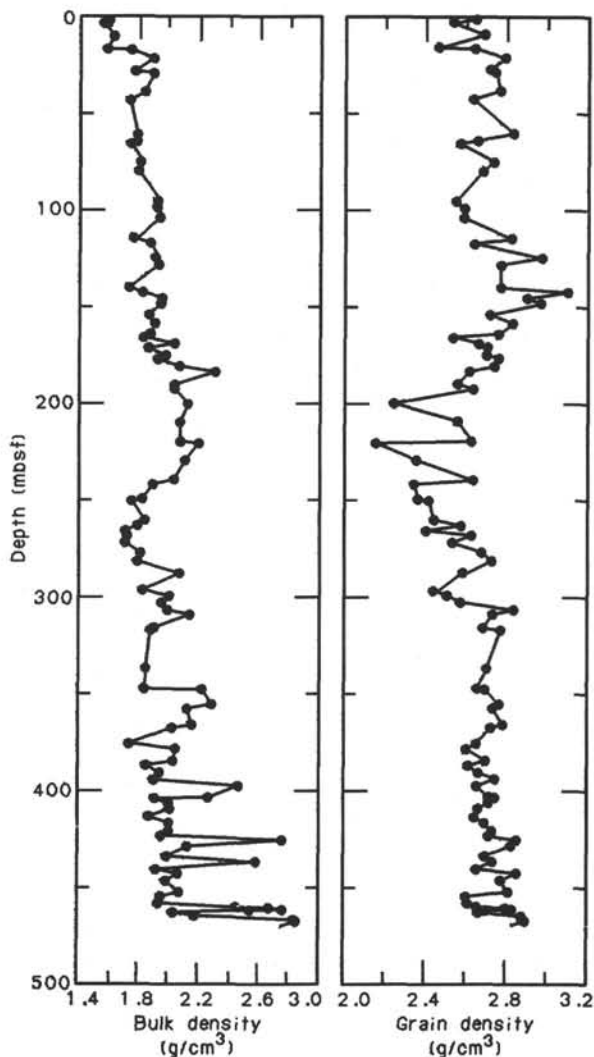


Figure 41. Bulk and grain densities vs. depth of sediment samples from Hole 766A.

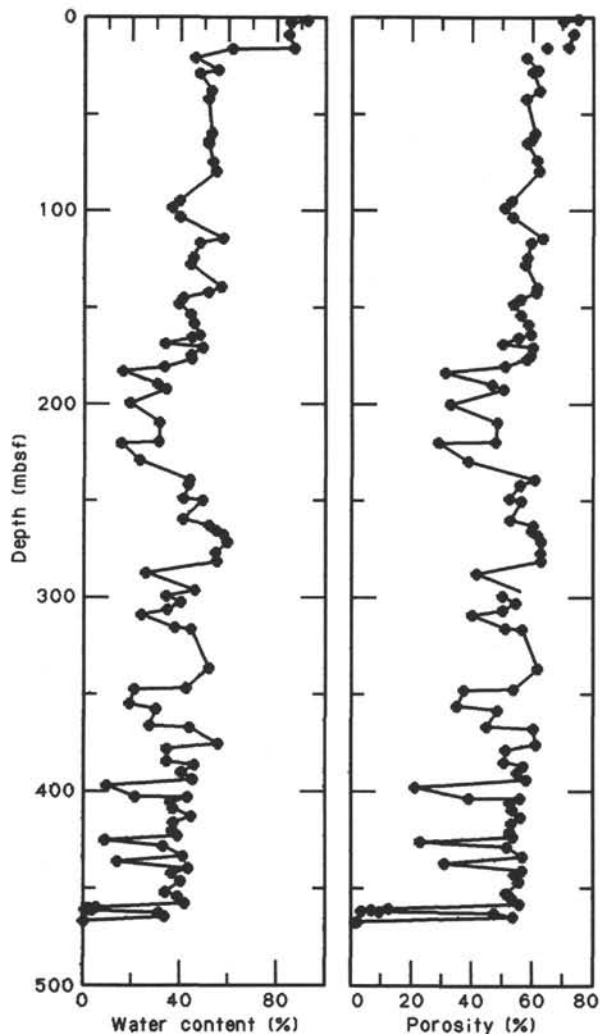


Figure 42. Water content and porosity vs. depth of sediment samples from Hole 766A.

87%, and Cores 123-766-48R, 123-766A-51R, 123-766A-54R, and 123-766A-55R yielded more than 100% recovery. Drift of the hole from vertical is 7° in these igneous rocks.

These igneous rocks can be divided into five lithostratigraphic units. The upper four units are gently inclined sills intruded into the sediments, while the lowest unit may be a dike intrusive into the overlying sills. The limits and lithologies of each unit are described below.

Unit 1 (Sparsely Clinopyroxene-Olivine-Plagioclase Phyric Basalt Sills)

This unit is placed between 460.4 and 462.4 mbsf, or between Sections 123-766A-48R-6, 147 cm and 123-766A-49R-1, 87 cm (between 459 and 461.5 mbsf, based on gamma-ray logging data; see "Schlumberger Logs" section, this chapter). The recovered thickness measures 1.9 m, while logging data indicate that the unit is as thick as 2.5 m. This lithologic unit is composed of at least three cooling units, which are bounded by distinct chilled zones. The boundaries between the cooling units are placed at 461.3 m (Section 123-766A-48R-7, 85 cm) and 461.6 m (Section 123-766A-49R-1, 8 cm).

The upper contact was recovered and is inclined at 20° (Fig. 24). The basalt is chilled against the overlying black siltstone, which is baked and hardened for 10 cm from the contact. The

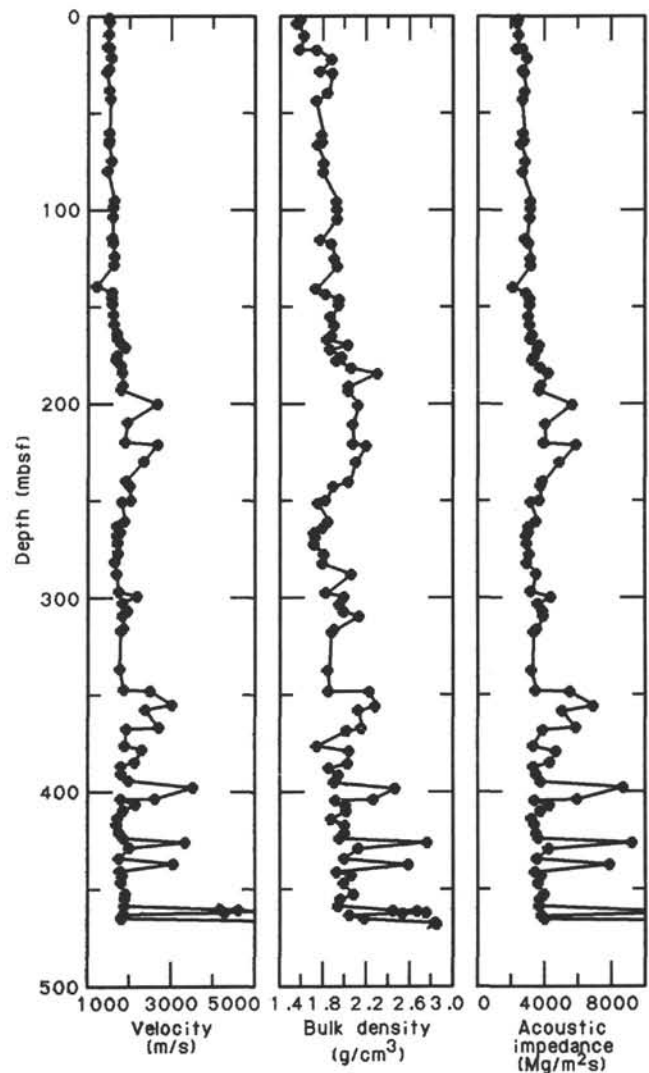


Figure 43. Compressional-wave velocity, bulk density, and acoustic impedance vs. depth of sediment samples from Hole 766A.

basalt near the contact is fractured, and calcite veins parallel to the contact fill the fractures. The lower contact was also recovered and is subhorizontal. The underlying black siltstone is also baked and hardened for 10 cm from the contact.

The sills are different from the other underlying units in phenocryst content. Phenocrysts of plagioclase, olivine, and clinopyroxene, as well as their glomerocrysts, occupy a small percentage of the rock, more than 10% in some highly phyric parts. The sills are very fine-grained (0.2 mm), even in their central parts, and include 2% or less vesicles filled by white or dark green alteration minerals.

This unit is also distinct in its chemistry and is not only the richest in TiO_2 (2.7 wt%), but the most enriched in niobium, strontium, and zirconium of all units (see "Igneous Rock Geochemistry" section, this chapter).

Between this unit and the next, 188 cm of black siltstones is present.

Unit 2 (Aphyric Basalt Sill or Flow)

This unit is placed between 466.2 and 466.7 mbsf, or between Sections 123-766A-49R-3, 124 cm, and 123-766A-49R-4, 18 cm, and represents one cooling unit. Its thickness measures 44 cm, but the unit was not detected by gamma-ray logging.

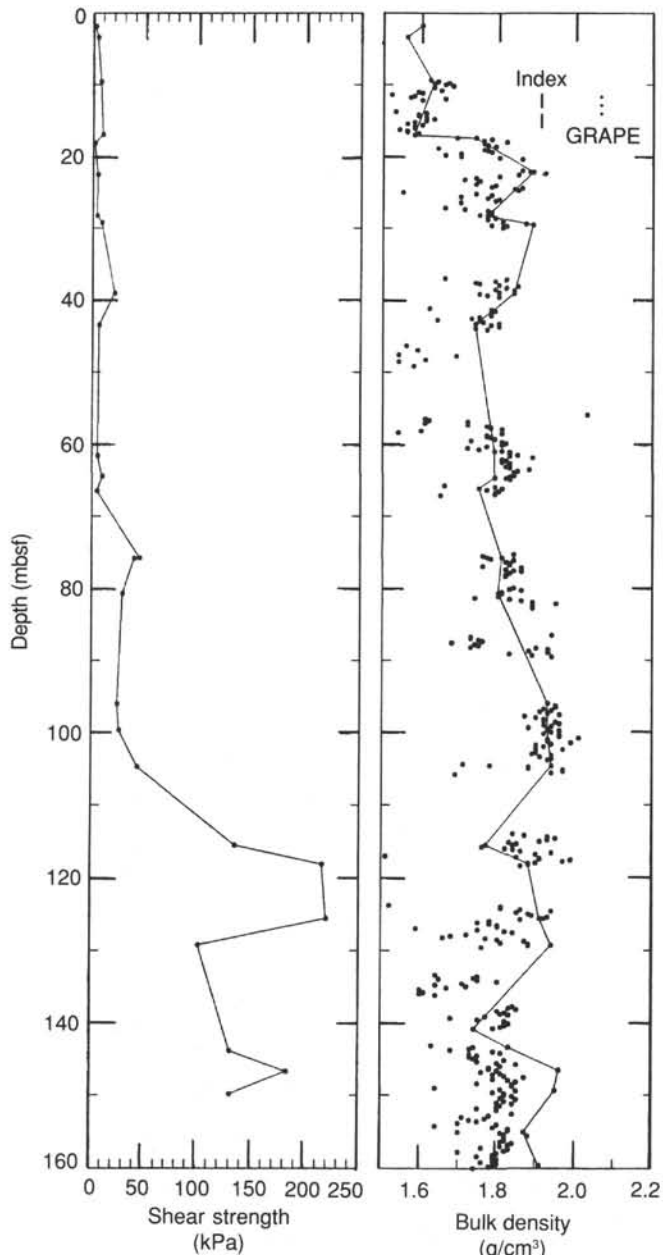


Figure 44. Shear strength and bulk density vs. depth of sediment samples from Hole 766A. Dotted data indicate GRAPE bulk densities.

The upper contact is irregular, and the sediment/basalt contact runs through the uppermost 15 cm in a sinuous manner. Sediments fill the embayed spaces in the basalt. The basalt is aphyric, sparsely vesicular, and microcrystalline, even in the center, but no volcanic glass is present along the contact. The lower contact was not recovered. This small basalt body may be a branch of an adjacent thicker sill.

A total of 45 cm of black siltstones is present between this unit and Unit 3.

Unit 3 (Aphyric Basalt Sill)

This cooling unit is placed between 467.1 and 468.2 mbsf, or between Sections 123-766A-49R-4, 63 cm, and 123-766A-49R-CC, 20 cm (between 466.6 and 468.6 mbsf by the logging data; see "Schlumberger Logs" section, this chapter). A possible fallen fragment of this unit is present in Section 123-766A-50R-1 at 19 to 26 cm (Piece 2). The recovered thickness mea-

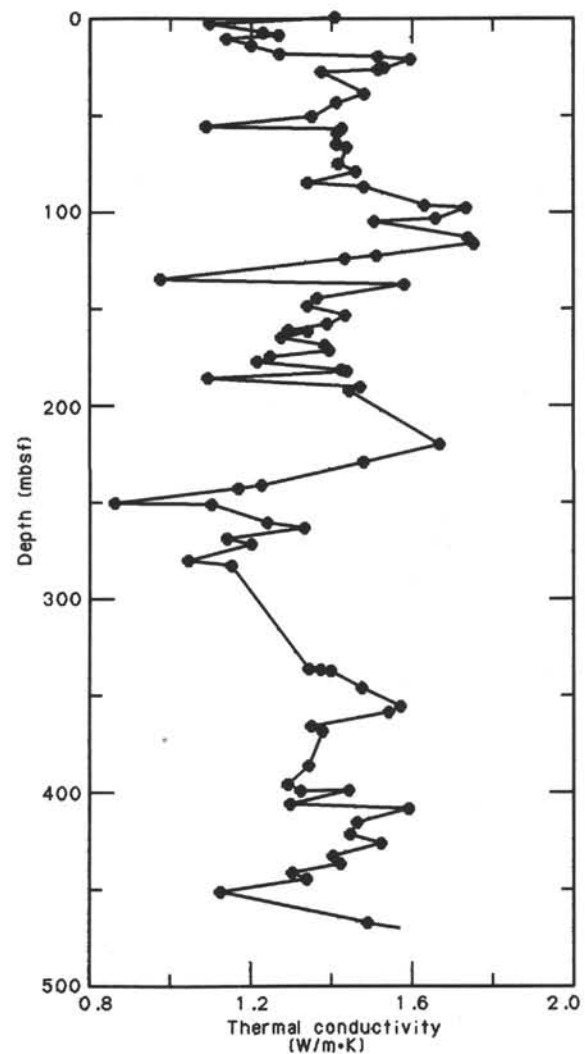


Figure 45. Thermal conductivity vs. depth of sediment samples from Hole 766A.

sures 1.71 m (including the fallen piece), while logging data indicate that the unit is actually 2.0 m thick.

The upper contact is chilled against the overlying sediments, and the contact is inclined 25° or 30° (Fig. 25). The lower contact was not recovered. Vesicles up to 1 cm in size are abundant in the uppermost part, but are rare elsewhere. The central part of the sill is fine-grained and well-crystallized.

The basalt is fairly aphyric, with only rare phenocrysts of plagioclase. This unit is chemically distinct from the other units and is characterized by its lowest contents of incompatible elements (niobium, cesium, zirconium, titanium, vanadium, and yttrium) and the highest chromium contents. This unit is the most primitive basalt in the igneous section at Site 766 (see "Igneous Rock Geochemistry" section, this chapter).

Logging data indicate that a 3.9-m-thick sediment interval is present between this unit and the next, but only rubble of black siltstone was recovered.

Unit 4 (Aphyric Vesicular Basalt Sills)

This unit is placed between 471.5 to 480.6 mbsf, or between Sections 123-766A-50R-1, 26 cm (Piece 3) and 123-766A-51R-1, 16 cm (Piece 1) and is indistinguishable from the next unit in the logging data. Unit 4 may be as thick as 9.1 m, but only a 4.45-m-long section was recovered. This unit includes at least two cool-

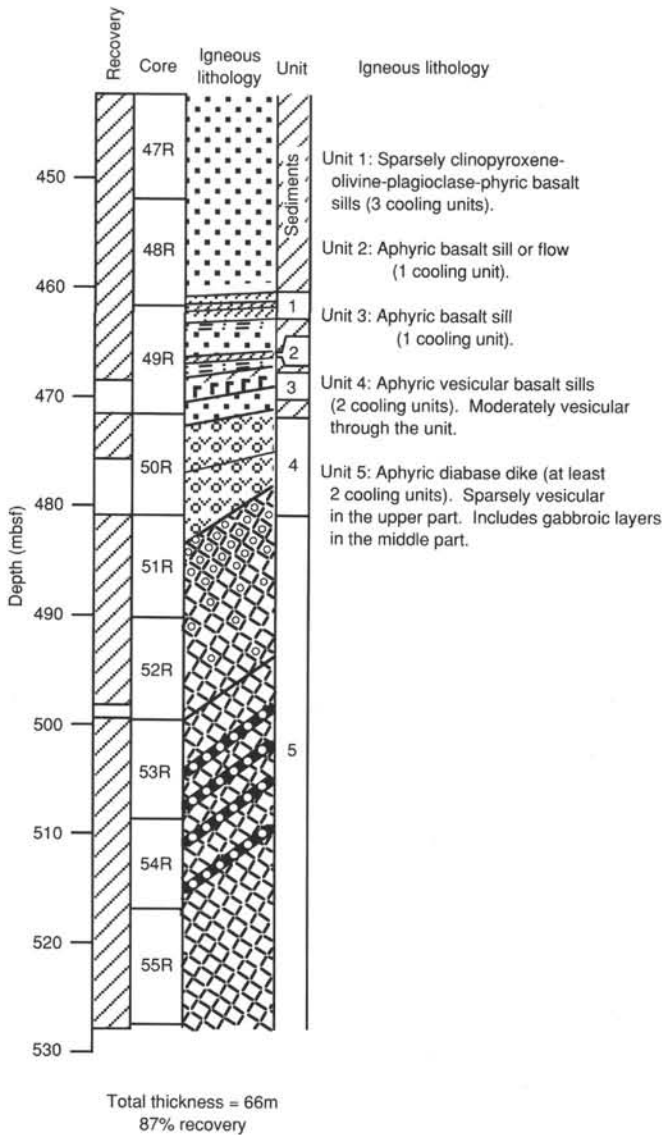


Figure 46. Summary of the lithostratigraphy of the igneous rocks, Site 766, with depth and recovery data.

ing units, the boundary of which is at Section 123-766A-50R-2, 46 cm (between Pieces 2 and 3).

The upper chilled zone was recovered as some rubble (Section 123-766A-50R-1, 27-75 cm, Pieces 3 to 9). The boundary between the two cooling units is well marked by microcrystalline chilled zones. This unit is distinguished from other units by an abundance of white and dark green spherical vesicles 1 or 2 mm in size. The white calcite-filled vesicles and the dark green clay-filled vesicles are distributed in separate areas.

The basalt is aphyric and contains as much as 3% vesicles. Crystallinity is low and is very fine-grained, even in the center of the cooling unit. The basalt geochemically resembles the diabase of Unit 5, but is richer in nickel (Ni) and Cr than any sample from Unit 5.

Unit 5 (Aphyric Diabase Dike)

This unit is placed between 480.6 and 527.16 mbsf (the bottom of the hole) or between Sections 123-766A-51R-1, 16 cm (Piece 2) and 123-766A-55R-8, 126 cm (Piece 10). Unit 5 may be

as thick as 46.6 m, of which 45.97 m (97.6%) was recovered. Internal features in the center of the diabase unit (Cores 123-766A-52R to 123-766A-54R), such as contacts between cooling units, gabbroic layers, and parallel fractures (platy joints) are consistently inclined at 50° or 60°, suggesting that the diabase body is a steeply inclined dike.

The upper and lower contacts were not recovered. The rock is a fine-grained basalt in Sections 123-766A-51R-1 and 123-766A-51R-2, but is dominantly a medium-grained diabase below. The upper part of Unit 5 is sparsely vesicular (in Section 123-766A-52R-1 and the upper core), but the middle and lower parts are completely free from vesicles. However, the diabase includes 5% to 20% interstitial mesostasis (devitrified glass), which gives it a speckled or patchy appearance from the dark color of the mesostasis.

Grain size repeatedly changes through the unit, suggesting the presence of many cooling units (see "Igneous Rock Petrography" section, this chapter). A clear and sharp contact between coarse- and fine-grained parts is observed only in Section 123-766A-52R-5 at 90-96 cm (Fig. 47). This contact dips at 60° and may be a boundary between two adjacent cooling units.

Four or more gabbroic layers, 5 to 10 cm thick, are present in the interval between 500 and 520 mbsf. These layers contain

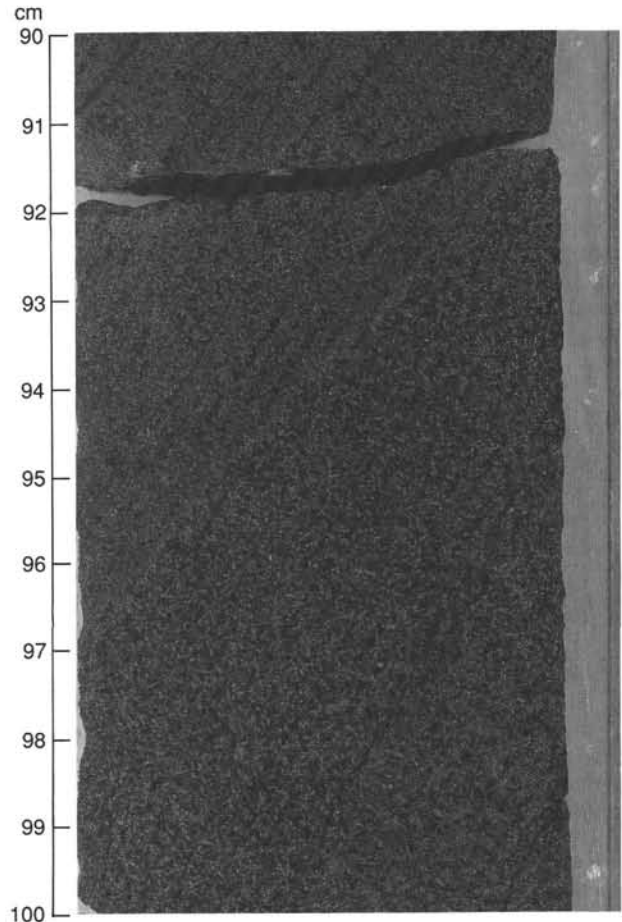


Figure 47. Boundary between the two cooling units in Unit 5 (aphyric diabase dike; Section 123-766A-52R-5, 90-100 cm). The fine-grained diabase may be intrusive against the coarser-grained diabase. The contact is marked by light-colored, very fine-grained zone, 1 to 2 mm thick. The "chilled" zone is holocrystalline under the microscope, suggesting that the wall was still hot at the time of intrusion. The boundary dips at 50°.

elongated clinopyroxene crystals as long as 7 mm and show very high magnetic susceptibility because of the large size of the titanomagnetite grains. The contact with the adjacent diabase is marked by a gradual increase of grain size. These gabbroic layers dip 50° or 60°.

A set of regular, parallel fractures concordant to other internal structures (cooling boundary, gabbroic layers, etc.) are developed through the unit. In some parts they are as frequent as one per 2-cm interval and separate the core into many elliptical disks. The dip of the parallel fractures is moderate (45°) in the upper part, steep (50° to 70°) in the middle and lower parts, and gentle (subhorizontal to 30°) in the lowermost part (Core 123-766A-55R). These fractures may represent a set of platy joints formed parallel to the isothermal surfaces during cooling of the diabase body. The change of the dip of the fractures through the stratigraphic succession suggests a curved isothermal surface and, hence, a curved shape for the body itself. Another set of wider fractures, perpendicular to the other internal structures, is also present, though less frequent than the parallel ones. The perpendicular set may represent columnar joints. These fractures are often filled by calcite, quartz, clay minerals, and pyrite.

The diabase is dominantly aphyric, showing an intergranular or subophitic texture, and includes 5% to 20% mesostasis in interstitial spaces. Some samples bear quartz in the mesostasis, suggesting that the magma is fractionated. The diabase intrusions are geochemically homogeneous, but the coarser-grained

parts tend to be more fractionated and may represent lenses of late-stage, slowly cooled tholeiitic magma.

IGNEOUS ROCK PETROGRAPHY

Five thin sections of the pebbles of igneous rocks encountered in the sedimentary section, and 23 thin sections of the igneous rocks obtained from the acoustic basement of Site 766 were observed under the microscope. The results of mineral identification and various petrographic determinations are listed in Table 15 and are displayed in Figure 48 with the lithostratigraphy.

These pebbles are mostly angular, less than 4 cm in size, and occur *in situ* in sedimentary ooze of ages ranging from Paleogene to Late Cretaceous. They are light yellow green or pale brown, highly altered basaltic rocks. The basalts and diabases forming the acoustic basement occur as sills and dikes cutting the Lower Cretaceous sediments (see "Igneous Rock Lithostratigraphy" section, this chapter).

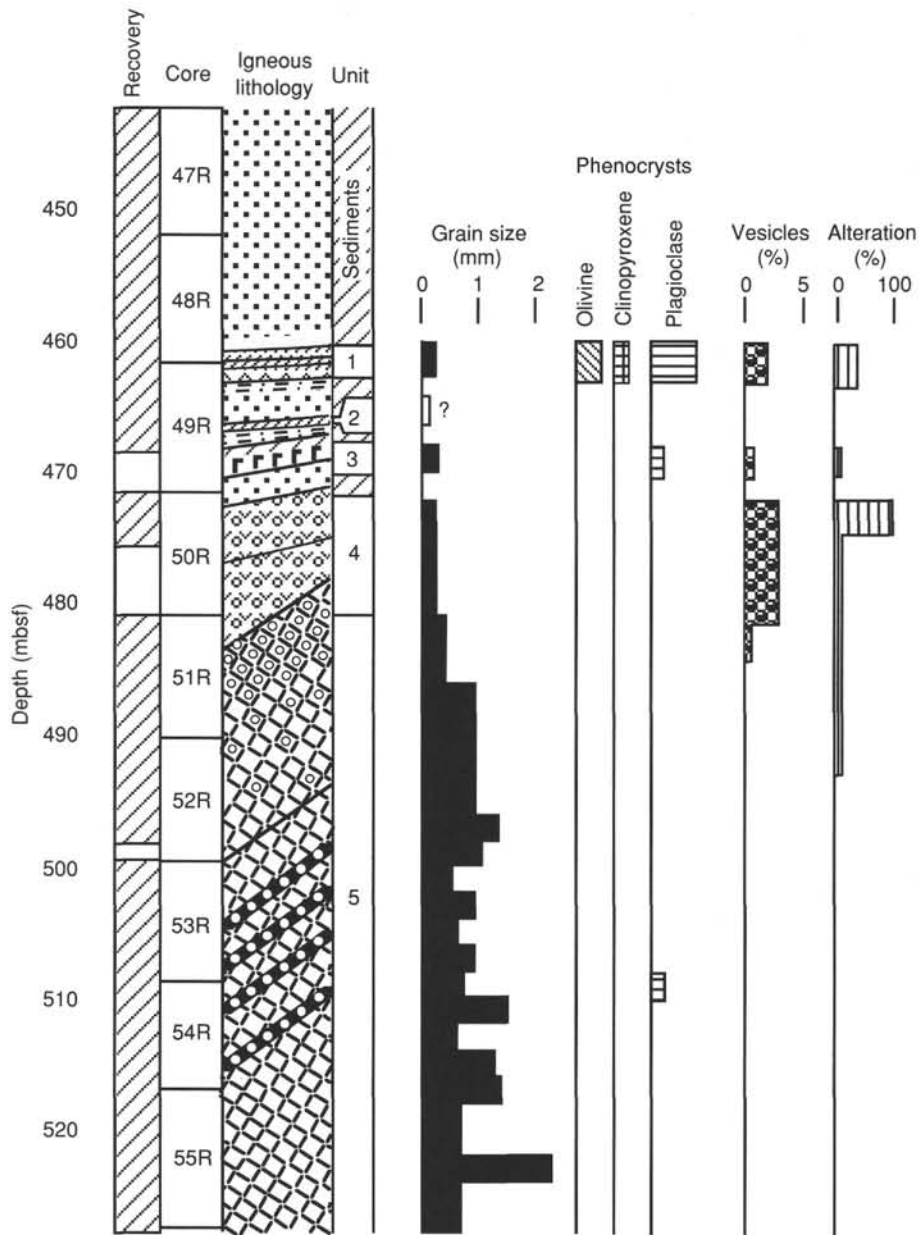
Phenocrysts

Pebbles are generally moderately to highly phyrlic. Phenocryst assemblages include olivine, plagioclase, and, rarely, clinopyroxene. Plagioclase phenocrysts, ranging from 0.9% to 16% in volume and up to 3 mm in size, are present in all pebbles. These are blocky and equant in shape and are different from the tabular plagioclase phenocrysts typical of ordinary ocean-floor basalts. Olivine phenocrysts are present in four out of five pebble

Table 15. Petrographic data for igneous rocks, Hole 766A.

Core, section, interval (cm)	Unit	Texture	Occurrence	Phenocrysts			Groundmass			Altr. (%)	Vesicles (%)	Rem.
				Ol (%)	Pl (%)	Cp (%)	Crys (%)	Size (mm)	Relic			
Pebbles in the sedimentary section												
5R-1, 15-16		Hyo	In	0.3	0.9	—	4	0.2	Cp	41	9.5	spher.
9R-5, 51-53		Ins	In	1.5	16.0	—	48	0.2	—	65	3.5	s.v.
9R-5, 63-65		Ins	In	1.0	8.5	—	42	0.1	—	81	0.4	
9R-5, 74-76		Ins	In	1.7	2.1	0.05	78	0.5	Cp	31	—	XRF s.v.
9R-5, 92-95		Ins	In	—	4.6	—	82	0.4	Cp	25	0.3	
Basal sheets and dikes												
48R-7, 24-27	1	Ins	SM	—	1.1	—	55	0.2	(Cp)	26	1.0	XRF s.v.
48R-7, 61-63	1	Ins	SC	0.1	0.1	—	56	0.2	Cp	33	3.0	s.v.
48R-7, 73-76	1	Hyo	SM	—	0.4	0.1	12	0.2	Cp	7	1.3	s.v. patchy
49R-1, 9-13	1	Ins	SM	1.8	8.7	0.1	60	0.2	Cp	6	0.3	patchy
49R-4, 106-108	3	Ing	SM	—	0.1	—	92	0.3	Cp	4	0.3	XRF vario.
50R-1, 53-55	4	Hyo	SM	—	0.4	—	10	0.2	—	100	2.5	spher.
50R-1, 68-70	4	Hyo	SM	—	0.6	—	5	0.2	—	6	3.0	XRF
50R-2, 26-28	4	Ins	SM	—	0.2	—	50	0.2	Cp	6	3.6	XRF s.v. patchy
51R-2, 8-10	5	Ing	SC	—	—	—	88	0.4	Cp	6	0.3	XRF s.v.
51R-5, 118-120	5	Ing	SC	—	—	—	93	0.9	Cp	7	—	XRF
52R-1, 25-27	5	Ing	SC	—	—	—	93	0.9	Cp	10	—	
52R-4, 47-49	5	sOp	SC	—	—	—	96	0.8	Cp	4	—	XRF
52R-5, 93-96	5	Ing	SC	—	—	—	88	1.3	Cp	—	—	
52R-6, 4-6	5	sOp	SC	—	—	—	90	1.0	Cp	1	—	XRF quartz
53R-1, 82-85	5	Ing	SC	—	—	—	92	0.5	Cp	2	—	Very fine
(contact)		Ing	SC	—	—	—	84	0.9	Cp	2	—	Just contact
53R-3, 91-93	5	Ing	SC	—	—	—	95	0.6	Cp	4	—	XRF quartz
53R-4, 75-77	5	Ing	SC	—	—	—	94	0.9	Cp	2	—	XRF
53R-7, 6-9	5	Ing	SC	—	0.6	—	94	0.7	Cp	tr.	—	
54R-1, 109-110	5	sOp	SC	—	—	—	80	1.5	Cp	3	—	
54R-3, 76-78	5	Ing	SC	—	—	—	96	0.6	Cp	2	—	(XRF 116-118)
(contact)		sOp	SC	—	—	—	90	1.3	Cp	3	—	quartz
54R-6, 121-123	5	sOp	SC	—	—	—	93	1.4	Cp	2	—	
55R-2, 74-76	5	Ing	SC	—	—	—	93	0.7	Cp	—	—	XRF quartz
55R-3, 105-107	5	Ing	SC	—	—	—	94	0.7	Cp	—	—	
(contact)		sOp	SC	—	—	—	85	2.3	Cp	—	—	XRF

Note: Altr. = alteration minerals, Crys. = crystallinity, Hyo = hyalo-ophitic, In = *in-situ* occurrence; Ing = intergranular, Ins = interstitial, sOp = subophitic, SC = sill center, SM = sill margin, Ol = olivine, Pl = plagioclase, Cp = clinopyroxene, tr. = trace amount; XRF = shipboard XRF analysis performed, s.v. = segregation vesicles, spher. = spherulitic, vario. = variolitic, quartz = interstitial quartz present.



Total thickness 66 m; 87% recovery
(including sediment intercalations)

Figure 48. Summary of the petrographic data from the acoustic basement section of Site 766 with the lithostratigraphy. Grain size is the average length of the plagioclase laths in the groundmass. Vesicles include segregation vesicles. "Alteration" represents volume percent of the alteration minerals.

samples. These phenocrysts are completely replaced by clay minerals and/or calcite. The olivine pseudomorphs in two pebble samples bear tiny spinel inclusions, which may be replaced by hematite. Clinopyroxene occurs in one specimen as microphe- nocrysts of an anhedral rounded shape, 0.3 mm in size. The basalt and diabase forming the acoustic basement are dominantly aphyric, and only two samples from Unit 1 contain more than

1% phenocrysts (1.1% and 10.6%). Olivine and clinopyroxene phenocrysts are restricted to Unit 1. Plagioclase phenocrysts commonly occur throughout Units 1 through 4, but are rare in Unit 5. The highly phyrlic basalt from Unit 1 (Sample 123-766A-49R-1, 9-13 cm) closely resembles the highly phyrlic basalt pebbles with respect to phenocryst assemblages (clinopyroxene-olivine-plagioclase) and equant crystal habit of plagioclase phenocrysts.

Groundmass

The crystallinity of the groundmass is variable among the pebbles and ranges from 4% to 82%, with textural variation from hyalo-ophitic to intersertal. In the acoustic basement, crystallinity is low in the thin sheets of Units 1 to 4 and ranges from 5% to 60%, except for the central part of Unit 3, which is crystalline (92%). Texture ranges from hyalo-ophitic to intersertal and is intergranular in the center of Unit 3. The diabase of Unit 5 is crystalline (80%–96%), but always contains some amount of interstitial glass (mesostasis), now devitrified or replaced by clay minerals. A diabase having more than 10% mesostasis shows a patchy or spotted appearance in hand specimen. Texture of this diabase is dominantly intergranular, sometimes sub-ophitic, but not ophitic, as is typical of most diabases having clinopyroxene oikocrysts enclosing many plagioclase laths.

Average grain size of the groundmass plagioclase is less than 0.5 mm in the pebbles, less than 0.3 mm in the upper thin sills of the acoustic basement, and more than 0.6 mm in the lower diabase dike. Average grain size generally exceeds 1.0 mm in the gabbroic layers and attains 2.3 mm in Sample 123-766A-55R-3, 105–107 cm. Clinopyroxene is generally smaller than plagioclase, but the gabbroic layers are larger than plagioclase and may be as large as 7 mm.

Vesicularity is variable in the pebbles and ranges from 0% to 9.5%. Two pebbles bear spherical segregation vesicles, which are composed of quench crystals of iron and titanium (Fe-Ti), clinopyroxene, plagioclase, and ilmenite. The upper sills of the acoustic basement are sparsely to moderately vesicular. Unit 4 is uniformly vesicular, with about 3% vesicles, and is distinguished from other units by this feature. Segregation vesicles are common in Unit 1 and also occur in Unit 4 and the uppermost part of Unit 5. Vesicles, other than segregation vesicles, are filled by clay minerals and/or calcite.

Those minerals constituting the groundmass of the pebbles include plagioclase, clinopyroxene, and Fe-Ti oxides. Clinopyroxene may be absent in rocks of the lowest crystallinity. Fe-Ti oxides are generally Ti-magnetite, but flaky ilmenite, resembling biotite in hand specimen, occurs in Sample 123-766A-9R-5, 74–76 cm. The groundmass mineral assemblages of the basalts in the acoustic basement are the same as those in pebbles. The Ti-magnetite is as large as 0.5 mm in the diabases and exhibits a characteristic skeletal form. Four diabase samples bear quartz (shape variable from euhedral to anhedral) in their glassy mesostasis.

The igneous rocks at Site 766 are relatively fresh. Igneous textures and igneous minerals other than olivine are well preserved in most samples. The alteration minerals occurring in the igneous rocks at Site 766 include clay minerals (mostly smectites), zeolite, calcite, quartz, hematite, and pyrite. Pebbles are 20% to 80% altered. In the acoustic basement, the top of Unit 1 is moderately altered (about 30%), the top of Unit 4 is 100% altered, but other parts are less than 10% altered. The middle and lower part of Unit 5 (diabase dike) is fairly fresh.

Conclusions

Each lithostratigraphic unit in the acoustic basement has distinct petrographic features. Unit 1 is clinopyroxene-olivine-plagioclase phyric basalt, Units 2 and 3 are aphyric crystalline basalt, Unit 4 is aphyric vesicular basalt, and Unit 5 is medium-grained diabase. Pebbles are clinopyroxene-olivine-plagioclase phyric basalts resembling Unit 1.

The occurrence of igneous quartz in the mesostasis of some diabase samples suggests silica-saturated and evolved magma for the diabase dike. The common occurrence of segregation vesicles, which may represent Fe- and Ti-rich residual liquid, in

the basalt pebbles and the basement basalts is also suggestive of evolved magma.

IGNEOUS ROCK ALTERATION

The basalt sills and dikes recovered in the lower part of Hole 766A are slightly to moderately altered at low temperatures. The secondary minerals present are smectite (probably saponite), calcite, zeolites, quartz, and pyrite. These minerals fill veins, cavities, and vesicles, and replace primary minerals and the mesostasis of the rock. Units 1 through 4 and the upper part of Unit 5 are the most highly altered, the degree of alteration decreases dramatically in the middle and lower part of Unit 5 (Fig. 46). Vesicles filled with secondary minerals are abundant in the upper parts of each lithologic unit (Fig. 46); veins filled with secondary minerals become less frequent with depth. The alteration in Hole 766A is described in relation to vesicle and cavity fillings, vein fillings, and background alteration.

Vesicle and Cavity Fillings

All igneous rocks in Hole 766A are vesicular to varying degrees, with their size and frequency increasing toward the upper contact of each unit. The vesicles are filled by a variety of secondary minerals; partly filled vesicles are rare. Several of the larger vesicles are concentrically zoned; their rims are white and composed of calcite, and centers are clear and composed of quartz (Fig. 49). Others are layered and filled entirely by calcite (Fig. 24). Several of the larger vesicles in Core 123-766-50R are only partly filled with sparry calcite and have open centers. Below Section 123-766A-52R-1, calcite-filled vesicles are absent.

With increasing distance from the top of Unit 4, vesicles become heterogeneous in the distribution of their fillings. Near veins, and for several centimeters on each side in the form of a

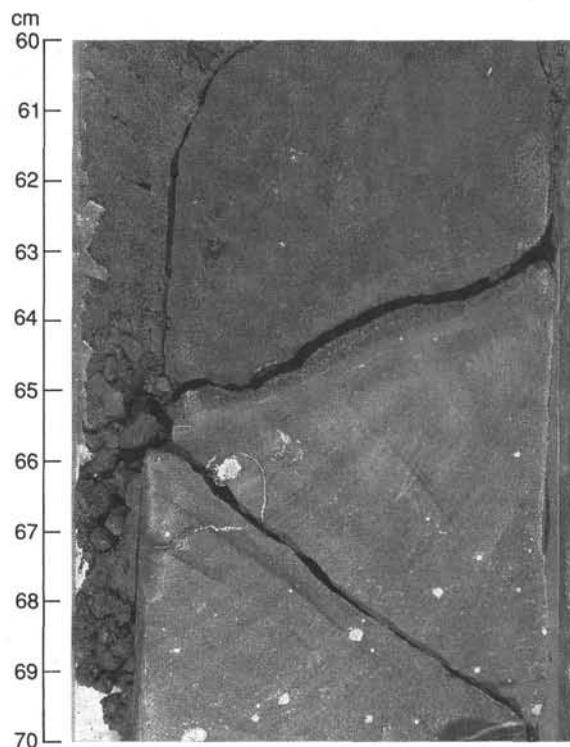


Figure 49. Vesicles filled by calcite \pm quartz adjacent to unit contact. Veins are filled with fibrous calcite \pm green clay mineral centers. Section 123-766A-49R-4, 60–70 cm.

halo, these vesicles are filled with dark homogeneous green clay minerals. Away from the veins and outside the halo, the vesicles are filled with white calcite. Only rarely are layered vesicles seen in which the order of precipitation can be confirmed. These vesicles occur on the outer edge of the halos, are lined with green clays, and have cores filled with calcite. This relationship suggests that vesicles nearest the veins were filled first by the same clay minerals precipitating in the fractures. Later, the circulating fluid must have changed composition to precipitate calcite in a more pervasive event that filled vesicles outside of the halos for tens of centimeters each side of the veins. The number of calcite-filled vesicles decreases downhole. The cause of this may be (1) that the fluids responsible for precipitating the clay minerals deeper in the hole were in residence longer; (2) that the clay mineral alteration was more intense deeper in the hole, filling vesicles that were to be filled later by calcite higher in the section; or (3) that the clay mineral alteration was confined principally to the deeper part of the hole.

Small grains of pyrite often accompany the green clay minerals; these become more common with increasing depth.

Veins

Fractures filled with secondary minerals are common throughout the basalt section (see "Igneous Rock Stress Measurements" section, this chapter), but lower in the hole they tend to be empty. Toward the upper contact of Unit 4, veins up to several millimeters thick are filled with fibrous white calcite (Fig. 24). These veins can have thin green clay-filled centers (Fig. 49). Thin quartz-filled veins are found in several cores and are parallel to the calcite veins. Deeper in the hole, veins are filled with green clay minerals, often with abundant pyrite. This pyrite can be in the form of a coating on the vein wall, or as discrete grains in the vein centers. Late-stage calcite can sometimes fill the centers of the clay mineral veins (Fig. 50). In the lowermost sections of the hole, the clay mineral veins are extremely thin. Several thick veins up to 1 cm wide occur in Unit 5 and contain a mixture of green clay minerals, calcite, and quartz, with scattered pyrite (Figs. 51 and 52). The clay minerals tend to be the first secondary mineral to precipitate in these veins, followed by calcite and quartz; the quartz appears to be the last phase in most cases. Multilayered zeolite(?) -filled veins are also evident. In a number of veins from lower in the hole, a waxy yellow green and dark green clay mineral are present; investigation by x-ray diffraction of these samples identifies two clay minerals, one having a basal peak at about 12\AA and the other with a basal peak at about 15\AA . X-ray studies of all other occurrences of the dark green clay mineral reveal basal spacings of about 12\AA . In Core 123-766A-51R there are several veins about 2 mm wide that are filled with dark green clay minerals surrounded by black halos up to 2 mm wide having sharp outer contacts. These veins are found only in this core; shore-based thin section study should help to determine their nature. The calcite veins have no associated halo.

Background Alteration

Reference to Figure 48 shows the variation of alteration with depth in Hole 766A expressed as a percentage of secondary minerals present in the rock. Alteration intensity decreases markedly with depth; the top of Unit 1 is 30% altered, the top of Unit 4 is 100% altered (elsewhere it is 10% altered), and the middle and lower parts of Unit 5 are relatively fresh. In Units 1 through 4 and in the upper part of Unit 5, mesostasis has altered to clay minerals by varying degrees. Primary minerals remain fresh, except for olivine, which is replaced by clay minerals. Deeper in the hole, the mesostasis is less altered.

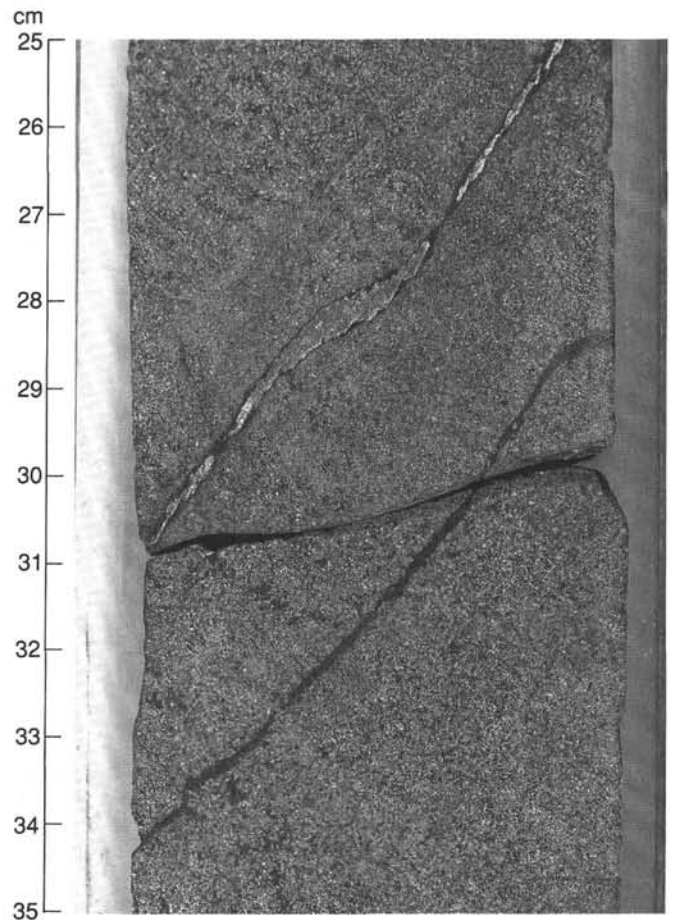


Figure 50. Vein at 33 cm is filled by green clay minerals; vein at 27 cm has a green clay mineral rim with calcite core. Section 123-766A-53R-7, 25-35 cm.

Conclusions

Igneous rocks from Hole 766A are slightly to moderately altered at low temperatures. Calcite and quartz precipitated after the clay minerals and pyrite. The basement section of the diabase sill, Core 123-766A-52R to the bottom of the hole, is essentially unaltered.

IGNEOUS ROCK GEOCHEMISTRY

Twelve samples of the intrusions recovered from the bottom of Hole 766A were analyzed for major and trace elements by shipboard XRF (see "Explanatory Notes," this volume, for analytical details; and Table 16 for analyses). Two of the samples are from the two small basaltic intrusions of Units 1 and 3 (see "Igneous Rock Lithostratigraphy" section, this chapter), and another 10 samples are from the massive diabases below (Units 4 and 5). The small basaltic intrusion of Unit 2 was not sampled for shipboard XRF analysis.

The units sampled are geochemically distinct. Figure 53 shows plots of MgO , Fe_2O_3 , and TiO_2 vs. depth. Unit 1 is a highly fractionated Fe-Ti basalt, with 17 wt% Fe_2O_3 and almost 3 wt% TiO_2 . Remarkably, only meters away, Unit 3 constitutes a primitive basaltic intrusion with almost 8 wt% MgO and only 10 wt% Fe_2O_3 . In contrast to this variability in the upper thin basaltic intrusions, the massive diabases of Units 4 and 5 have uniform chemistry. A step in both MgO and Fe_2O_3 between Units 4 and 5 is such that the diabase of Unit 4 has a lower FeO/MgO value than the diabase of Unit 5. This would suggest that Unit 4

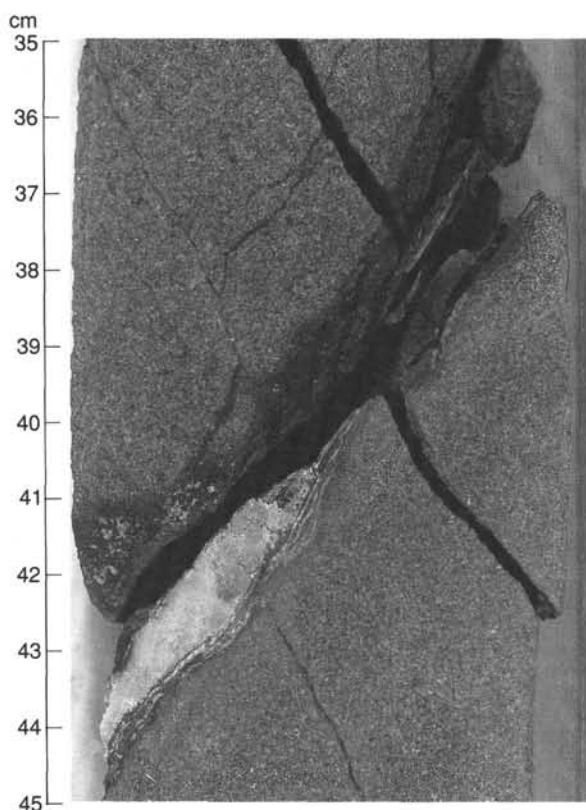


Figure 51. Thick vein in igneous Unit 5 filled by green clay minerals, calcite, and pyrite. Section 123-766A-53R-6, 35–45 cm.

is slightly less evolved than Unit 5; however, immobile incompatible elements, such as TiO_2 and V, are higher in the sample from Unit 4, which would suggest just the opposite. (Unfortunately, the other sample from Unit 4, from the upper chilled contact, was altered, with more than 3 wt% loss-on-ignition. Nonetheless, the distinction between Units 4 and 5 is subtle and based largely on the vesicular nature of Unit 4. Within Unit 5, MgO increases and Fe_2O_3 decreases slightly with depth, suggesting *in-situ* differentiation of the diabase intrusion. One of the inclined, coarse-grained, “gabbroic” layers within Unit 5 was analyzed (Sample 123-766A-53R-3, 91–93 cm). The evolved nature (low MgO and chromium, and high TiO_2 and zirconium) of this sample supports the hypothesis that these gabbroic layers represent pockets of late-stage, slowly crystallized magma.

One of the pebbles recovered in the upper, sedimentary section of Hole 766A was analyzed. The chemistry of this pebble is different from the intrusives below. It has high contents of both compatible and incompatible elements (chromium = ~700 ppm, niobium = ~14 ppm) for major element contents comparable to the fractionated basalt of Unit 1. This pebble is particularly rich in the alkali and alkaline earth elements (potassium, rubidium, strontium, and barium), and thus may be an alkali basalt.

A larger-scale geochemical variation that extends over individual units is a dramatic decrease in both Al_2O_3 and strontium with depth, from Unit 1 to the top of the monotonous Unit 5 (Fig. 54). The high Al_2O_3 and strontium of the upper units may reflect accumulation of plagioclase phenocrysts, which are not present in the lower diabase.

Although substantial variation exists between the lithologic units, this variation is consistent with that produced during fractional crystallization of a common parental magma. For example, CaO and MgO decrease with increasing TiO_2 (increasing crystallization) along well-defined linear trends from the primi-

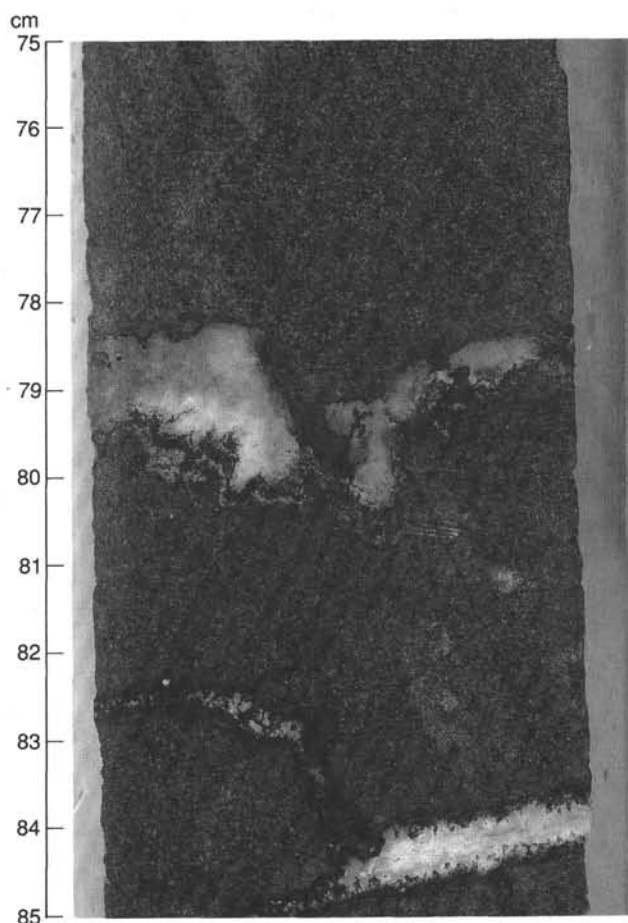


Figure 52. Series of thick veins in Unit 5 filled by green clay minerals, calcite, pyrite, and quartz. Section 123-766A-53R-4, 75–85 cm.

tive basalt of Unit 3, to the diabases of Units 4 and 5, to the evolved basalt of Unit 1 (Fig. 55). These trends are consistent with the fractional crystallization of clinopyroxene, or more generally, crystallization along a basalt cotectic. The ratios of the immobile incompatible elements titanium, zirconium, and vanadium (Fig. 56) remain remarkably constant through all five units and provide further evidence that these intrusives are related to a common parental magma.

Compared to the basalts recovered from Site 765, as well as to the MORBs erupted at the modern Indian Ocean spreading system, the intrusives of Site 766 are highly fractionated. A plot of TiO_2 vs. MgO (Fig. 57) shows that although Site 765 basalts are unusually fractionated for MORBs, all of the samples from Site 766 (with the exception of the primitive basalt from Unit 3, which plots within the modern Indian Ocean MORB field) are even more fractionated. The fractionated nature of these diabases is also indicated by the presence of quartz in the mesostasis of some samples. The fractionated intrusives of Site 766 average more than 14 wt% FeO, and thus may be considered ferro-basalts.

Although these Site 766 intrusives are more fractionated than the Site 765 basalts, they are quite similar in their trace element signatures. For example, the Site 766 intrusives have zirconium/yttrium values distinct from and lower than modern Indian Ocean MORBs and overlap with the zirconium/yttrium values of the basalts from Site 765 (Fig. 58). This observation is true of all ratios involving elements zirconium, titanium, yttrium, vanadium, and phosphorus. Thus, there is some coherency in the mantle sources of the magmas from the two sites. The overall

Table 16. Shipboard XRF analyses of Site 766 intrusives.

Core-sect.:	9R-5	48R-7	49R-4	51R-2	51R-5	50R-1	50R-2	52R-4	52R-6	53R-3	53R-4	54R-3	55R-2	55R-3
Interval:	73-75	25-27	106-108	8-10	118-120	68-70	26-28	47-49	4-6	91-93	75-77	116-118	74-76	105-108
Unit:	Pebble	1	3	5	5	4(Alt)	4	5	5	5(Gab)	5	5	5	5
Depth (mbsf):	82.0	461.1	467.1	482.0	487.6	471.9	473.0	494.9	497.4	503.0	504.4	512.5	519.9	521.8
Major elements (wt %)														
SiO ₂	51.29	47.51	50.06	50.88	51.02	47.01	49.09	51.04	50.72	50.35	50.48	50.88	50.48	50.69
TiO ₂	2.53	2.79	1.03	1.69	1.66	2.11	1.79	1.60	1.58	1.99	1.61	1.64	1.59	1.61
Al ₂ O ₃	17.78	16.68	14.95	13.15	13.16	14.77	14.53	13.07	13.16	12.02	13.14	13.09	13.21	13.06
^a FeO	9.27	15.72	9.45	14.10	13.95	16.39	13.12	13.84	13.79	15.73	13.23	13.40	13.47	13.86
MnO	0.10	0.15	0.16	0.22	0.20	0.12	0.24	0.21	0.23	0.26	0.22	0.20	0.21	0.22
MgO	4.91	5.50	7.86	6.51	6.81	10.30	7.15	6.92	7.12	6.42	7.02	7.03	7.12	6.83
CaO	8.26	7.17	13.35	10.56	10.34	3.60	9.94	10.55	10.91	9.84	11.12	10.68	10.86	10.83
Na ₂ O	3.71	3.86	2.66	2.36	2.41	3.47	2.83	2.51	2.52	2.61	2.36	2.42	2.27	2.48
K ₂ O	1.38	0.08	0.06	0.05	0.05	0.84	0.05	0.05	0.04	0.05	0.05	0.05	0.04	0.05
P ₂ O ₅	0.37	0.26	0.07	0.14	0.13	0.17	0.16	0.13	0.12	0.16	0.13	0.13	0.12	0.13
Total	99.63	99.71	99.64	99.67	99.73	98.78	98.90	99.91	100.20	99.44	99.37	99.53	99.37	99.76
Trace elements (ppm)														
LOI	2.51	2.26	1.10	0.02	0.23	3.39	1.43	-0.01	0.10	1.23	1.31	1.10	1.71	0.68
Nb	13.5	4.6	1.9	3.0	3.0	2.4	2.5	2.3	2.3	3.1	2.8	3.1	3.0	2.9
Zr	163.3	168.0	56.7	99.4	87.6	113.8	97.4	92.1	89.9	113.2	92.5	90.9	86.8	94.9
Y	28.6	44.5	25.3	42.2	40.0	39.8	41.4	38.8	39.2	47.3	37.9	40.9	39.9	43.9
Sr	225.5	135.6	112.1	81.9	83.3	93.2	102.7	82.8	81.5	81.1	87.3	84.3	81.2	80.2
Rb	54.6	0.0	0.0	0.3	0.0	2.7	0.9	0.0	0.0	0.0	0.2	0.4	0.5	0.4
Zn	251.8	146.3	78.8	120.8	103.9	331.9	123.8	98.5	97.9	114.2	97.3	101.4	101.8	114.8
Cu	106.3	91.8	116.0	95.7	93.8	113.2	100.6	91.2	91.3	94.6	98.5	80.3	94.1	102.2
Ni	45.1	60.2	68.9	62.1	58.0	81.9	67.9	63.2	61.0	40.2	61.6	61.7	64.4	63.2
Cr	764.5	168.9	332.3	133.1	127.9	169.8	148.9	131.4	143.4	26.3	140.6	124.5	144.2	129.9
V	339.0	620.1	304.3	429.7	423.3	481.4	436.0	420.1	413.8	495.7	419.1	430.5	420.6	405.6
Ce	26.9	17.9	4.7	12.6	11.6	21.0	9.5	8.2	7.8	10.3	4.7	8.9	11.4	9.2
Ba	108.5	9.0	0.0	3.2	5.0	5.2	4.0	0.0	12.9	8.2	6.4	6.2	3.1	5.8

^a Total iron as FeO. Gab = gabbro, coarse-grained; Alt = altered.

Note: See "Explanatory Notes" chapter (this volume) for analytical details. LOI = wt% loss-on-ignition at 1030°C.

similarity in chemistry between the diabbases of Site 766, intruded at the ocean/continent boundary, and the lavas of Site 765, erupted at a nascent spreading center, suggests that the diabbases of Site 766 tapped a similar magma to that which was supplying the nascent spreading center basinward of Site 766.

IGNEOUS ROCK PALEOMAGNETISM

Analyses

All the archive halves of basement basalt cores from Hole 766A were measured with a pass-through cryogenic magnetometer at natural remanent magnetization (NRM) and at alternating field (AF) demagnetization steps of 10 and 15 mT. Additional demagnetization at 20 mT was done for Sections 123-766A-49R-2, 123-766A-49R-3, 123-766A-51R-2, 123-766A-51R-3, 123-766A-51R-6, 123-766A-52R-1, 123-766A-52R-4, and 123-766A-52R-5 to examine their directional change upon higher demagnetization. Four whole-round blocks for strain measurements (Samples 123-766A-51R-5, 93-114 cm; 123-766A-52R-2, 131-147 cm; 123-766A-55R-6, 33-57 cm; and 123-766A-55R-6, 57-76 cm) were measured and demagnetized at 10 and 15 mT. Measurements of discrete samples were performed for two minicores (Samples 123-766A-51R-1, 52-54 cm, and 123-766A-51R-1, 94-96 cm) to examine the stability of remanence in more detail. These samples were subjected to progressive AF demagnetizations from 2, 4, 8, 10, 12, 15, 20, to 25 mT and measured after each step with a Minispinner magnetometer.

Magnetic susceptibilities of whole-round cores were measured at 10-cm interval using a Bartington MSB1 susceptibility meter.

Magnetic Properties

Figure 59 is a summary of NRM measurements of archive halves. In contrast to the typical low intensities of sediments (3

to 60 mA/m) within Cores 123-766A-48R and 123-766A-49R (451.8-471.2 mbsf), NRM intensities of basalts from Site 766 range from 1000 to 10,000 mA/m. In particular, intensities of the thick basalt recovered from Cores 123-766A-50R to 123-766A-55R range from 2000 to 7000 mA/m.

Cores 123-766A-51R through 123-766A-55R (480.4-527.2 mbsf) are characterized by extremely consistent NRM declinations. This clearly contrasts the upper basalt cores, which display irregular declinations and positive inclinations that seem to represent primary magnetizations. The anomalous declination concentration indicates that these cores acquired a significant amount of viscous remanent magnetization (VRM) during storage in the core laboratory before being measured. This rapid VRM acquisition can be ascribed to the rapid change in grain size, increasing down from Core 123-766A-51R (see "Igneous Rock Petrography" section, this chapter).

After demagnetizations at 15 mT, the cores displayed remarkable changes both in declination and inclination (Fig. 60). Declinations of Cores 123-766A-51R to -53R (480.4-508.3 mbsf) tend to scatter, as in the overlying cores, and inclinations of some portions shift downward (positive), suggesting a reversed polarity. Declinations of Core 123-766A-54R (508.3-511.7 mbsf), which consists of one continuous basalt core, cluster between 180° and 220°. Intensities decrease rapidly by one order of magnitude. These results suggest that the secondary overprint carried by the coarse-grained basalt, including VRM components acquired during storage, may be removed by higher AF demagnetization treatments.

Two different magnetic properties were obtained from preliminary measurements of discrete samples. Figure 61 shows an example of stable magnetization of the coarse diabase (Sample 123-766A-51R-1, 94-96 cm). A secondary overprint was erased by increasing the demagnetization intensity up to 8 mT, reveal-

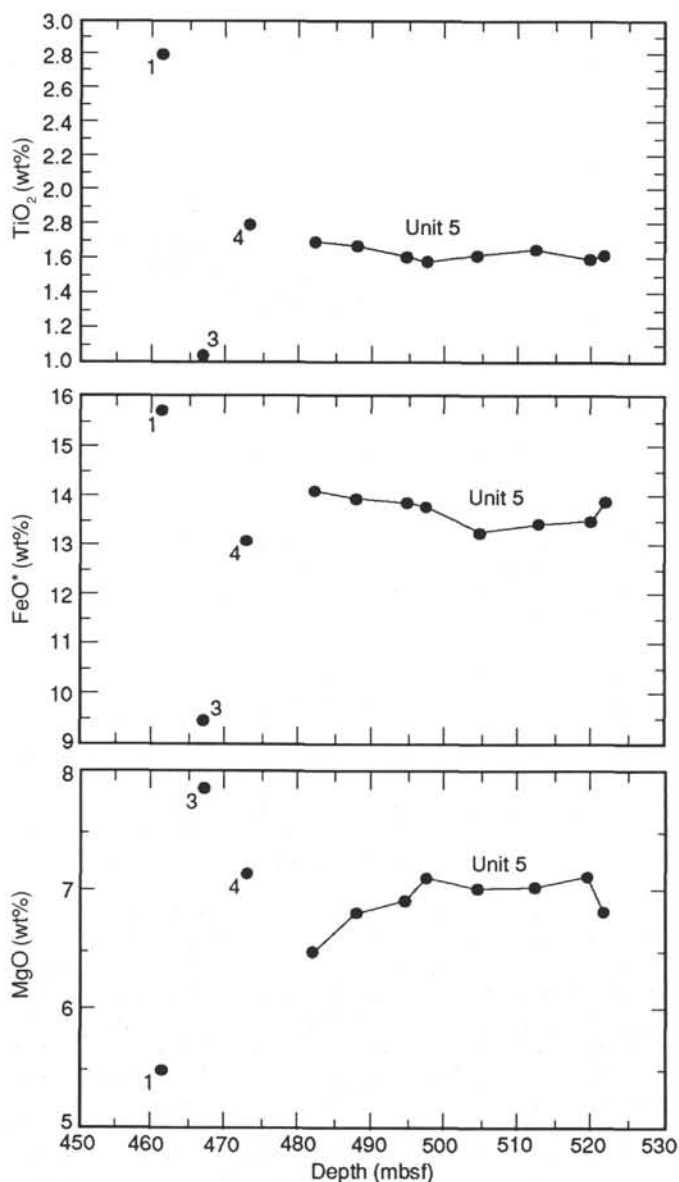


Figure 53. TiO_2 , FeO , and MgO variations with depth (1, 3, and 4 refer to igneous units), Site 766.

ing a stable magnetization of reversed polarity. The magnetic coercivity is high. In contrast, however, the other discrete sample taken from the same section (Sample 123-766R-51R-1, 52-54 cm), exhibits remarkably unstable behavior (Fig. 62). Although the intensity decreased rapidly with demagnetization below 5 mT, the direction changed in an irregular manner with higher progressive demagnetization steps.

The extremely viscous, or soft, magnetic properties of the basalt make it necessary to measure the other discrete samples in a special magnetic environment, free from any external magnetic field to cause viscous magnetization; this will be performed on shore.

Susceptibility

Figure 63 is a summary of susceptibility measurements of Cores 123-766A-47R to -55R. The extremely low susceptibilities, values of K less than 1×10^{-4} cgs units, were obtained from the sediments of the uppermost two cores (442.2-461.0 mbsf) and at an interval between 462.5 to 465.0 mbsf. Susceptibility values

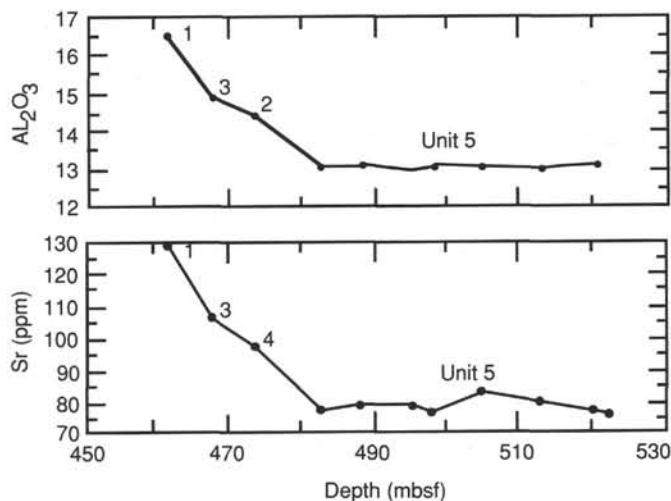


Figure 54. Al_2O_3 and Sr variations with depth. Both Al_2O_3 and Sr are high above the monotonous Unit 5, suggesting the accumulation of plagioclase phenocrysts in the upper units.

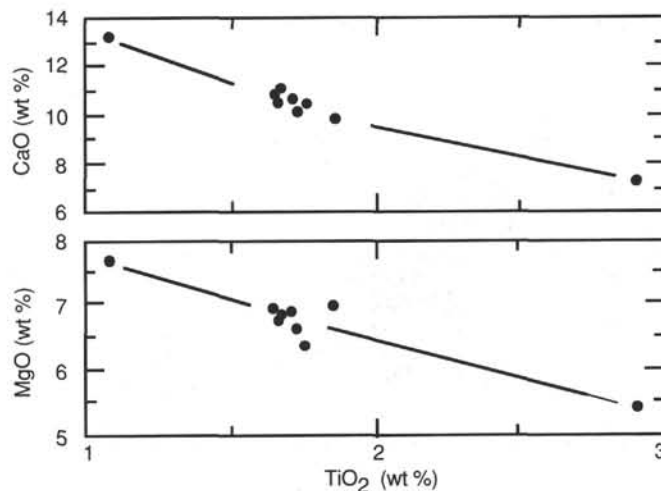


Figure 55. CaO and MgO fractionation trends in the intrusive, Site 766. These trends are consistent with fractional crystallization of clinopyroxene from a common parental magma.

of the basalt are 1 to 6×10^{-3} cgs, with most at 3 to 4×10^{-3} cgs. It is clear in this figure that susceptibilities increase rapidly from the surface of the thick diabase (467 mbsf), in accord with the grain size variation. The high susceptibilities can be ascribed to the coarse grain size of the diabase, as well as the extremely viscous magnetic properties.

IGNEOUS ROCK PHYSICAL PROPERTIES

Introduction

Physical properties determined from the igneous rocks at Site 766 include compressional-wave velocity (as measured using a Hamilton Frame velocimeter), index properties (i.e., bulk density, grain density, porosity, and water content, as determined by a pycnometer and balance), and thermal conductivity. Velocities and index properties were measured on samples from each core. Values of the various physical-property measurements are listed

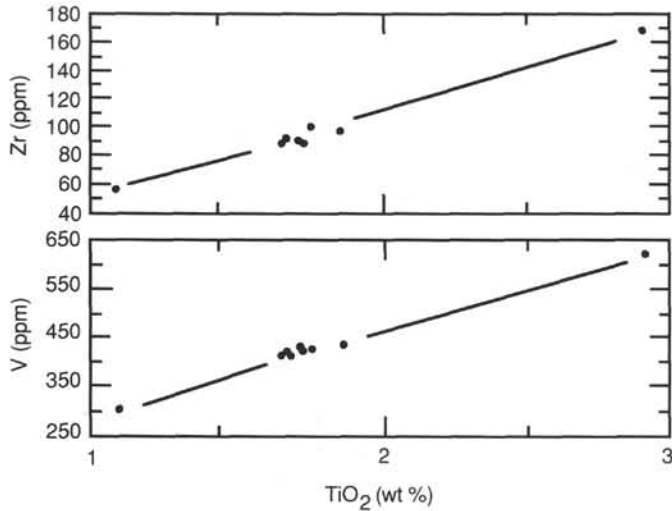


Figure 56. Plots showing the constant Zr/Ti and V/Ti ratios of the intrusives of Site 766, suggesting that the different intrusives are co-genetic.

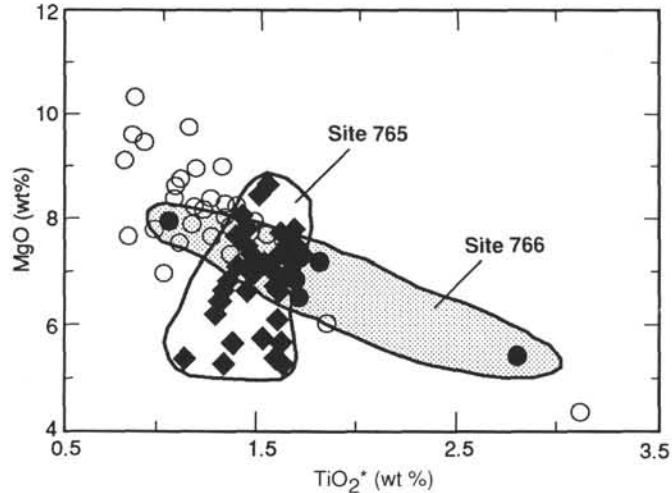


Figure 57. TiO₂ vs. MgO for Indian Ocean basalts. Solid circles are Site 766 intrusives; closed diamonds are Site 765 basalts (data from "Basement Geochemistry" section, Site 765 chapter); open circles represent basalts from the active Indian Ocean Ridge spreading system (see Fig. 68 caption, "Basement Geochemistry" section, Site 765 chapter, for data sources). Site 765 basalts are more fractionated (higher TiO₂ and lower MgO) than modern Indian Ocean basalts, while most Site 766 intrusives are more fractionated than the Site 765 basalts.

in Tables 17 and 18, and variations of these properties with depth are illustrated in Figures 64 through 67.

Results

Index Properties

Bulk density, grain (or matrix) density, porosity, and water content (dry basis) of the samples from the igneous rock portion of Hole 766A are listed in Table 17 and plotted relative to depth in Figures 64 through 66. The igneous rock portion of Hole 766A consists of three basic units: Unit A (459–463 mbsf), Unit B (463–467 mbsf), and Unit C (467–527 mbsf; last measurement at 516 mbsf).

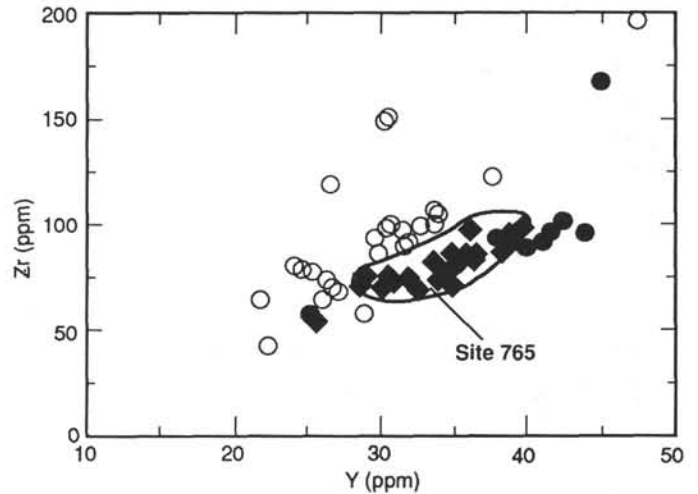


Figure 58. Symbols and data sources are same as in Figure 72. The similar Zr/Y ratios between Site 766 and 765 samples suggest a similarity in mantle sources, which are distinct from those tapped by modern Indian Ocean basalts.

Unit A (459–463 mbsf) consists of a thin basalt sill. Index properties vary considerably across the unit, from the outside edges toward the center. Grain densities at the upper and lower boundaries have an average value of 2.68 g/cm³, whereas the value in the center of the sill is 2.84 g/cm³. This trend is also apparent in terms of the water content and porosity. The former ranges from an average of 4.9% at the edges to 1.5% at the center. The latter varies from an average of 11.4% to 4.0% from the outside to the center.

Unit B (463–467 mbsf) consists of a thin, dark, shale sediment layer. This sediment is similar to that observed in the lowermost portion of the sediment column, as described in the "Sediment Physical Properties" section (this chapter). Although only two data points are available, grain densities exhibit considerable variation, with values ranging from 2.67 to 2.88 gm/cm³. Water contents and porosities show considerably less variation, with average values of 32.8% and 50.9%, respectively.

Unit C (467–516 mbsf) consists of a thick diabase sill. Although some variation occurs in the index properties in the uppermost portion of the unit, the values for most of the unit remain constant with little variation. The average bulk and grain densities are 2.86 ± 0.07 g/cm³ and 2.91 ± 0.05 g/cm³, respectively. Both water content and porosity exhibit a slight decrease with depth. Average values remain low at 1.06 ± 0.52% and 2.89 ± 1.30% for the water content and porosity, respectively.

While reducing the index-properties data, we found that the difference between the wet and dry volumes was often less than the accuracy of the pycnometer. The problem became manifest in a significant number of instances where dry volume was found to exceed the wet volume. Therefore, in calculating the index properties, the wet or total volume was determined using an averaged sample diameter and height, as measured to the nearest 0.002 cm by a set of calipers. This volume, along with the wet and dry weights, was used to develop the phase relationships and, hence, the index properties for the igneous rock.

Velocity

Compressional-wave velocity data, as determined using the Hamilton Frame apparatus, are shown in Figure 66. Velocities for the uppermost basalt unit vary considerably across the section. The average velocity at the upper and lower boundaries is 4216 m/s, whereas the value at the center is 5179 m/s. Within the sediment layer, velocity decreases significantly to an average

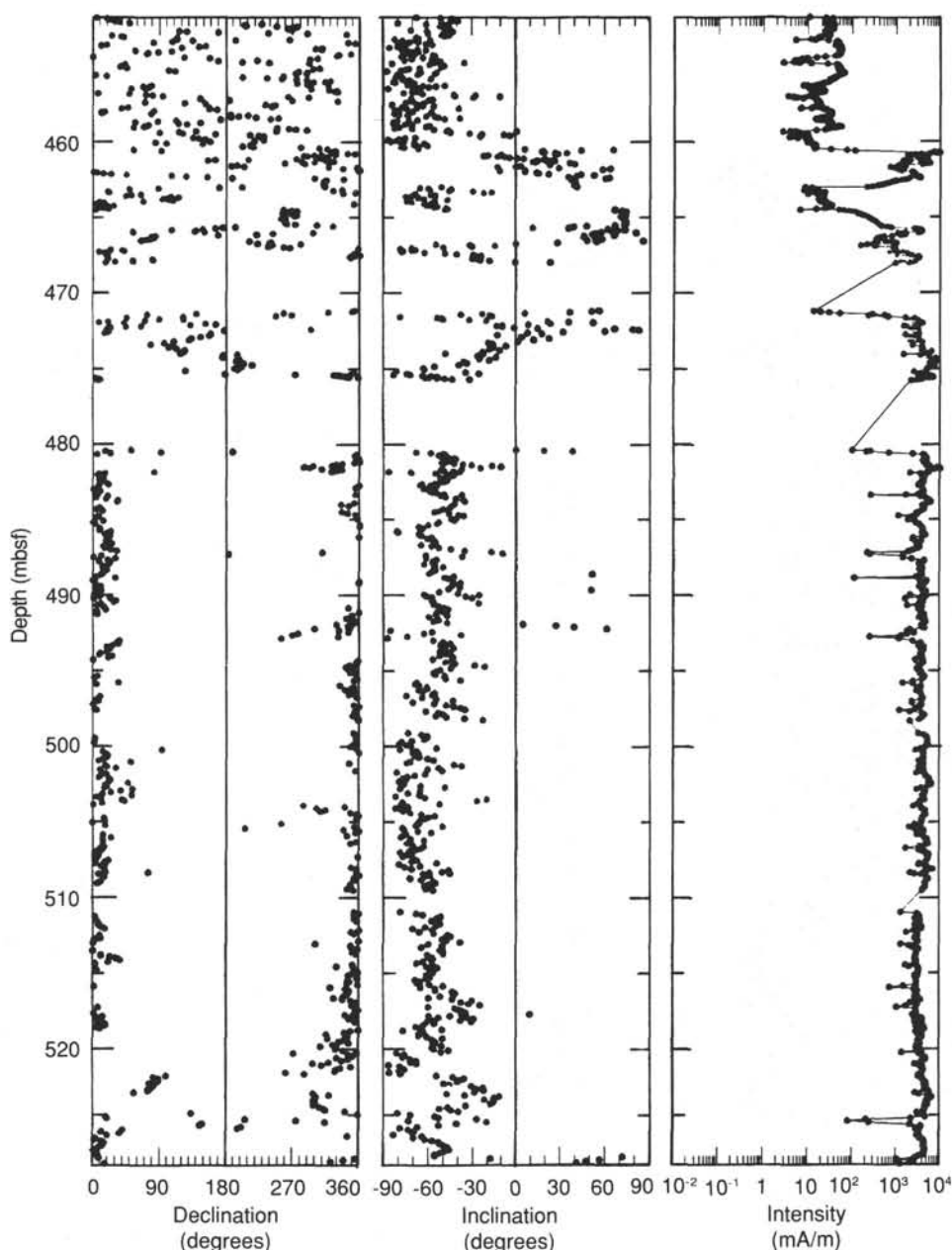


Figure 59. NRM-depth plots, Cores 123-766A-48R to 123-766A-55R.

value of 1848 m/s. The lowermost basalt unit shows some slight variations in velocities, with an average value of 5450 ± 350 m/s.

As an additional means of comparing index properties with velocity data, an acoustic impedance plot (Fig. 66) was created by multiplying the igneous rock bulk density by the corresponding velocity and plotting the result as a function of depth.

Thermal Conductivity

The thermal conductivities listed in Table 18 are illustrated in Figure 67. Thermal conductivity tests were performed on samples from the lowermost basalt unit only. Thermal conductivity of this basalt increases with depth from 1.49 W/mK at 467 mbsf to 1.82 W/mK at 493 mbsf, thereafter it remains constant at 1.82 W/mK.

Conclusions

Igneous rock index properties, compressional-wave velocities, and thermal conductivities allow one to characterize the igneous rock portion of Site 766 into three physical properties units. Unit A is a thin basalt sill that extends from 459 to 463 mbsf. Physical properties vary considerably across the unit, from sediment characteristics at the edges to true basalt characteristics at the center. Unit B is a thin layer of dark shale that extends from 463 to 467 mbsf. This shale is similar to the same material identified in the lowermost portion of the sediment column. A significant decrease in compressional-wave velocities was observed. Unit C is a thick diabase sill that extends from 467 to 527 mbsf. Physical properties vary slightly in the uppermost portion, but remain relatively constant throughout the unit.

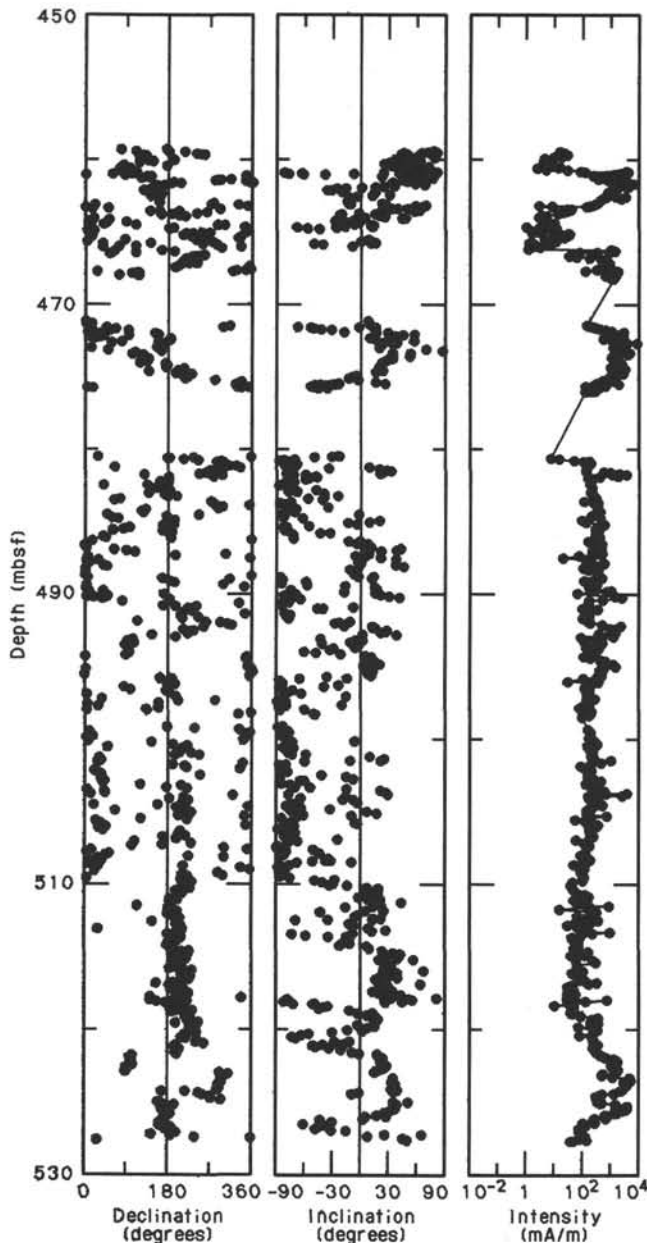


Figure 60. Magnetizations after 15-mT demagnetization vs. depth plots, Cores 123-766R-48R to 123-766A-55R.

Compressional-wave velocities increase slightly with depth, going from 5450 m/s at 467 mbsf to 5900 m/s at 511 mbsf. Thermal conductivity increases through the upper part of Unit C and then remains constant with depth.

IGNEOUS ROCK STRESS MEASUREMENTS

Anelastic Strain Recovery Experiments

Introduction

Sample selection and experimental procedures for anelastic strain recovery work was described in "Basement Stress Measurements" section (Site 765 chapter). These same procedures were followed at Site 766, and the same overall laboratory conditions prevailed. None of the sediment cores recovered from Hole 766A were sufficiently lithified to be suitable for anelastic

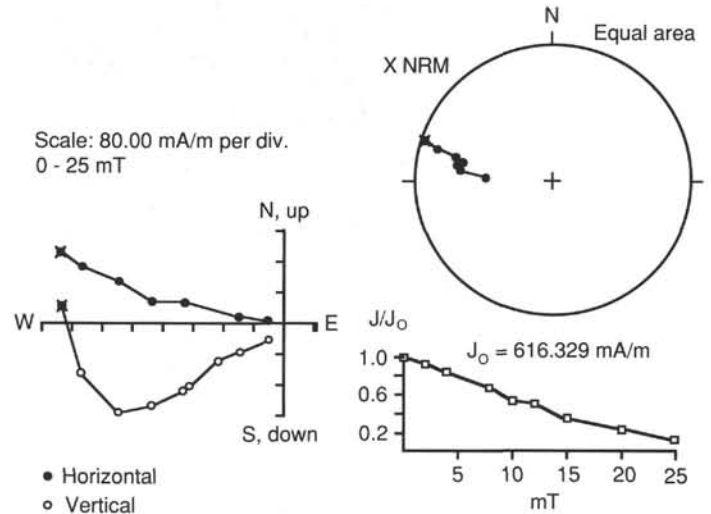


Figure 61. Vector (Zijderveld) and equal-area plots of progressive AF demagnetization for Sample 123-766A-51R-1, 94-96 cm, showing a stable magnetic behavior. Secondary overprint was removed by increasing the demagnetization intensity to 8 mT.

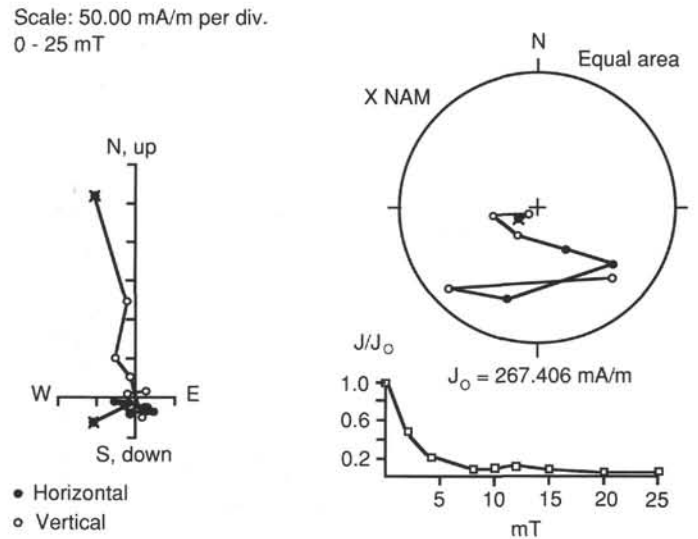


Figure 62. Vector (Zijderveld) and equal-area plots of progressive AF demagnetization for Sample 123-766A-51R-1, 52-54 cm, showing rapid removal of viscous components and unstable magnetic behavior with higher demagnetization steps.

strain recovery experiments, but four diabase samples were taken from Cores 123-766A-51R, 123-766A-52R, and two adjacent samples from Core 123-766A-55R.

Preliminary Results

Results from a preliminary assessment of these data are shown in Table 19. This table presents the computation of magnitudes of the vertical and maximum and minimum horizontal strains, the orientation of the maximum strain relative to present-day north, and the time elapsed from the onset of strain relief monitoring to full relaxation of the sample. Also shown in Figure 68 are plots of the computed vertical and the maximum and minimum horizontal strain relief curves for Sample 123-766A-55R-6, 57-76 cm (Bas 15). A more comprehensive and complete analysis of this data will be conducted as part of the shore-based studies, together with instrument drift corrections of the raw data. These results are thus subject to change.

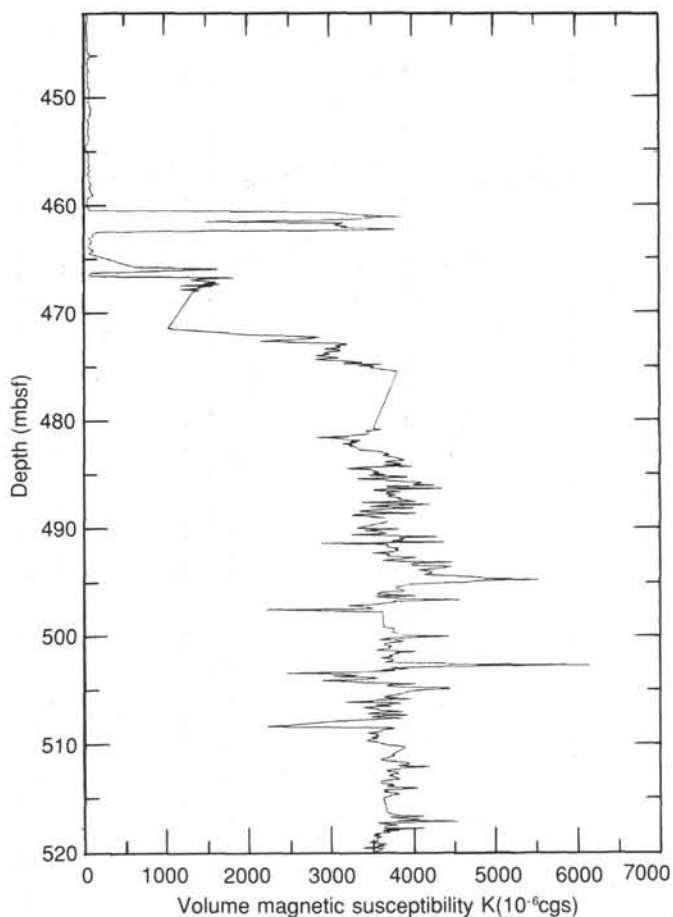


Figure 63. Summary of magnetic susceptibility of Cores 123-766A-47R to -55R.

Table 17. Index properties and compressional-wave velocities of igneous rock samples from Hole 766A.

Core, section, interval (cm)	Depth (mbsf)	Bulk density (g/cm ³)	Grain density (g/cm ³)	Porosity (%)	Water content (%)	Velocity (m/s)
123-766A-						
48R-3, 36	455.16	1.96	2.61	53.8	39.2	1901
48R-5, 78	458.58	1.94	2.62	56.3	42.3	1890
48R-7, 8	460.70	2.45	2.66	13.0	5.7	4161
48R-7, 61	461.23	2.67	2.80	7.1	2.8	4603
49R-1, 25	461.75	2.76	2.84	4.0	1.5	5179
49R-1, 78	462.28	2.54	2.71	9.7	4.1	4270
49R-2, 50	463.50	2.04	2.67	47.9	31.7	1874
49R-3, 65	465.15	2.18	2.88	53.9	33.9	1822
49R-4, 116	467.16	2.84	2.89	2.9	1.0	5451
49R-5, 38	467.83	2.85	2.90	2.2	0.8	5439
50R-1, 135	472.55	2.66	2.76	5.5	2.1	4821
50R-3, 112	475.14	2.77	2.85	4.6	1.7	4787
50R-4, 13	475.52	2.74	2.85	5.8	2.2	4877
51R-1, 90	481.30	2.84	2.89	2.6	0.9	5515
51R-5, 17	486.38	2.86	2.94	4.1	1.5	5372
52R-1, 25	490.15	2.88	2.93	2.8	1.0	5498
52R-3, 98	493.95	2.89	2.92	1.8	0.6	5740
52R-5, 55	496.29	2.90	2.95	2.2	0.8	5162
53R-1, 35	499.45	2.90	2.93	2.0	0.7	5567
53R-3, 52	502.22	2.91	2.95	2.1	0.7	5757
53R-5, 62	504.51	2.90	2.95	2.5	0.9	5730
53R-7, 91	507.60	2.91	2.96	2.4	0.9	5117
54R-2, 108	510.70	2.91	2.94	1.6	0.6	5901
54R-4, 96	513.22	2.93	2.97	1.8	0.6	5898
54R-6, 118	515.68	2.92	2.96	2.1	0.8	5731

Table 18. Thermal conductivity of igneous rock samples from Hole 766A.

Core, section, interval (cm)	Depth (mbsf)	Thermal conductivity (W/mK)
123-766A-		
49R-4, 77	466.77	1.4900
50R-3, 48	474.50	1.6850
51R-3, 86	484.21	1.6800
52R-1, 79	490.69	1.6950
52R-3, 0	492.97	1.8200
53R-3, 45	502.15	1.8250
54R-4, 67	512.93	1.8000
55R-7, 136	527.02	1.8350

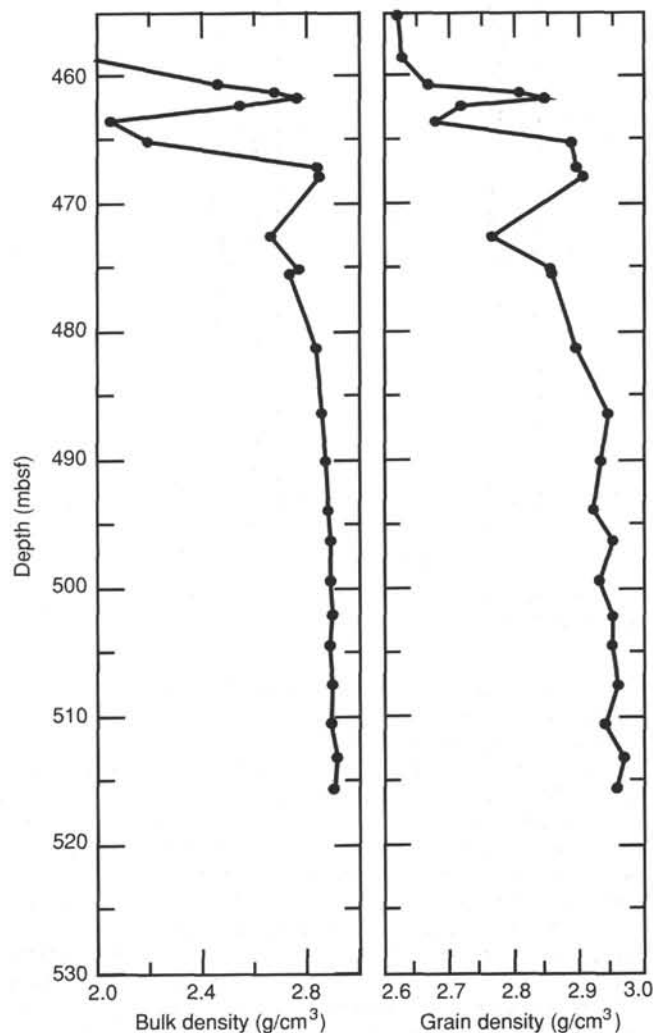


Figure 64. Bulk and grain densities vs. depth of igneous rock samples from Hole 766A.

Diabase samples from Hole 766A were less invaded by calcite veins than those from Hole 765D and were selected to be as feature-free as possible. The last two samples (Bas 14 and Bas 15) were taken from the same core section and were immediately adjacent to one another. The break in the rock between these two samples could be matched so that one continuous scribe line could be drawn from one to the other. This allowed us to re-

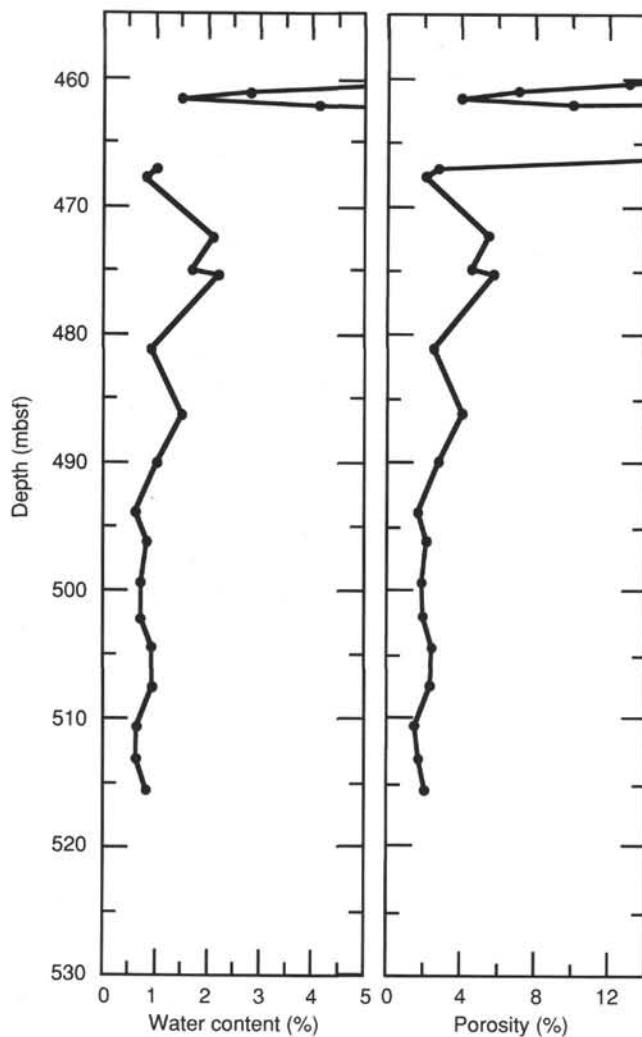


Figure 65. Water content and porosity vs. depth of igneous rock samples from Hole 766A.

produce the results that were assessed between two halves of what is essentially one sample.

First, both the vertical and minimum horizontal strain relief for all the samples is negative. For the last three samples (Bas 13, Bas 14, and Bas 15) the magnitude of both the vertical and the deviatoric horizontal strain relief is comparable. An interesting aspect of Sample 123-766A-51R-5, 93-114 cm, (Bas 12) is that although the final maximum horizontal strain relief is relatively large and positive, for the first 2 hr from the onset of strain relief monitoring the trend was negative. As described in "Basement Stress Measurements" section (Site 765 chapter), orientations of the samples were determined from paleomagnetic measurements. Orientations of the maximum horizontal strain relief is, except for the second sample (Bas 13), comparable. However, although orientations of the maximum strain relief relative to the scribe line marked onto the sample for the last two, essentially the same, samples were 21° apart, orientations of the paleomagnetic measurements for those samples were 41° apart.

Fracture Analysis

Introduction

The major objective of this study is to address the possible relationship between preexisting fractures and present-day and/

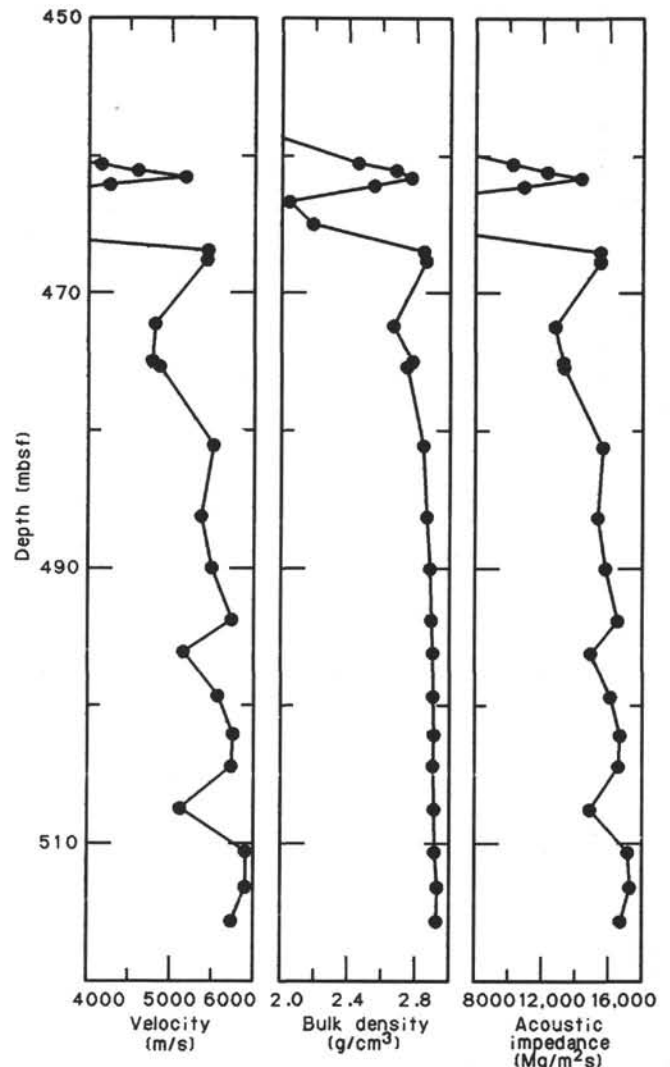


Figure 66. Compressional-wave velocity, bulk density, and acoustic impedance vs. depth of igneous rock samples from Hole 766A.

or paleo stress regime. To understand the processes associated with the formation of fractures, joints, and other extensional features, orientations of structures observed in the cores were constructed. Tracings of these features were constructed from seven cores, from 450 to 527 mbsf. These cores are marked by an abundance of through-going fractures, with dips that range from $5^\circ+$ to $80^\circ+$, although most of the fractures fell within $45^\circ+$ to $50^\circ+$ (Figs. 69 and 70). Many of these fractures were hairline cracks, filled with calcite, smectite, or pyrite (Figs. 71 through 73).

Methods

Tracing was performed on a continuous piece of clear shrink tubing wrapped around specimens that were larger than 10 cm long. The up-direction and the saw-cut line were carefully annotated on each piece. The top of the core was annotated by hole number and letter, section number, and piece number. Calcite-filled fractures were differentiated between other fractures that were open or healed with other secondary minerals (Fig. 73). Voids were outlined and appropriately annotated. Estimates of the fracture dip were determined on through-going fractures and rounded to the nearest 5° . Post-cruise processing will incorporate core-orientation data collected from paleomagnetic data.

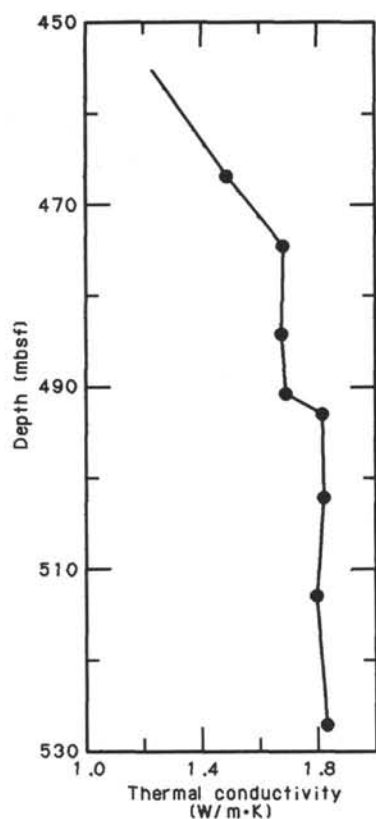


Figure 67. Thermal conductivity vs. depth of igneous rock samples from Hole 766A.

Table 19. Preliminary results of anelastic strain recovery experiments performed on basalt samples from Hole 766A.

Core, section, interval (cm)	Depth (mbsf)	Final principal strain			Orientation (degrees)	Elapsed time ^a (hr)
		H _{max} (με)	H _{min} (με)	Vert (με)		
Bas 12						
123-766A-51R-5, 93-114	487.14	147.9	-47.3	-5.2	42 ± 30	19.7
Bas 13						
-52R-2, 131-147	492.72	-6.1	-22.1	-39.3	73 ± 30	14.8
Bas 14						
-55R-6, 33-57	524.56	-22.5	-40.2	-29.8	43 ± 30	19.5
Bas 15						
-55R-6, 57-76	524.80	7.7	-7.7	-34.7	22 ± 30	19.5

^a From onset of strain relief monitoring.

Results

Most of the cracks were filled with smectite and minor amounts of pyrite. Secondary crack growth was often associated with another trend that would crosscut the preexisting trend at oblique angles (Figs. 71 and 72). Late-forming fractures were often filled with calcite; however, this was not always the case.

The dominant dip angle appears to be near 45°+ with respect to the vertical. Other populations of fractures are evenly distributed between 5°+ and 30°+, and between 65°+ and 90°+ (Figs. 69 and 70). A systematic variation in fracture orientations occurs across several sections of a single core (Fig. 70). The predominant dip angle for cracks within Core 123-766A-54R is near 45°+ above and 20°+ below Core 123-766A-54R. Within Core 123-766A-54R, cracks grow progressively steeper

(75°+ to 80°+) before their dip angle diminishes to 20°+ in Core 123-766A-55R.

The pervasive trend and occurrence of the cracks strongly suggest that the diabase is intrusive in origin. As the body of molten rock cooled and contracted, small hairline thermal contraction cracks formed within the rock's interior. If these contraction cracks are parallel to the isotherms and thus parallel to the cooling surface as would be expected, one can estimate the dip of this intrusion. In this case, the dominant dip angle may be about 45°+, suggesting that the intrusion was a dike dipping 45°+ or less. The abrupt change in dip angle of the cracks (i.e., Core 123-766A-54R) further suggests that the morphology of the intrusive body has changed with depth. This change in morphology might take on the form of a ledge or an offshoot from the main intrusive mass.

Thermal elastic stresses occurring within a cooling body are certainly a viable explanation for these observations. However, an alternate explanation takes into consideration the thermal stresses, as well as the tectonic stresses operating during the time the molten material was intruded. A superposition stress model may explain why the fractures tend to fall within three distinct trends: 20°+, 45°+, and 80°+. If the intrusion occurred either within the spreading center itself or somewhere along the hypothesized transitional crust, the stress field most likely would be extensional in nature. In this case, some of the fractures would develop along planes that dip approximately 45°+, measured with respect to vertical. Normal faults along oceanic spreading centers generally strike subparallel to the spreading axis and dip at about 45°+. Presumably, the strike of these normal faults would be perpendicular to the direction having the least principal stress. The predominant dip angle of 45°+ observed in the cores (Fig. 69) probably reflects the paleo-tectonic stress field operating at the time the basalt formed. In contrast, the cluster of fractures dipping near 20°+ and 80°+ (Fig. 70) probably represents cracks that formed in response to the thermoelastic stresses as the rock was cooling. The location of these extreme fracture angles may be dominated by geometry and size of the intruded body, not by the ambient stress field.

SCHLUMBERGER LOGS

Introduction

Hole 766A was rotary cored from the seabed to 527 mbsf. (Table 20 lists the logging-tool and curve abbreviations used here.) Seawater was used as drilling fluid, with Driscol added in 25-bbl slugs at the end of each core run to act as a sweep mud. Density of the slug was 8.9 pounds per gallon (ppg; 1.07 g/cm³). Monitoring of shale stability during coring using the Baroid capillary suction test (CST; Wilcox et al., 1984) indicated that shales would require stabilization by adding KCl before logging. On the basis of the Baroid CST, 4% KCl (12 pounds per barrel [ppb]) was added to the mud during hole conditioning. A total of 52 ppb barite was added to bring the mud weight to 10.8 ppg (1.3 g/cm³). We decided to set the base of the drill pipe at 245 mbsf to avoid problems with upper clays. From seabed to 245 mbsf, it was possible to obtain a gamma-ray spectrometry log through the drill pipe. The first logging run, using the seismic stratigraphy string (SS), encountered a bridge at 443 mbsf. After several attempts to get through this bridge, we decided to log the open-hole section and pull out of the hole. In addition, we decided that rather than run the sidewall entry sub (SES) to log past the bridge into basalts, it would be more advantageous to run pipe to total depth (TD) and to log using the geochemical logging tool (GLT) in the drill pipe. Hole 766A was then logged with the GLT from TD to the seabed (527 m). A total of 15 m of seawater was logged for statistical and chemical control. After completion of the GLT run, the litho-porosity

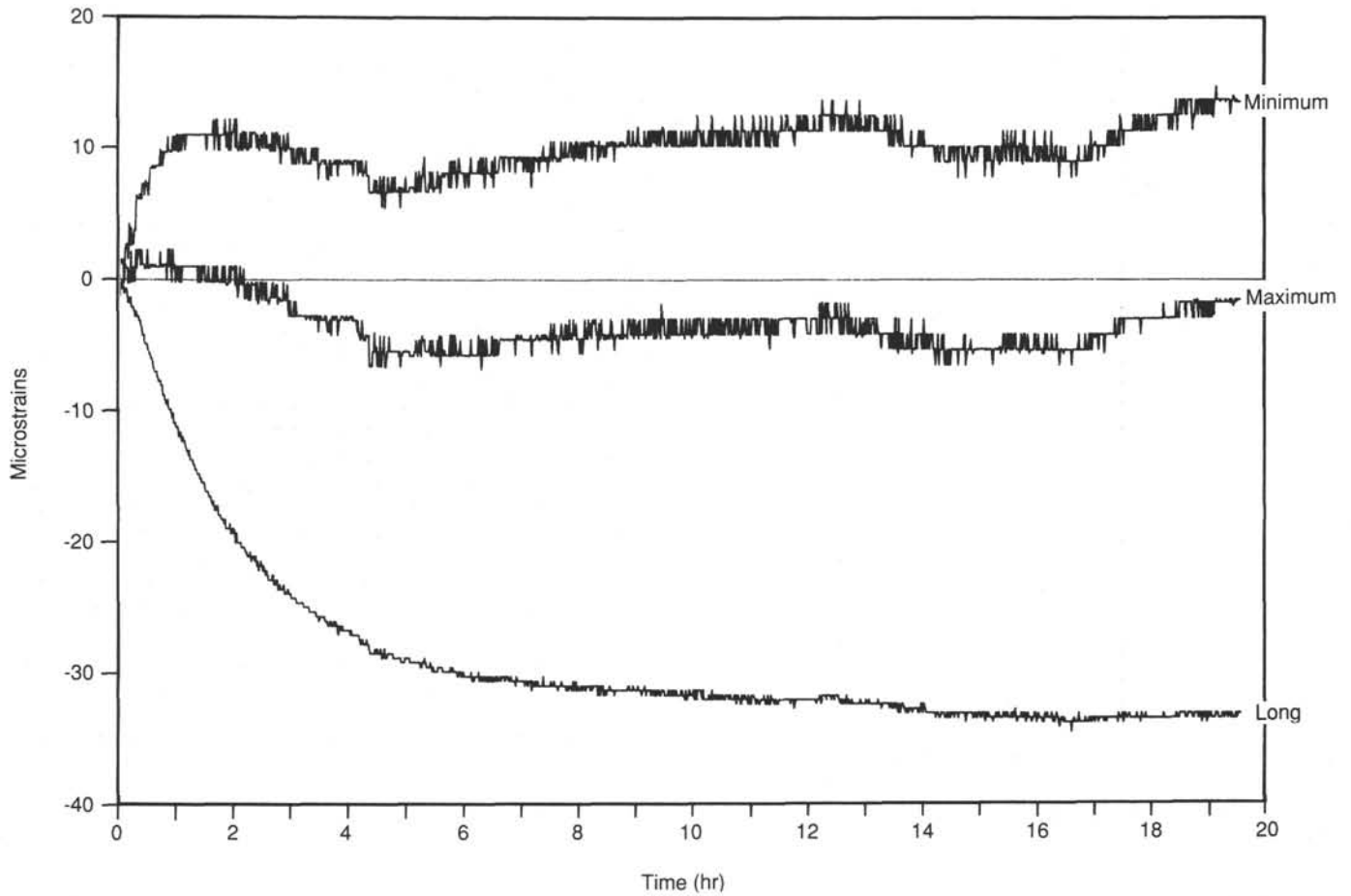


Figure 68. Strain relief curves of the maximum and minimum horizontal and vertical strains for Sample 123-766A-55R-6, 57-76 cm (Bas 15).

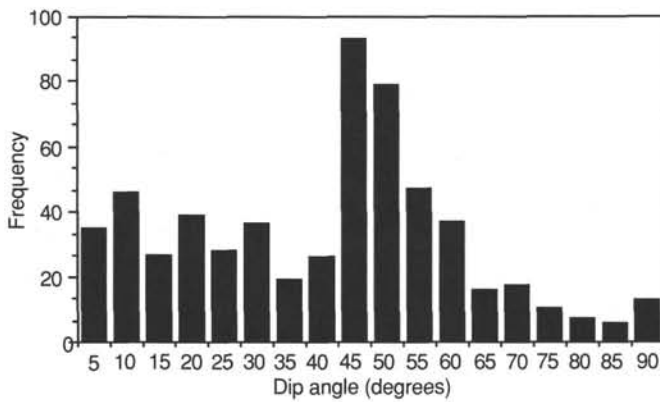


Figure 69. Plot of the number of fractures vs. fracture dip with respect to vertical. The peak at about 45°+ seems to be the predominant dip angle for this section of oceanic crust. Distribution of fractures along shallower trends is associated with a change in orientation in Core 123-766A-55R, where the fractures begin to dip below 20°+.

string (LPS) was run with the drill pipe again raised to 245 mbsf, and we attempted to reach TD. The LPS hit a bridge at 448 mbsf, and we decided to log up from this depth. Output of the litho-density tool (LDT) was disallowed on entry into drill pipe, and logging of gamma-ray spectrometry and thermal neutron porosity continued to seabed.

Coverage by various measurements is presented in Tables 21, 22, and 23. All abbreviations used in these tables are listed in Table 20.

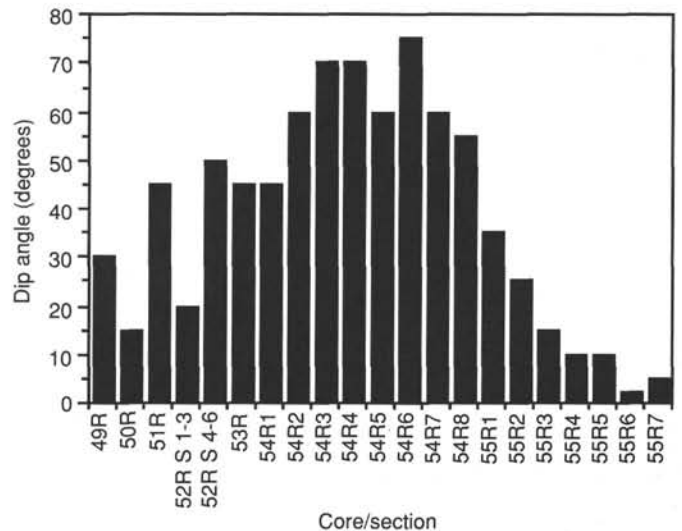


Figure 70. Plot of the distribution of fracture orientation as a function of core number. Depth may be substituted for core number, but the objective of this figure is to illustrate the abrupt change in trend within Core 123-766A-54R. Above Core 123-766A-54R, cracks dip near 45°. Within Core 123-766A-54R, the dip angle increases markedly up to 75° to 80°. Within Core 123-766A-55R, the dip angle decreases rapidly down to an average of 20°.

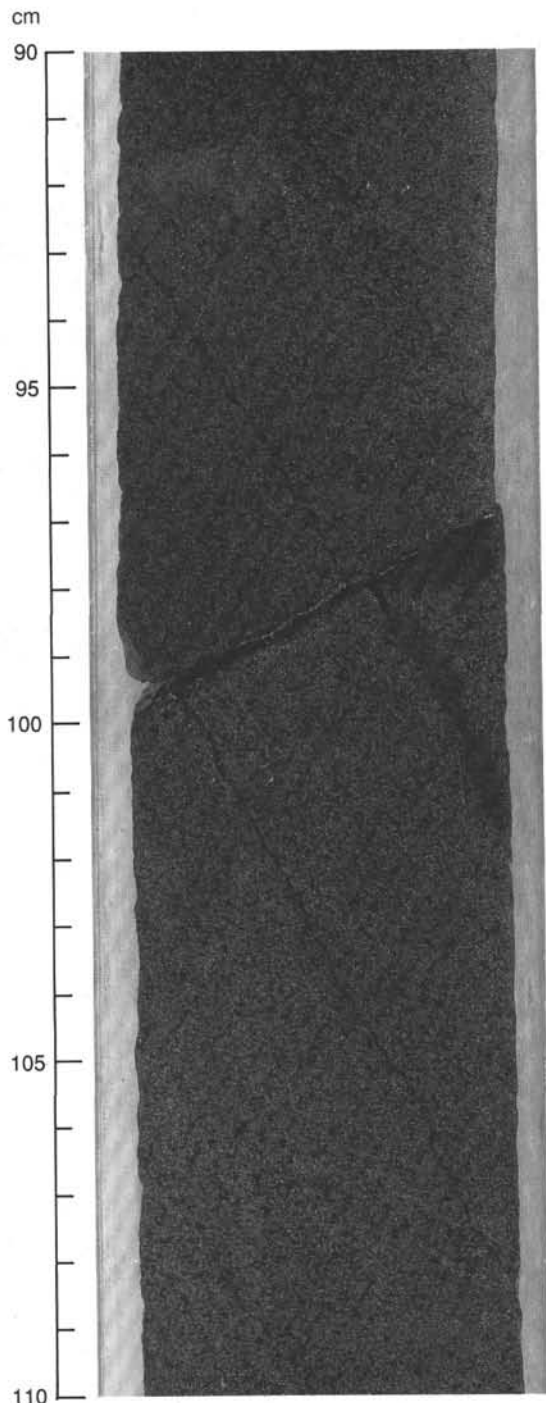


Figure 71. Close-up photograph of Section 123-766A-52R-4 at 92–110 cm. The saw cut was made so as to show the true dip angle. This particular core sample is a typical representation of the fracture dip angle and the level of calcite filling observed at this site. Note the conjugate fractures dipping about 45° .

Quality of Logs

Borehole Conditions and Caliper Measurements

Depth Matching

The tools were zeroed at the mud line using the SGR. Values of GLT depths were used as the accurate depth. Other logs were corrected to match the GLT depth. The correction to the SS log was 1.5 ft, while a distance of 8 ft was subtracted from the LPS logs. Since the logs were recorded in 6-in. intervals, correction

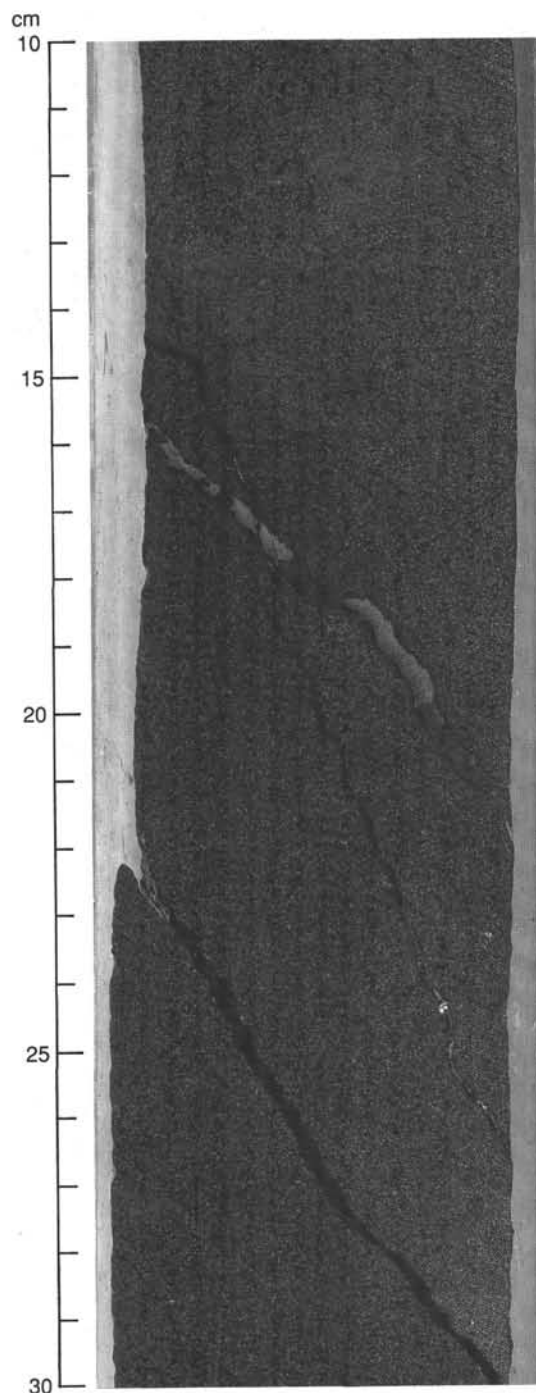


Figure 72. Close-up photograph of Section 123-766A-52R-4 at 10–30 cm. The saw cut was made so as to show the true dip angle. In some cases, fractures may have been major conduits for low-temperature hydrothermal activity. In this example, veins are filled with a combination of calcite and smectite minerals. Note the dark alteration halo that extends to the left out to 10 cm.

must be in units of 6 in. to give an exact number of samples. The values on the field tapes and prints have not been corrected. Correlation with driller's depth at the sea bed is good, and at present there is no reason to propose a core-depth to log-depth shift. This may change when core data are examined in detail.

Hole Size

The caliper tool was measuring 1.41 in. too high, according to calibration in casing on Site 765 (with a true ID of 10.88 in.

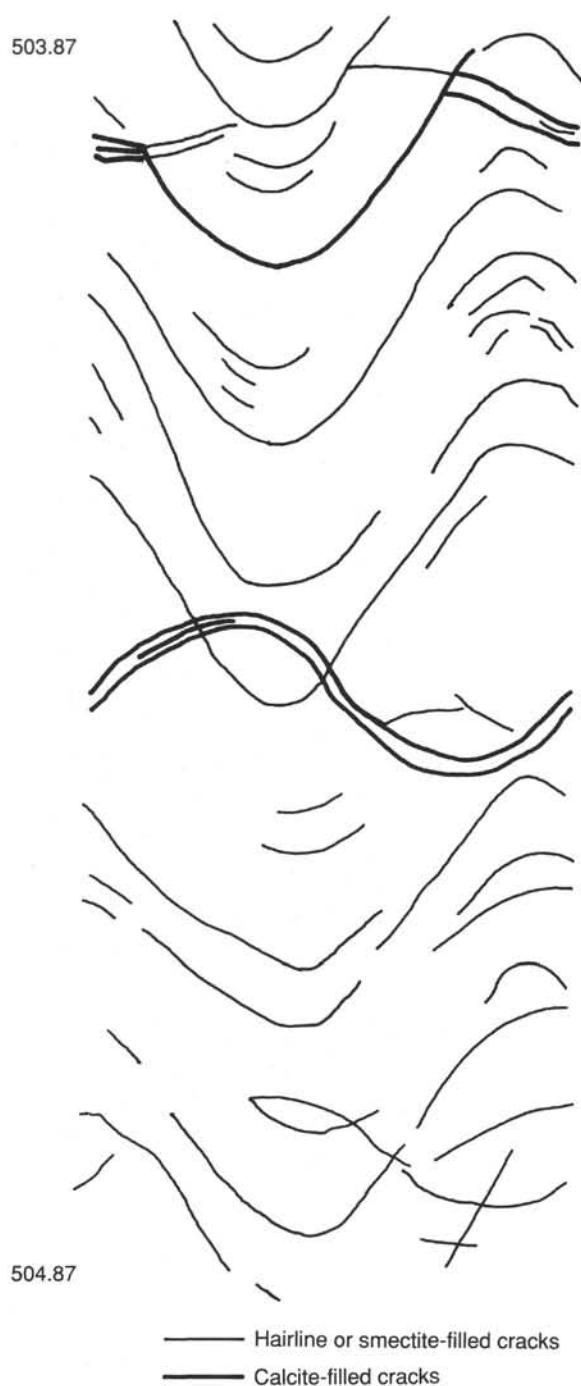


Figure 73. Digitized plot of fracture tracings from Core 123-766-A-53R-5 between 503.87-504.87 mbsf. Fractures are hairline cracks (thin lines) with minor amounts of secondary minerals and open (thick lines) calcite-filled fractures.

in 11.75 in. casing). This was corrected by the logging scientists before further log processing, but not before the CSU corrections were performed during logging. This should affect borehole corrections made for density, neutron, and gamma-ray logs. Earlier runs conducted in 10.88 in. casing at Hole 765D suggested that the response is linear, at least to this diameter. Maximum caliper extension is 15.9 in.

Nuclear Effects

Density log corrections also have been affected because the LPS does not carry a caliper tool. The only correction for hole size that can be made to these readings in real time is a static bit-size correction. For logging in Hole 766A, the static hole size used was 8 in., which means in effect that no correction for hole size was made to the bulk density (RHOB) values. This can lead to errors of up to 0.02 g/cm^3 when reading logs. The RHOB plot shown in Plate 1 (back pocket foldout) has not been corrected for hole size. The addition of KCl to the conditioning mud should affect the K readings for all the NGT runs. A correction for 4% KCl was applied in the CSU while recording the logs. On later examination, it was clear that significant overcorrection had occurred, and the K readings were negative. The CSU tapes were then re-processed after removing the KCl correction; field tapes were not corrected for KCl. A valid correction for KCl in the mud will prove difficult, but the use of XRF data from the sediments should help.

Sonic Log

The sonic log reading was checked in free drill pipe both before and after the run, where this log gave values of around $57 \mu\text{s}/\text{ft}$. The velocities that are compared with those derived from core measurements of physical properties shown in Plate 1 (back-pocket figure) are derived from reprocessed sonic data using the median slowness. The sonic values on field tapes and prints were not altered. The agreement between log values and physical-property values is generally acceptable, with a few exceptions.

Natural Gamma-Ray Spectrometry

The NGT tool was run on all the strings. A logging speed of 300 m/hr was used for the SS and LPS strings, whereas the GLT string was run at 150 m/hr. This enabled us to compare the gamma-ray spectra in both the open hole and the drill pipe. Correction for attenuation of gamma rays caused by several thicknesses of steel pipe is possible, as reported for Site 765. At the present stage of processing, the attenuation equation in the depth range 250 to 367 mbsf, where there are both open-hole and drill-pipe data, may be of the form:

$$\begin{aligned} \text{True gamma} &= 50.225 - 1.0764 (\log \text{ gamma}) \\ &+ 0.028144 (\log \text{ gamma})^2 \quad r^2 = 0.929. \end{aligned}$$

The total gamma (SGR) recorded through pipe by the NGT tool on the GLT string shows marked attenuation of tool joints occurring approximately every 10 m from 85 to 360 mbsf (Fig. 74). This is similar to the effect noted in the Site 765 summary (Hole 765C). The above equation can be considered a preliminary solution to attenuation for both tool joints and pipe in the region from 250 to 367 mbsf, but it is not valid for the drill-collar region below 367 mbsf. The SGR trace shown in Plate 1 was corrected using this equation from 250 to 367 mbsf. Further processing on shore will be necessary to remove these pipe attenuation effects. Comparison among all three spectrometer channels for three NGT runs, shows that K is affected most by drill collars and tool joints, whereas U is not severely attenuated by the steel. In the case of U , the effect of neutron activation before the LPS run is far more severe than the effect of pipe attenuation. Thorium shows both tool joint and drill collar attenuation effects.

Density Log

The DRHO (a measure of density quality) curve is largely negative, as is expected in a barite mud. Values are within ac-

Table 20. Abbreviations and terms used in site-summary and data-acquisition tables for Hole 766A.

Measurements	
CCA	GST calcium measurement
CCHL	GST chlorine measurement
CFE	GST iron measurement
CGR	Natural gamma ray-radiation minus the uranium contribution (API units)
CHY	GST hydrogen measurement
CSI	GST silica measurement
CSUL	GST sulphur measurement
DRHO	Difference between long- and short-spaced source-receiver pair response from the density tool
DTLF	Acoustic transit time (far-spacing; $\mu\text{s}/\text{ft}$)
DTLN	Acoustic transit time (near-spacing; $\mu\text{s}/\text{ft}$)
ENPH	Epithermal neutron porosity (free hydrogen index)
HD	Hole diameter from the mechanical caliper (in.)
IDPH	Deep induction resistivity (ohmm)
IHV	Integrated hole volume (in. ³)
IIR	GST iron indicator ratio
IMPH	Medium depth induction resistivity (ohmm)
ITT	Integrated transit time (ms)
LIR	GST lithology indicator ratio
NPHI	Thermal neutron porosity (total, including bound hydrogen index)
PEF	Photoelectric factor (barns/electron)
PIR	GST porosity indicator ratio
POTA	Potassium content from gamma-ray spectrometry
RHOB	Bulk density (g/cm^3)
SFLU	Spherically focused induction resistivity (shallow depth; ohmm)
SGR	Total natural gamma-ray radiation (0.2 to 3.0 MeV; API units)
SIR	GST salinity indicator ratio
THOR	Thorium content from gamma-ray spectrometry (ppm)
URAN	Uranium content from gamma-ray spectrometry (ppm)
Quality	
G	Good quality
M	Moderate quality
P	Poor quality
A	Attenuated (in pipe)

Table 21. Quality of data acquired using the seismic stratigraphy string in Hole 766A.

Depth (mbsf)	Sonic			Resistivity			Gamma-ray spectrometry					Hole geometry	
	DTLF	DTLN	ITT	IDPH	IMPH	SFLU	SGR	CGR	POTA	THOR	URAN	HD	IHV
245 to 448 (open hole)	M	M	M	G	G	P	G	G	G	G	G	G	G

Note: See Table 20 for explanation of terms.

Table 22. Quality of data acquired using the litho-porosity string in Hole 766A.

Depth (mbsf)	Compensated neutron		Litho-density			Gamma-ray spectrometry				
	ENPH	NPHI	RHOB	DRHO	PEF	SGR	CGR	POTA	THOR	URAN
0 to 245 (in pipe)		AM				AM	AM	AM	AM	AM
245 to 448 (open hole)	G	G	M	M	M	M	M	G	M	G

Note: See Table 20 for explanation of terms.

Table 23. Quality of data acquired using the geochemical string in Hole 766A.

Depth (mbsf)	Geochemical										Gamma-ray spectrometry				
	LIR	SIR	PIR	CSUL	CFE	CCHL	CHY	CCA	CSI	ALU	SGR	CGR	POTA	THOR	URAN
0 to 511 (in pipe)	AG	AG	AG	AG	AG	AG	AG	AG	AG	AG	AG	AG	AG	AG	AG

Note: See Table 20 for explanation of terms.

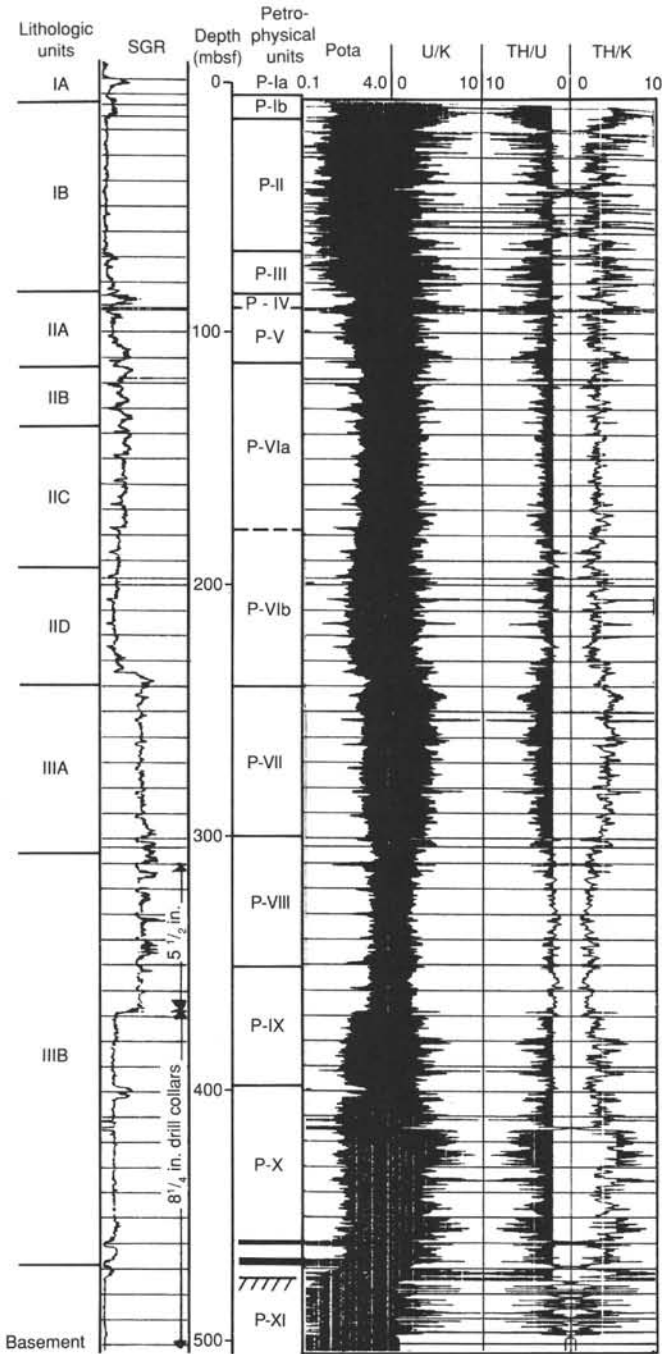


Figure 74. Hole 766A petrophysical unit subdivisions and correlation with lithostratigraphic units.

ceptable limits down to 425 mbsf, where hole size increases to the point that DRHO values indicate a density log of poor quality. This can be seen in Plate 1, where the log bulk-density curve deviates markedly from the physical-property values below 425 mbsf.

Photoelectric Factor (PEF)

The use of 11% barite in Hole 766A probably affected PEF values. Correction will be necessary at shore-based laboratories.

Neutron Logs

Thermal neutron porosity values (NPHI) recorded by the neutron porosity (CNT-G) tool exhibit good agreement with

physical-property values in Hole 766A, as can be seen in Plate 1. Epithermal neutron porosity values are higher than thermal neutron values (from 2 to 40 porosity units).

Both types of neutron values should be corrected for hole rugosity using the corrected caliper from the SS string before being used further.

Resistivity Logs

Hole conditions were not optimal for induction logging. The ratio of mud filtrate resistivity to formation fluid resistivity (R_{mf}/R_w) was about 1.0; the drilling fluid was seawater. The spherically focused induction resistivity log (SFLU) did not produce reliable results.

The deep and medium induction resistivities (IDPH and IMPH, respectively) tracked well with no apparent quality problems.

Elemental Analyses

Estimates of elemental concentrations from the GLT will require further processing at shore-based laboratories before reliable values can be presented.

Results

Results of the various logging runs (apart from the GLT elemental concentrations) can be seen in Plate 1. A proposed subdivision into 11 petrophysical units is presented in Figure 74. Note that at this stage, the subdivisions are based only on visual inspection of the traces. Later, quantitative subdivision will be based on multivariate statistical and syntactic analyses (Griffiths, 1988). The units are described below.

Subunit P-Ia (0–7.0 mbsf)

This unit is characterized by a high gamma-ray peak. These high gamma-ray values are caused by an increase in U just below the seabed.

Subunit P-Ib (7.0–15.5 mbsf)

This unit has a higher gamma-ray value than Unit P-II, but in this case was caused by an increase in Th values rather than U, as can be seen in Plate 1. This subunit has a high Th/U ratio.

Unit P-II (15.5–68.5 mbsf)

Low K values and high-amplitude variations in the spectrometer values within this unit differentiate it from those above and below. The U/K, Th/U, and Th/K ratios all vary from 0 to 8 within this unit.

Unit P-III (68.5–84.5 mbsf)

K and Th values decrease steadily upward in Unit P-III, but only increase over a short distance at the boundary with Unit P-II.

Unit P-IV (84.5–89.0 mbsf)

This unit is dominated by Th and K peaks, which give a pronounced total increase in gamma rays.

Unit P-V (89.0–111.0 mbsf)

Unit P-V also is characterized by a steady upward decrease in K. Th values remain constant. Units P-III and P-V perhaps might be seen as part of a continuous process interrupted by Unit P-IV, or as two cyclic processes, each starting with high K and Th values and decreasing upward.

Subunit P-VIa (111.0–177.0 mbsf)

Having higher K and Th values, this subunit corresponds roughly to magnetic susceptibility Subunit S-2b, with its high-amplitude, high-frequency variation in magnetic susceptibility. However, gamma-ray spectrometer data do not vary as much as

in the overlying units, and the subunit is characterized by rather low-amplitude variation. The lithostratigraphic subunits recorded over this interval are Subunits IIB and IIC. Subunit IIB is a zeolitic calcareous ooze and clay with thin carbonates, whereas Subunit 2C is a bioturbated zeolitic nannofossil ooze with chalk. The increase in K and Th possibly reflects either an increase in clay volume or change in clay type.

Subunit P-VIb (177.0–234.7 mbsf)

This subunit is marked by a slight decrease in K and Th and an increase in U at the top of the unit. There is a decrease in the Th/K ratio, whereas the U/K and Th/U ratios are not markedly different from those of Subunit P-VIa.

Unit P-VII (234.7–300.0 mbsf)

A marked change occurs from Unit P-VI to Unit P-VII. Total gamma rays increase from around 20 to 40 API units. This increase mainly results from an increase in K and Th. Th increases relative to both K and U in this unit, which corresponds to lithostratigraphic Subunit IIIA (comprising claystones with disseminated glauconite and radiolarians), and magnetic susceptibility Unit S-4 with very low susceptibility. The magnetic susceptibility of this unit is similar to that of the overlying magnetic susceptibility Unit S-3, separated by a high susceptibility sand. Although there is a marked shift in total gamma activity at the boundary between Subunit P-VIb and Unit P-VII, the Th/U and Th/K ratios are more similar to those of Subunit P-VIb than those of the underlying Unit P-VIII. As can be seen in Plate 1, there is a marked change in resistivity, velocity, bulk density, and neutron porosity at 300 mbsf.

Unit P-VIII (300.0–348.5 mbsf)

In Unit P-VIII, the K and U values have increased relative to Th, and K has increased relative to U. The Th/U values decline below 2.0 for much of this unit, in contrast to most of the rest of the section. The epithermal neutron values are near those of the thermal neutron values (at around 50%) throughout the unit. Bulk density increases to 2.0 g/cm³, and velocity varies from 1900 to 2400 m/s with high-amplitude, low-frequency oscillations. Resistivity in this unit is the highest in the logged section. Unit P-VIII corresponds to the top of magnetic susceptibility Unit S-5, which also has high susceptibilities and large amplitude oscillations. Core recovery in this unit was poor (5% to 41%).

Unit P-IX (348.5–396.5 mbsf)

Unit P-IX is influenced by the boundary between drill collars and drill pipe at 368 mbsf. The change in pipe attenuation characteristics at this boundary dominates the GLT gamma-ray spectrometry (which is otherwise the most precise because of the low logging speed). The logs obtained from the SS and litho-porosity strings, however, show that Unit P-IX is a gradational unit characterized by an upward increase in velocity, resistivity, and bulk density. Neutron porosity decreases upward. The top of the unit is marked by a high-resistivity, high-velocity peak from 348.5 to 350 mbsf. The base of Unit P-IX also corresponds approximately to the base of the high magnetic susceptibility Unit S-5 and the change from the moderate-to-low susceptibility underlying Unit S-6.

Unit P-X (396.5–459.2 mbsf; last occurrence possibly 478.0 mbsf)

This unit is characterized by more stable resistivity and velocity values. The K, Th, and U values are difficult to estimate reliably before reprocessing on shore to remove the collar attenuation effects. The top 15 m of the unit may be gradational, with similar velocity characteristics to that of the overlying Unit P-

IX. Unit P-X corresponds to magnetic susceptibility Unit S-6, and the shape of the spectrometer ratio curves matches the variation in magnetic susceptibility within this unit. Higher susceptibility may be associated with increased Th/K and Th/U ratios in this particular unit. Such a correspondence is not apparent elsewhere in the section.

Unit P-XI (459.2–461.7 mbsf; 466.5–469.5 mbsf; possibly 471.5–475.0 mbsf, 478.0–500 mbsf; end of log coverage)

This unit corresponds to the occurrence of basic igneous rock, which is intercalated with Unit P-X (sediment) signatures at least twice before the main body of basalt (see Fig. 74 and Pl. 1). The gamma-ray spectrometer signature is one of low Th/U, U/K, and Th/K ratios. Total gamma rays and K are low (below 0.1 wt% K and about 6 API [attenuated values in drill collars]). The K values oscillate with high frequency within Unit P-XI, possibly indicating fracturing without the alteration that led to much broader high-K zones at Site 765.

General Comments

The most prominent changes in the petrophysical signatures within the section occur at 15.5 mbsf (upward increase in total gamma-ray activity), 84.5 mbsf (pronounced upward decrease in K), 234.7 mbsf (pronounced upward decrease in total gamma-ray activity), 300 mbsf (upward decrease in velocity and resistivity, increase in Th), 459.2 mbsf (pronounced upward increase in K, Th, and U, and their ratios). These events appear to correspond to chronostratigraphic events as follows:

1. 15.5 mbsf—Eocene/Pliocene boundary;
2. 84.5 mbsf—K/T boundary;
3. 234.7 mbsf—Aptian/Barremian boundary;
4. 300 mbsf—Barremian/Hauterivian boundary;
5. 459.2 mbsf—Sediment/basalt interface.

SEISMIC STRATIGRAPHY

Site Selection

The location of Site 766, originally designated as Site EP2A, was proposed in a revision of ODP Proposal 121B that was submitted to the JOIDES Planning Committee in May 1986 (von Rad et al., 1986). The site was developed following two successful site-survey cruises (Legs 55 and 56) conducted aboard the Australian Bureau of Mineral Resources (BMR) research vessel *Rig Seismic* during March through May 1986. Parts of these two cruises were devoted to the search for specific sites without safety hazards on the Exmouth Plateau and Argo Abyssal Plain. During Leg 55 (10 March through 10 April 1986) 1150 km of multifold seismic data were collected, mainly as seven regional lines along the western margin of the Exmouth Plateau (Lines 55/2, 4, 5, 6, 7, 8, and 9; Fig. 75). In addition, a detailed multifold site survey was performed for Site EP2, located at the foot of the southwestern escarpment of the Exmouth Plateau (Fig. 75). Further details of this cruise are presented in a BMR cruise report (Exon and Williamson, 1988).

The 94-km site survey grid covers a 5 to 10 km area around the EP2 site area (Fig. 2). It consists of the western end of Line 55/2 plus several short segments designated Lines 55/3A, 3B, 3C, 3D, and 3E (Fig. 2). To the east, Line 55/3E becomes regional Line 55/4. Bathymetrically, the area slopes gently to the southwest, with water depths of about 4000 m (Fig. 2). The seabed is gently terraced, with each step downward probably representing progressive erosion of the sediments, perhaps by boundary currents along the plateau slope (Figs. 2 and 3).

Seismic data in the site area reveal a layered sedimentary section overlying a high-amplitude reflection that was designated as reflector Red (Fig. 3). Two other prominent reflections were

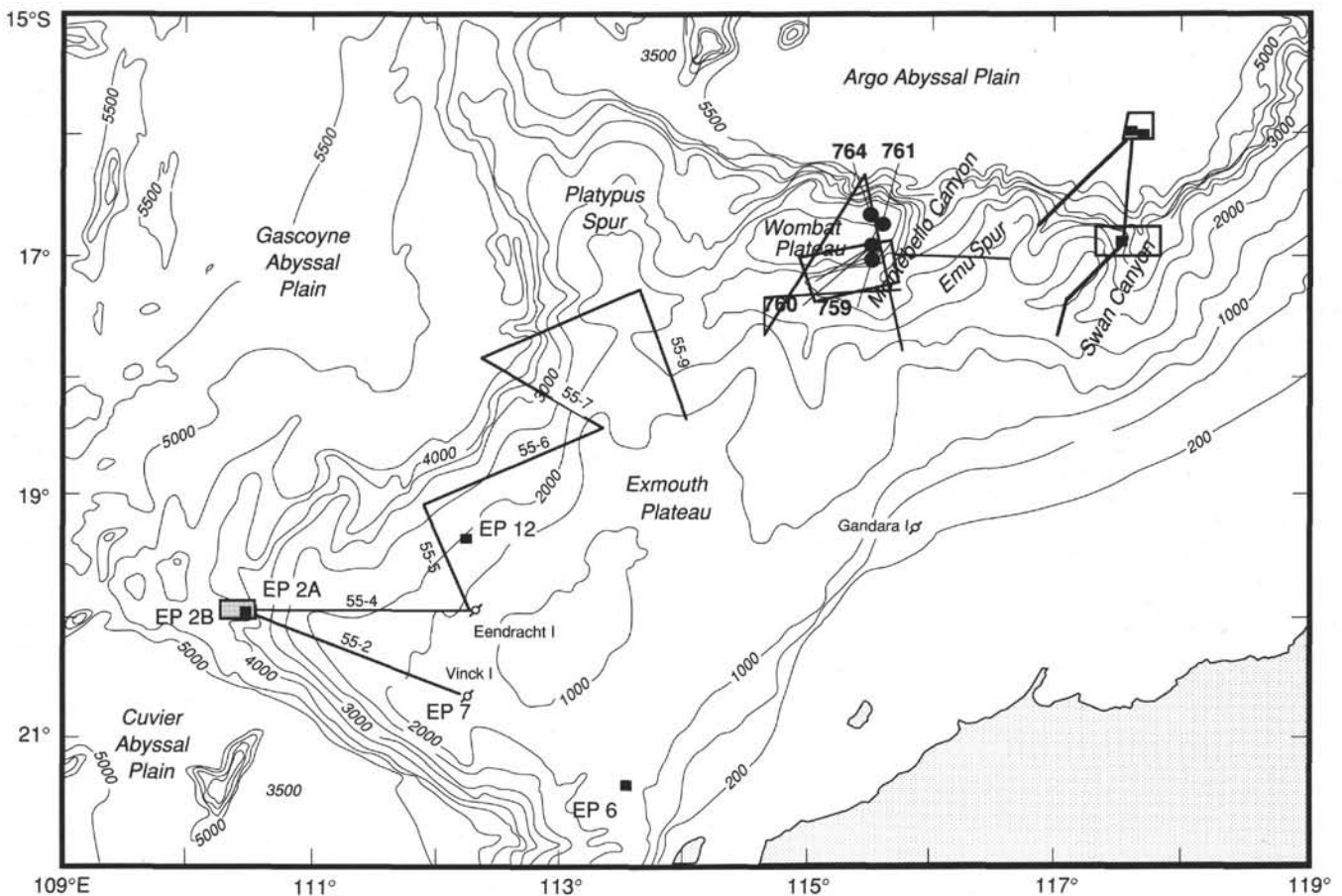


Figure 75. Bathymetric map of Exmouth Plateau showing location of EP2 site area and regional Lines 55/2 and 55/4, along with other site-survey data collected during BMR *Rig Seismic* cruises 55 and 56 in 1986 (from Exon and Williamson, 1988).

designated as reflectors Blue and Green. Based on ties with wells on the Exmouth Plateau and tentative correlations along Lines 55/2 and 55/4, a preliminary interpretation of the shipboard monitor records by the site proponents suggested the following assignment of tectonic and stratigraphic correlations (Fig. 4, von Rad et al., 1986a, 1986b, 1988).

1. Green—top Barrow Group; top late-rift phase or early post-breakup phase deposition; top Neocomian overlain by Upper Cretaceous,
2. Blue—top Dingo Claystone equivalent; top early-rift phase; Upper Jurassic overlain by Lower Cretaceous,
3. Red—top Triassic rift-onset unconformity, as recognized on the Rankin Trend beneath the shelf; upper Triassic overlain by Lower to Upper Jurassic or younger.

A higher block to the west was postulated to be underlain by volcanic basement (Fig. 4). A preliminary isopach map of the post-reflection Red sedimentary section (in two-way traveltime) (Fig. 76A) shows that the section thins to the west by both depositional onlap onto reflector Red as well as erosion along the seafloor (Figs. 3, 4, to 76). A structure map (in two-way traveltime) on reflector Red indicates a broad syncline that plunges gently to the south and generally trends parallel to the foot of the plateau slope (Fig. 76B). The lower unit (Red to Blue) pinches out to the west along the faulted surface of reflector Red (Figs. 4 and 76B). The thickest section follows this synclinal trend (Fig. 76A).

Subsequent analysis of seismic data by the site's proponents suggested alternative (younger) ages for the sequences at the proposed site (indicated in parentheses in Fig. 4). A younger age for the section, mainly Lower Cretaceous, also was suggested by the Leg 123 Shipboard Scientific Party before drilling. This was based on analysis of the available seismic data, drilling results from Site 765, the regional setting, and the inferred age of initial rifting and opening of the adjacent ocean basins. In addition, the newly processed seismic data at the site showed that reflector Red was acoustic basement (probably volcanic) throughout the area, as no obvious reflections were observed below this reflector. Furthermore, the overlying sedimentary section was believed to be considerably thinner than originally estimated, perhaps about 500 m thick.

The primary objectives of drilling in this small rift basin perched along the western flank of the Exmouth Plateau near the continent/ocean boundary are aimed at resolving questions concerning the early rifting history of passive continental margins (von Rad et al., 1986, 1988). Specifically, the site was designed to test subsidence and stretching models for rift and subsequent continental margin evolution, leading to marginal plateau formation. Here, presumably pre-rift, rift-phase, and post-breakup sedimentary sections that represent an evolution from nonmarine to deep marine are accessible to ODP drilling (Fig. 4). The establishment of paleowater depths and environments should allow scientists to construct definitive subsidence curves and to test various models for margin evolution. Understanding the exact nature and age of this thinned, presumably intruded, transi-

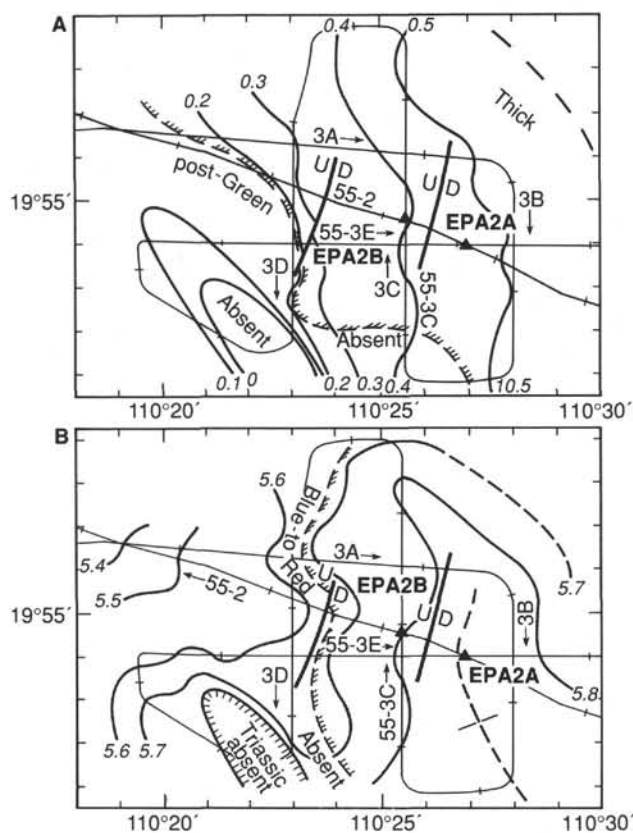


Figure 76. A. Isopach map (in two-way traveltime) of sedimentary section between reflector Red and seafloor. Post-Green section absent west of hatched line because of erosion at seafloor. B. Structure contour map (in two-way traveltime) of reflector Red section between reflectors Red and Blue, absent west of hatched line because of onlap onto acoustic basement (modified from von Rad et al., 1986a, 1986b).

tional crust formed exactly at the ocean/continent boundary is another important objective.

The primary site was EP2A (von Rad et al., 1986a, 1986b, 1988), which subsequently became Site 766 drilled during Leg 123.

Site Approach

Site 766 was approached by intersecting BMR multifold site-survey Line 55/3-4 and then paralleling it to the west (Fig. 2) (*JOIDES Resolution* Line 2). During the approach, singlefold seismic data were collected. The monitor record displayed on the Raytheon recorder (Fig. 77) was used to compare these data with the multifold seismic line data (Fig. 78) for the final site selection. The beacon was dropped at 1241 hr local time on 19 October 1988, when the final site was located on the second erosional bench (Fig. 77) (approximately 75/0833 on BMR Line 55/3E; Fig. 78). This site was chosen to optimize the thickness of sediments overlying reflector Red, which is located near the intersection with Line 55/2 and 55/3B and near the originally designated site EP2A (Fig. 2). The final position of the site, determined by averaging numerous satellite fixes after site occupation was 19°55.925'S and 110°27.243'E.

Data Base

A preliminary seismic stratigraphic framework for Site 766 was established using the grid of multifold seismic data collected during the BMR cruise described above (Fig. 2). The lines have been fully processed. Recording parameters, the processing

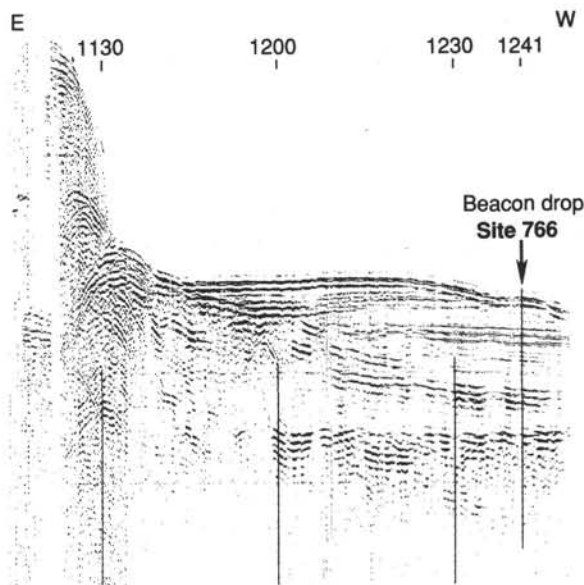


Figure 77. Shipboard monitor record of seismic line collected during approach to Site 766 (located at beacon drop 12417).

sequence, and the display parameters for these lines are summarized in Table 24. The final sections presented here (Figs. 78 and 79) are displayed with automatic gain control (AGC) applied.

Seismic Sequences

The sedimentary section overlying basement was subdivided into five seismic sequences at the site area (Figs. 78 and 79). Each of the five sequences are numbered from top to bottom and described briefly below.

Sequence 1

Sequence 1 represents all of the upper part of the sedimentary section lying above the prominent, high-amplitude reflection previously designated as reflector Green (5.465 s at Site 766, Fig. 79). This lower boundary extends across most of the area, but is truncated at the seafloor to the west. It is a prominent unconformity characterized by onlap above and truncation below (Fig. 78). The upper boundary of the sequence is the eroded seafloor. The sequence consists of alternating, continuous to discontinuous, high- to low-amplitude reflections. Two prominent high-amplitude, continuous reflections characterize the sequence north and east of the site. Several irregular and disconformable surfaces occur within the sequence and probably represent additional unconformities, but they could be mapped only locally.

Sequence 2

Sequence 2 extends from 5.465 to 5.530 s at Site 766 (Fig. 79). Internally, this sequence is characterized by moderately continuous, high- to low-amplitude reflections. Its lower boundary also is a prominent unconformity characterized by onlap above and truncation below. The sequence outcrops to the west along the seafloor.

Sequence 3

Sequence 3 is a complex, composite sequence consisting of three subsequences (A, B, and C), each separated by local unconformities. The sequence extends from 5.530 to 5.640 s at Site 766 (Fig. 79) and is characterized by alternating high- and low-amplitude, moderately continuous reflections. Two higher-amplitude reflections mark the unconformities between the subse-

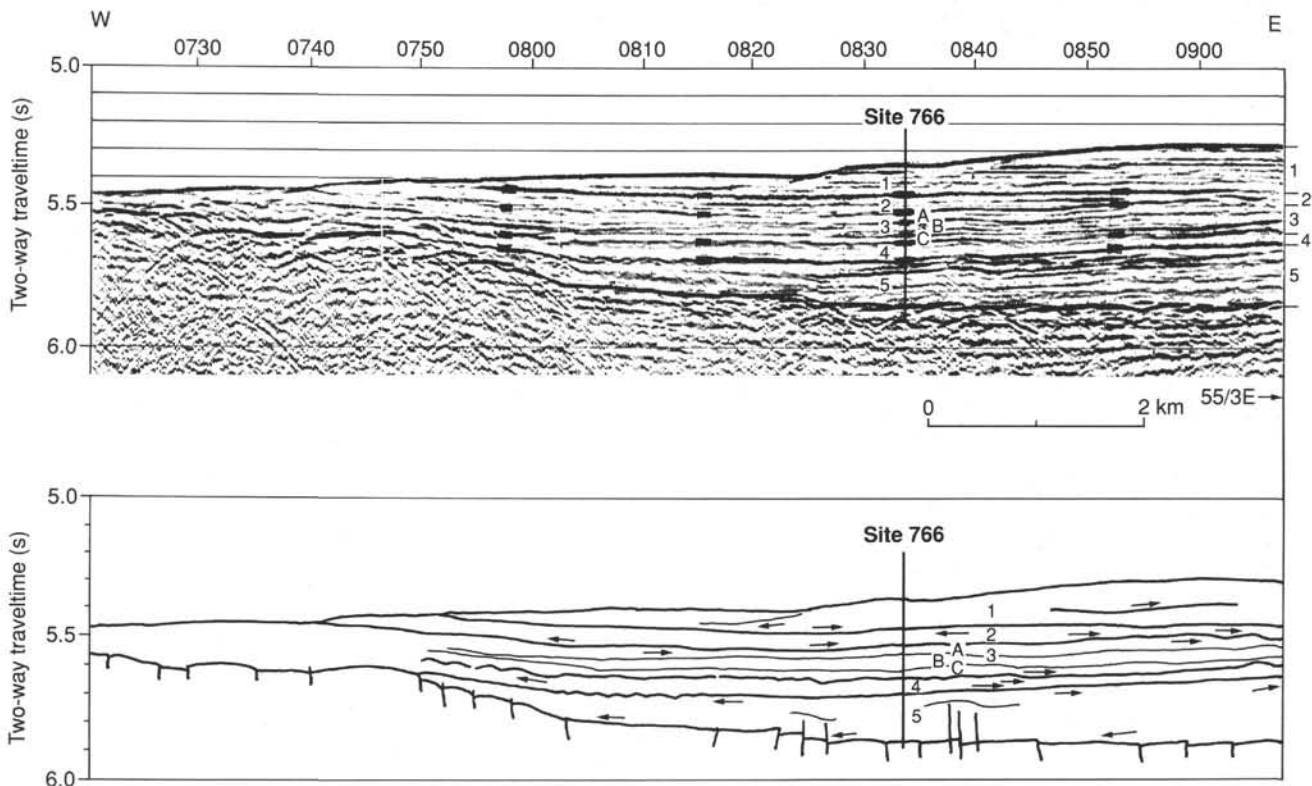


Figure 78. BMR seismic Line 55/3E with interpreted line drawing showing location of Site 766 and seismic sequences mapped in the area. Arrows denote unconformable relationships at sequence boundaries (onlap and truncation).

Table 24. Recording parameters, processing sequences, and display parameters for BMR multifold seismic Lines 55/2 and 55/3 in the EP2A site area.^a

Recording parameters			
Vessel:	<i>Rig Seismic</i>	Date recorded:	March 1985
Ship speed:	5.5 kt	Shot interval:	50 m
Source:	1 × 8.1 × 1.6 L guns	Source depth:	8 m
Group length:	50 m	Nominal cable depth:	10 m
No. of traces:	48	Leading trace:	1
CDP spacing:	25 m	Coverage:	24-fold
Near offset:	247 m	Maximum offset:	2597 m
Sample rate:	2 ms	Record length:	7500 ms
Processing sequence			
1. Geometry defined			
2. Reformat to disk internal format			
3. Resample to 4 ms			
4. Static correction applied			
5. F-K shot records			
6. Velocity analysis			
7. Spike edit			
8. Spherical divergence correction			
9. Spike deconvolution 100-point operator			
10. Normal moveout correction			
11. Inside trace mute to attenuate multiple			
12. Stack, 24-fold			
13. Predictive deconvolution 50-point operator			
14. Time-gated bandpass filter:			
WB to WB + 1500 ms 15–60 Hz			
WB + 3000 ms to end data 8–35 Hz			
15. AGC with 500 ms gate			
Display parameters			
Trace density:	15.7 traces/cm	Time scale:	10 cm/s
Polarity:	Normal	Display gain:	0.75
Horizontal scale:	1:39,400 (1cm = app.394m)	Display date:	December 1987

^a This seismic section was processed at the Seismic Processing Centre of the Bureau of Mineral Resources, Geology and Geophysics, Canberra, Australia, by I. Moxon and M. Swift. Copyright reserved by Commonwealth of Australia, 1987.

quences, both characterized by erosional truncation and onlap (Fig. 78). The lower boundary, only of moderate amplitude, is a prominent irregular erosion surface characterized in places by small diffraction hyperbola. The unit thins to the west over the basement high, where the subsequence boundaries appear to merge. The unit also outcrops along the seafloor to the south-west (Fig. 78).

Sequence 4

Sequence 4 extends from 5.640 to 5.690 s at Site 766 (Fig. 79). It has a uniform thickness over most of the area and is characterized by low-amplitude reflections (almost transparent). It thins and eventually pinches out against a fault block over the basement high to the west (Fig. 78). Its lower boundary is a prominent high-amplitude unconformable surface characterized by onlap above and erosional truncation below. In places, the sequence is an irregular surface characterized by diffraction hyperbola (Fig. 78). This is the reflector that was designated as Blue in the original site proposal (von Rad et al., 1986a, 1986b, 1988) (Fig. 4).

Sequence 5

Sequence 5 extends from 5.690 s down to acoustic basement at 5.850 s at Site 766 (Fig. 79). The unit has a wedge-shaped geometry, thickening to the east and south and thinning by onlap or downlap to the north and west (Fig. 78). It thins and finally pinches out to the west against the faulted basement surface (Figs. 76 and 78). At Site 766 and to the east, the sequence is characterized by a thin upper zone of continuous to discontinuous, high-amplitude reflections. These are underlain by a thicker package of moderately continuous, moderately to low-amplitude reflections. To the west as the unit thins and steps up over basement faults, it changes character to a more discontinuous,

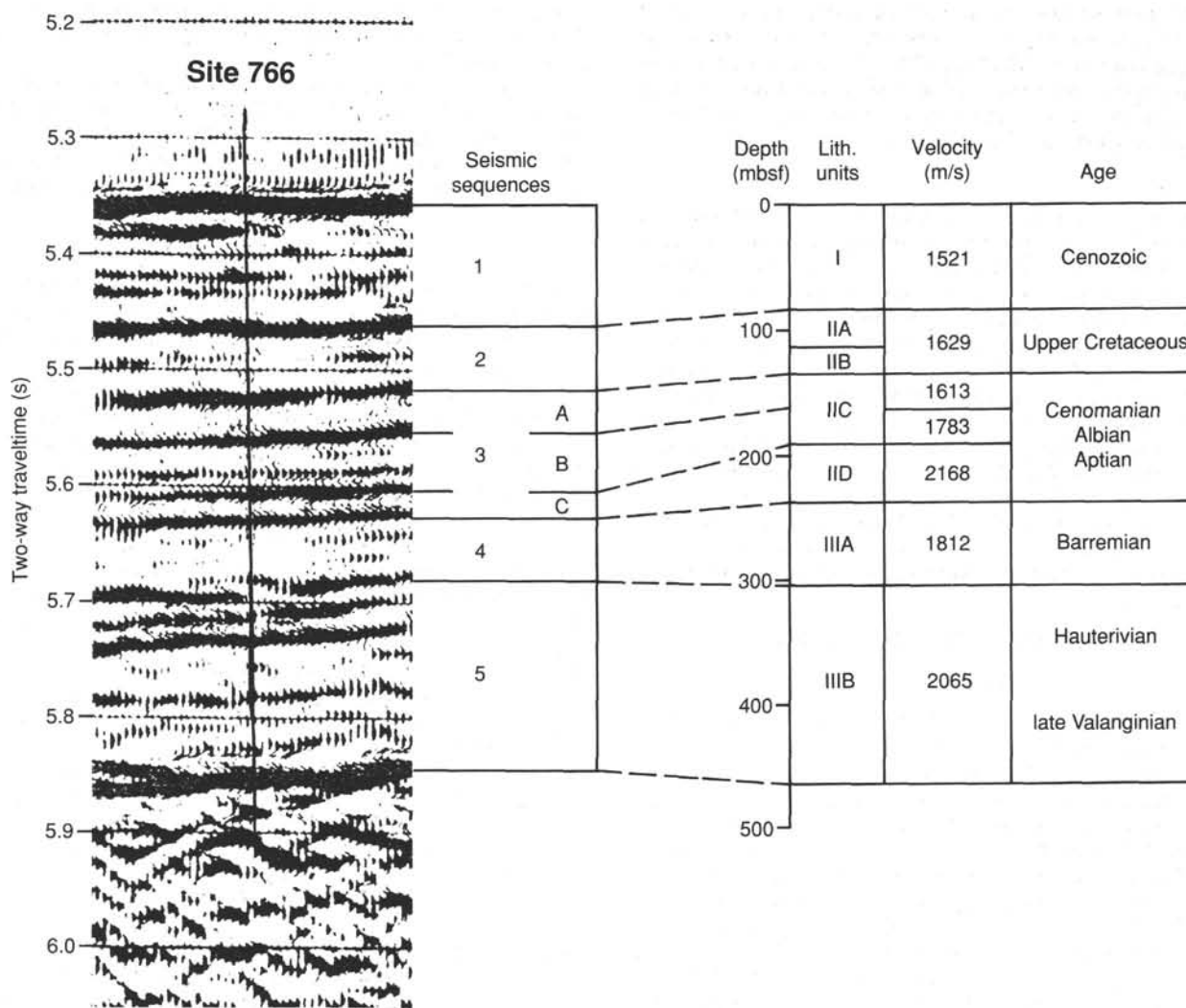


Figure 79. Portion of Line 55/3E at Site 766 showing correlation of seismic sequences with drilling results.

low-amplitude facies. This may represent disruption caused by faulting, or it may represent a real geologic facies change. In places, basement faults extend up through and offset this sequence but do not appear to cut the overlying sequences. The basal boundary or acoustic basement is equivalent to reflector Red (von Rad et al., 1986a, 1986b, 1988).

Correlation With Site 766

Using averages of the laboratory-measured *P*-wave velocities for the various lithology units (see "Sediment Physical Properties" section, this chapter), the seismic section at Site 766 can be tentatively correlated with the results of drilling. These correlations are briefly discussed below and shown in Figure 79.

Sequence 1

Sequence 1 correlates with the Cenozoic oozes of lithologic Unit I, mainly the thick lower Eocene through Paleocene section (Fig. 79). The late Cenozoic section cannot be resolved with the seismic data, but may be present in the more complete section just to the east. The lower unconformable boundary occurs approximately at the Cretaceous/Tertiary boundary, but also may correspond to the major lithology break just above in the lower Paleocene at the lithologic Unit I/IIA boundary (increase in clays and graded carbonate sequences).

Sequence 2

Sequence 2 correlates with the Upper Cretaceous section drilled at Site 766 (Fig. 79), which is equivalent to the oozes and graded carbonate sequences of lithologic Subunits IIA and IIB. The unconformity at the base of the unit correlates with the Cenomanian/Turonian boundary in Core 123-766A-15R.

Sequence 3

Sequence 3 is equivalent to the mid-Cretaceous Aptian through Cenomanian section of oozes and chalks that constitute lithologic Subunits IIC and IID. Subsequence 3A is equivalent to the upper part of lithologic Subunit IIC, while Subsequence 3B is equivalent to the lower part of lithologic Subunit IIC. The boundary unconformity may be related to a marked increase in velocity and a possible paleontology hiatus between Cores 123-766A-17R and -18R within lithologic Subunit IIC. The sequence boundary between Subsequence 3B and 3C corresponds approximately to the lithology boundary between lithologic Subunits IIC and IID.

Sequence 4

Sequence 4 correlates with the dark Barremian claystones of lithologic Subunit IIIA. Its low-amplitude seismic character fits

with this interpretation. The irregular, unconformable nature of the upper boundary suggests a major unconformity between the Aptian and Barremian. The base of the unit marks another major unconformity between the Barremian and Hauterivian at the lithology change from claystone to sandstones and siltstones (the lithologic Subunit IIIA/IIIB boundary).

Sequence 5

Sequence 5 is the lowermost unit that correlates with the thick wedge of upper Valanginian through Hauterivian sandstones and siltstones overlying and intruded by volcanic sills and dikes. The group of high-amplitude reflections at the top probably represent the more sandy upper part of the section, while the lower-amplitude section below probably represents the finer-grained, more uniform siltstones in the lower part of the section. The lateral facies change to the west above the higher fault blocks at the base of the section may represent disruption by faulting or the overlying irregular unconformity. Alternatively, it may represent a real geologic change from mass-flow deposits in the deeper parts of the rift basin to more distal or pelagic sediments on the higher blocks. The thickening to the southwest suggests a local source in that direction. Faulting that affected only this unit apparently ceased by late Hauterivian-early Barremian time.

HEAT FLOW MEASUREMENTS

Introduction

The temperature logging tool (TLT) was used successfully twice in Hole 766A. The TLT was pressure-activated at least 200 m above the seafloor (3800 mbsf), logging openhole in the sediment section and within pipe. During these two runs, the TLT was attached to the bottom of the Schlumberger seismic stratigraphy and litho-density tool combinations. Both the SS/TLT and the LD/TLT strings logged the sediment section in the open hole (448-245 mbsf) and through pipe up to the seafloor (245-0 mbsf). Two thermistors located in the tool are designed to measure both stable and short-term thermal perturbations of the hole. Both logging tools encountered an obstruction at 448 mbsf and thus were unable to log the intrusive section. Temperatures recorded should reflect the amount of heat flowing out from the basalts, because this obstruction was located near the sediment/basalt interface.

Depths in the temperature profiles shown in Figure 80 were computed from pressure data measured by the tool. The pressure-to-depth conversion assumed hydrostatic pressure using a density of 1.02 g/cm³ for seawater at about 0°C. This pressure-to-depth conversion scheme is the reason for the high-frequency noise seen in the data. These depths are strictly estimates and thus should not be used for exact depth correlations. More accurate depths will be determined when elapsed time data from the TLT is merged with elapsed time data from the Schlumberger logs.

The equilibrium thermal gradient can be determined using at least two temperature logging passes. In practice, slower and more accurate upgoing logs are used in temperature calculations.

Results

Both runs have markedly different temperature profiles. The first run, performed shortly after circulating fluid in the hole before logging, shows that the hole is nearly isothermal (Fig. 80), measuring a bottom-hole temperature of about 5.8°C at 445 mbsf, near the basement/sediment interface. About 16 hr later at the same depth, the second logging run measured a bottom-hole temperature of about 10.0°C. The apparent temperature inversion near 180 mbsf results from the TLT remaining

stationary while the telemetry tool was being repaired. This additional piece of information will constrain the equilibrium temperature profiles.

Discrete measurements of thermal conductivity taken from the core samples (see "Physical Properties" section, this chapter) will be compared to the computed thermal conductivity based on the Schlumberger geochemical/mineralogical logging information (see "Schlumberger Logging" section, this chapter).

SUMMARY AND CONCLUSIONS

ODP Site 766 is located at 19°55.925'S, 110°27.243'E, at the foot of the western escarpment of the Exmouth Plateau, in a water depth of 3997.5 m. A total of 527 mbsf was penetrated; igneous rocks were encountered at 466.7 mbsf. Average recovery for the site was 66%. All coring was performed using the rotary core barrel. Three petrophysical logs were completed at this site; in the section below 260 mbsf in open hole and through pipe for the geochemical log. A total of 8 days of operations was conducted at this site.

Biostratigraphy

Calcareous nannofossils are generally abundant and well preserved throughout the lower Pleistocene to Aptian of Hole 766A, allowing for a detailed zonation. In contrast, the Barremian to upper Valanginian interval is characterized by assemblages of low diversity and low abundance, indicating provincialism. Distinctive floras at the Valanginian/Hauterivian boundary interval exhibit close affinities to those of the Boreal Realm. The presence of temperate or cool-water assemblages in the Cenozoic is suggestive of a middle latitude position of this site. Albion to Santonian floras yield rare *Seribiscutum primitivum*, a species of high-latitude affinities.

Planktonic foraminiferal biostratigraphy was applied to the interval at 0 to 240 mbsf, which includes Holocene to Aptian zones. The succession contains many hiatuses, with a major unconformity identified within Core 123-766A-3R (17.30-26.54 mbsf; lower Eocene to Pliocene). The lower Eocene to Aptian succession is condensed, but assemblages indicative of most stages are represented. The Neogene fauna has a subtropical aspect. The Paleogene and Upper Cretaceous assemblages appear to be diverse, but generally are affected by severe dissolution. The Lower Cretaceous (Aptian-Albian) fauna is well preserved and composed mainly of small *Hedbergella*.

Benthic foraminifers in Hole 766A are mainly cosmopolitan, deep-water species, and their biostratigraphy compares well with Cenozoic and Upper Cretaceous stratigraphic schemes developed in the Atlantic Ocean. Lower Cretaceous benthic assemblages are sparse, but the presence of several cosmopolitan species allowed us to correlate them to Atlantic biostratigraphic schemes.

A complete sequence of dinoflagellate cysts is present between the Aptian and uppermost Valanginian. These assemblages are well preserved and diverse. Younger assemblages were not recovered.

Well-preserved radiolarians recovered from the topmost two cores provided useful relative age assignments in the Pleistocene and indicate a cool-water influence at this site.

Lower Cretaceous radiolarians are moderately preserved, except for the Barremian-Aptian interval, where silica-rich cherts and scattered cherts occur. In this interval, well-preserved assemblages provide relative ages and suggest open oceanic conditions from the lower Aptian onward. Barremian to Valanginian radiolarian assemblages were scarce and may represent peculiar upwelling faunas, similar to those found in radiolarite layers at Site 765.

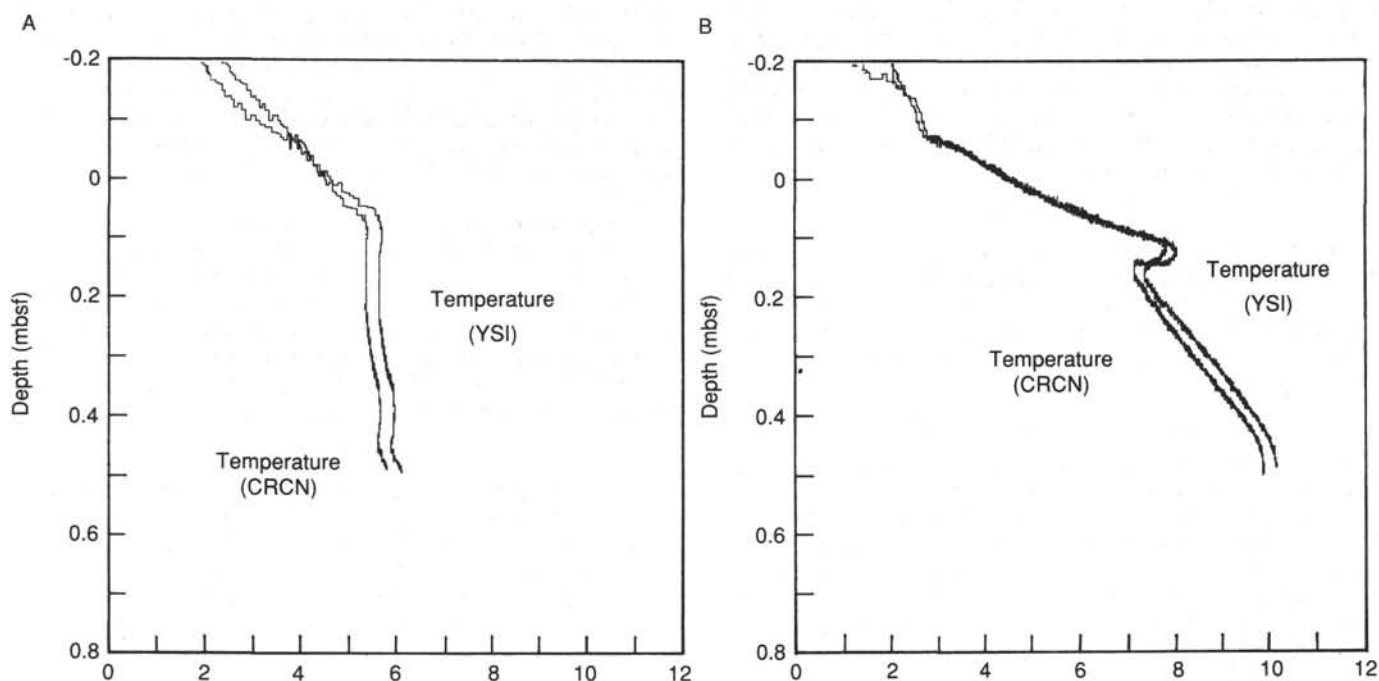


Figure 80. A. Temperature vs. depth profile of Hole 766A collected during the Schlumberger seismic stratigraphy logging run. Only the upgoing log is indicated. B. Temperature vs. depth profile of Hole 766A collected during the Schlumberger litho-density logging run. Only the upgoing log is shown.

Paleoenvironment

Colder water influence (from mid-latitudes) in the early Pleistocene at Site 766 (see "Biostratigraphy" section, this chapter) restricted the paleoceanographic environment at both sites from Berriasian/Valanginian to Barremian. Normal, oceanic conditions were established by earliest Aptian.

Sedimentology

The oldest sediment recovered at Site 766 was uppermost Valanginian siltstone, alternating with inclined basaltic intrusions. A Hauterivian to uppermost Valanginian progradational wedge is composed largely of volcanoclastic and shallow marine grains (shallow marine components, including echinoderms and bryozoans, increasing upward), originating most likely from the outer Exmouth Plateau, or possibly a conjugate block (Greater India?). The wedge is equivalent to a prominent unconformity on the western Exmouth Plateau. The sediments are dissimilar from the Barrow Group sediments underlying the unconformity at Sites 762 and 763 on the Exmouth Plateau. Intervals toward the base, interpreted as bentonites, are roughly equivalent to those bentonites observed at Site 765. Barremian claystone with abundant radiolarians is coincident with a proposed highstand of sea level and apparently signals abandonment of the progradational wedge.

A brief lower Aptian hiatus marks a drastic change in sedimentation (juvenile to mature ocean?) at Site 766. The mature ocean stage consists dominantly of nannofossil oozes and chinks. The Paleocene to lower Aptian section is heterogeneous, including siliceous sediments in the Aptian, color-banded zeolitic clays and chinks/oozes particularly in the Turonian and Cenomanian, and thin, redeposited calcareous sequences throughout. Abundant zeolitic sediments coincide with the Turonian to Cenomanian highstand of sea level. Similar sediments at the same stratigraphic position at Site 763 suggest another mechanism besides CCD fluctuations near Site 766.

The Pleistocene to upper Paleocene section consists of homogeneous nannofossil ooze, representing pelagic sedimentation above the CCD (present water depth of 4000 mbsl). Displaced basaltic and bioclastic grainstone pebbles occur locally, but their presence is problematic. No lithologic evidence was recognized for an upper Pliocene to upper Eocene hiatus, except possibly for abundant zeolite at/or near the hiatus. Pleistocene oozes contain abundant foraminifers and radiolarians.

The basal sedimentary unit at Site 766 consists of two distinct, but apparently genetically related very dark greenish gray lithologies. The first lithology is silty sandstones, sandy siltstones, and sandstones. These vary in composition, but are everywhere dominated by some combination of altered volcanoclastic grains, glauconite, quartz, and neritic carbonate bioclasts dominated by echinoderm fragments. The second lithology is claystone containing abundant dispersed silt- to sand-sized glauconite grains and radiolarians. Many of the radiolarians exist only as empty molds, others are filled with glauconite or clay.

The upper Paleocene through Pleistocene succession at Site 766 consists of nannofossil ooze. The current depth of this site is 4000 mbsl, which indicates that the CCD has been deeper than this depth in the Indian Ocean since at least the Neogene (depends on burial curve for this site).

Organic Geochemistry

A prominent feature of the calcium carbonate data is the transition from low (<20 wt%) carbonate contents in Valanginian through Barremian sediments to relatively high (>60 wt%) carbonate in Aptian cherty-limestone sediments. While the Upper Cretaceous nannofossil chinks are punctuated by some occurrences of low carbonate sediments, the carbonate content is predominantly >50 wt% in the Upper Cretaceous through Tertiary sediment record. These data reflect a transition from primarily terrigenous to pelagic sedimentation during the Aptian.

Sedimentary TOC is generally undetectable in the high carbonate sediments from the sediment surface to about 250 mbsf

(Tertiary through Aptian). TOC increases in Barremian dark green claystones to near 1 wt%, is lower in the Barremian-Hauterivian sandstone-siltstones, and increases with increasing depth in the Hauterivian-Valanginian sediments to about 1.6 wt%. Rock-Eval pyrolysis indicates that the organic matter in these "organic-rich" Barremian through Valanginian sediments is predominantly of terrestrial origin.

Igneous Rocks

A series of tholeiitic intrusions of comparable geochemistry to Site 765 basement intrude the oldest sediments recovered at Site 766. These intrusions are small sills and a moderately inclined dike. The association of deep-sea fan sediments and MORB-type magmas indicates that Site 766 was associated with final stages of rifting.

Interstitial-Water Chemistry

Changes in interstitial-water chemistry at Site 766 are less pronounced than at Site 765, mostly because of its lower organic matter content, which results in less sulfate reduction and lower alkalinity, phosphate, and ammonium concentrations. Calcium increases and magnesium decreases in an approximate 1:1 ratio with increasing sediment depth from the alteration of volcanic material and basement basalt. High silica concentrations correlate with sediment intervals having abundant and well-preserved radiolarians.

Physical Properties

The sediment physical properties at Site 766 allow one to characterize the sediments into five basic units. Unit A extends from the seafloor to 100 mbsf and consists of calcareous ooze. The changes in physical properties follow normal compaction trends for marine sediment. Unit B from 100 to 185 mbsf consists of a mixed sediment of claystone and chalk. The physical properties remain constant with depth, with the exception of the vane shear strengths, which increase significantly in the claystone and decrease in the weaker chalk. Unit C extends from 185 to 240 mbsf and is composed predominantly of chalk with hard chert layers. Significant variations are observed in the physical properties, especially the compressional-wave velocities, due to the presence of chert layers. Unit D consists of a brown to reddish brown claystone that extends from 240 to 300 mbsf. The physical properties remain relatively constant throughout this unit. Unit E extends from 300 to 459 mbsf and is composed primarily of a green to gray glauconitic siltstone and sandstone having periodic layers of highly lithified bioclastic sandstone. The presence of the lithified sandstones causes considerable variations in physical properties data, especially compressional-wave velocities. Major velocity spikes were observed at 300 mbsf and throughout the interval from 350 to 440 mbsf. The lowermost 20 m of the unit consists of a gray to black sandstone.

The physical properties of the basement rock allow one to characterize the section in terms of three basic units. Unit A is a thin basalt sill that extends from 459 to 463 mbsf. Physical properties vary considerably when going from the outside edges to the center of the unit. Compressional-wave velocities are lower than those observed in the underlying, more massive basalt structure. Unit B is a thin layer of dark shale that extends from 463 to 467 mbsf. Physical properties are essentially the same as those observed in the similar material found in the lowermost portion of the sediment column. Unit C is a thick basalt sill that extends from 467 to 527 mbsf. Its physical properties vary slightly at the surface but remain fairly constant with depth.

Petrophysical Logging

A geochemical reference for the subduction of old oceanic crust of fast spreading rates (Site 765) was successfully sampled

with nearly a complete Schlumberger suite of geochemical and petrophysical logs. This includes velocity, density, porosity, spectrometry data, and high-resolution geochemical logs. A similar suite of logs was also collected at Site 766. The resolution of these logging data was sufficient to produce independently a petrophysical/lithological section that agreed well with the available cores and filled in the gaps where core recovery was poor or incomplete.

These petrophysical logs indicated that a low K event occurred earlier in the marginal Site 766 than the abyssal Site 765. At Site 766, this low K event occurred at the K/T boundary, whereas at Site 765 it is seen at the early/middle Miocene boundary. This may result from the influence of large turbidite influxes at the deeper site. The Aptian sequence is deprived of K in both sites. Both the K/T and the Eocene/Pliocene boundaries at Site 766 are marked by an increase in Th.

Geophysics

An excellent correlation exists between seismic sequences at Site 766 and the lithologic and biostratigraphic units. The lower sandstone/siltstone unit (lithologic Subunit IIIB) has a wedge-shaped geometry that thickens to the southwest and onlaps the underlying faulted basement, suggesting a local source to the southwest. A short seismic survey just to the southwest of the site indicates that lithologic Subunit IIIB was downfaulted along the adjacent margin. The sequences drilled appear to correlate with sequences on the adjacent plateau, which can be correlated with Site 762 along BMR Line 55/4. These correlations suggest wedges of sediments that are (1) younger (late Valanginian through Hauterivian) than the distal Barrow Group drilled at Sites 762/763 and (2) possibly have as their source a local landmass.

REFERENCES

- Bé, A. W., 1977. An ecological, zoogeographic and taxonomic review of recent planktonic foraminifers. In Ramsay, A.T.S. (Ed.), *Oceanic Micropaleontology* (Vol. 1): London (Academic Press), 1-100.
- Belford, D. J., 1960. Upper Cretaceous foraminifers from the Toolong Calcilitite and Gingin chalk, western Australia. *Australia Bur. Min. Res. Geol. Geophys. Bull.*, 57:1-198.
- Bouma, A. H., 1962. *Sedimentology of Some Flysch Deposits*: Amsterdam (Elsevier).
- Bralower, T. J., 1987. Valanginian to Aptian calcareous nannofossil stratigraphy and correlation with the upper M-sequence magnetic anomalies. *Mar. Micropaleontol.*, 11:293-310.
- Bukry, D., 1981. Pacific Coast stratigraphy between Point Conception and Cabo Corrientes, Deep Sea Drilling Project Leg 63. In Yeats, R. S., Haq, B. U. et al., *Init. Repts. DSDP*, 63: Washington (U.S. Govt. Printing Office), 445-471.
- Claypool, G. A., and Kvenvolden, K. A., 1983. Methane and other hydrocarbon gases in marine sediments. *Annu. Rev. Earth Planet. Sci.*, 11:299-327.
- Dailey, D. H., 1983. Late Cretaceous and Paleocene benthic foraminifers from Deep Sea Drilling Project Site 516, Rio Grande Rise, western South Atlantic Ocean. In Barker, P. F., Carlson, R. L., Johnson, D. A., et al., *Init. Repts. DSDP*, 50: Washington (U.S. Government Printing Office), 757-782.
- Davies, G. R., 1977. Turbidites, debris sheets, and truncation structures in upper Paleozoic deep-water carbonates of the Sverdrup Basin, Arctic Archipelago. In Cook, H. E., and Enos, P. (Eds.), *Deep-Water Carbonate Environments*. Soc. Econ. Petrol. Mineral. Spec. Publ. 25:221-247.
- Espitalié, J., Madec, M., and Tissot, B., 1977. Source rock characterization method for petroleum exploration. *Proc. Offshore Technology Conf.*, 3:439-443.
- Exon, N. F., and Williamson, P. E., 1986. *Exmouth Plateau; Sedimentary Basin Framework: Rig Seismic Cruise 56 (April/May 1986)*. Bur. Miner. Resources, Canberra, internal post-cruise Rept. 57.
- _____, 1988. *Rig Seismic Research Cruises 7 and 8, Sedimentary Basin Framework of the Northern and Western Exmouth Plateau*. Australian Bur. Miner. Resources Record 1988/30, 1-62.

- Fullerton, L. G., Sager, W. W., and Handschumacher, D. W., 1989. Late Jurassic-early Cretaceous evolution of the eastern Indian Ocean adjacent to Australia. *J. Geophys. Res.*, 94(B3):2937-2955.
- Gartner, S., Jr., 1977. Calcareous nannofossil biostratigraphy and revised zonation of the Pleistocene. *Mar. Micropaleontol.*, 2:1-25.
- Geroch, S., and Nowak, W., 1984. Proposal of zonation for the late Tithonian to late Eocene, based upon arenaceous foraminifers from the outer Carpathians, Poland. *Benthos '83: 2nd Int. Symp. Benthic Foraminifers, Proc.*, 225-239.
- Gieskes, J. M., 1983. The chemistry of interstitial waters of deep-sea sediments: interpretation of Deep-Sea Drilling data. In Riley, J. P., and R. Chester (Eds.), *Chemical Oceanography* (Vol. 8): London (Academic Press), 222-269.
- Griffiths, C. M., 1988. The language of rocks: an example of the use of syntactic analysis in the interpretation of sedimentary environments from wireline logs. *Proc. Geol. Soc. (London) Pet. Gr. Mtg. on Geological Applications of Wireline Logs*.
- Habib, D., and Drugg, W. S., 1983. Dinoflagellate age of Middle Jurassic-Early Cretaceous sediments in the Blake-Bahama Basin. In Sheridan, R. E., Gradstein, F. M., et al., *Init. Repts. DSDP*, 76: Washington, (U.S. Govt. Printing Office), 623-638.
- Haig, D. W., 1979. Cretaceous foraminiferal biostratigraphy of Queensland. *Alcheringa*, 3:171-187.
- _____, 1981. Mid-Cretaceous foraminiferids from the Wahgi Valley, Central Highlands of Papua, New Guinea. *Micropaleontology*, 27: 337-351.
- Haq, B. U., Hardenbol, J., and Vail, P. R., 1987. Chronology of fluctuating sea levels since the Triassic. *Science*, 235:1156-1166.
- Hay, W. W., and Mohler, H. P., 1967. Calcareous nannoplankton from early Tertiary rocks at Point Labau, France and Paleocene-Eocene correlations. *J. Paleontol.*, 41:1505-1541.
- Helby, R., Morgan, R., and Partridge, A. D., 1987. A palynological zonation of the Australian Mesozoic. *Mem. Assoc. Australasian Paleontologists*, 4:1-94.
- Herb, R., and Scheibnerova, V., 1977. Synopsis of Cretaceous planktonic foraminifers from the Indian Ocean. In Heirtzler, J. R., Bolli, H. M., Davies, T. A., Saunders, J. B., and Sclater, J. G., *Indian Ocean Geology and Biostratigraphy*: Washington D.C. (Am. Geophys. Un.), 399-415.
- Kent, D. V., and Gradstein, F. M., 1985. A Cretaceous and Jurassic geochronology. *Geol. Soc. Am. Bull.*, 96(11):1419-1427.
- Krashennikov, V. A., 1974. Cretaceous and Paleogene planktonic foraminifers, Leg 27 of the Deep Sea Drilling Project. In Veevers, J. J., Heirtzler, J. R., et al., *Init. Repts. DSDP*, 27: Washington (U.S. Govt. Printing Office), 663-671.
- McIlreath, I. A., 1977. Accumulation of a middle Cambrian, deep-water limestone debris apron adjacent to a vertical, submarine carbonate escarpment, southern Rocky Mountains, Canada. In Cook, H. E., and Enos, P. (Eds.), *Deep-Water Carbonate Environments*. Soc. Econ. Paleont. Mineral. Spec. Publ., 25:113-124.
- Middleton, G. V., 1970. Experimental studies related to problems of flysch sedimentation. In Lajoie, J. (Ed.), *Flysch Sedimentology in North America*. Geol. Assoc. Can. Spec. Pap., 7:253-272.
- Mutter, J. C., Larson, R. L., and the Northwest Australian Study Group, 1988. Extension of the Exmouth Plateau: deep seismic reflection/retraction evidence for simple and pure shear mechanisms. *Geology*, 16.
- Okada, H., and Bukry, D., 1980. Supplementary modification and introduction of code numbers to the low-latitude coccolith biostratigraphic zonation (Bukry, 1973; 1975). *Mar. Micropaleontol.*, 5(3): 321-325.
- Okada, H., and Honjo, S., 1973. The distribution of oceanic coccolithophorids in the Pacific. *Deep Sea Res.*, 20:355-374.
- Ogg, J. G., 1987. Early Cretaceous magnetic polarity time scale and the magnetostratigraphy of Deep Sea Drilling Project Sites 603 and 534, western central Atlantic. In van Hinte, J. E., Wise, S. W., Jr., et al., *Init. Repts. DSDP*, 93: Washington (U.S. Govt. Printing Office), 849-879.
- Ogg, J. G., and Steiner, M. B., 1988. Late Jurassic and Early Cretaceous magnetic polarity time scale. *Proc. 2nd Jurassic Stratigr. Symp.*
- Playford, G., Haig, D. W., and Dettmann, M. E., 1975. A mid-Cretaceous microfossil assemblage from the Great Artesian Basin, north-western Queensland. *Neues Jahrb. Geol. Pal. Abh.*, 149:333-362.
- Perch-Nielsen, K., 1985. Cenozoic calcareous nannofossils. In Bolli, H. M., Saunders, J. B., and Perch-Nielsen, K. (Eds.), *Plankton Stratigraphy*: Cambridge (Cambridge Univ. Press), 427-554.
- Sanfilippo, A., Westberg-Smith, M. J., and Riedel, W. R., 1985. Cenozoic Radiolarians. In Bolli, H. M., Saunders, J. B., and Perch-Nielsen, K. (Eds.), *Plankton Stratigraphy*: Cambridge (Cambridge Univ. Press), 631-712.
- Schaaf, A., 1985. Un nouveau canevas biochronologique du Cretace Inferieur et moyen: les biozones a radiolaires. *Sci. Géol. Bull. Strasbourg*, 38:227-269.
- Shackleton, N. J., and Shipboard Scientific Party, 1984. Accumulation rates in Leg 74 sediments. In Moore, T. C., Jr., Rabinowitz, P. D., et al., *Init. Repts. DSDP*, 74: Washington (U.S. Govt. Printing Office), 621-637.
- Sliter, W. V., 1980. Mesozoic foraminifera and benthic environments from Deep Sea Drilling Project Sites 415 and 416, eastern North Atlantic. In Lancelot, Y., Winterer, E. L., et al., *Init. Repts. DSDP*, 50: Washington (U.S. Govt. Printing Office), 353-428.
- Tarling, D. H., 1983. *Paleomagnetism: Principles and Applications in Geology, Geophysics and Archaeology*: New York (Chapman and Hall).
- Tjalsma, R. C., and Lohmann, G. P., 1983. Paleocene to Eocene bathyal and abyssal benthic foraminifers from the Atlantic Ocean. *Micropaleontol. Spec. Publ.*, 4.
- van Morkhoven, F.P.C.M., Berggren, W. A., and Edwards, A. S., 1986. Cenozoic cosmopolitan deep-water benthic foraminifera. *Bull. Centres Rech. Explor.-Prod. Elf Aquitaine*, Mem. 11.
- Veevers, J. J. (Ed.), 1984. *Phanerozoic Earth History of Australia*: Oxford (Clarendon Press).
- von Rad, U., Haq, B. U., et al., 1990. *Proc. ODP, Init. Reports*, 122: College Station, TX (Ocean Drilling Program).
- von Rad, U., Exon, N. F., Williamson, P., and Boyd, R., 1986a. *Revision of ODP Proposal 121B (ODP Leg Exmouth Plateau-Argo Abyssal Plain, E. Indian Ocean)*. JOIDES Proposal 121B.
- _____, 1986b. *ODP Leg Off NW Australia-Argo Abyssal Plain-Exmouth Plateau*. JOIDES ODP Proposal 121B (revised May 1986).
- von Rad, U., Haq, B., Gradstein, F., Ludden, J., and O'Connell, S., 1988. *Legs 122 and 123 Scientific Prospectus, Exmouth Plateau and Argo Basin*. ODP Sci. Prospectus Nos. 22 and 23, 1-86.
- Whelan, J. K., and Hunt, J. M., 1983. C1-C7 volatile organic compounds in sediments from Deep Sea Drilling Project Legs 56 and 57, Japan Trench. In von Huene, R., Nasu, N. J., et al., *Init. Repts. DSDP*, 56,57 (Pt. 2): Washington (U.S. Govt. Printing Office), 1349-1365.
- Wilcox, R. D., Fisk, J. V., Jr., and Corbett, G. E., 1984. Filtration method characterizes dispersive properties of shales. Soc. Pet. Engrs. Pap. 13162 presented at the SPE 59th Annu. Tech. Conf., Houston.
- Yurewicz, D. A., 1977. Sedimentology of Mississippian Basin carbonates, New Mexico and West Texas—the Rancheria Formation. In Cook, H. E., and Enos, P. (Eds.), *Deep-Water Carbonate Environments*. Soc. Econ. Paleontol. Mineral. Spec. Publ., 25:203-219.

Ms 123A-105

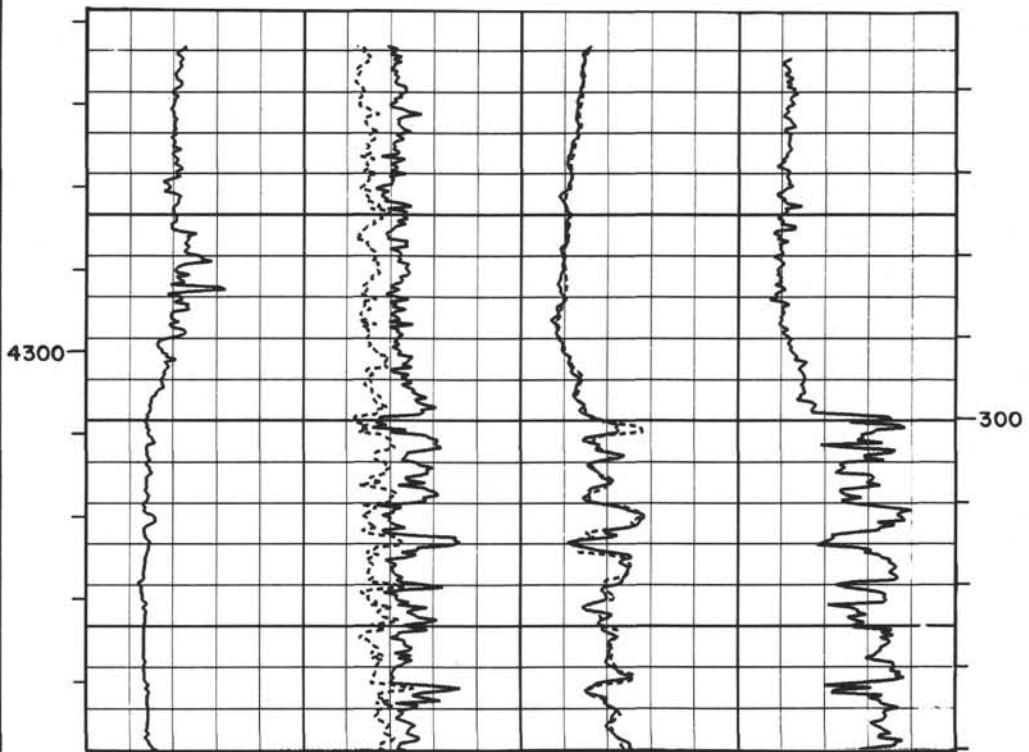
NOTE: All core description forms ("barrel sheets") and core photographs have been printed on coated paper and bound as Section 3, near the back of the book, beginning of page 355.

Summary Log for Site 766A

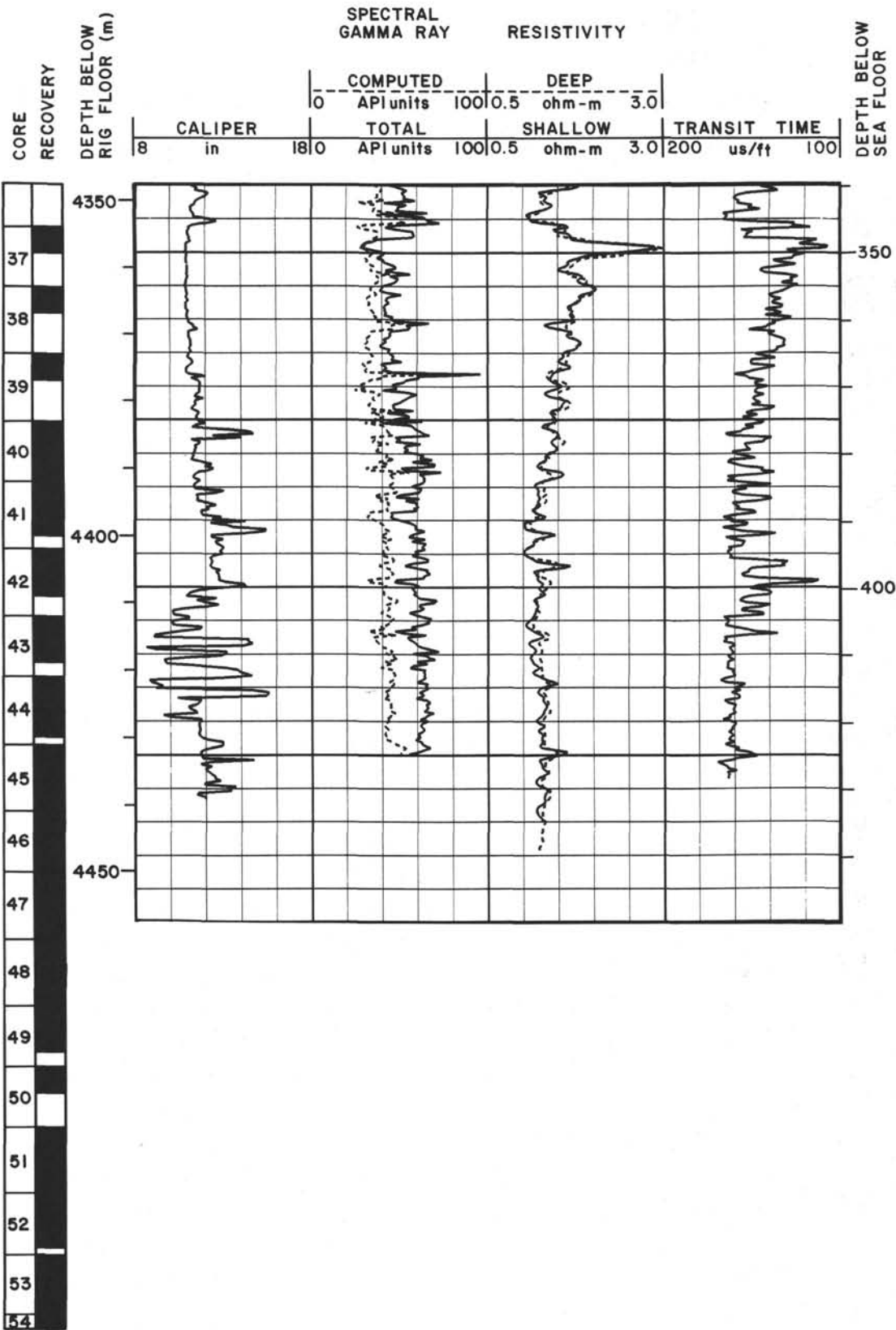
CORE RECOVERY	DEPTH BELOW RIG FLOOR (m)	SPECTRAL GAMMA RAY		RESISTIVITY		TRANSIT TIME		DEPTH BELOW SEA FLOOR
		COMPUTED	DEEP	SHALLOW	DEEP	200	100	
		API units	ohm-m	ohm-m	ohm-m	us/ft	us/ft	
		0	100	0.5	3.0			
		8 in	180					
		TOTAL						
		API units	100	0.5	3.0	200	100	

19
20
21
22
23
24
25
26
27
28
29
30
31
32
33
34
35
36

DATA RECORDED OPENHOLE

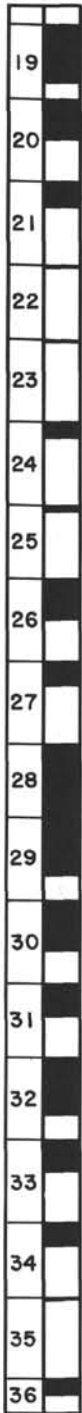


Summary Log for Site 766A (continued)

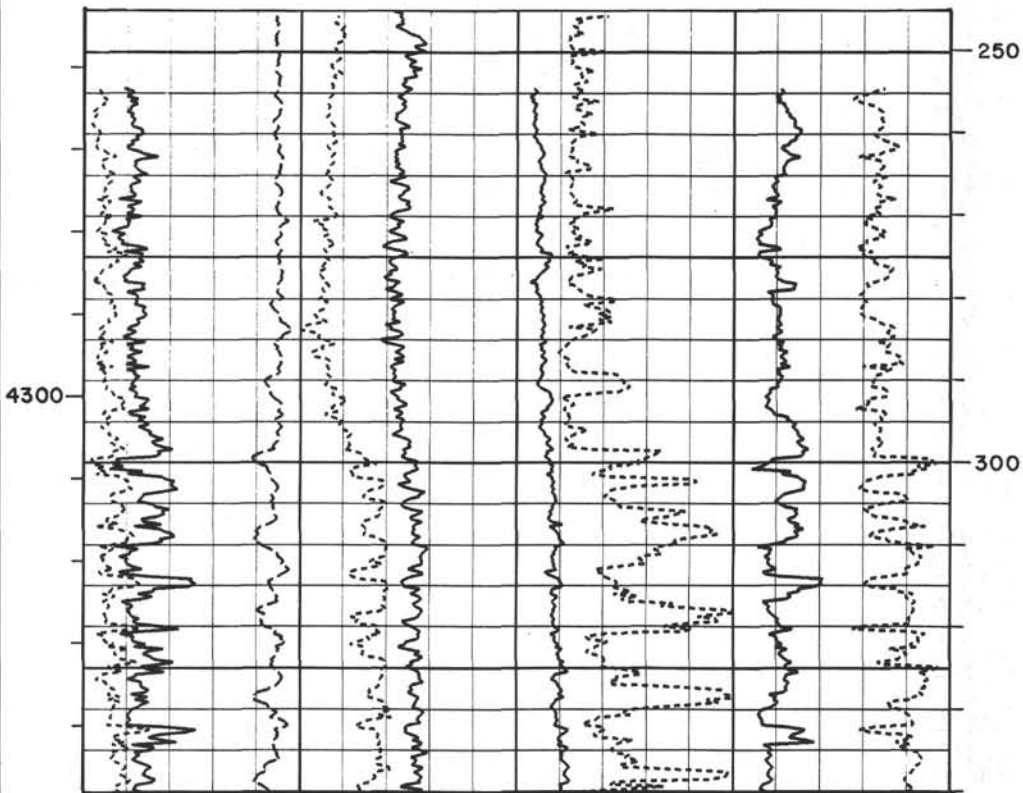


Summary Log for Site 766A (continued)

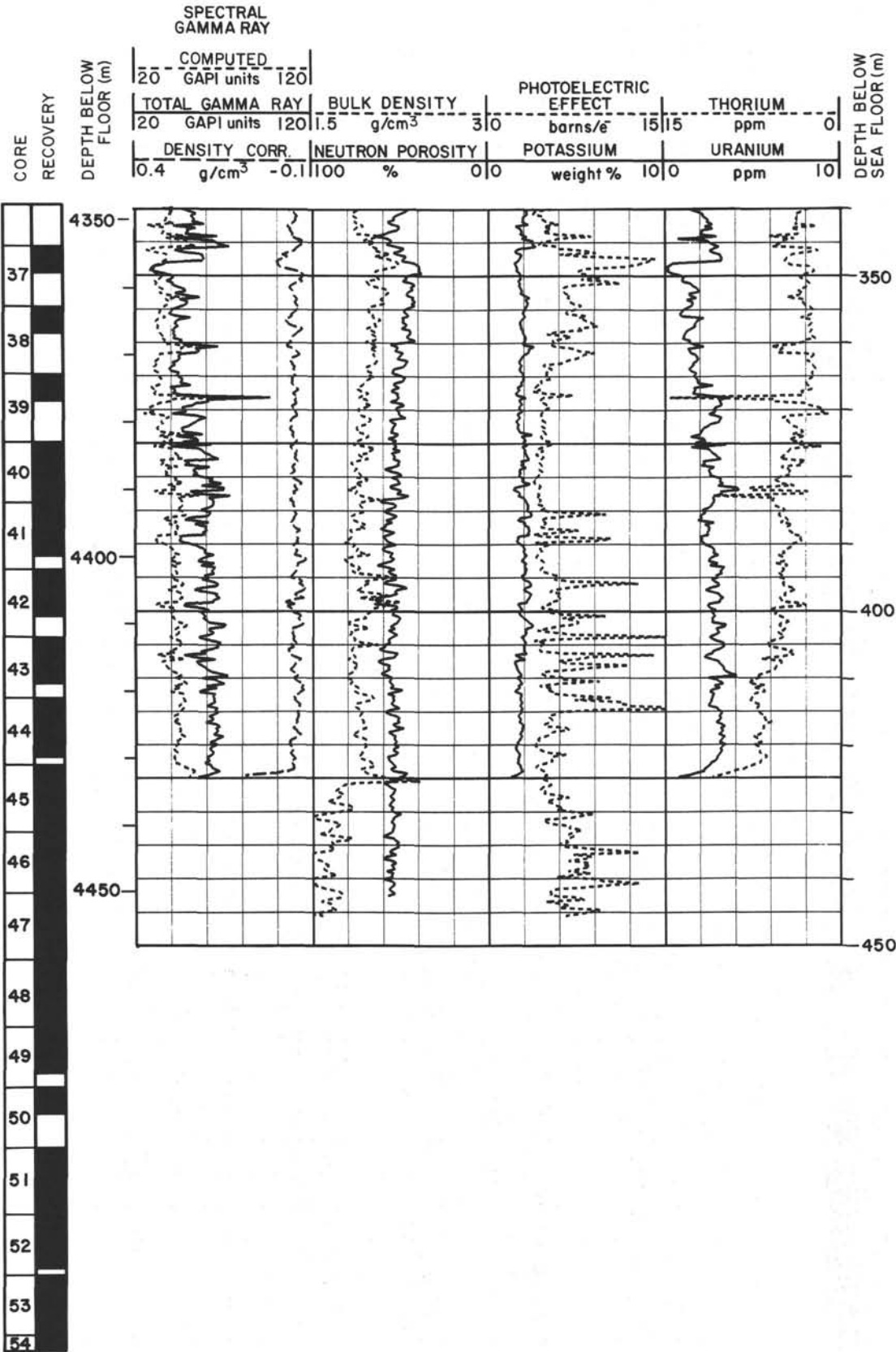
CORE RECOVERY	SPECTRAL GAMMA RAY										DEPTH BELOW SEA FLOOR (m)
	COMPUTED		TOTAL GAMMA RAY		BULK DENSITY		PHOTOELECTRIC EFFECT		THORIUM		
	20	120	20	120	1.5	3.0	15	15	0	0	
	GAPI units		GAPI units		g/cm ³		barns/e		ppm		
DENSITY CORR.		NEUTRON POROSITY		POTASSIUM		URANIUM					
0.4 g/cm ³ -0.1		100 % 0 0		weight % 10 0		ppm		10			



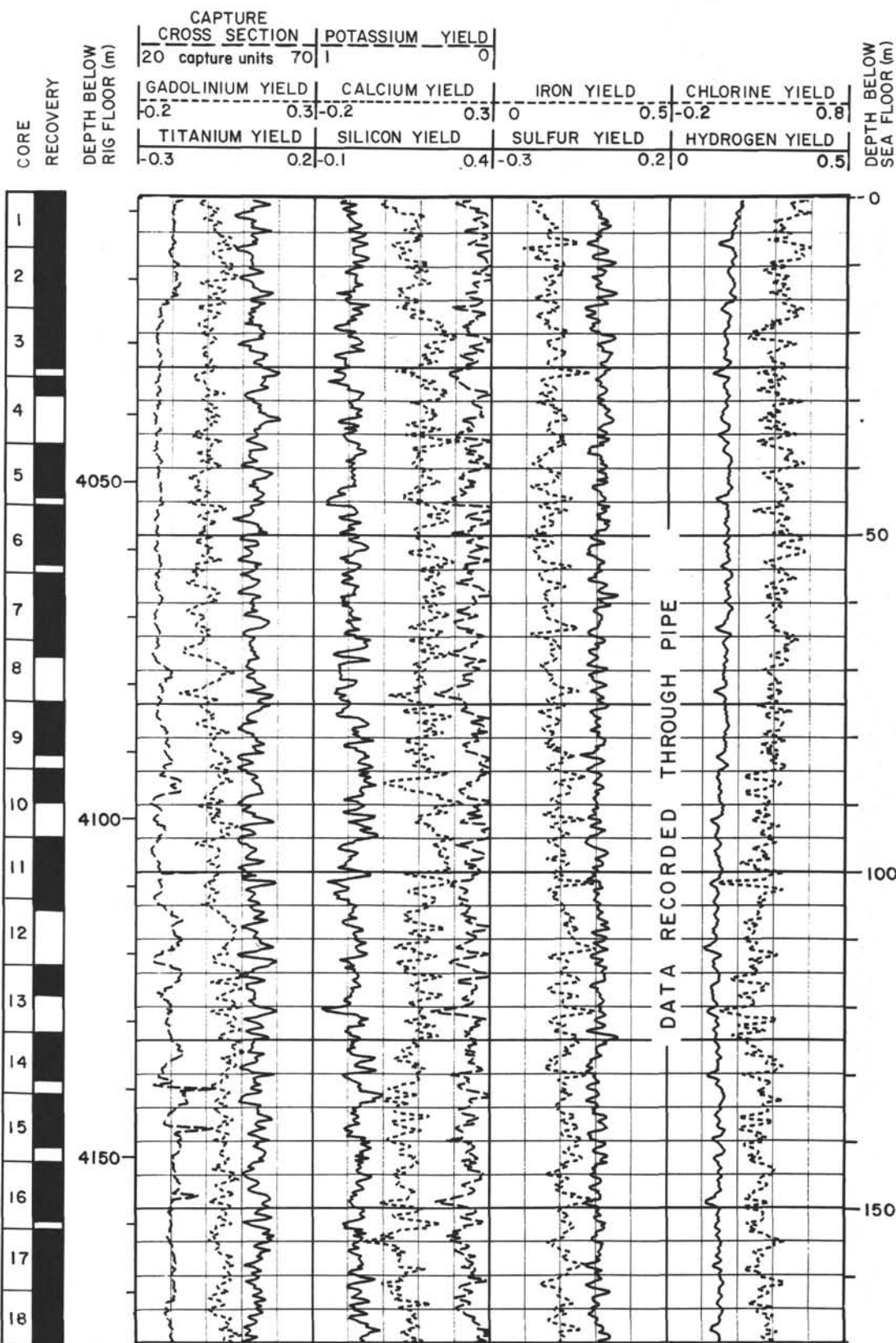
DATA RECORDED OPENHOLE



Summary Log for Site 766A (continued)

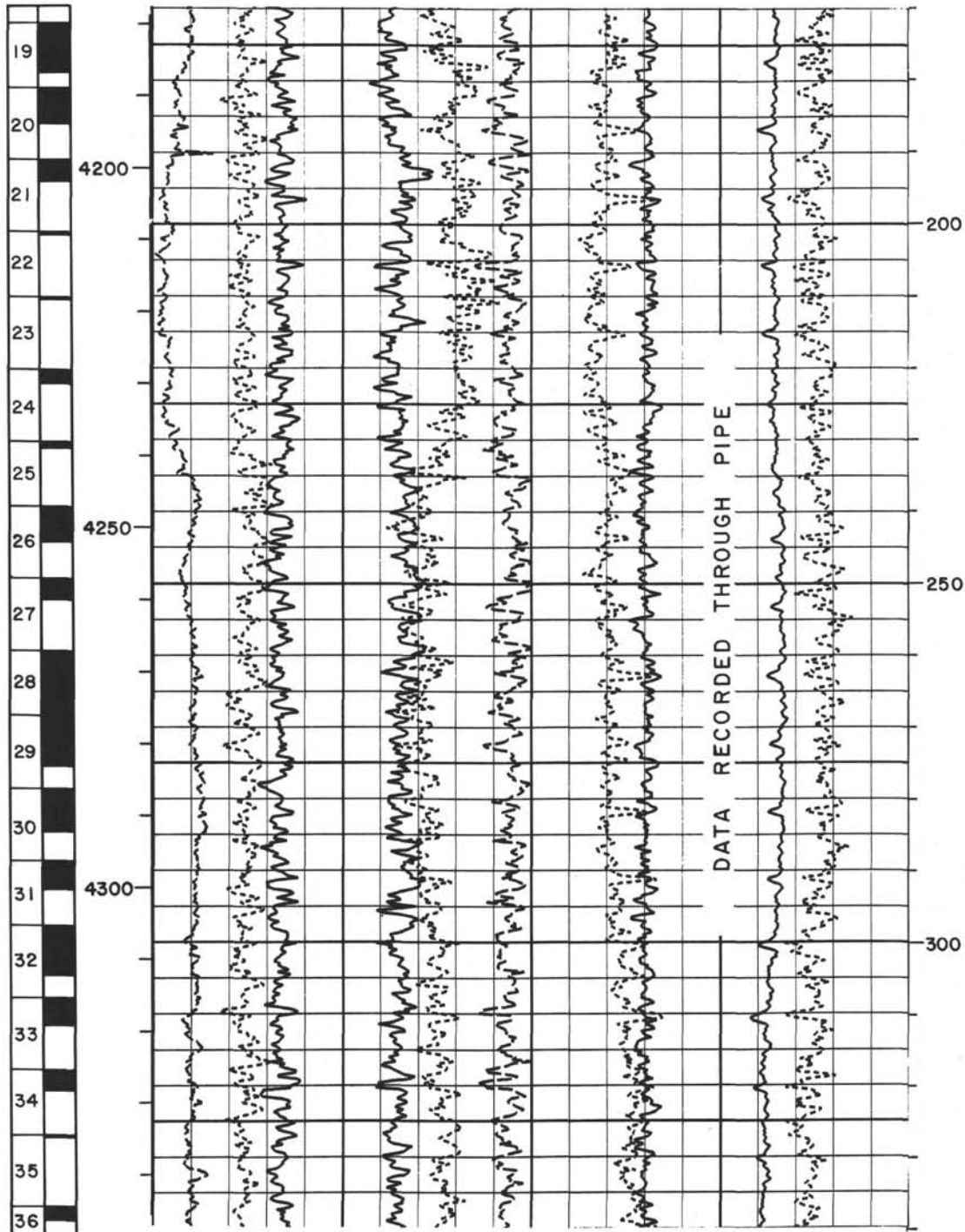


Summary Log for Site 766A (continued)



Summary Log for Site 766A (continued)

CORE RECOVERY	CAPTURE		POTASSIUM		YIELD		DEPTH BELOW SEA FLOOR (m)	
	CROSS SECTION		70		1			
	20 capture units				0			
DEPTH BELOW RIG FLOOR (m)	GADOLINIUM YIELD		CALCIUM YIELD		IRON YIELD		CHLORINE YIELD	
	-0.2		0.3		-0.2		0.3	
	0.5		-0.2		0.8			
DEPTH BELOW SEA FLOOR (m)	TITANIUM YIELD		SILICON YIELD		SULFUR YIELD		HYDROGEN YIELD	
	-0.3		0.2		-0.1		0.4	
	-0.3		0.2		0		0.5	



Summary Log for Site 766A (continued)

